UNIVERSIDADE DE LISBOA

INSTITUTO SUPERIOR TÉCNICO

Displacement Measurement through InSAR Geodesy for Structural Health Monitoring

Dora Luísa Ferreira da Luz Roque

Supervisor: **Doctor** Ana Paula Martins Falcão Flôr

Co-supervisors: **Doctor** Ana Maria de Barros Duarte Fonseca

Doctor José Antero Senra Vieira de Lemos

Thesis approved in public session to obtain the PhD Degree in

Civil Engineering

Jury final classification: Pass with Distinction

2020

UNIVERSIDADE DE LISBOA
INSTITUTO SUPERIOR TÉCNICO

Displacement Measurement through InSAR Geodesy for Structural Health Monitoring

Dora Luísa Ferreira da Luz Roque

Supervisor: **Doctor** Ana Paula Martins Falcão Flôr
Co-supervisors: **Doctor** Ana Maria de Barros Duarte Fonseca
Doctor José Antero Senra Vieira de Lemos

Thesis approved in public session to obtain the PhD Degree in
Civil Engineering

Jury final classification: Pass with Distinction

Jury

Chairperson: Doctor António Heleno Cardoso, Instituto Superior Técnico da Universidade de Lisboa

Members of the Committee:

Doctor Maria de Lurdes Baptista da Costa Antunes, Laboratório Nacional de Engenharia Civil

Doctor Joaquim João Moreira de Sousa, Escola de Ciências e Tecnologia da Universidade de Trás-os-Montes e Alto Douro

Doctor Maria da Conceição Esperança Amado, Instituto Superior Técnico da Universidade de Lisboa

Doctor Rui Pedro Carrilho Gomes, Instituto Superior Técnico da Universidade de Lisboa

Doctor Ana Paula Martins Falcão Flôr, Instituto Superior Técnico da Universidade de Lisboa

FUNDING INSTITUTIONS

Laboratório Nacional de Engenharia Civil
Fundação para a Ciência e a Tecnologia

2020

To my father

Título Medição de deslocamentos através de geodesia InSAR para o controlo de segurança de estruturas

Nome Dora Luísa Ferreira da Luz Roque

Doutoramento em Engenharia Civil

Orientador Ana Paula Martins Falcão Flôr

Co-orientadores Ana Maria de Barros Duarte Fonseca e José Antero Senra Vieira de Lemos

Resumo

A interferometria por RADAR de abertura sintética é uma técnica de geodesia aplicada, que permite a medição de deslocamentos a partir de imagens de satélite. A revisão da literatura dos princípios da técnica e de estudos anteriores relativos à sua aplicação ao controlo de segurança de estruturas possibilitou a identificação de alguns entraves à utilização operacional desta tecnologia de elevado custo-benefício na monitorização de estruturas.

Foram definidas três linhas de investigação. A primeira foi o desenvolvimento de uma estratégia de exploração de dados para extração de informação relativa ao comportamento estrutural, a partir de séries temporais de deslocamento de milhares de pontos na região de interesse e com dezenas de épocas de observação para cada ponto. A segunda linha foi a integração de deslocamentos obtidos por esta técnica num sistema de monitorização de estruturas já existente, tendo este sido ampliado para um maior número de pontos na estrutura e na sua envolvente. A terceira linha foi o desenvolvimento de uma infraestrutura experimental para a realização de testes para validação de deslocamentos e determinação da sua incerteza. A infraestrutura incluiu um novo modelo de refletor artificial para os sinais do satélite, desenvolvido nesta tese.

Os métodos desenvolvidos permitiram a monitorização bem-sucedida de diferentes tipos de estruturas civis e geotécnicas. Foi monitorizado o comportamento de taludes na vizinhança de albufeiras, foram detetadas inclinações em edifícios numa zona de património cultural e identificadas as reações de uma barragem de betão a variações de temperatura. O trabalho experimental mostrou concordância entre os deslocamentos da técnica e os obtidos por outros métodos geodésicos, tendo sido obtidas incertezas para os deslocamentos de aproximadamente 2 mm.

Concluindo, a interferometria por RADAR de abertura sintética é uma técnica promissora, com capacidade para fornecer informação útil para a monitorização de estruturas, como apoiar o planeamento de monitorizações *in situ* e identificar padrões espácio-temporais no

comportamento estrutural. Graças à sua cobertura espacial, período de observação de alguns dias e incerteza obtida, é vantajoso complementar sistemas de monitorização de estruturas já existentes com dados desta técnica.

Palavras-chave: sistemas de monitorização de estruturas; geodesia; interferometria por RADAR de abertura sintética; exploração de dados; análise de incerteza.

Title Displacement measurement through InSAR geodesy for structural health monitoring

Abstract

Interferometric synthetic aperture RADAR is an applied geodesy technique, which enables displacement measurement through satellite images. A literature review of the technique principles and of previous studies regarding its application to structural health monitoring allowed the identification of a few bottlenecks to the operational usage of this cost-effective technology for monitoring purposes.

Three research lines were defined. First, a data mining strategy was developed to extract structural behaviour information from displacement time series from thousands of points on the region of interest, with tens of observation epochs each. Second, displacements from this technique were integrated into a previously existing monitoring system and were used to expand it to a larger number of points on the structure and to its surroundings. Third, an experimental infrastructure was deployed in order to perform several tests for displacement validation and uncertainty assessment. The infrastructure included a new model of artificial reflector to the satellite signals, purposefully developed in the scope of this study.

The developed methods enabled the successful monitoring of different types of civil and geotechnical structures. Slope behaviour around water reservoirs was assessed during both the reservoir first impoundment and regular operation. Differential displacements were detected on building-blocks at a cultural heritage urban area and concrete arch dam responses to temperature loads were identified. The experimental work showed the achieved displacements agreed with those of other geodetic techniques and uncertainties around 2 mm were obtained for the measurements.

In conclusion, interferometric synthetic aperture RADAR is a promising technique, able to provide useful information for structure monitoring, such as aiding in the planning of *in situ* monitoring activities and in identifying space-time patterns in structural behaviour. Thanks to its spatial coverage, observation period of a few days and achieved displacement uncertainty, it is advantageous to complement existing monitoring systems with data from this technique.

Key-words: structure monitoring systems; geodesy; interferometric synthetic aperture RADAR; data mining; uncertainty analysis.

Acknowledgements

Many people have contributed to the study presented in this thesis. I would like to express my gratitude to everyone who manifested their interest on the subject of InSAR, who made questions, comments, suggestions and helped with the data interpretation. Special acknowledgements are due to:

- My supervisors, Professor Ana Paula Falcão, Researcher Ana Maria Fonseca and Researcher José Vieira de Lemos, for accepting to supervise this research, the fruitful discussions, support and timely feedback;
- Professor Daniele Perissin, the author of SARPROZ, for allowing me to use his amazing software and for his help with data processing at the initial stage of the study;
- Everyone in LNEC's Concrete Dam Department, especially in the Applied Geodesy Unit. Here I must highlight Researcher Nuno Lima, for expressing interest in this work and support with the usage of the GNSS data; Researcher Maria João Henriques, also for her interest in this study and for letting me use the computer for InSAR processing; Technicians Aires Moita and José Alberto Santos for doing the levelling operations and support with the reflectors' installation and maintenance;
- The team of LNEC's Scientific Instrumentation Centre, for designing, building and installing the bidirectional reflector I idealised;
- Professor João Catalão, from the Faculty of Sciences of the University of Lisbon, for lending the triangular trihedral reflectors;
- The colleagues at LNEC for their encouragement, support and good mood at lunch time;
- My family and long-time friends, for all their support – my mother, my sister, Daniel, Cláudia, Fábio, Luísa, Ana Sofia, Rute, Sara;
- The National Laboratory for Civil Engineering, the Foundation for Science and Technology and the European Social Fund, for funding and providing the conditions for the execution of this study;
- EDP – Energias de Portugal, for allowing the usage of Baixo Sabor dam data.

Table of contents

List of figures

List of tables

List of acronyms and abbreviations

ADA	Active Deformation Areas
AGU	Applied Geodesy Unit
APS	Atmospheric Phase Screen
AR	AutoRegressive models
CAT	Compact Active Transponder
CDD	Concrete Dam Department
COVID-19	Coronavirus Disease 2019
CPS	Cousin Persistent Scatterers
CRInSAR	Corner Reflector Interferometric Synthetic Aperture RADAR
CRs	Corner Reflectors
csv	Comma-Separated Values
CTTC	Centre Tecnològic de Telecomunicacions de Catalunya
CUPiDO	Connecting Undifferenced Points in Deformation Observations
DBSCAN	Density-Based Spatial Clustering of Applications with Noise
DEM	Digital Elevation Models
DePSI	Delft University of Technology PSI method
DFT	Discrete Fourier Transform
DInSAR	Differential Interferometric SAR
DSs	Distributed Scatterers
DTW	Dynamic Time Warping
DWT	Discrete Wavelet Transform
EnviSat	Environmental Satellite
ERS	European Remote-sensing Satellite
ESA	European Space Agency
EU-DEM	European Digital Elevation Model
GCP	Ground Control Point
GINS	Geographical Information National System
GIS	Geographic Information Systems
GLONASS	GLObal NAvigation Satellite System
GNSS	Global Navigation Satellite System
GPS	Global Positioning System
GRD	Ground Range Detected
HMM	Hidden Markov Models
HST	Hydrostatic-Seasonal-Time
HTT	Hydrostatic-Temperature-Time
IDW	Inverse Distance Weighted
InSAR	Interferometric Synthetic Aperture RADAR
IPTA	Interferometric Point Target Analysis
IW	Interferometric Wide
k-NN	k-Nearest Neighbour

LCSS	Longest Common Subsequence
LiDAR	Light Detection And Ranging
LNEC	*Laboratório Nacional de Engenharia Civil*
LOS	Line-Of-Sight
LPC	Linear Predictive Coding
LUT	Look-Up-Table
MAI	Multiple Aperture Interferometry
MHT	Multiple Hypothesis Testing
MUSE	MUltipass Scattering Equipment
MVC	Method of Variation of Coordinates
NASA / JPL	National Aeronautics and Space Administration / Jet Propulsion Laboratory
OBIA	Object-Based Image Analysis
PCA	Principal Component Analysis
pdf	Portable Document Format
POLInSAR	Polarimetric SAR Interferometry
POT	Pixel-Offset Tracking
PSC	Permanent Scatterers Candidates
PSI	Persistent Scatterer Interferometry
PSIG	PSI Chain of the Geomatics Division
PSInSAR	Permanent Scatterers InSAR
PSP	Persistent Scatterer Pairs
PSs	Persistent Scatterers
QPS	Quasi-Permanent Scatterers
RADAR	Radio Detection and Ranging
RCS	RADAR Cross Section
RMSE	Root Mean Square Error
ROI	Region of Interest
RPCD	Recurrence Patterns Compression Distance
RTK	Real-Time Kinematic
SAR	Synthetic Aperture RADAR
SBAS	Small BAseline Subset
SCR	Signal-to-Clutter Ratio
SDQI	SAR Dataset Quality Index
SHM	Structural Health Monitoring
SISTEM	Simultaneous and Integrated Strain Tensor Estimation from Geodetic and Satellite Deformation Measurements
SLC	Single Look Complex
SRTM	Shuttle RADAR Topography Mission
SSE	Sum of Squared Error
StaMPS	Stanford Method for Persistent Scatterers
STL	Seasonal-Trend decomposition procedure based on Loess
TomoSAR	Tomographic SAR
TOPSAR	Terrain Observation with Progressive Scans SAR

UAV	Unmanned Aerial Vehicles
UTC	Coordinated Universal Time
VHR	Very High Resolution
WLS	Weighted Least Squares
WRF	Weather Research and Forecasting Model
ZWD	Zenith Wet Delays

Chapter 1. Introduction

1.1. Motivation

The research presented in this thesis intends to explore data from the Interferometric Synthetic Aperture RADAR (InSAR) technique and to evaluate the contribution this technology may be able to provide in the field of Structural Health Monitoring (SHM). InSAR is an applied geodetic technique, based on Radio Detection and Ranging (RADAR) images, which enable a remote and non-invasive assessment of the object of interest condition through the analysis of the interaction between the object and microwave radiation. This technique has been used in construction of Digital Elevation Models (DEM), deformation monitoring or atmospheric studies (Massonnet and Feigl, 1998). The presented research was focused on the use of the technique for displacement measurement, which was the reason why the term "InSAR geodesy" was referred to in the title. For the sake of brevity, only "InSAR" will be used throughout the remainder of the text. The study relied on Synthetic Aperture RADAR (SAR) systems transported by satellites, with revisit periods of a few days; therefore, only slow varying displacements were considered and dynamic analysis was not performed, which would only be possible through ground-based systems with an observation frequency of a cycle in a few minutes (Monserrat *et al.*, 2014).

The importance of remote monitoring is increasing in nowadays fast changing world. Climate change is bringing more extreme meteorological events (Aalst, 2006), with increased frequency, which were not considered in the design of older structures. Furthermore, seismic actions to be considered in design have become more severe in many regions and new design codes often impose stricter requirements (Lynch and Loh, 2006). SHM is a key activity to verify if structures still follow their behaviour requirements, through the analysis of their responses to the new loads they are subjected to, and whether they fulfil their expected safety conditions.

Remote monitoring systems enable large scale monitoring tasks (Kim *et al.*, 2013), resulting in economic and environmental benefits, as the transportation of monitoring teams can be reduced.

In the actual context of Coronavirus Disease 2019 (COVID-19) pandemics, this topic becomes even more relevant.

Among the many variables considered for SHM, displacements measured through geodetic techniques are a valuable input (LNEC, 1989). A cost-effective and remote method for displacement measurement at the structures and their surroundings may provide important data for the evaluation of the safety conditions, by detecting early signs of possible displacement anomalies, which would enable a more efficient planning of *in situ* monitoring tasks.

InSAR based on satellite platforms are a promising choice for a remote displacement measurement technique. This technology enables displacement measurement for large areas, possibly thousands of square kilometres observed simultaneously, which may include the structure and its surroundings, and with a revisit period of a few days. The usage of RADAR technology allows the observation of Earth surface during both day and night and through cloud cover (Ferretti, Monti-Guarnieri, *et al*., 2007). Large SAR image datasets can be used for displacement measurement at a high number of points, naturally materialised on the structure and its surroundings, possibly located in difficult access places and with millimetre precision. Although InSAR is an already operational technique for monitoring geodynamic events, such as deformation caused by earthquakes or volcanic eruptions, its application to structure monitoring, which requires a lower displacement uncertainty, still poses a challenge. InSAR measurements are performed along the sensor Line-Of-Sight (LOS), which is oblique with respect to the Earth surface and hardly coincides with the directions of interest for structure monitoring. The slant direction of LOS leads to geometric effects, which avoid displacement measurement at locations in the signal shadow or superposition areas (Ferretti, Monti-Guarnieri, *et al*., 2007).

Technologic advances and recent data availability policies are having an important role in the spreading of this technology through the scientific community. The first used InSAR technique enabled displacement measurement with centimetre precision (Massonnet and Feigl, 1998), later improved to millimetre precision mesurements (Ferretti *et al*., 2001), when systematic image acquisition began in the 1990s and larger image datasets became available. High resolution images appeared around 2007, allowing an increase in the number of object points from hundreds to thousands or even tens of thousands per square kilometre in urban areas. The European Space Agency (ESA) has adopted a policy of sharing the data from its satellites for free, through the Copernicus programme, facilitating the access to the data and representing an important contribution to the cost-effectiveness of the technique.

This study was performed at the Applied Geodesy Unit (AGU) of the Concrete Dam Department (CDD) of the Portuguese National Laboratory for Civil Engineering (*Laboratório*

Nacional de Engenharia Civil – LNEC) and at the Department of Civil Engineering, Architecture and Georesources of Technical Superior Institute – University of Lisbon, Portugal. AGU has decades of experience of displacement measurement through geodetic methods for structure monitoring, such as classic surveying methods or Global Navigation Satellite System (GNSS). The portfolio of techniques for the acquisition of geographic information with the goal of aiding SHM has grown to include Earth observation and Unmanned Aerial Vehicles (UAV) data. This thesis intends to contribute to the inclusion of InSAR into the set of available techniques at AGU, in order to complement the existing information from other methods. The research was developed in the scope of a research project of LNEC's 2013-2020 plan for research and innovation called "InfraSAR – SAR interferometry with permanent scatterers (PSInSAR) applied to displacement detection in geodynamics and infrastructures".

1.2. Research objectives

InSAR is a promising technique for displacement measurement, but the usage of its displacements for structure monitoring led to some research questions, which this study intends to answer, namely:

- How to explore the InSAR data to detect changes in the structures' behaviour that may aid to identify anomalies?
- Is it possible to obtain displacements along the directions of interest for structure monitoring through data combination, with uncertainty similar to that of the traditional geodetic methods?
- How much is the uncertainty of InSAR displacements?

The main objective of this thesis was to evaluate the potential and limitations of InSAR displacements to be applied to SHM and to develop strategies to overcome some of the identified difficulties. In order to pursue this goal, three research areas were identified, from which three research objectives were defined.

First, InSAR products, if multitemporal techniques are used, can provide displacement measurements for a large number of points, during a long time interval and with high observation frequency, which results in a large amount of data to analyse. The visual analysis of thousands of displacement time series, with tens of observation epochs each, is time consuming and subjective. Automatic methods for time series analysis are needed to objectively identify patterns in the data and to detect signs that may correspond to eventual anomalies in structure behaviour.

Second, InSAR is useful to monitor structures where there are no other data available, such as old structures without embedded equipment that are not frequently observed through other

geodetic techniques, or even to monitor the structures' surroundings, whose stability contribute largely to the structure safety conditions, but are not evaluated so often. However, InSAR may also bring value added to complement the observations from other techniques in existing structure monitoring systems, by providing measurements at new points, new epochs, along a distinct direction and enabling the extension of the existing systems, focused on the structure, to its surroundings. Thus, there is the need for the development of techniques to integrate InSAR data into existing structure monitoring systems, evaluate the achieved measurement uncertainty and search for eventual displacement anomalies.

Third, unlike other geodetic methods, InSAR is a displacement measurement technique without redundant observations, as each point is observed a unique time at each image acquisition epoch; therefore, *a posteriori* variances, which are of vital importance for SHM as they provide the uncertainty level of the displacements, are not determined. Besides, several variables influence the quality of InSAR measurements, such as the brightness of the reflective target with respect to its surroundings (Signal-to-Clutter Ratio – SCR), the adequacy of the measured displacements to an assumed displacement model or even the direction along which the displacement occurs. Experimental installations, formed by artificial reflectors to the SAR signal, are required to enable the evaluation of the influence of each parameter on the displacement uncertainty. These devices enable the univocal identification of the SAR reflective centre, necessary to compare displacements from InSAR and a reference (more precise) geodetic technique, in order to perform displacement validation and uncertainty assessment.

Therefore, the objectives of this research are:

- To design a workflow (and implement it in a computer tool) that allows the evaluation of a large number of displacement time series in an objective way and application-independent;
- To evaluate displacements resulting from combination of InSAR datasets, or of InSAR with other techniques, and verify if the uncertainty-level required for SHM is achieved;
- To design, implement and operate an experimental corner reflector infrastructure that will enable the determination of displacement uncertainty in different scenarios.

1.3. Contributions

The main contribution of this research is the uptake of InSAR technology for structure monitoring purposes, with all its inherent benefits, regarding the observed area, number of object points, observation frequency and measurement precision. Furthermore, this study led to the development of computer tools that allow a more efficient exploration of the InSAR derived data

and of new equipment, which besides uncertainty analysis, may also be useful to establish the connection between data from InSAR and other measurement techniques.

In the scope of this thesis, two computer tools were developed in R software (R Core Team, 2018). One executes the automatic analysis of InSAR displacement time series and aggregates object points into clusters of similar displacement patterns, facilitating the identification of eventual anomalies on structure behaviour. The other tool uses a well-known technique, the Method of Variation of Coordinates (MVC), to integrate InSAR displacements into an existing GNSS monitoring system, to determine adjusted displacements along LOS direction and *a posteriori* variances for object points on a structure and on its surroundings. Furthermore, a new model of artificial reflector to the SAR signal, capable to provide measurements for the same target from distinct SAR acquisition geometries, is proposed, after being projected, constructed, deployed and tested at LNEC.

The research associated to the first objective, the analysis of InSAR displacement time series, was presented at SARWatch Workshop – Advances in the Science and Applications of SAR Interferometry through an oral presentation in Lisbon, Portugal, in 2018, for one of the case studies presented in this document (Roque *et al.*, 2018). Studies related to the third objective, InSAR displacement uncertainty evaluation at artificial reflectors, were presented as a poster at Living Planet Symposium, in Milan, Italy, in 2019 and as an oral presentation by invitation at *Colloque G2 2019 Géodésie & Géophysique*, in Le Mans, France, in 2019. The submission of three papers, one regarding each objective, are planned for the near future.

1.4. Outline of the document

The thesis is formed by seven chapters. The first one is the present introduction, where the motivation for the proposed research is presented, the research objectives are highlighted, together with the contributions and publications achieved so far.

The second chapter presents a literature review of InSAR methods and of previous applications of this technology in the field of SHM.

Chapters 3, 4 and 5 are dedicated to each of the objectives presented in the previous section, with Chapter 3 regarding the analysis of InSAR displacement time series, called RADAR interpretation; Chapter 4 considering the integration of InSAR data in existing structure monitoring systems and Chapter 5 containing the measurements' uncertainty evaluation at an infrastructure of artificial reflectors. Each of these chapters contains a dedicated literature review, a methods section presenting the strategy proposed in each case, a section presenting how the proposed methods were applied to the particular case studies, the achieved results, their discussion and the conclusions.

Chapter 3 considers two case studies: the slopes around an embankment dam during the reservoir first impoundment and the buildings at a heritage urban area. Chapter 4 presents one case study: a concrete arch dam and its neighbour slopes. Finally, Chapter 5 is referred to an infrastructure of artificial reflectors to SAR signal installed at LNEC *campus*.

Chapter 6 contains a discussion considering the contributions of the previously mentioned three chapters to promote the operational usage of InSAR displacements at SHM applications. Chapter 7 summarises the main conclusions of the study and suggests some research topics for future research.

The document also contains a list of the bibliographic references cited throughout the text and three annex sections, one for each research objective, providing additional figures and tables.

Chapter 2. The usage of InSAR data for structure monitoring

2.1 Interferometric synthetic aperture RADAR

This section presents a literature review of InSAR techniques. It reports some basic principles of SAR image formation, the available acquisition systems and modes, applications and the evolution of the interferometric techniques. The first InSAR methods enabled DEM construction with precisions in the order of tens of metres and displacement determination at centimetre-level. The growing availability of stacks of SAR images, after the launch of satellites with SAR sensors on board for systematic acquisition in the 1990s, allowed a more precise determination of the parameters of interest, with altitudes and displacements being computed with metre and millimetre precisions, respectively. In the last 20 years, several research teams developed distinct InSAR methods and the combination of those strategies permitted the assessment of altitude and displacements with high precision for a large number of natural points, both on man-made structures and natural landscapes. A brief description of other techniques using SAR data is also provided in this section.

RADAR systems are active sensors that operate in the microwave band of the electromagnetic spectrum. The sensor itself emits the signal, which is reflected by the illuminated surface and returns to the sensor. As the system is independent of sunlight, data can be acquired during both day and night. Besides, microwave radiation can pass through clouds; therefore, image acquisition can be performed in all-weather conditions. The all-time and all-weather imaging capabilities of RADAR data can be important information sources in many situations. Emergency management is one of the fields in which RADAR remote sensing has a valuable contribution, e.g. for flood

monitoring through cloud cover (Pulvirenti *et al.*, 2011; Roque *et al.*, 2014), detection of wildfire scars (Kasischke *et al.*, 1992; Menges *et al.*, 2004) or oil spill detection (Azevedo, 2010).

RADAR images from the Earth surface started being acquired during the 1950s and in the 1970s image pairs began being analysed through the interferometric technique. An interferogram is an image of the phase difference between two RADAR images acquired in distinct epochs and it reflects, at each pixel, the distance between the sensor and the Earth surface (Massonnet and Feigl, 1998). Massonnet and Feigl (1998) listed several applications of the interferometric technique, such as monitoring deformation caused by earthquakes, volcanoes, glaciers, landslides, subsidence and agriculture activities. Due to the technique's capability to measure altitudes, DEM construction is also a frequent application (Goldstein *et al.*, 1988). The usage of interferograms to evaluate water vapour content in the atmosphere is also being exploited (Mateus *et al.*, 2017).

RADAR systems evolved to SAR systems, which result from the simulation of an antenna larger than its physical dimension by integrating observations of the same object acquired from distinct positions. This strategy allows an improved spatial resolution[1] along the direction of the platform movement with respect to real aperture RADAR systems and the images used nowadays are achieved through this method.

SAR sensors can be transported by different platforms. Data from sensors on board of satellites are widely used by the scientific community, due to their potential global coverage and availability from space agencies. Besides satellites, SAR sensors have been transported in other platforms, such as the space shuttle (Farr and Kobrick, 2000), unmanned aerial vehicles (Rosen *et al.*, 2006; Hensley *et al.*, 2008) or ground rails (Monserrat *et al.*, 2014; Di Traglia *et al.*, 2018; Carlà, Tofani, *et al.*, 2019). The present study uses satellite images and only these will be considered in the remainder of the text.

National Aeronautics and Space Administration / Jet Propulsion Laboratory (NASA / JPL) Seasat satellite, which operated only during 110 days in 1978, provided the first dataset of SAR images for scientific use. An increase in the usage of this type of data started in the 1990s, with the launch of European Remote-sensing Satellite-1 (ERS-1) by ESA in 1991, enabling the global coverage of the planet and the acquisition of images suitable for interferometry every 35 days (Massonnet and Feigl, 1998; ESA, 2020). ERS-1 was operated until 2000, but before the end of its mission, ESA launched its successor, the European Remote-sensing Satellite-2 (ERS-2), functioning between 1995 – 2011. ERS-2 was followed by the Environmental Satellite (EnviSat) between 2002 – 2012 and nowadays the mission is assured by Sentinel-1A and Sentinel-1B, launched in 2014 and 2016, respectively. ESA SAR sensors from ERS-1, ERS-2 and EnviSat

[1] Pixel size.

assured the continuity and compatibility of the images, allowing the analysis of long time series of data. Sentinel-1A/B brought a new generation of SAR images, achieved through a new imaging mode, improved spatial resolution, higher and regular acquisition frequency and wide coverage of a single scene. ESA SAR images are characterised by a coarse spatial resolution (in the order of tens of metres), usage of microwave C-band (wavelength of approximately 6 cm) and free distribution. ERS-1/2 and EnviSat data are available to scientific community through submission of a project proposal. However, Sentinel-1 data are freely available to any user through the European Union Copernicus program (managed by the European Commission and ESA).

Other spatial agencies have invested in Earth observation systems using SAR also for commercial purposes. It is the case of the Canadian, German, Italian, Japanese or South Korean space agencies, which commercialise data from the satellites Radarsat-1/2 (Canada), TerraSAR-X / TanDEM-X (Germany), COSMO-SkyMed-1/2/3/4 (Italy), JERS-1 and ALOS-1/2 (Japan), KOMPSAT-5 (South Korea). While Radarsat also has a C-band sensor, TerraSAR-X / TanDEM-X, COSMO-SkyMed-1/2/3/4 and KOMPSAT-5 transport X-band sensors (wavelength around 3 cm), which brought an increase in spatial resolution. The first of these sensors was launched in 2007 and their systems made available the first high resolution SAR images, appropriate for urban applications. The sensors on board of the Japanese satellites JERS-1 and ALOS-1/2 acquired / acquire images in L-band (wavelength around 24 cm), able to pass through vegetation foliage, which turn them appropriate to study vegetated areas. Despite being commercially available, small sets of images have been made freely available for research, under a project proposal, by the German, Italian, Japanese and South Korean agencies.

Recently, collaboration between agencies from different countries led to the launch of more satellites with SAR sensors. It is the case of Spanish satellite PAZ, launched in 2018, which follows the same orbit as TerraSAR-X / TanDEM-X and whose images are fully compatible to those from the German satellites. The images are destined to both military and commercial purposes. Argentina launched the SAOCOM-1A satellite in 2018, through a collaboration with the Italian agency, which transports an L-band sensor. A second satellite is expected to be launched in 2020. The Indian agency is collaborating with NASA to launch an L-band sensor on board of satellite NISAR planned to 2022, after having deployed RISAT-1 in 2012 in C-band (ESA, 2020). Figure 1 presents the satellites from space agencies that held or still hold SAR sensors on board.

Recently, private companies are entering the SAR business, which is contributing to the advance in this field of Earth observation. The Polish and Finnish company ICEYE is launching the first constellation of very small satellites with SAR sensors, with three spacecrafts on space in 2020, and they plan to start providing daily Very High Resolution (VHR) SAR images, for

commercial use, in 2021. The current system, which uses X-band sensors, already enables image acquisition with spatial resolution of 25 cm (ICEYE, 2020). The most recently launched satellites (both from private and national agencies) were transported to orbit by SpaceX Falcons, reducing the waiting time required for satellite launch approval and enabling the "return to launch site recovery" of the rocket, in some cases (ESA, 2020).

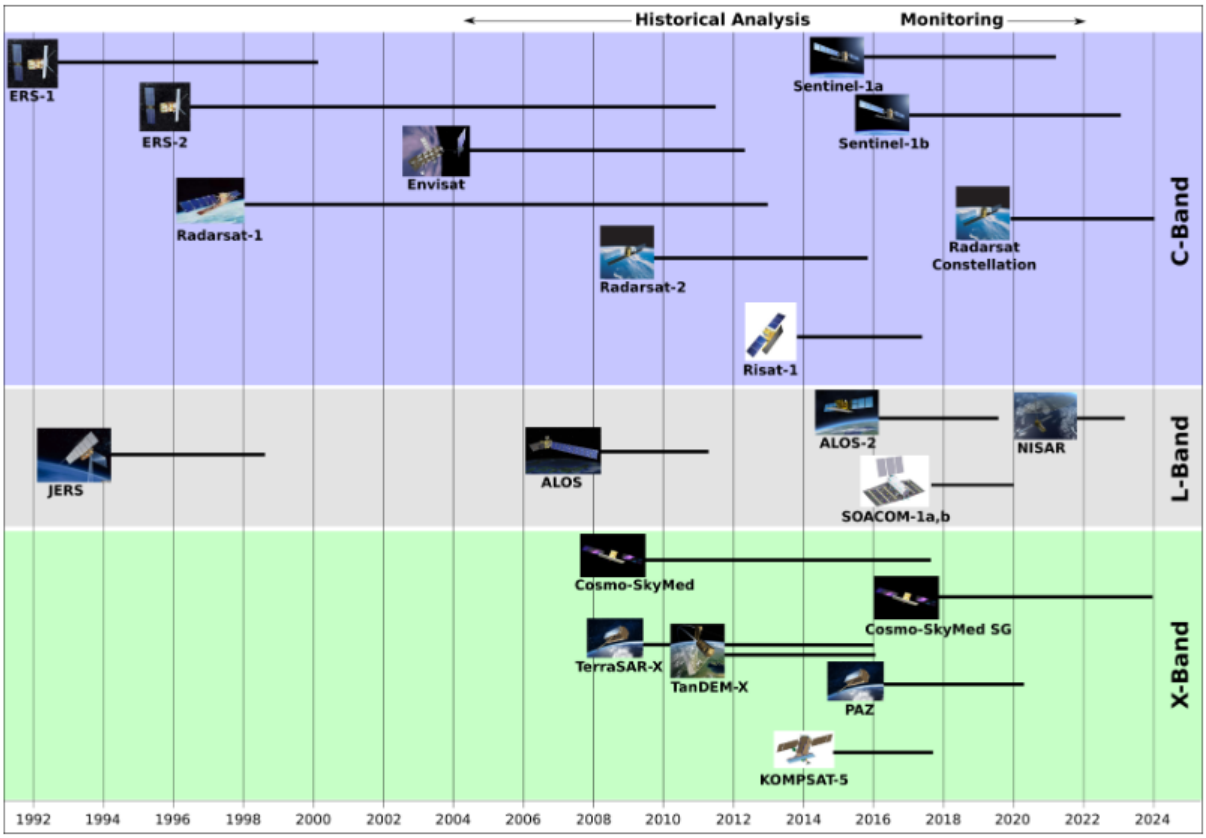

Figure 1 – Summary of satellites with SAR sensors, from (UNAVCO, 2020a).

There are distinct SAR image operation modes, which influence image spatial resolution and covered area. Stripmap mode considers a fixed antenna and the imaging of a continuous strip along the direction of satellite movement (along-track). In Spotlight mode, the antenna is steered along the direction of satellite movement, in order to increase the observation time of a Region of Interest (ROI) and the spatial resolution along that direction. On the other hand, the imaged area is limited to that ROI and continuous acquisition is not performed (Moreira *et al.*, 2013). ScanSAR mode steers the antenna in elevation, enabling a wider covered area, but lower spatial resolution along the direction of satellite movement. A new type of ScanSAR is used by the sensor on Sentinel-1 (Terrain Observation with Progressive Scans SAR – TOPSAR), where the antenna is steered in both elevation and along-track directions (ESA, 2020).

For example, for TerraSAR-X system, Stripmap images have a spatial resolution of 3 m x 3 m, Spotlight images have 2 m cross-track (perpendicular to direction of satellite movement) and 1 m

along-track, while ScanSAR images have 16 m x 16 m. Regarding swath coverage, it is lower than 1500 km along-track x 30 km cross-track for Stripmap, 10 km x 10 km for Spotlight and lower than 1500 km along-track x 100 km cross-track for ScanSAR (ESA, 2020).

At the image formation process, each portion of Earth surface, which is represented in a pixel (resolution cell) is attributed a two-dimensional coordinate: azimuth and slant range (Figure 2a). Azimuth is determined along the direction of the satellite movement and the image spatial resolution in this direction depends on the antenna dimension. In order to achieve a better resolution, a larger antenna is simulated by integrating the data of a certain location observed from different points along the orbit (SAR system). The slant range coordinate corresponds to the distance between the imaged point and the sensor and it is determined along the sensor LOS, which is perpendicular to the satellite trajectory and oblique with respect to the Earth surface. Spatial resolution in slant range direction depends on the pulse duration (Bamler and Hartl, 1998; Massonnet and Feigl, 1998). Satellites transporting SAR sensors have quasi-polar orbits, with azimuth direction being approximately in the north – south direction and the ground range (projection of slant range on the horizontal plane) almost along east – west. Images can be acquired with two geometries: ascending, when the satellite passes from south to north, and descending, when it passes from north to south (Figure 2b).

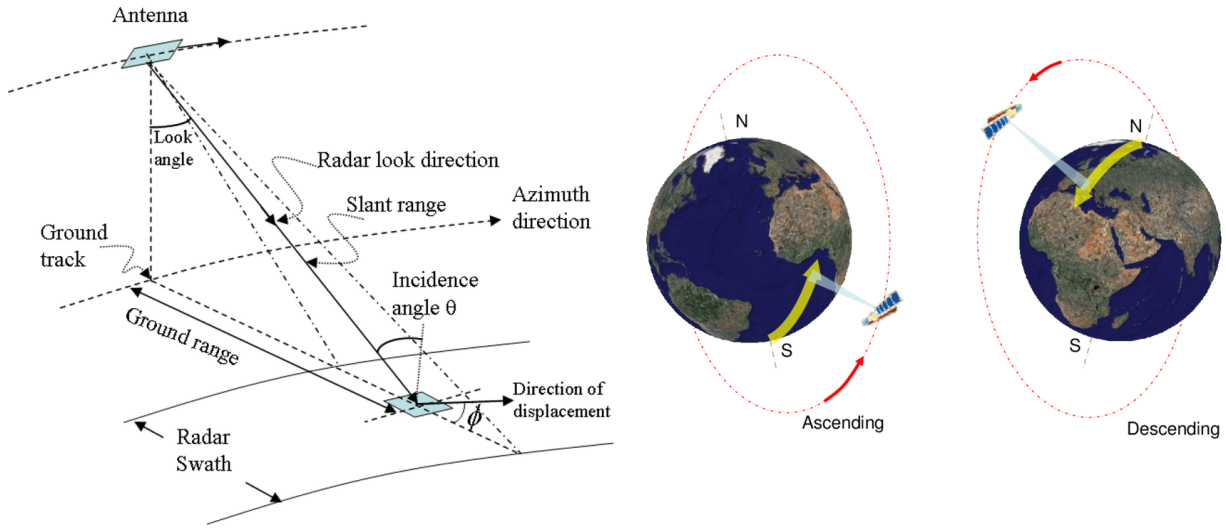

(a) (b)

Figure 2 – SAR imaging geometry (a), ascending and descending passes (b), from Confuorto (2016) and Bateson *et al.* (2010), respectively.

The electromagnetic signal reflected by the Earth surface and represented in a pixel is characterized by an amplitude and a phase, which are registered as a complex number. The amplitude is the strength of the signal reflected by the elements in the resolution cell and it

corresponds to the absolute value of the complex number. The phase is the argument of the complex number and results from the sum of the phases of the signal reflected by all elements represented in the pixel (Massonnet and Feigl, 1998).

An interferogram is a phase difference image that can be obtained after the corregistration[2] of a pair of SAR images. It is computed through the multiplication of the value of each pixel from one image (the master) by the complex conjugate of the corresponding value in the second image (the slave). There are several variables that contribute to the phase difference: orbital differences, terrain altitude, target motion, changes in atmospheric conditions, variations of scattering behaviour of imaged elements and instrumental artifacts. However, phase differences are known as a fraction of a cycle, having values varying between -π and π radians (wrapped phase). Altitude and displacements form fringe patterns in the interferograms and can be determined from them. For displacement computation, a DEM of the ROI can be used to remove the altitude-related fringes from the interferogram in order to isolate those caused by displacement (Figure 3). This technique is known as Differential Interferometric SAR (DInSAR). One fringe corresponds to a relative displacement between two points with magnitude of half a wavelength (Massonnet and Feigl, 1998).

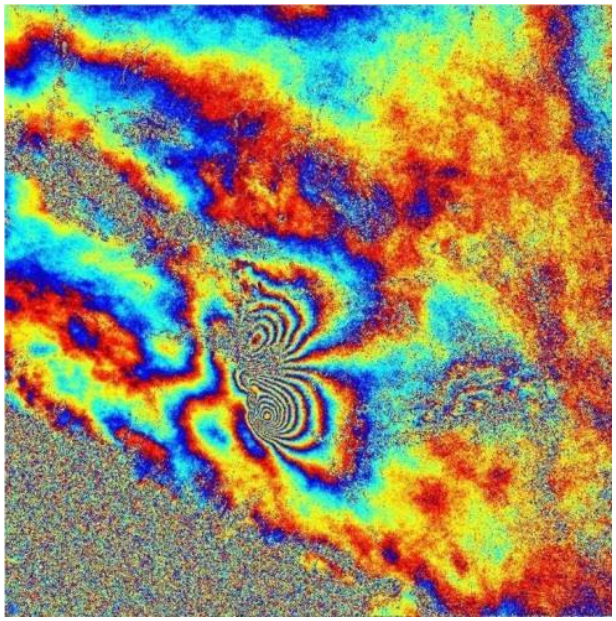

Figure 3 – Interferogram showing a fringe pattern caused by deformation during the Bam earthquake in Iran (Dentz *et al.*, 2006).

Phase unwrapping is the process of estimating the absolute phase values from the wrapped ones along a finite number of points. Its main assumption is that the diffence in unwrapped phase between neighbour points (either in space or in time) is lower than π and phase differences are

[2] The alignment between the images, pixel by pixel.

integrated along paths connecting the points where that condition is fulfilled. However, the above-mentioned assumption is not always verified, due to unsufficient point sample, displacement discontinuities or topographic effects on SAR images, which lead to errors that are integer multiples of 2π. Existing algorithms try to mitigate this limitation (e.g., Costantini, 1998; Hooper and Zebker, 2007; Piyush and Zebker, 2010).

The normalized cross-correlation coefficient between two SAR images i and j is called interferometric or spatial coherence ($\zeta^{i,j}$). It is determined for each pixel through Equation (1), where E[] is the mathematical expectation, * is the complex conjugate of a complex number and s_i and s_j are the complex numbers registered for the pixel in images i and j, respectively (Perissin and Wang, 2012). It provides a measure of the interferogram quality.

$$\zeta^{i,j} = \frac{E[s_i s_j^*]}{\sqrt{E[|s_i|^2]E[|s_j|^2]}} \quad (1)$$

When several interferograms are available, the multiinterferometric complex coherence γ can be considered, given by Equation (2), where N is the number of interferograms and w are the phase residuals resulting from the difference between the observed phase and a phase model across all interferograms (Colesanti *et al.*, 2003).

$$\gamma = \frac{1}{N}\sum_{i=1}^{N} e^{jw} \quad (2)$$

The absolute value of the multiinterferometric complex coherence $|\gamma|$ is called temporal coherence and provides a measure of the quality of the fit between the modeled and the observed phases. Its values vary between zero and one, with better fits corresponding to values closer to one.

DInSAR enables spatially continuous displacement measurement for wide areas; however, the results are affected by changes in targets' scattering properties and in SAR sensor point of view (named temporal and geometric decorrelations, respectively) and by atmospheric effects (Ferretti *et al.*, 2001). Temporal decorrelation happens when the time interval between image acquisitions is large, while geometrical decorrelation occurs for large distances between the image acquisition points. Atmospheric effects are caused by differences in atmospheric conditions at the image acquisition epochs, mainly related to the presence of water vapour, which introduces a delay in the signal. This results in a precision of tens of metres to altitude and of centimetres to displacement.

The continuously increasing archive of SAR images after the launch of ERS-1 enabled the development of new interferometric techniques to solve the limitations of DInSAR. Ferretti *et al.* (2001) proposed a method based on multitemporal SAR images. Instead of analysing all the pixels in an interferogram, they recommended the selection of a subset of pixels that keep their reflective properties in all images. These pixels, called Permanent Scatterers, do not suffer from temporal nor geometric decorrelation. The scatterer dimension should be smaller than that of the resolution

cell and they are identified in the images through an amplitude dispersion index (the ratio between the standard deviation and the average of amplitude values for all images in the stack), which approximates phase stability when signal to noise ratio is large. These points are called Permanent Scatterers Candidates (PSC) and they are used to estimate the atmospheric effects for each image (Atmospheric Phase Screen – APS). For the estimation, a set of interferograms is considered, in which one single image is selected as the master, while the remaining ones are used as slaves. The master image is chosen in order to minimise both temporal and normal baselines[3] of the image dataset. For each PSC in each interferogram, Equation (3) is used to estimate a constant (a1) and linear terms of APS (p_ξ and p_η), altitude (q) and average velocity[4] of the PSC along LOS (v). The equation is solved iteratively as the observed interferometric phase is wrapped.

$$\Phi = a1^T + p_\xi \xi^T + p_\eta \eta^T + Bq^T + Tv^T + E \quad (3)$$

In Equation (3), Φ is the interferometric phase, ξ and η are azimuth and slant range pixel coordinates, respectively, B is normal baseline, T is temporal baseline and E is the residuals, which contain remaining APS, non-linear displacement and phase noise due to decorrelation.

One of the components in the residuals of Equation (3) is the turbulent component of APS. In order to determine it, the residuals are filtered to isolate a low pass spatial component, which is then interpolated for each pixel. The interpolated values are removed from differential interferograms and the resulting phases (φ_n) are inputted into a periodogram, which corresponds to the temporal coherence (absolute value of Equation 2). For each pixel, the average velocity and the correction to the altitude that maximize the temporal coherence are estimated (Equation 4).

$$\arg\max_{\Delta q, v} \left\{ |\gamma| = \left| \frac{1}{N} \sum_{n=1}^{N} e^{j\varphi_n} \cdot e^{-j\left(\frac{4\pi}{\lambda R \sin\theta} \cdot B \cdot \Delta q + \frac{4\pi}{\lambda} \cdot T \cdot v\right)} \right| \right\} \quad (4)$$

In Equation (4), Δq is the correction for the initial DEM altitude value (called residual height), v is velocity, $|\gamma|$ is temporal coherence, N is the number of interferograms, λ is the signal wavelength, R is the distance between the sensor and the scatterer and θ is the incidence angle (angle between LOS and the vertical). Altitude correction and velocity precisions depend on phase stability and on the dispersion of normal and temporal baselines, respectively. This procedure is valid for small areas, where atmospheric and orbital effects can be considered linear, and for linear displacements. It is applied to a new pixel selection – the Permanent Scatterers – for which residual height and average velocity are determined. Furthermore, displacement time series are also computed for each Permanent Scatterer.

[3] Temporal baseline is the time interval between image acquisitions; normal baseline is the projection of the distance between the image acquisition points in the direction perpendicular to the master LOS.
[4] A linear displacement model is considered.

In Ferretti *et al.* (2000), the previously described algorithm was improved in order to better separate the atmospheric effect from the non-linear motion present in the residuals of Equation (3). The residuals are first averaged to obtain the APS of the master image. This APS signal is then removed from the original residuals, which are low pass filtered in space to isolate the non-linear displacement. The final APS of each interferogram is achieved by adding the master APS to the result of the application of a high pass filter in time and a low pass filter in the spatial domain to the original residuals. With this processing strategy, it is possible to isolate the atmospheric effects and to obtain sub-metre and millimetre precisions for altitude and displacements, respectively. This technique is known as Permanent Scatterers InSAR – PSInSAR.

After PSInSAR, many research groups developed new InSAR methods based on the analysis of multiple SAR images. The set of methods that uses a single master image is called Persistent Scatterer Interferometry (PSI) and the analysed scatterers are called Persistent Scatterers (PSs).

Interferometric Point Target Analysis (IPTA) is a method presented in Werner *et al.* (2003). It considers a single master approach and relies on the linear relationships between interferometric phases and perpendicular and temporal baselines for pairs of nearby scatterers. The regression slopes correspond to the relative residual height and velocity between the two scatterers. These are iteratively improved in successive algorithm applications.

Costantini *et al.* (2008) developed the Persistent Scatterer Pairs (PSP) method, which considers arcs between close scatterers. Scatterer selection depends on the arc quality and is performed iteratively until there are no new scatterers to add. Differential residual height and velocity are determined for each arc and integrated to obtain their values for each scatterer. After their removal from each scatterer phase, unwrapping is performed to obtain a non-linear component of displacement. As arcs tend to connect nearby scatterers, APS and orbit corrections can be neglected, which improves the algorithm performance with respect to other techniques.

Berardino *et al.* (2002) presented the Small BAseline Subset (SBAS) technique. Instead of considering a single master, each image from the dataset is connected to one or more images as long as their normal baselines are small, in order to minimise decorrelation effects. Their model estimates residual heights and constant velocity (or another displacement model known *a priori*) and it is applied on multilooked unwrapped differential interferograms. APS is estimated similarly to Ferretti *et al.* (2000, 2001). Velocity values are integrated to obtain phase and displacement values for each date. Pixel selection is performed based on coherence. Therefore, this method enables displacement measurement for a larger number of pixels than PSInSAR, especially in non-urban areas. This method uses Distributed Scatterers (DSs) instead of PSs, i.e., it considers the

phase contributions from all scatterers within the resolution cell and not only a dominant one like in PSInSAR.

In order to increase the number of scatterers in non-urban areas, Hooper *et al.* (2004) developed the Stanford Method for Persistent Scatterers (StaMPS). Instead of using amplitude time series for pixel selection (which are stable mainly on urban areas), this method selects pixels based on their phase stability. Scatterers are aggregated into patches with a certain dimension, within which displacement, atmospheric effect and orbit inaccuracies are spatially correlated. The interferometric phase is subtracted by the average phase of the scatterers inside the patch and a phase component is estimated for the residual height. The obtained residue is used to compute the temporal coherence and PS are selected through coherence thresholding (large coherence corresponds to low phase noise and therefore, to a PS). After PS selection, the estimated residual height is removed from the interferometric phase and phase unwrapping in space and time is performed. Except for the displacement component of phase, after the unwrapping, the other phase components which are spatially correlated are uncorrelated in time, thus displacement can be isolated through filtering. The strategy of selecting PS through phase stability instead of amplitude enables the detection and analysis of low amplitude scatterers typical from non-urban areas that would not have been selected by the PSInSAR algorithm.

The PSI method proposed by Delft University of Technology (DePSI) performs an initial selection of PSC with large amplitude stability and uses an iterative procedure to estimate the parameters of interest for a first order network that connects the PSC. At the iterative procedure, the integer phase ambiguities[5] and the floating values of displacement and altitude along the network are determined through integer least squares. Then, the parameters are unwrapped and hypothesis testing is used to identify incoherent points, which are removed from the analysis. APS and orbit inaccuracies are estimated for the remaining PSC, their components are removed from phase and the process is repeated. When the final network configuration and respective parameters are determined, the network is densified and the parameters for the new points are achieved from the parameters of the first network (Kampes, 2005; Ketelaar, 2008; Sousa *et al.*, 2011).

Another method developed to deal with the low scatterer density in non-urban areas is the Quasi-Permanent Scatterers (QPS), developed by Perissin and Wang (2012) that detects temporary scatterers, i.e., scatterers that do not keep their reflective behaviour stable in all images. For each scatterer, only the subset of the interferograms in which the scatterer shows good coherence is used. This is achieved by using spatial coherence (Equation 1) as a weight in the periodogram to

[5] The unknown number of integer cycles the signal travelled from the sensor to the object.

estimate velocity and residual height. A multimaster set of interferograms is used. Noise is reduced by filtering.

Hooper (2008) proposed a method to combine both PS and DS in order to increase the number of analysed points. The two types of scatterers are identified separately, from the same images, but from different interferograms. They are then combined before phase unwrapping, by recomputing differential phases for the PSs using the interferograms with the small baselines used for DSs. As this increases the density of analysed scatterers, phase unwrapping is more successful.

Ferretti *et al.* (2011) presented the SqueeSAR algorithm for the joint processing of PSs and DSs, also to increase the number of analysed scatterers. They start by identifying DSs as scatterers surrounded by other scatterers with similar behaviour. The phases of the similar scatterers are filtered and used to compute a coherence matrix, which includes all possible interferograms for the analysed images. It is considered that all identified similar scatterers belong to the same object and should have the same phase. Optimal phase values for each image date are estimated from the coherence matrix and attributed to the DS. DSs are then introduced into the original PSInSAR algorithm and processed together with the traditional PS. This approach enables the increase of the point density (Figure 4), from which results better unwrapping and APS estimations.

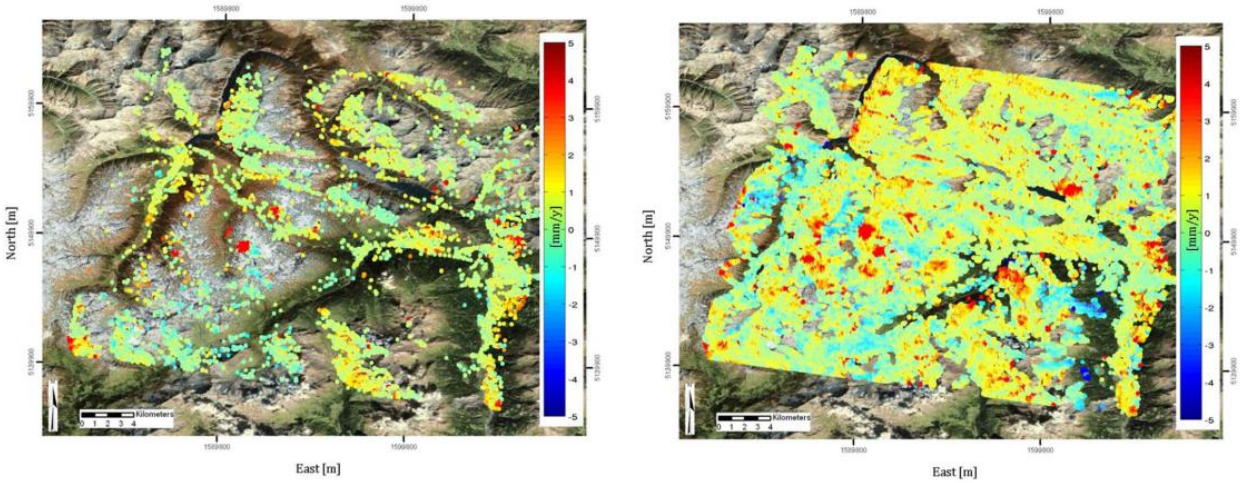

Figure 4 – Comparison of scatterer density using PSInSAR (a) and SqueeSAR (b), from Ferretti *et al.* (2011).

The Centre Tecnològic de Telecomunicacions de Catalunya (CTTC) proposed the method PSI Chain of the Geomatics Division (PSIG), which relies on unwrapping quality to achieve displacement and residual height estimations (Devanthéry *et al.*, 2014). The study performs a selection of similar persistent scatterers providing a dense coverture of the ROI (the Cousin PSs – CPS). A redundant graph of interferograms is defined and phase unwrapping is performed for the CPSs considering the redundant set of interferograms. Phase unwrapping quality is verified and

CPSs for further analysis are selected. APS is estimated for those points. A new network of points, denser then the CPSs, is selected for velocity and residual height estimation. APS and residual height are removed from the redundant interferograms, which are subjected to unwrapping in order to determine the displacement component of phase.

Figure 5 presents the relationship between the InSAR methods described in this Chapter.

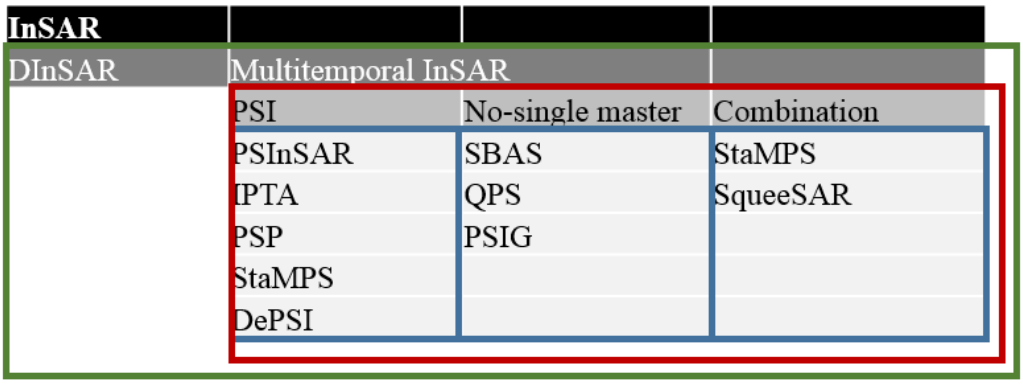

Figure 5 – Classification of InSAR techniques according to the set of used interferograms.

There are also other techniques that use SAR data. Tomographic SAR (TomoSAR) enables the distinction between scatterers with different heights represented in the same pixel, e.g. on steep slopes or building façades, where layover occurs (Fornaro and Serafino, 2006). Differential approaches of this method have been tried for deformation monitoring (Lombardini, 2005; Fornaro and Serafino, 2006). Pixel-Offset Tracking (POT) determines displacements in both slant range and azimuth directions from the offsets between corresponding pixels in different images during the corregistration. Multiple Aperture Interferometry (MAI) applies filters in the azimuth direction to build auxiliary interferograms from which displacement along the azimuth direction can be retrieved (Hu *et al.*, 2014). Polarimetric SAR Interferometry (POLInSAR) is a technique that combines the exploration of SAR data from multiple polarizations with InSAR and it has been applied for tree height estimation (useful for biomass studies) or coherence optimization (Corr *et al.*, 2003; Cloude, 2011). Radargrammetry uses coregistered SAR images from different acquisition geometries (parallel tracks or pairs of ascending and descending scenes) to determine disparities between common points at the images and to compute objects' heights (Wegmüller *et al.*, 2003; Dubois *et al.*, 2013).

2.2 InSAR methods for structural health monitoring

This section contains the literature review of the application of InSAR methods to structure monitoring studies. An evolution was observed, with the earliest researches being the direct application of InSAR techniques to targets on structures. Then, the InSAR algorithms were

adapted in order to provide better results in these specific problems. Later, InSAR data were introduced into structure behaviour models, providing information for a larger number of object points and with an observation period of a few days.

SHM is the process of identifying the presence of damages in a structure, with damage being changes in the material or geometry that may compromise the structure's performance. Damages are detected through comparison between different states of the structure: the one being evaluated and a previous, undamaged, one (Farrar and Worden, 2010). Structural safety is the structure capability to fulfil its behaviour requirements during its lifecycle (LNEC, 1989) and its assurance is of vital importance for human life well-being and property maintenance, whether civil or geotechnical structures are considered. The information required for assessing structural safety is achieved through monitoring systems, which consist on a set of equipments to collect values of variables relevant to the safety of each specific type of structure. For example, for concrete dams, it is frequent to monitor horizontal and vertical displacements, uplift pressures, seepage rates or strains (LNEC, 1989; Brownjohn, 2007). The main concerns regarding bridge safety are their dynamic behaviour and eventual responses to earthquakes, wind and traffic (Brownjohn, 2007). Regarding buildings and towers, the dynamic behaviour in response to earthquakes and storms are also of concern (Brownjohn, 2007). For geotechnical structures, such as slopes, embankment dams, tunnels or foundations, there are also several variables of interest, e.g., shear strength, compressibility, permeability, temperature, strain, stress, settlements or deflections (Pei *et al.*, 2014; Hong *et al.*, 2016).

Visual inspections performed by experts can be used for SHM (Chang *et al.*, 2003; Majumder *et al.*, 2008), sometimes supported by digital image acquisition and processing (Roque *et al.*, 2015). Many variables of interest to assess key information about the structure condition are acquired through embedded equipment and the usage of fibre optical sensors has been increasing due to their advantages related to size, weight, absence of electromagnetic interference and no corrosion problems (Nöther *et al.*, 2009; Ye *et al.*, 2014). The monitoring frequency of embedded equipment can be high and they allow for real-time monitoring whenever automated monitoring systems are available. On the other hand, some of the sensors have to be installed during the construction phase and they are not present in older structures.

Geodetic methods have been used for displacement measurement on structures with respect to their surroundings. A network of points located on the structure being monitored (the object points) and of points outside of it (the benchmarks) is materialised and vertical and/or horizontal displacements are determined for the object points with respect to the benchmarks. The object

points are installed at key locations for the structure condition assessment and the benchmarks are materialised at areas considered stable after a geotechnical inspection. Vertical displacements for all points may be determined from observations of height differences between pairs of points through geometric or trigonometric levelling, while horizontal displacements can be achieved from observed distances and bearings, which may be inputted at triangulations or traverses (Casaca, Henriques and Mateus, 2009; Casaca, Henriques, Coelho, *et al.*, 2009). Sub-millimetre and millimetre precisions are achieved for vertical and horizontal diplacements, respectively; however, the high costs associated to field campaigns may lead to the reduction of the observation frequency. Robotic total stations enable both static and dynamic monitoring of structures with accuracies of a few millimetres (Stiros and Psimoulis, 2012; Marendić *et al.*, 2016; Alamdari *et al.*, 2019). Satellite-based techniques, such as GNSS have also been used for structure monitoring, with the possibility of providing real-time data and measuring high rate dynamic displacements (Psimoulis *et al.*, 2008; Lima, 2015b, 2015a; Lima *et al.*, 2015; Yigit and Gurlek, 2017; Paziewski *et al.*, 2018, 2019). GNSS antennas are installed at structure locations of interest and their displacements are measured, in relative mode, with respect to one or more reference GNSS antennas deployed at nearby locations considered stable. The measurement precision depends on the observation duration and it may reach the sub-millimetric level in case observations are performed continuously (Lima *et al.*, 2015; LNEC, 2018). Both horizontal and vertical displacements are determined. The major disadvantages of this technique are the high costs of the equipment and the exposure to acts of vandalism.

InSAR is an applied geodetic technique, which enables displacement measurement at a large number of points and covering a wide area that may contain both the structure and its surroundings. The observation points exist naturally in the terrain, without need for being materialised, and if multitemporal data are used, millimetre precision measurements are achievable, with a revisit period that depends on the platform return time to the ROI. InSAR also has the advantage of allowing the study of past events, through the evaluation of archived images. At the present moment, the technique still presents some limitations regarding structure monitoring, such as the difficulty for controlling the points location (only possible through artificial reflectors, which will be discussed later), displacement measurement only along LOS or the non-availability of *a postetiori* variances for the measured displacements. Nevertheless, there are several examples of application of this technique to SHM reported in the literature. The types of structures most frequently analysed are bridges, dams, buildings, railways and slopes.

Regarding bridges monitoring, Sousa and Bastos (2013) proposed InSAR displacements as a source to inform early warning systems for their structural safety. They verified historical

displacements for the 5.5 years prior to the collapse of Hintze Ribeiro bridge, in Portugal. Four scatterers were detected on the bridge, with those located on the later collapsed pillar showing a displacement rate of 20 mm/year. Del Soldato *et al.* (2016) used L- and X-band SAR images to measure displacements on a bridge during different time intervals. They found the bridge itself was stable, but there were settlements at embankment areas at the connection between the bridge and the abutments for both banks. Besides, angular distortion[6] values larger than the safety limit were present at the same area. The results from the different time intervals showed that the settlements had been stronger right after the bridge construction and that the structure was stabilizing. Poreh *et al.* (2016) used PSI to monitor a railway bridge, which was verified to present a stable behaviour, with velocities ranging from -0.9 mm/yr to 0.05 mm/yr. Agreement between displacement and temperature time series was found.

Thermal expansion of the materials along the longitudinal axis of the bridge is often found to be one of the main causes for InSAR non-successful performance in monitoring this type of structures, leading many authors to adapt the original PSI algorithms to deal with it. Lazecky *et al.* (2015) proposed an adapted version of the usual PSI algorithm that exploits the linear relationship between phase and temperature changes. This improved version estimated for each scatterer residual height, velocity and a thermal expansion coefficient. They applied this method on bridges and, although a precise estimate of thermal expansion coefficient was achieved, the uncertainty of the average velocity was too large. To overcome this limitation, the authors recommended the analysis of a minimum of two years of images to correctly separate the thermal component from the linear trend. Lazecky *et al.* (2017) presented a method to improve observed temperature values and to calibrate them in order to match structure properties (bridges in this case). First, they used the relationship between phase residuals and thermal expansion coefficient estimated from SAR data as in Lazecky *et al.* (2015) to correct possible temperature observation errors. Then, these corrected temperature values were calibrated for the estimated thermal expansion coefficient to match a theoretical value obtained from the structure properties. This method enabled the decrease of residuals Root Mean Square Error (RMSE), leading to an increase of temporal coherence. The main limitation pointed by the authors was the fact that a single temperature value was used for the whole structure, when temperature differences along it should be considered.

The effect of temperature was also identified on high buildings. Reale *et al.* (2013) adapted the TomoSAR algorithm in order to account for structures' thermal expansion. As the height of the scatterers increased, the displacement time series deviated more from a linear behaviour due to the temperature load, resulting in a decrease in the number of evaluated points. Therefore, a thermal

[6] The ratio between differential settlement and the distance between points.

coefficient was estimated together with height and velocity. The inclusion of this term in the model not only enabled the construction of thermal expansion coefficient maps, but it also allowed the detection of a larger number of scatterers.

Besides the temperature effect, other improvements in the algorithm may be required to obtain better results on structures. Zhao *et al.* (2017) improved the estimation of velocity values on a bridge by first improving the altitude data. The authors performed iterative altitude estimation from progressively increasing normal baselines interferograms until altitude corrections became small. Those altitude values were then used in the model from which velocities were retrieved. Both velocity and scatterers location benefited from this method.

Tapete *et al.* (2015) also considered the correct determination of scatterers altitude as a key factor to structure monitoring through InSAR. They proposed the usage of GNSS Real-Time Kinematic (RTK) to improve the three-dimensional location of the scatterers along linear structures, such as aqueducts. Object points on the structure and on the ground were surveyed using Global Positioning System (GPS) RTK. As scatterers planimetric locations were determined with an error of 1 m, their altitude and planimetric location with respect to the GPS RTK benchmarks enabled the identification of their location: the structure top, the wall or the ground. This position improvement allowed a better evaluation of the observed deformation, specifically on determining to which part of the structure the observed displacement was referred to. Classes based on velocity values and trends on the displacement time series were attributed to the scatterers.

InSAR has been used for displacement measurement on both embankment and concrete dams. Wang *et al.* (2011) monitored displacements at the Three Gorges dam, in China, between 2003 and 2008, when part of the structure was still under construction. As the DEM available to the study was older than the SAR images, the authors used the QPS technique to perform a first estimate of the dam height and of its surrounding elements as well as of the average velocity. The estimated height values were used as input for a PSI processing from which displacement time series were derived with better precision. The analysis of those displacements revealed the dam settlement finished before the end of the studied time interval and the effects of temperature and water pressure on the structure were visible in the data.

Di Martire *et al.* (2014) evaluated displacements on an embankment dam using EnviSat data during eight years. They found displacement with magnitude of 3 cm in the central zone of the dam and 2 cm on the lateral areas. The data were validated through comparison to extensometer measurements of the same time interval, with differences between 2.9 mm and 5.2 mm between them.

Milillo, Bürgmann, *et al.* (2016) monitored displacements at the Mosul dam, in Iraq, before and during the stopping of maintenance actions required to keep the structure safe due to the geological

properties of its location. The authors combined datasets from different sensors, time intervals and geometries to evaluate vertical and east – west displacements on the dam. They found that most of the displacement occurred in the vertical direction, being compatible to subsidence. An increase in the subsidence rate was found from 2004 – 2010 to 2014 – 2015, probably due to the lack of maintenance since 2014. However, the ground dissolution rate has been kept approximately equal for both time intervals, maybe due to the lower water volume in the reservoir during the second one.

Emadali *et al.* (2017) used both InSAR and *in situ* measurements to monitor an embankment dam in Iran. They applied SBAS on a dataset of TerraSAR-X spotlight images, achieving a dense coverture of scatterers on the structure (Figure 6). InSAR and *in situ* data were compared to validate the measurements, after projecting *in situ* to LOS direction, achieving a correlation coefficient of at least 0.95 between the two techniques. Between 2014 and 2015, displacement away from the sensor was detected on the crest (13 cm/yr) and on the downstream slope (7 cm/yr). The authors considered the value at the crest to be above the expected for a dam of that height 15 years after its construction, as it represented a settlement rate of 0.08% of the dam height, when after 2 – 3 years after construction, it was expected to have a settlement rate of 0.02%.

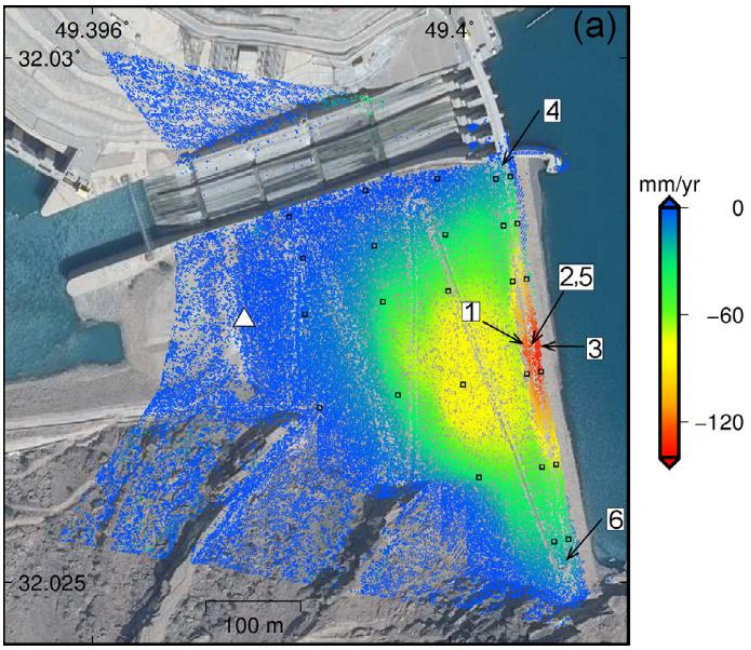

Figure 6 – Average displacement rate along LOS on an embankment dam achieved by applying SBAS to TerraSAR-X data (Emadali *et al.*, 2017).

The Morandi Bridge, in Genoa, Italy, collapsed in 2018 and Milillo *et al.* (2019) used back-analysis to detect increasing displacements on the damaged area, starting in 2015 and their acceleration in 2017. The authors used data from three distinct geometries from COSMO-SkyMed

and Sentinel-1, which were combined through Markov Chain Monte Carlo in order to achieve three-dimensional displacements at the structure.

Recent studies combined InSAR displacements with structural behaviour knowledge to interpret the data. Ciampalini *et al.* (2014) stated that InSAR data can be useful for both prevention and post-event risk evaluation. They used several datasets, from different time intervals, to assess velocities in buildings located at a landslide area. An average velocity was computed for each building from all scatterers located on the structure. The building velocity map was compared to a building damage map obtained from visual inspections and they agreed to each other.

Pratesi *et al.* (2015) proposed a building classification system, composed of five degrees. The classifications were attributed based on three indexes derived from InSAR data. The completeness of information index evaluated the scatterer coverage of the building (and of a small neighbourhood around it) and provided the confidence level on the other indexes. The conservation criticality index was the maximum observed velocity on the building, whose dispersion was evaluated by the velocity distribution index. This last index identified if the scatterers on the building showed similar velocity values or if there was a localized deformation.

Qin *et al.* (2017) monitored high-speed railways through an adapted InSAR algorithm. Analysis was limited to scatterers located on a buffer around the railway and that fulfilled a constraint on height (height difference between neighbours should be less than three times the height standard deviation). After scatterer identification, phase residuals were analysed in order to estimate the thermal expansion coefficient. Subsidence and negative values of the thermal expansion coefficient were detected for railway stretches near residential and industrial areas, possibly related to groundwater cycles. Risk analysis was performed through a weighted average of ranks given to subsidence rate, angular distortion and thermal expansion coefficient.

Milillo, Perissin, *et al.* (2016) proposed dam monitoring through the combination of InSAR displacements with dam behaviour models. They performed a sensitivity analysis of each dataset with respect to displacements in radial and vertical directions on the dam. They found that all datasets have similar sensitivity to vertical displacements along the entire dam crest. Regarding the radial displacements, ascending datasets were more sensitive in the centre and the southernmost part of the structure, while descending datasets were more sensitive only at the centre. Displacements from ascending and descending geometries for the same time interval were combined and vertical and radial displacements were obtained. Scatterers located on the crest centre showed radial displacement uncertainties below 3.00 mm. An ageing effect was searched for in the vertical displacements, but it was not present. Radial displacements were used as input to the Hydrostatic-Seasonal-Time (HST) and the Hydrostatic-Temperature-Time (HTT) models,

which relate radial displacements with seasonal, hydrostatic or temperature loads on the dam (Figure 7). For HST model, a linear trend was detected (with a rate of 0.5 mm/yr and uncertainty of 0.22 mm/yr), which could indicate possible anomalous behaviour of the structure. For HTT model, this trend presented the rate of 0.001 mm/yr with uncertainty of 0.003 mm/yr.

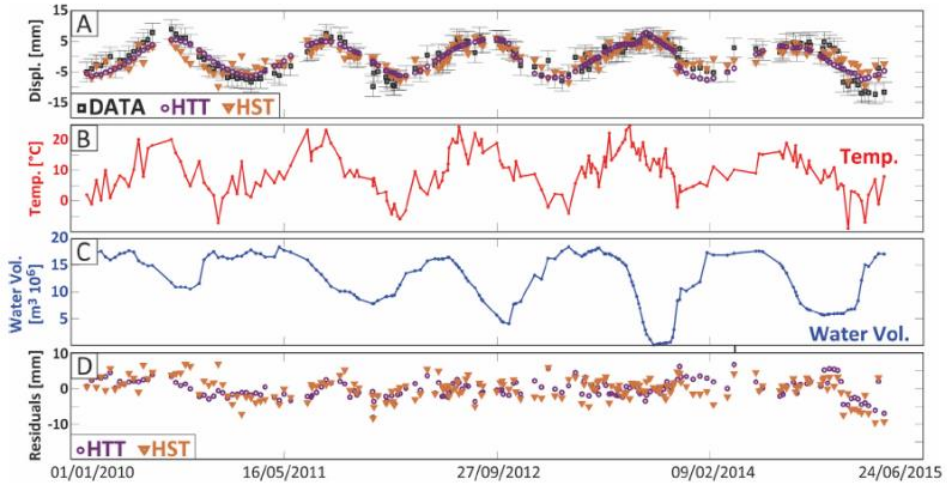

Figure 7 – Comparison between observed and modelled displacements, temperature, water volume and model residuals (Milillo, Perissin, *et al.*, 2016).

Cerchiello *et al.* (2017) combined InSAR displacements with building models to achieve a risk map for part of the city of Rome. The buildings were modelled using a laminated beam model, in which only the main elements of the building were considered. These models could relate the InSAR displacements to geometric and material properties of the buildings and enabled the determination of the strain. Testing different values of building properties within acceptable ranges, critical values of strain were obtained and used to build a hazard map. Vulnerability maps were achieved from the area, height and materials of the buildings. Risk maps for several time intervals were computed by multiplying the hazard and the vulnerability maps, allowing the analysis of the risk evolution for the study object.

Milillo *et al.* (2018) used InSAR data to assess damages on buildings located over a tunnel being constructed. The method relied on the comparison of strain values from the buildings with limit values that were related to damage classes. The strains were obtained from deflection ratios, which are the ratios between the relative deflection between two points and their horizontal distance. First, deflection ratios were determined through a model that did not consider the existence of buildings in the affected area and used the type of soil, depth and diameter of the tunnel as well as the excavated volume. Then, the authors determined the deflection ratios from displacements observed through InSAR for scatterers located on the ground and on the buildings,

independently. The two values were used to compute a modifying factor, from which strains were obtained. InSAR displacements were validated through comparison to levelling.

Infante *et al.* (2019) proposed a method for vulnerability assessment along linear structures based on Geographic Information Systems (GIS), which integrated data from InSAR, altitude, landslide inventory maps and field surveys. PSI displacements along LOS were converted to slope direction, using a DEM, inside a buffer surrounding the structure. The scatterers were then compared to a threshold and clustered in order to identify unstable areas. These areas were compared to landslide inventory maps and crossed with structure damage information collected from visual inspections. Each cell from a grid covering the structure buffer was attributed a qualitative vulnerability degree (low, moderate, high or very high), according to its kinematics properties (PSI displacement crossed with existing landslide inventory) and level of damage. The method was applied to road monitoring and an updated landslide inventory map was achieved.

Giardina *et al.* (2019) proposed that InSAR data are valuable for damage monitoring caused by tunnel excavation from the analysis of deformation on buildings located over the tunnels. Displacements from PSs on the buildings above the tunnel were used to build deformation profiles that characterised the soil-structure interaction induced by the tunnel. The authors stated that the usage of high resolution SAR data for a study of this nature was of the utmost importance.

Figure 8 presents a summary of the strategies that have been used for SHM with InSAR-derived data.

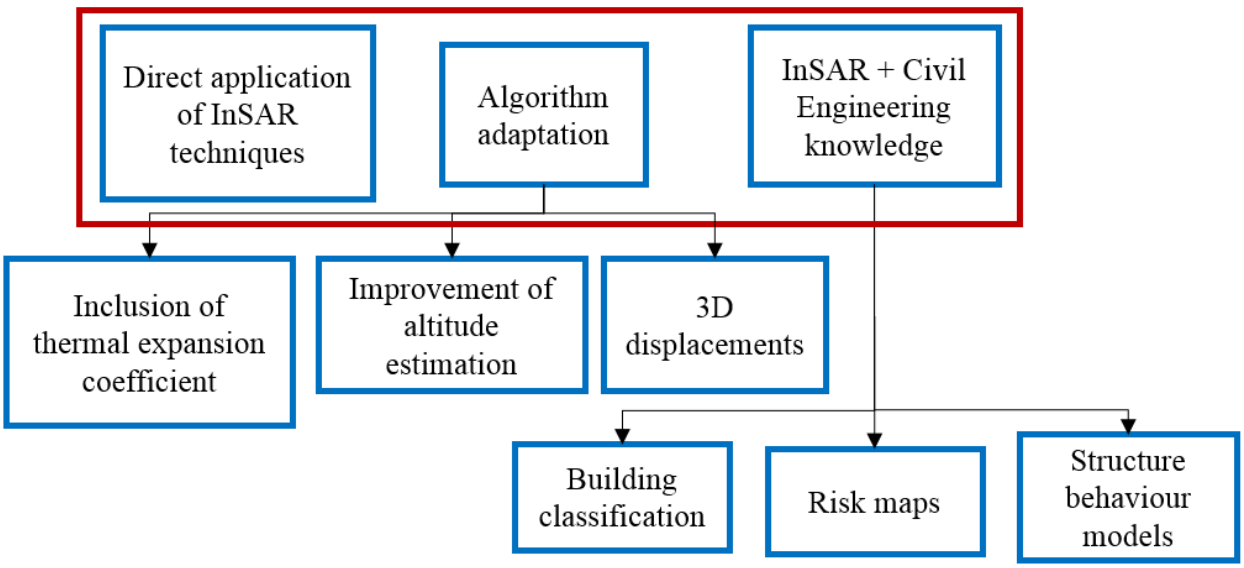

Figure 8 – Summary of methods for individual structure monitoring with InSAR techniques.

Although InSAR has been successfully used for individual structure monitoring as reported above, the strongest point of the technique is displacement monitoring at a regional level. Urban subsidence has been frequently evaluated using this type of data. Osmanoğlu *et al.* (2011) detected

subsidence rates of 300 mm/year at Mexico City, caused by groundwater extraction. Amelung *et al.* (1999) also used the technique to monitor subsidence at Las Vegas together with uplift resulting from aquifer recharge. Besides changes due to groundwater levels, the effect of hydrocarbon extraction on ground has been monitored through InSAR as well (Ketelaar, 2008). InSAR is an adequate technique for such studies due to its capability to cover wide areas throughout long time spans, enabling the identification of the subsiding area limits and its confrontation with geological elements, e.g., faults or lithology (Amelung *et al.*, 1999). Ground movements have also been searched at the city of Lisbon, one of the case studies in this thesis, with subsidence being detected (Heleno *et al.*, 2011; Catalão *et al.*, 2016). The studies show the subsidence was related to the lack of acquifer recharge with groundwater, caused by the expansion of the subway line and increasing soil impermeability.

Another application of InSAR methods commonly found in the literature is the study of landslides. According to Solari *et al.* (2020), InSAR is an advantageous technique for these studies due to its capability to monitor wide areas, at a large number of points, with a short revisit period, millimetre precision, all-day and all-weather image acquisition, data provision at difficult access areas and large image archives; thus being a cost-effective technique for this end. This applied geodetic technique has been used for back-analysis of past landslides in order to search for precursory signs of ground instability (e.g., Carlà, Intrieri, *et al.*, 2019), which may be identified in future analysis allowing an early response from authorities. Landslide characterization is performed by crossing data from distinct sources, such as different SAR geometries and *in situ* data (e.g., Czikhardt *et al.*, 2017). InSAR displacements can also be used as input for landslide model calibration (e.g., Bru *et al.*, 2018), to map new landslides (e.g., Ciampalini *et al.*, 2016), to update existing inventory maps (e.g., Rosi *et al.*, 2018) or for slope monitoring (e.g., Ye *et al.*, 2004). Some of the reported limitations for the application of the technique in this field are SAR geometric effects (shadow, foreshortening and layover) and the frequent presence of vegetation (Shi *et al.*, 2017, 2019).

Chapter 3. RADAR interpretation of InSAR displacement time series

This chapter proposes a big data method for the radar interpretation of InSAR displacement time series achieved through PSI. The followed strategy performs the clustering of displacement time series in an automatic way and without the need for previous knowledge on the case study, which turns the method appropriate for monitoring any type of events. Although an automatic solution is always provided, the user has the possibility of changing the scale of the analysis into different levels of detail and to include additional data to aid in the displacement interpretation. The method proved to be able to detect and isolate object points with displacements affected by unwrapping errors, as well as, to identify distinct structural behaviour patterns in two case studies of distinct natures: slopes during the first impoundment of a water reservoir and cultural heritage buildings.

3.1 Introduction

3.1.1 RADAR interpretation

The importance of extracting information from InSAR displacement time series, instead of analysing only variables such as average velocity or cumulative displacement during a certain time interval, has increased recently. Possible reasons may be the growing interest in InSAR applications characterized by non-linear displacements or the increase in the number of scatterers, which are becoming possible due to the improvements in the algorithms, the easiness in accessing image datasets and increasing computational capacity. Several strategies for retrieving information from InSAR displacement time series, named RADAR interpretation, have been developed in the last years.

Lanari *et al.* (2004) used SBAS to analyse seasonal displacements in Los Angeles. They fitted a sinusoidal model to the displacement time series of each scatterer and evaluated the spatial distribution of amplitude and phase shift with respect to a reference date. This enabled the identification of areas where seasonal behaviour was stronger and of delays that were related to the location of faults. Similarly, in Lanari *et al.* (2010) SBAS displacement time series were fitted to an exponential model that described the evolution of the displacements after an earthquake. Least squares adjustment was used to determine the amplitude (the value towards which displacements tend to with time) and the decay constant, which was then mapped and related to the displacement magnitude.

Cigna *et al.* (2011) presented two methods for interpreting the displacement time series obtained for geological hazards in urban environment. In the first method, the displacement time series was divided in small time intervals and displacement rate was computed for each of them. Rate differences from consecutive intervals, after being normalized for accounting with different interval lengths, were used to evaluate the scatterer evolution. The second method consisted on the scatterers classification into the "unaffected" or "affected" classes. Scatterers considered to be unaffected by the geological hazard were stable or showed linear trends, while the "affected" label was attributed to scatterers with changes in their displacement time series, which could be temporary or permanent. Both methods were applied manually to the scatterers. The interpretation of the InSAR displacement time series complemented *in situ* data in order to identify the probable cause of the damages found in the buildings: tectonics. The authors stated that the implementation of this type of strategies for RADAR interpretation needs to be adapted for each situation at study.

Cigna *et al.* (2012) presented an evolution of the previous research towards semi-automation. Two deviation indexes were proposed. One was used to detect behaviour changes prior to the occurrence of geological hazards, for example volcanic eruptions, to help predict the event. It required the manual selection of a breaking epoch in the displacement time series and a linear regression model was adjusted to the data from the first time interval. That model was expanded to the dates of the second time interval and the deviations from the predicted and observed displacements were computed. The deviation index was the average of those deviations divided by the standard error of the regression. Large values of the deviation index corresponded to large deviations between the predicted and observed displacements in the second time interval with respect to the data variability in the first one. The second index was applied to identify sudden displacement changes, like in tectonic motion. It also relied on the selection of a breaking epoch and two linear regression models were adjusted to the data (one to each time interval). Those models were used to predict the displacement values for the breaking epoch at each interval and

the index value was their difference. Mapping the indexes values for each scatterer enabled the analysis of their spatial distribution.

Raspini *et al.* (2018) proposed a similar method for continuous monitoring of displacements. Their technique was applied every time a new SAR image was available. Displacement time series were divided in two parts and if the rate difference between the two parts was larger than a certain threshold, the scatterers were labelled as anomalous. However, an anomaly was only considered if the behaviour change was seen for at least two consecutive images and if the scatterer was not isolated. The method was applied at a regional level and a bulletin for each region (municipality) was provided, where they were classified regarding the absence/presence of anomalies. The presence of anomalies was divided into three subcategories: new anomalies, persistent anomalies and persistent anomalies putting key infrastructures (such as roads or hospitals) at risk. The classification into this last subcategory required the execution of field works to assess the dimension of the problem.

Milone and Scepi (2011) applyed cluster analysis to displacement time series obtained from PSInSAR (Figure 9). They proposed the usage of the clustering large applications (CLARA) algorithm, which is a partitioning cluster technique that uses medoids[7]. Dissimilarities were evaluated between each scatterer and a certain seed of the cluster (the medoid, which is supposed to be in the central part of the cluster) and, based on those dissimilarities, the scatterers were attributed to the cluster with the more similar medoid. CLARA had the advantage of being able to deal with large datasets, when compared to other clustering algorithms of the same type. A sample of elements (scatterers in this case) was selected and the partitioning method explained above was applied iteratively only on that sample until the best medoids were found. Then, the remaining elements were attributed to each cluster based on their dissimilarity to each medoid. This sampling strategy enabled a reduction in the processing time; however, the quality of the final result depended on the sample size. Furthermore, this technique tended to form clusters approximately of the same size and the number of clusters had to be known *a priori*. The authors considered that the application of this algorithm was successful and they were able to relate the clusters to tectonic elements and water extraction.

Berti *et al.* (2013) created an automatic system (PS-Time) for scatterer classification based on the comparison of their displacement time series to a library of expected behaviours of points located in landslide areas. The algorithm performed a series of hypothesis tests in order to accept or reject each PS into a certain class. The considered classes were: "uncorrelated", which corresponds to stable points, "linear", "quadratic" or "bilinear". The "bilinear" class was divided

[7] The median of the considered values.

into three categories: “continuous in time”, “discontinuous with constant velocity” and “discontinuous with velocity change” (Figure 10). Seasonal displacements were also considered and identified through frequency analysis. A crucial parameter for this algorithm was the level of significance used at hypothesis testing. The authors trained the algorithm by manually classifying the displacement time series for 1000 scatterers and by running PS-Time several times with different levels of significance. The values that provided the classification closer to the manual one were selected and applied on the classification of the whole dataset.

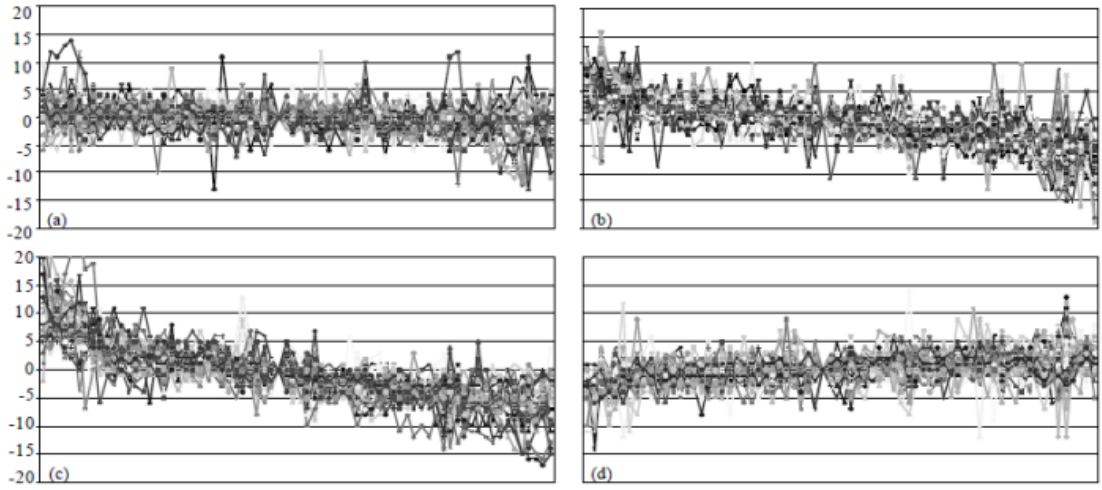

Figure 9 – Displacement time series belonging to different clusters (Milone and Scepi, 2011).

Notti *et al.* (2015) provided a series of methods for RADAR interpretation, resulting from a compilation of proposals from previous works that can help the data evaluation at different phases of the analysis: pre-processing, post-processing and trend analysis. The pre-processing phase consisted on the evaluation of the SAR Dataset Quality Index (SDQI) that relied on information such as the number of images, the time span of the study, temporal and spatial baseline distributions and image spatial resolution to assess the adequacy of a certain dataset to perform the study. The post-processing phase included four methods to improve the quality of the displacement time series: the removal of noise and regional trends (by subtracting a trend determined from displacement time series of stable scatterers), removal of anomalous values at individual dates (when one third of the stable scatterers showed large anomalous values at the same epoch), correction of unwrapping errors (by adding or removing half a wavelength to the displacement when there were jumps with magnitudes larger than one quarter of the wavelength) and noise reduction by averaging neighbour scatterers with similar behaviour. The trend analysis included the PS-Time and deviation indexes proposed by Berti *et al.* (2013) and Cigna *et al.* (2012), respectively. Besides, this study also proposed the evaluation of velocity time series, which consisted on determining velocity values for segmented intervals in the displacement time series

inside a moving window. These procedures were successful when applied to different datasets processed with different algorithms, showing its general applicability.

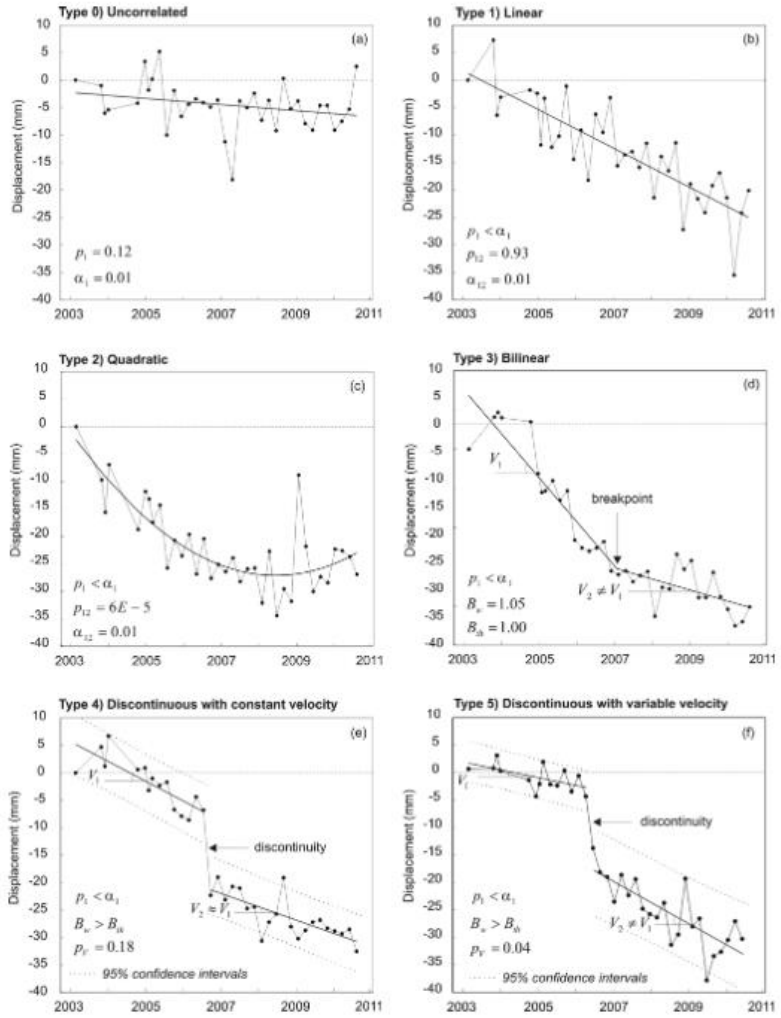

Figure 10 – Behaviour classes considered at PS-Time technique (Berti *et al.*, 2013).

Bonì *et al.* (2016) applied Principal Component Analysis (PCA) on displacement time series (in vertical or east – west direction). Ground motion areas were defined by selecting scatterers with large scores in each principal component and PS-Time method was applied on them in order to identify the displacement model in each case. The ground motion areas were superimposed to geological, hydrogeological, optical images and other data in GIS software to help the data analysis and interpretation.

Shirzaei *et al.* (2013) presented a wavelet decomposition of InSAR displacement time series for the flank of the Kilauea volcano. The method was also applied on GPS data, whose results were compared to those computed for SAR scatterers located inside a radius of 200 m. The results from both techniques agreed with each other, indicating that InSAR displacements were not affected by atmospheric effects. For validation, the spatial distribution of the wavelet coefficients

was compared to the output of a hierarchical cluster procedure and it was verified that there was agreement between the results. The authors found different behaviours bounded by faults that corresponded to aseismic deformation.

Chang and Hanssen (2016) proposed a Multiple Hypothesis Testing (MHT) strategy to associate each scatterer to pre-defined behaviour models. In the first step, a hypothesis test was employed to verify if the scatterer displacement time series had linear trend (the null hypothesis). Whenever that hypothesis was rejected, alternative hypothesis corresponding to each pre-defined behaviour model were tested sequentially. The hypothesis test was adapted for each model, considering the different number of parameters to be estimated, and the model presenting the largest value of test statistic was selected. The parameters considered in the selected model (e.g., thermal expansion coefficient, discontinuity magnitude, among others) were then estimated together with their precision and their spatial distribution was evaluated. Van de Kerkhof *et al.* (2020) complemented this research by reducing the displacement time series dimensionality through applying a machine learning technique. Then, the clustering approach Density-Based Spatial Clustering of Applications with Noise (DBSCAN) was used to cluster the reduced information. Each cluster was represented by the average of the displacement time series of all scatterers belonging to it and the MHT proposed in Chang and Hanssen (2016) was applied only on those average time series. After the identification of the behaviour model of each cluster, the MHT method was applied to each scatterer of the cluster, but considering the selected model in the null hypothesis, for parameter estimation at each point. This procedure enabled the reduction of the computation time and also increased the quality of the estimated parameters.

Costantini *et al.* (2018) presented a method for InSAR data analysis in space and time for SHM. They proposed a hierarchical clustering approach, which aggregated neighbour scatterers based on their spatial distance and on the difference between their displacement time series. Multiple regression models were applied to segments of the displacement time series, determining the values of several regression parameters: a constant, a linear trend and the amplitude and phase of periodic displacement. Anomalous behaviour was found for some buildings, which was later confirmed by visual identification of cracks on the walls. Zhu *et al.* (2018) complemented this research by proposing an automatic system to assess the stability of buildings. The results from cluster analysis and the regression model were evaluated together with the maximum observed settlement, differential settlement and angular distortion for each building, which allowed the detection of damaged structures.

Besides the data exploration, a user-friendly interface also facilitates the interpretation of InSAR results. Sousa *et al.* (2013) developed a MATLAB® tool for visualization and analysis of the data produced by StaMPS.

Bakon *et al.* (2017) proposed a series of multivariate data mining techniques for outlier detection in order to include in the analysis scatterers with low coherence that still provide useful information. The method used a clustering method to aggregate the scatterers in three groups: group, islands and noise. PCA was applied on each cluster to detect outlier candidates that were then compared to their neighbours and had their coherence reevaluated to decide if they must be kept or rejected.

Recently, machine learning techniques have also been used to retrieve information from InSAR data. Anantrasirichai *et al.* (2018) applied convolutional neural networks to classify wrapped interferograms, at a global scale, as presenting resting or unresting volcanoes. Their goal was to automatically detect unresting volcanoes on the large volume of data generated by Sentinel-1 satellites.

Tomás *et al.* (2019) proposed a semi-automatic method to classify groups of scatterers as landslides, sinkholes, subsidence or settlements. They defined Active Deformation Areas (ADA) through the analysis of neighbor scatterers, velocity thresholds and average cumulative displacements. Each ADA was then organized in cells and average horizontal (east – west) and vertical displacements were computed from ascending and descending data. Each ADA was then classified into one of four possible hazard classes, based on the horizontal displacements, geological class, slope, vector maps of urban areas and old hazard inventory maps. The method presented a good performance; however, the completeness of its applicability depended on the availability of the auxiliary data and it was subjective, as many thresholds needed to be user-defined and a final verification of the results must be performed due to conflicting class attribution to the same ADA.

Table 1 shows a summary of the studies previously described in the field of RADAR interpretation. An evolution in the presented strategies was found throughout the last decade. Different cluster analysis techniques have been used to identify scatterers with similar behaviour. The mapping of change detection indexes also enabled the evaluation of the spatial distribution of behaviour heterogeneities. The comparison of displacement time series with pre-defined models stored in libraries, such as PS-Time, has been applied by several authors, reflecting the acceptability of this method by the scientific community.

Table 1 – Comparison of different techniques for RADAR interpretation.

Authors	InSAR Technique	Problem	Data mining technique	Summary
Lanari et al. (2004)	SBAS	Aquifer recharge in urban area	Regression models	Built maps of amplitude and phase shift from sinusoidal functions fitted to the data.
Lanari et al. (2010)	SBAS	Earthquake	Exponential model	Built maps of amplitude and decay constant for post-seismic data through fitting an exponential model through least squares adjustment.
Milone and Scepi (2011)	PSInSAR	Tectonics and water extraction	Cluster analysis	CLARA algorithm was used to aggregate PS in clusters.
Cigna *et al.* (2011)	PSInSAR	Tectonics	Time series subdivision; classification	Manual determination of indexes built from subsets of the displacement time series to evaluate velocity changes; classification of the PS into "unaffected" and "affected" classes.
Cigna *et al.* (2012)	PSInSAR	Volcano / Tectonics	Deviation indexes	Semi-automatic deviation indexes to detect behaviour changes prior to the geological event and to identify sudden changes.
Berti *et al.* (2013)	PSI	Landslides	PS-Time	A series of statistical tests were applied to classify the PS displacement time series into a set of pre-defined categories frequently found in landslide areas.
Shirzaei *et al.* (2013)	WabInSAR (wavelet based InSAR)	Volcano flank	Wavelet	Performed wavelet decomposition of InSAR time series. Validated result with cluster analysis.
Sousa *et al.* (2013)	StaMPS	Urban stability	viStaMPS	Development of software for InSAR results visualization and analysis.
Notti *et al.* (2015)	Several	Landslides and subsidence	Pre-processing, post-processing and trend analysis	Compilation of several techniques: SDQI, improved time series, PS-Time, deviation indexes, velocity time series. Applicable in different situations.

Authors	InSAR Technique	Problem	Data mining technique	Summary
Chang and Hanssen (2016)	DePSI	SHM	Multiple hypothesis testing	A set of statistical tests were sequentially used to evaluate the displacement time series of the scatterers in order to attribute a pre-defined model to it. After model selection, parameter values were estimated.
Bonì *et al.* (2016)	SqueeSAR	Aquifer recharge in urban area	PCA + PS-Time	Used PCA to define ground motion areas which were then classified using PS-Time and analysed with ancillary data in GIS.
Bakon *et al.* (2017)	PSInSAR	Slopes	Clustering + PCA	Used several multivariate data mining techniques for outlier detection.
Costantini *et al.* (2018)	PSP	SHM	Cluster analysis and regression models	Performed spatio-temporal analysis of scatterers located on buildings using cluster analysis and regression models to detect linear and periodic behaviours.
Anantrasirichai *et al.* (2018)	DInSAR	Volcano	Machine learning	Applied Convolutional Neural Networks on interferograms to identify unresting volcanoes at a global scale.
Zhu *et al.* (2018)	PSP	SHM	Cluster analysis and regression models	Same method from Costantini *et al.* (2018) complemented by maximum settling, differential settling and angular distortion for each building.
Raspini *et al.* (2018)	SqueeSAR	Hydrogeological risk mitigation	Deviation indexes	Adapt deviation indexes from Cigna *et al*. (2012) to be applied on continuously updated displacement time series.
Tomás *et al.* (2019)	SqueeSAR	Several geohazards	Classification	Defined ADAs and classified them based on auxiliary data.

Authors	InSAR Technique	Problem	Data mining technique	Summary
van de Kerkhof *et al.* (2020)	DePSI	SHM	Machine learning; cluster analysis; MHT	Used machine learning to reduce data dimensionality and cluster analysis to aggregate scatterers with similar behaviour; MHT was applied only on cluster aggregated time series for model selection and it was then used for parameter estimation for all points.

3.1.2 Clustering of time series

Time series are sequences of a finite number of real-valued variables ordered along time at a regular sampling. The analysis of time series is used in different fields, such as engineering, science, finances, healthcare, economy, business, among others (Aghabozorgi *et al.*, 2015; Abanda *et al.*, 2019). However, the large dimension of data available, with a high number of observation epochs (data points) for each time series, make the extraction of information a big data problem. According to Esling and Agon (2012), there are seven data mining techniques frequently applied on time series:

i) Query by content, which consists on the identification of the time series pertaining to a database that answer a certain query provided by the user;

ii) Clustering, where the time series are aggregated into homogeneous groups through an unsupervised process;

iii) Classification, a supervised process, in which labels are attributed to a training dataset of time series, possibly based on prior information on the data, and the remaining series are then associated to the label corresponding to the most similar series in the training data;

iv) Segmentation, which is an approximation of the original time series with the reduction of the data dimension;

v) Prediction, where the values of new data points are foreseen based on the values already in the time series;

vi) Anomaly detection, which is the detection of subsequences of the time series with a behaviour considered as abnormal;

vii) Motif discovery, where subsequences, called motifs, that are represented several times in a time series, are identified.

3.1.2.1. Clustering is the most used technique of data mining for time series (Fu, 2011) and, being an unsupervised technique, it is adequate to analyse large amounts of data without any prior knowledge on the observed phenomenon (Aghabozorgi *et al.*, 2015), which makes it appropriate for the purpose of the present research. Therefore, this study used this technique and the following state-of-the-art is focused on it. Clustering methods are organized into three types: clustering of the complete time series as a whole, clustering of subsequences inside a single time series and clustering of consecutive data points with similar values (Aghabozorgi *et al.*, 2015), but in this research only whole time series clustering was considered. Due to their dynamic nature, the clustering of time series requires some adaptation with respect to the traditional clustering operations. Either the clustering algorithms may be adapted to deal with the time series without transforming them, the time series may be transformed into lower dimension elements or the combination of both strategies (Aghabozorgi *et al.*, 2015). The adaptation of clustering algorithms may comprise the adaptation of dissimilarity measures. On the other hand, the transformation of time series can be performed through representation techniques[8], from which feature vectors or model parameters are retrieved.

3.1.2.2. Aghabozorgi *et al.* (2015) refer six types of algorithms that have been applied to clustering time series (hierarchical, partitioning, model-based, density-based, grid-based and multi-step).

Hierarchical algorithms can be agglomerative / divisive and consist in the sequential aggregation / separation of the most similar / most distinct clusters achieved in a previous step based on a dissimilarity measure. The procedure is repeated until all elements belong to a single cluster (in agglomerative method) or all elements are represented in individual clusters (in the divisive approach). The similarity measure is called linkage distance and can be evaluated in different ways. Single linkage uses the distance between the nearest elements in each cluster. Complete linkage is computed from the farthest elements. Average linkage relies on the average distance between all elements in the cluster. Centroid method utilizes the distance between the clusters' centroids. Finally, Ward method minimises the distance between elements inside each cluster and maximizes it between clusters (Hair *et al.*, 2009). The main advantage of these methods is that prior knowledge on the number of clusters to use is not required, as the dissimilarity measures between consecutive clusters aid in the analysis of each cluster homogeneity and on the decision of how many clusters must be built. On the other hand, the quality of the clustering may be compromised due to the fact that the clusters achieved at each step depend on those from the

[8] Time series representation techniques enable the reduction of the time series dimensionality, improving the processing time and memory usage, but reducing the quality of the dissimilarity measurement.

previous one, not being readjusted, which may lead to clustering inaccuracies. Besides, these algorithms are computationally demanding, with quadratic complexity, which makes their application difficult for large datasets (Aghabozorgi *et al.*, 2015).

Partitioning algorithms lead to a set of clusters, whose number needs to be defined beforehand, and aggregates elements according to their similarity to a prototype. The aggregation is performed iteratively, with the prototype being redefined at each iteration. This procedure is repeated until changes stop occurring, which leads to high quality clusters. The definition of the prototype can be determined in different ways, for example, the average or the median of the elements in the cluster in the previous iteration, for the algorithms k-Means or k-Medoids, respectively. This class of clustering algorithms has a fast performance, however it requires *a priori* knowledge of the number of clusters, which is usually unknown.

Model-based clustering assumes the elements belonging to a cluster follow a certain model. Centroids for each cluster are randomly selected, subjected to the addition of Gaussian noise, and then the closest elements to each centroid are attributed to the respective cluster. The method dependency on the initial assumptions may affect the quality of the clusters and it performs slowly for large amounts of data.

Density-based methods rely on the elements density to form the clusters, in which the groups are formed at high element density regions separated by low density ones. These algorithms are quite complex, which limit its applicability to time series problems.

Grid-based clustering organizes the elements space into cells, where the clustering is performed. According to Aghabozorgi *et al.* (2015), this method had never been applied to the clustering of time series.

Finally, multi-step approaches combine several of the previous methods in order to take advantage from the positive points of each of them and to limit the influence of their drawbacks in the results.

3.1.2.3. Time series clustering methods rely on dissimilarity measures between pairs of time series. When comparing time series, the human brain has the ability to do the comparison beyond differences in amplitude and time scales, noise or outliers. Dissimilarity measures do not intend to identify equal time series, but similar ones (Fu, 2011). Therefore, the developed techniques must perform the analysis in a way similar to that of the human brain. Dissimilarity measures can be based on shape, editions, features or structures (Esling and Agon, 2012). Shape-based methods use the comparison of the general shape of the time series. Edit-based ones, primarily developed for string comparison, rely on the number of changes required to transform a time series into another one. Feature-based approaches reduce the time series dimensionality by describing it through

features. Structure-based strategies can be divided into two categories: model-based, in which a model is fitted to the time series and the parameters of the model for each time series are used to do the comparison, and compression-based, where similar time series achieve higher compression ratios than non-similar ones. Examples of similarity / dissimilarity measures are correlation coefficients or distances. Distance measures may be lock-step, when the evaluation between series is performed for corresponding epochs, or they may be elastic, with the values from each epoch being compared with those from other epochs.

Euclidean distance and Dynamic Time Warping (DTW) are the most used similarity measures in the clustering of time series, according to Aghabozorgi *et al.* (2015). Both evaluate dissimilarities based on shape. Euclidean distance between two time series is the sum of the Euclidean distances between data points from two time series observed at the same epoch. DTW is an elastic distance, originally developed for speech recognition, and firstly applied to the identification of patterns in time series by Berndt and Clifford (1994). The rationale behind this technique is the comparison of the time series with a template, not necessarily with the same length, in which the time axis is deformed in order to minimise the distance between the two series (Figure 11a). A distance measure between data points from the two time series is selected, δ, such as the absolute value of the difference of the values or its square. DTW between time series S and template T is the minimum cumulative distance of all possible cumulative distances along the paths W that connect the k pairs of data points, as in Equation (5).

$$\mathrm{DTW}(\mathrm{S},\mathrm{T}) = \min_{\mathrm{W}}\left[\sum_{\mathrm{k}=1}^{\mathrm{p}} \delta(\mathrm{w_k})\right] \tag{5}$$

The cumulative distance γ for a certain pair of data points (i, j) is the distance between those data points added to the minimum of the cumulative distance achieved at the neighbour elements (Equation 6) in Figure 11b.

$$\gamma(\mathrm{i},\mathrm{j}) = \delta(\mathrm{i},\mathrm{j}) + \min[\gamma(\mathrm{i}-1,\mathrm{j}), \gamma(\mathrm{i}-1,\mathrm{j}-1), \gamma(\mathrm{i},\mathrm{j}-1)] \tag{6}$$

The calculation of all possible paths is computationally demanding and the patterns to match usually occur at similar epochs. The computational performance of DTW can be improved through the imposition of constraints (Figure 12), which may be windows, where a strip around the diagonal is defined for limiting the search area, or slopes, controlling the dimension of each step (Sakoe and Chiba, 1978; Berndt and Clifford, 1994).

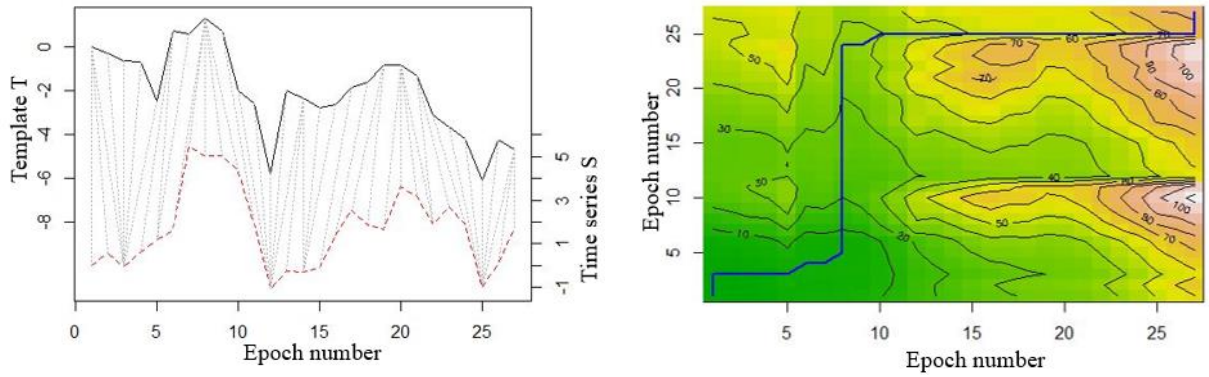

(a) (b)

Figure 11 – Alignment between the time series S and the template T (a); density matrix with the cumulative distances for each pair of data points and selection of the minimum cumulative distance path (blue line) in (b).

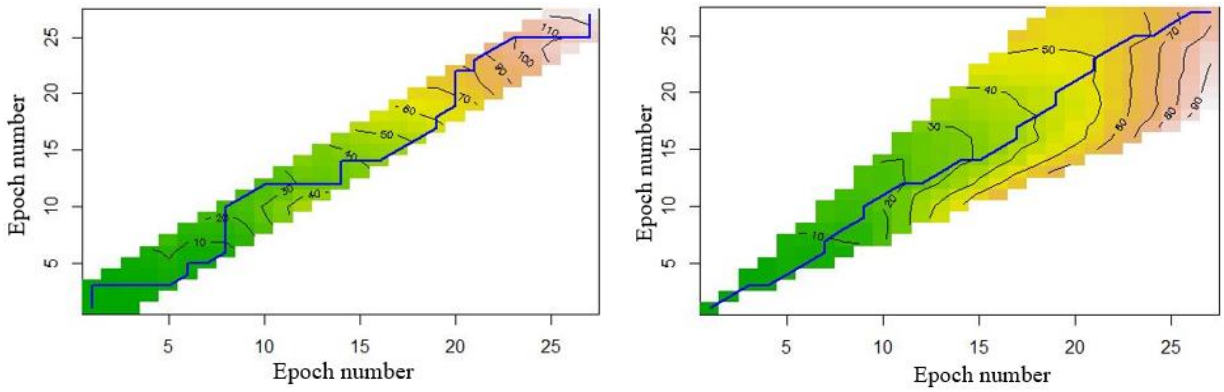

(a) (b)

Figure 12 – Constraints on DTW search area based on band (a) and on slope (b).

Longest Common Subsequence (LCSS) is used as an edit-based distance and it corresponds to the similarity between two time series defined by the maximum number of similar elements between them, without changing the elements' order (Bergroth *et al.*, 2000). The distance between two time series is the minimum cost required to transform a time series X into another time series Y, where individual costs are attributed to the operations of removing, adding or replacing elements in X. The distance Dist(X,Y) is defined by Equation (7):

$$\mathrm{Dist}(X, Y) = n + m - 2 \cdot r(X, Y) \quad (7)$$

where "n" is the length of time series Y, "m" is the length of time series X and "r(X, Y)" is the length of the LCSS between X and Y. The major problems of this approach reported in the literature are the processing time and the large memory usage (Bergroth *et al.*, 2000).

In feature-based distances, the original elements of time series are replaced by feature vectors that characterize those time series, e.g. frequencies contained in the data and obtained through Discrete Fourier Transform (DFT) or Discrete Wavelet Transform (DWT). Traditional clustering

methods can be applied directly to the feature values, whose reduced dimension improves computational performance. This procedure is adequate to compare periodic time series; however, it is not suitable to analyse cause-effect relationships (Esling and Agon, 2012).

Structure-based distances are divided into model and compression methods. Model-based distances benefit from *a priori* knowledge on the analysed phenomenon. The distance is determined through the likelihood of a certain time series being generated by a model. Hidden Markov Models (HMM) have been used to build similarity matrices that can be utilized to cluster time series. For example, Panuccio *et al.* (2002) evaluated the probability L_{ij} of time series S_j being created by model λ_i (trained for time series L_i) and used it to build a similarity matrix (Equation 8).

$$L_{ij} = P(S_j | \lambda_i), \quad 1 \leq i, j \leq N \tag{8}$$

Kalpakis *et al.* (2001) proposed AutoRegressive (AR) models in the definition of a model-based distance measure between time series. Stationary time series can be described by AR models according to Equation 9 (Xiong and Yeung, 2004),

$$x_t = \phi_0 + \sum_{j=1}^{p} \phi_j x_{t-j} + e_t \tag{9}$$

where "x_t" is the value in the time series at epoch "t", "ϕ_0" is a constant value, "ϕ_j" are the model parameters, "x_{t-j}" are the values in the time series for epochs before "t", "e_t" is white noise and "p" is the order of the model. The Linear Predictive Coding (LPC) cepstral coefficients, which consist on the computation of the cepstrum[9] of the autoregression parameters "ϕ_j", are then used to describe the time series and the distance used in the clustering was performed using the Euclidean distance between the cepstra as dissimilarity measure. The advantages of utilizing the cepstra instead of other methods were the reduction of the number of parameters to use in the computation, higher discriminatory capability and the possibility of dealing with time series with different characteristics (length, differences in amplitude and in time axis). The main limitation was that the application of this method was only feasible to time series that can be described by autoregressive models.

Silva *et al.* (2013) proposed Recurrence Patterns Compression Distance (RPCD) as a compression similarity measure. This method combined the representation of time series as distance images and the application of image compression techniques, originally used for video compression, that was used as distance measure between the time series (Figure 13).

[9] Cepstrum is the inverse Fourier transform of the logarithm of the amplitude achieved by applying a Fourier transform at a time series (Kalpakis *et al.*, 2001).

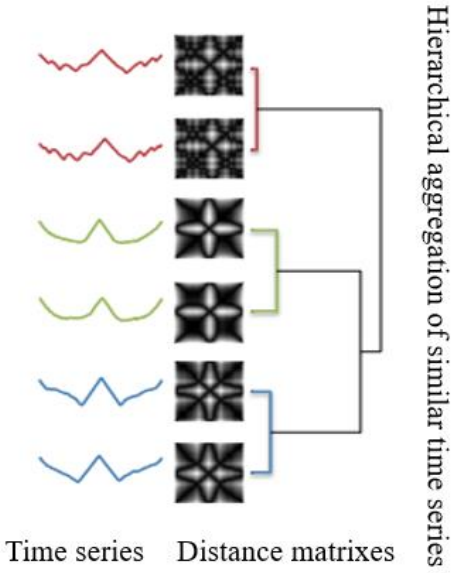

Figure 13 – Clustering of time series based on RPCD similarity measure, adapted from Silva *et al.* (2013).

Shape, edit and feature-based dissimilarity measures are appropriate to evaluate the distance between short time series, but their performance is lower for long time series. Structure-based measures are suitable to both short and long time series.

3.1.2.4. Every clustering process requires the evaluation of the cluster quality, which can be performed by visualisation or through a scalar measure of accuracy. The visual analysis of the clustering performance by a human operator may be considered as ground truth. As for the scalar measures of accuracy, they can be divided into two types: external or internal indexes. The first type requires the existence of ground truth data to which compare the clustering results. One example of external index is purity, which evaluates the ratio between the number of elements correctly attributed to a cluster and the cluster size. Normalized Mutual Information is a normalized version of purity, which can be used to compare clustering solutions with different number of clusters. Internal indexes evaluate the dissimilarity of the elements inside each cluster, without using ground truth data. They must not be used to compare clustering solutions achieved through different methods or distinct dissimilarity measures. The most frequently used internal index is the Sum of Squared Error (SSE), with lower values corresponding to more homogeneous clusters (Aghabozorgi *et al.*, 2015).

Figure 14 shows a representation of the steps to perform the clustering of time series, the options available for each step and examples of dissimilarity measures (in grey).

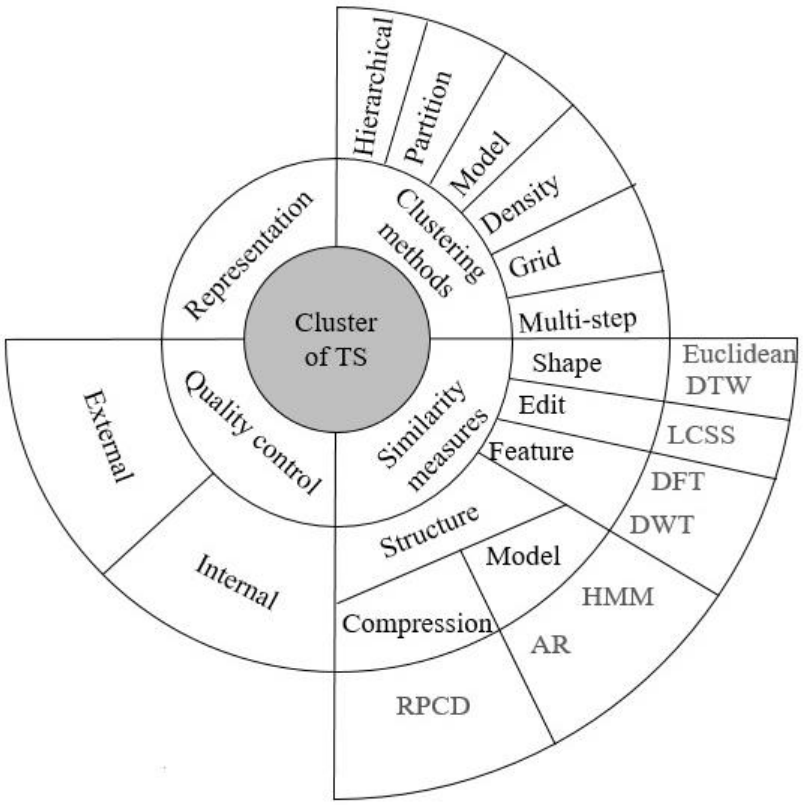

Figure 14 – Summary of strategies to cluster time series.

3.2 Methods

The aim of the presented research, in the field of RADAR interpretation, was the development of an automatic tool for the post-analysis of InSAR displacement time series, in order to identify eventual displacement anomalies, which may reflect the presence of damages in structures.

The InSAR technique considered in the study was the PSI method implemented in SARPROZ© software (Perissin *et al.*, 2011), which follows the PSInSAR algorithm described in section 2.1.

The RADAR interpretation method developed in this study was intended to be objective and independent of *a priori* information. Therefore, clustering was selected for the analysis, for being an unsupervised technique, and hierarchical clustering was chosen due to its independence of previous knowledge on the number of clusters. Several experiments executed in Ding *et al.* (2008) showed that DTW has a similar or better accuracy than other dissimilarity measures. To benefit from its accuracy, DTW was the distance measure used for displacement time series dissimilarity evaluation. Two versions of the tool were developed in R software (R Core Team, 2018). One considers only one SAR acquisition geometry, enabling an analysis of displacements along LOS (version 1D of the tool), while the other (version 2D) combines data from ascending and descending passes, allowing the determination of two displacement components: vertical and horizontal (along a direction of interest indicated by the user).

3.2.1. The first step of the analysis is the estimation and removal of the reference point effect. The PS selected as reference may not be completely stable during the entire time interval of the study, affecting the displacements of the remaining PSs which are referred to it. On the other hand, residual atmospheric effects may still be present in the data and require the adoption of mitigation measures. In this research, the method proposed in Notti *et al.* (2015) is adapted. PSs with temporal coherence above a certain threshold and considered stable are identified and their displacement time series are averaged, by computing the average displacement from all time series for each epoch. The resulting time series is the correction used to mitigate the mentioned errors and it is subtracted from the time series of all PSs in the study area.

Notti *et al.* (2015) consider PSs with average velocity with absolute value equal or lower than 0.5 mm/year as stable. However, in this research, a non-linear displacement model is considered at PSI processing (sections 3.3.1.2 and 3.3.2.2) and average velocity is not estimated. Instead, cumulative displacements during the time interval of the analysis are available for each PS.

Two methods for the identification of stable PSs were tested. The first test considered as stable PSs presenting absolute value of cumulative displacement equal or lower to $0.5 \cdot \Delta t$ mm, where Δt was the time interval considered in the study, in years. The second approach fitted a linear model to the displacement time series of each PS and selected those with absolute value of slope equal or lower than 0.5 mm/year. Figure 15 shows the correction time series achieved from averaging the displacement time series of the selected PSs for each situation. It is evident that different PSs were selected in each case, as the time series obtained for the first approach (cumulative displacement) presented a trend that was not represented in the second approach (slope of linear model). In case the result achieved from the first approach was used to perform the correction, the removal of this trend would affect the time series of all PSs, including those where the trend was not originally present. Therefore, the second approach was selected.

This step is performed at both 1D and 2D versions of the tool. In version 1D, it is applied to the single geometry available to the analysis. On version 2D, it is applied to the LOS displacements of each geometry independently of each other.

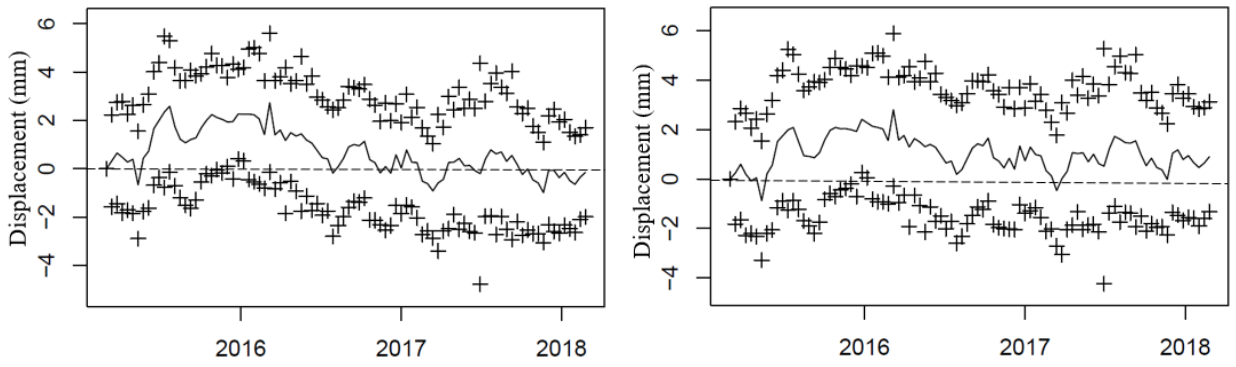

Figure 15 – Examples of correction time series (full lines) built from stable PSs selected based on cumulative displacement (a) and velocity (b) criteria; crosses are average displacement plus and minus one standard deviation for each epoch.

3.2.2. The second step of the algorithm is the merging of displacements from ascending and descending geometries and it is performed only at the 2D version of the tool. In order to obtain vertical and horizontal displacements for each PS, it is required that displacements from both LOS geometries are known for all PSs and at the same epochs. Thus, interpolations in both space and time are needed. For the interpolation in space, Inverse Distance Weighted (IDW) is the selected method, in which the inverse of a power of the distance between the sample points and the interpolation point is used as a weight. In Equation (10), from Bartier and Keller (1996), $z_{x,y}$ is the interpolated value of variable z at the point with coordinates (x,y), z_i is the value of z at sample point i, $d_{x,y,i}$ is the distance between sample point i and interpolation point on coordinates (x,y) and β is the power of the distance. In this research, the value 2 is used for this parameter.

$$z_{x,y} = \frac{\sum_{i=1}^{n}\left(z_i \cdot d_{x,y,i}^{-\beta}\right)}{\sum_{i=1}^{n} d_{x,y,i}^{-\beta}} \tag{10}$$

The interpolation in time is performed through linear interpolation.

Let us consider one of the acquisition geometries as the reference geometry and the other one as the auxiliary geometry. LOS displacements from the auxiliary geometry are spatially interpolated to the PSs from the reference one and LOS displacements from the reference geometry are interpolated to the PSs of the auxiliary one, using IDW. Then, for each PS, displacements from the auxiliary geometry are linearly interpolated to the dates of the reference one. Thus, LOS displacements from the reference and the auxiliary geometries become known for all PSs at the epochs of the reference geometry observations. Vertical and horizontal displacements are determined for all PSs from both acquisition geometries, for the epochs at which displacements from both directions are known. The equations to compute vertical and horizontal displacements

were derived from Dentz *et al.* (2006), where displacement along LOS (d_{LOS}) is defined in function of displacements in vertical (d_V), easting (d_E) and northing (d_N) directions, as in Equation (11).

$$d_{LOS} = d_V \cdot \cos\theta - \sin\theta \cdot \left[d_N \cdot \cos\left(\alpha_h - \frac{3\pi}{2}\right) + d_E \cdot \sin\left(\alpha_h - \frac{3\pi}{2}\right)\right] \quad (11)$$

In the Equation, θ is the incidence angle and α_h is the satellite heading. The satellite heading is given by Equations (12) and (13) for ascending (α_h^{ASC}) and descending (α_h^{DESC}) geometries, respectively.

$$\alpha_h^{ASC} = \beta \quad (12)$$

$$\alpha_h^{DESC} = \pi - \beta \quad (13)$$

The angle β is the angle between the projection of the LOS onto the horizontal plane and the east – west direction, which is given by Equation (14):

$$\beta = \operatorname{asin}\left(\frac{\cos\alpha}{\cos\varphi}\right) \quad (14)$$

where α is the inclination of the satellite orbit and φ is the latitude. Let d_H be the displacement along the direction of interest on the horizontal plane (e.g., the direction perpendicular to a dam's crest or the direction along a slope) and γ be the azimuth of the direction perpendicular to that direction of interest. From Dentz *et al.* (2006), if it is assumed that all horizontal displacement occurs in the direction perpendicular to that defined by γ, Equation (15) takes place:

$$\begin{bmatrix} d_E \\ d_N \end{bmatrix} = \begin{bmatrix} \cos\gamma \\ \sin(-\gamma) \end{bmatrix} \cdot d_H \quad (15)$$

Combining Equations (11), (12), (13) and (15) for both ascending and descending geometries, Equations (16) and (17) are obtained, where d_{LOS}^{ASC} is the LOS displacement from the ascending geometry, d_{LOS}^{DESC} is the LOS displacement from the descending geometry, θ^{ASC} is the incidence angle from the ascending geometry and θ^{DESC} is the incidence angle from the descending geometry.

$$d_{LOS}^{ASC} = d_V \cdot \cos\theta^{ASC} - d_H \cdot \sin\theta^{ASC} \cdot \cos(\beta - \gamma) \quad (16)$$

$$d_{LOS}^{DESC} = d_V \cdot \cos\theta^{DESC} + d_H \cdot \sin\theta^{DESC} \cdot \cos(\beta + \gamma) \quad (17)$$

Solving the system formed by Equations (16) and (17), Equations (18) and (19) for d_V and d_H are achieved.

$$d_V = \frac{d_{LOS}^{DESC} \cdot \sin\theta^{ASC} \cdot \cos(\beta-\gamma) + d_{LOS}^{ASC} \cdot \sin\theta^{DESC} \cdot \cos(\beta+\gamma)}{\cos\theta^{ASC} \cdot \sin\theta^{DESC} \cdot \cos(\beta+\gamma) + \cos\theta^{DESC} \cdot \sin\theta^{ASC} \cdot \cos(\beta-\gamma)} \quad (18)$$

$$d_H = \frac{d_{LOS}^{DESC} \cdot \cos\theta^{ASC} - d_{LOS}^{ASC} \cdot \cos\theta^{DESC}}{\cos\theta^{ASC} \cdot \sin\theta^{DESC} \cdot \cos(\beta+\gamma) + \cos\theta^{DESC} \cdot \sin\theta^{ASC} \cdot \cos(\beta-\gamma)} \quad (19)$$

3.2.3. The third step of the algorithm is the construction of the dissimilarity matrix to be used in the cluster analysis. As previously mentioned, a hierarchical clustering is applied, using DTW as dissimilarity measure. Therefore, DTW is computed between the time series of all pairs of PSs

and a distance matrix is built from those values. Pre-processing operations, such as representation (section 3.1.1) or normalisation are not performed, as these techniques may introduce changes in the time series structure, which can affect the success of their comparison (Esling and Agon, 2012; Aghabozorgi *et al.*, 2015).

Romano and Scepi (2006) stated that DTW is not an appropriate dissimilarity measure for PSI-derived displacement time series, due to the noise the series present. In this research, a visual inspection of the clustering results performed on the original displacement time series has shown indeed that neighbour PSs (e.g., PSs on the same roof) with similar displacement time series could be set to different clusters, while PSs with distinct behaviours and geographically far from each other could be aggregated into the same cluster. Therefore, a moving average, with a window size of three, is applied at the time series for noise reduction purposes, which enables the inclusion of these PSs in the correct clusters. The filtered time series are used exclusively for the DTW computation. All the following steps of the algorithm are applied on the non-filtered time series, to preserve the original data and to keep the measurement precision.

Loads affect displacements of neighbour PSs at close epochs and it is intended that PSs showing similar displacements at distant epochs are included in different clusters. Therefore, a constraint in the search area of DTW is applied, in order to avoid the association of displacement values observed at far epochs. A Sakoe Chiba band of size 2 is applied to limit the search area into a small neighbourhood of the original epoch. The usage of a constraint has the additional benefit of reducing the number of comparisons, which results in the decreasing of the computation time.

Nevertheless, due to the large number of PSs and observation epochs usually obtained through PSI technique, the computation time and memory usage are still limitations for this procedure. In order to reduce even more the computation time, the code for the construction of the dissimilarity matrix is parallelized. To deal with large datasets, the developed code is adapted to be run in Jupyter[10].

The implementation of this step differs for the 1D and 2D versions of the tool. In the 1D version, DTW is applied to the univariate LOS displacement time series. In the 2D version, the user may choose from three options: univariate vertical displacement time series, univariate horizontal displacement time series or multivariate displacement time series with both vertical and horizontal displacements being evaluated simultaneously.

3.2.4. The forth step is the selection of the number of clusters and the consequent clustering of the time series. The hierarchical agglomerative clustering method is applied based on the

[10] Project Jupyter is a non-profit organization for the development of open-source software, standards and services (Project Jupyter, 2020).

dissimilarity matrix built from DTW and all PSs are iteratively aggegagted until they form a single cluster. Three aggregation criteria are available at the tool: single linkage, complete linkage and Ward method (section 3.1.2). The distances required to merge two clusters at each step of the iterative procedure are the linkage distances and they provided information on each cluster homogeneity. Small linkage distances mean that the time series in each cluster are similar among them, while large linkage distances correspond to the fusion of heterogeneous clusters.

The linkage distances enable the automatic selection of the number of clusters, which correspond to the number of clusters achieved before the largest step in linkage distance occurs. However, there is not an optimal criterion for the selection of the number of clusters for all situations and the user must evaluate the results achieved by using the proposed number and verifying if the obtained solution is satisfactory for the problem under analysis. The tool creates two types of outputs: a displacement time series representative of each cluster and cluster centroids.

The representative time series results from the average of the displacement time series from all PSs in each cluster. A Seasonal-Trend decomposition procedure based on Loess (STL) is applied to the representative time series to achieve seasonal and trend displacement components (Cleveland *et al.*, 1990). Centroids are average values of certain variables for all PSs in each cluster, which may be computed during PSI processing (e.g., residual height or cumulative displacement) or provided by the user as raster images. The usage of these raster images is optional and they can provide any type of information the user found may be useful to the cluster interpretation (e.g. slope inclination or distance to a river). All results computed by the tool are exported into Comma-Separated Values (csv) or into Portable Document Format (pdf) files. The csv files can be imported into a GIS software for a spatial visualization of the results. If the user is satisfied with the level of detail provided by the automatic solution, the procedure is finished. However, if the user wishes to change the aggregation level, it is possible to increase or to decrease the number of clusters to a manually selected number and to achieve a new organization of the data. The reclustering operation is performed based on the previous dissimilarity matrix, without recomputing the DTW, and it can be repeated until the user is satisfied with the results. This last step is performed equally for both 1D and 2D versions of the tool. The workflow of the whole procedure is presented in Figure 16.

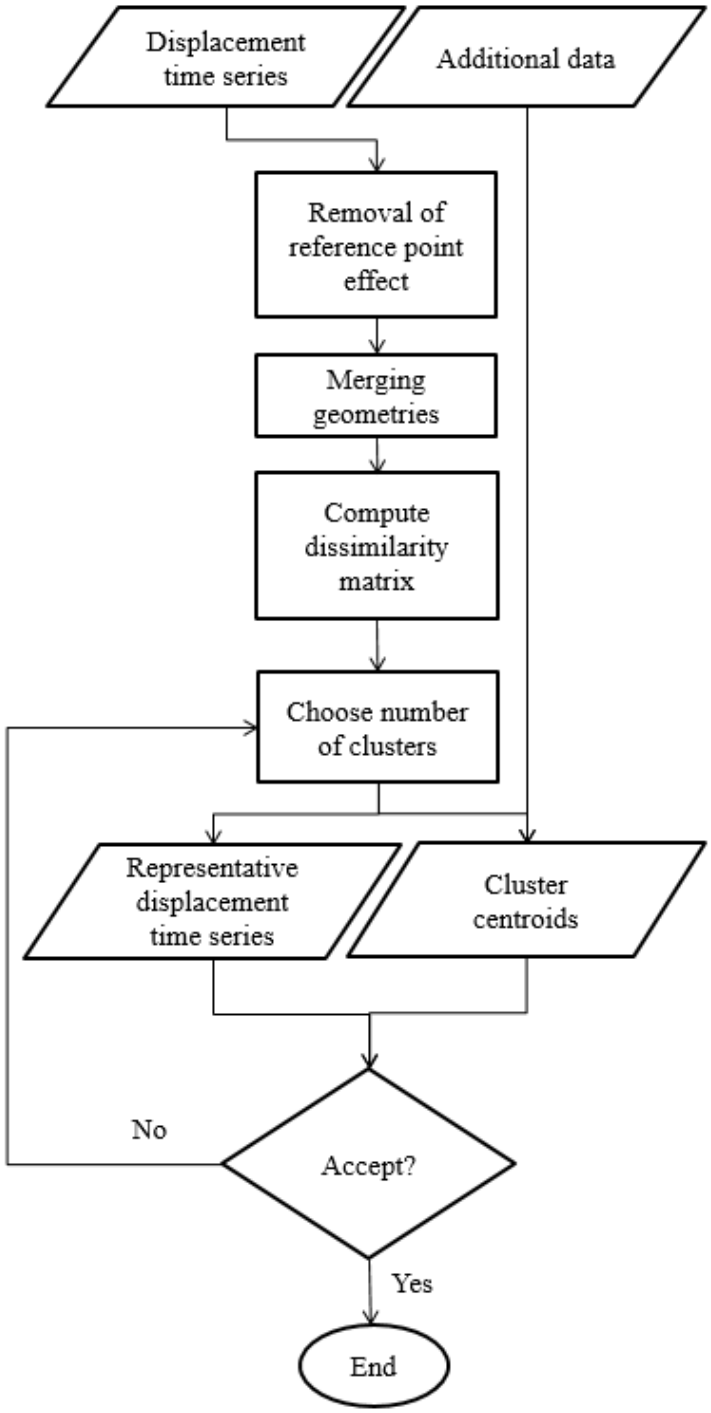

Figure 16 – Proposed workflow for the time series clustering.

3.3 Application to case studies

The method proposed in section 3.2 for RADAR interpretation of PSI displacement time series was tested for two case studies. The 1D version of the tool was used to analyse displacements on the slopes around a water reservoir during its first impoundment, while the 2D version monitored a heritage urban area with 260 years old buildings located on alluvial soil.

3.3.1 Odelouca slopes

3.3.1.1 Description of study area

The first case study were the slopes around Odelouca dam, in Monchique municipality, Faro district, Portugal, owned by Águas do Algarve, SA (Figure 17). Odelouca is the second largest embankment dam in the country. The structure height above the foundation is 76 m and the crest is 418 m long. The reservoir spans an area of 7.8 km^2, storing 128 hm^3 of water at its full capacity and it is an important source of water supply and irrigation in its region (Águas do Algarve, 2020).

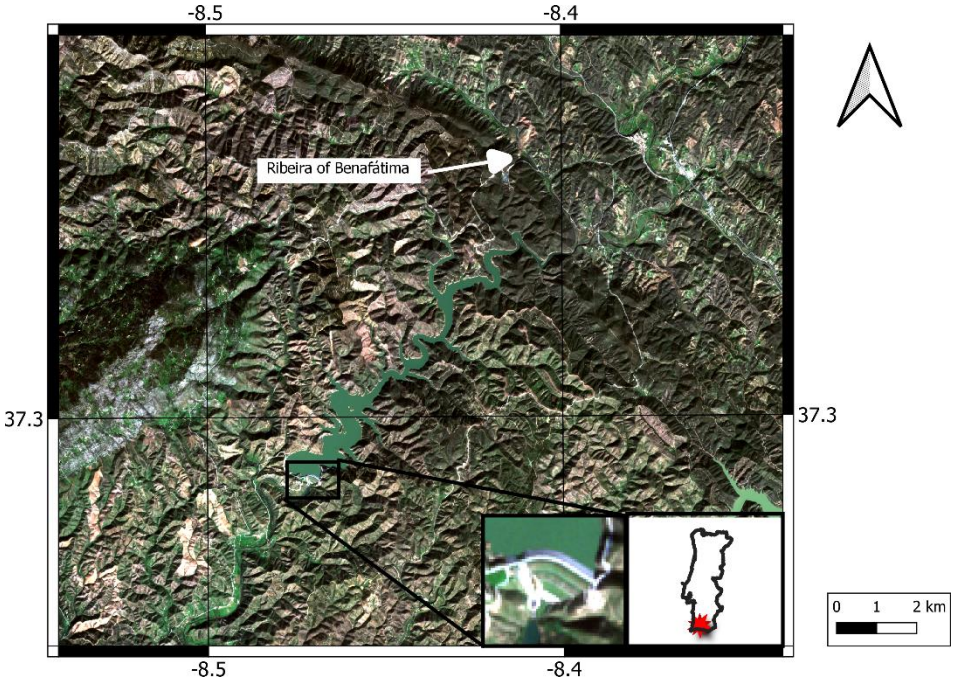

Figure 17 – Location of Odelouca dam and its reservoir. The inset on the left shows the dam and the one on the right highlights the dam location in Portugal (red star); background is a Sentinel-2 image from February 2020. Coordinate grid in WGS84.

The predominant geological formations around Odelouca reservoir are Mira and Brejeira formations, both from the Carboniferous period, Paleozoic era (Figure 18). The northeastern region is occupied by Mira formation, with shales and greywacks as main lithologies (Pereira *et al.*, 2008). Southwest of Mira formation, there is Brejeira formation, formed by greywacks and quartz wacks interbedded with shales (Fernandes *et al.*, 2012). At the border with Mira formation, Brejeira formation contains a band of quartz wackes and quartzites. Most of the reservoir is surrounded by steep slopes, with 79% of the hillsides presenting slope inclination larger than 14º and 61% between 19º and 33º. These properties turn the slopes around the reservoir susceptible to land and rockslide occurrence, especially downstream of Ribeira of Benafátima junction with the

reservoir. The most susceptible areas are those subjected to changes in the soil saturation, mainly areas that are emerged or submerged, depending on the time of the year (Nemus - Gestão e Requalificação Ambiental, 2007).

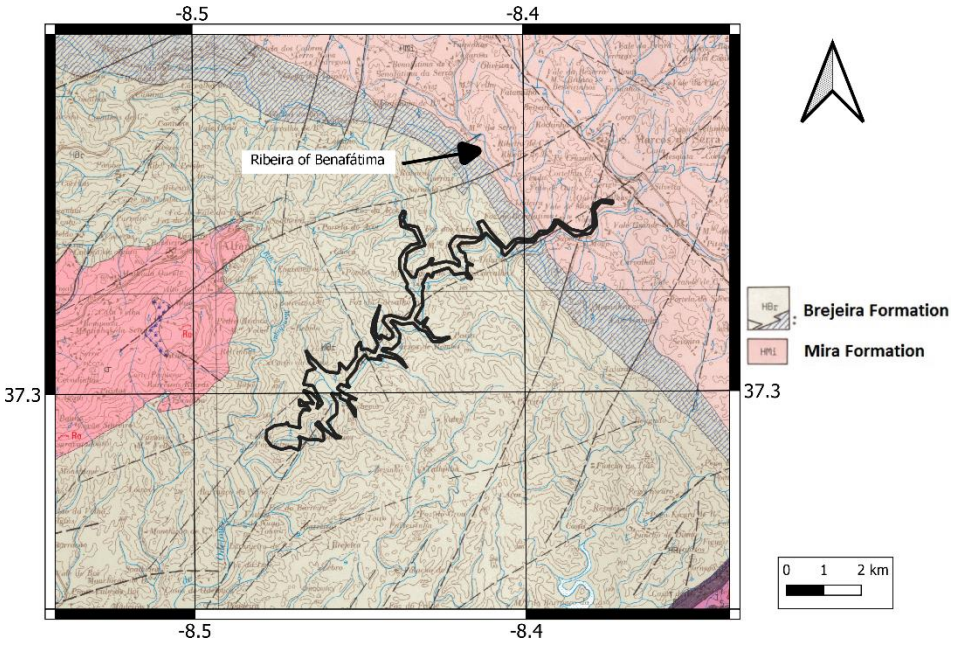

Figure 18 – Geological map at 1:100000 from the National Laboratory for Energy and Geology (1992); black line is the reservoir boundary in February 2020 manually delimited from a Sentinel-2 image. Coordinate grid in WGS84.

The first impoundment of a reservoir is a critical phase for slope stability, as the shear strength of flooded slopes decrease, the rise in water hydrostatic pressure reduces sliding resistance and the stored water presses groundwater contributing to slope saturation; thus, increasing landslide susceptibility (Fujita, 1977; Hui, 2015). In this study, the analysis of displacements during the first impoundment of Odelouca reservoir was performed, in order to verify if there were measurable changes on the emerged slopes caused by the water accumulation. The first impoundment began in December 2009 and water extraction started in May 2012 (Águas do Algarve, 2020).

3.3.1.2 PSI processing

The slopes around Odelouca reservoir were covered with vegetation, which led to the selection of L-band SAR images from the sensor PALSAR-1 on board of ALOS-1 Japanese satellite to be selected for the study. This sensor was active between 2006 and 2011, covering part of the first impoundment period. The dataset selected for the analysis was from the high-resolution mode, with a swath width of 70 km, with single and dual polarization. The spatial resolution for single polarization images was of 10 m x 10 m, while for dual polarization it was of 20 m x 20 m. These later images were oversampled to match the resolution of those with single polarization. Only HH

polarization data were used for the analysis. The images were from an ascending pass of the satellite, acquired around 11 pm UTC, from path 10 and frame 730. The Japanese space agency provided the images in level 1.1 (SLC) and with an orbit accuracy below 1 m (Nakamura *et al.*, 2007; JAXA, 2008). Despite the nominal acquisition frequency of 46 days, there were many gaps in the image time series, resulting in only 20 images acquired for the required geometry during the whole period of the sensor activity (Figure 19).

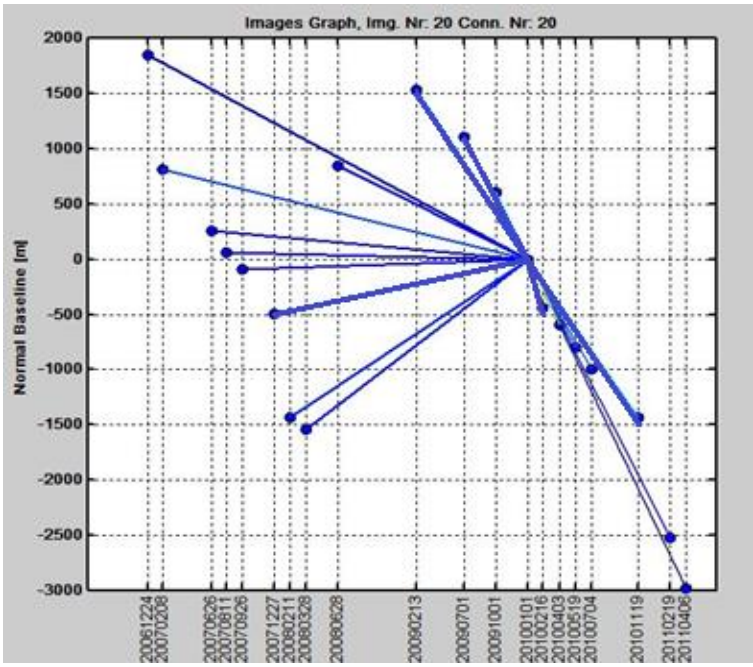

Figure 19 – Distribution of normal and temporal baselines.

The PSI processing was performed in SARPROZ© software. From the stack of SAR images, one of them was selected as master image, which minimised the set of temporal and normal baselines (the image from August 1, 2010). The remaining images were corresgistered into the master's geometry, based on initial approximations using orbital data and refined through cross-correlation. The image dataset was geocoded with respect to a DEM, through the manual selection of a Ground Control Point (GCP), allowing the removal of flat Earth and altitude phase components. The utilized DEM was the European Digital Elevation Model (EU-DEM), freely provided through Copernicus Land Monitoring Service, with spatial resolution of 25 m and vertical accuracy of 7 m (Copernicus Programme, 2020). APS was estimated at pixels presenting large values of amplitude stability index ($1 - \frac{\mu_A}{\sigma_A}$), where σ_A was the amplitude standard deviation and μ_A was its average. The APS was interpolated for all pixels and it was also removed from phase. A larger set of pixels was selected for displacement and residual height estimation. As this research was dedicated to structure monitoring, where non-linear displacements are often found (e.g., seasonal effects or ageing), a non-linear displacement model was considered, instead of the usual

PSI method with linear displacements as presented in Equation 4. The non-linear displacement model resulted from the application of a moving average on the unwrapped residual heights (Milillo, Perissin, *et al.*, 2016). Only points with temporal coherence above 0.9 were considered as PSs. Each PS provided a residual height, a cumulative displacement and a displacement time series, with an observation at each SAR image acquisition epoch.

This procedure was performed for an area of 18 km x 18 km. However, the subsequent analysis was executed only for a buffer varying between 750 m and 1000 m around the reservoir, in order to limit the evaluation to the slopes in the reservoir area of influence.

3.3.1.3 Cluster analysis

The displacement time series along LOS direction for the achieved PSs were analysed through the clustering method proposed in section 3.2. After data input, the reference point effect was determined and removed from all time series. The reference point was located 3 km away from the reservoir and it was one of the most stable PSs in the 18 km x 18 km area analysed at the PSI processing. Remaining movement of that point and residual atmospheric artifacts were estimated through the average of displacement time series of PSs considered stable (section 3.2) and subtracted from the displacements of all other scatterers (Figure 20). The correction time series showed that the reference point may have moved away from the sensor between 2006 and 2009 and may have moved towards it from that year on, causing the reverse behaviour on the other studied PSs. However, that effect may have been caused by residual atmospheric effects, as well.

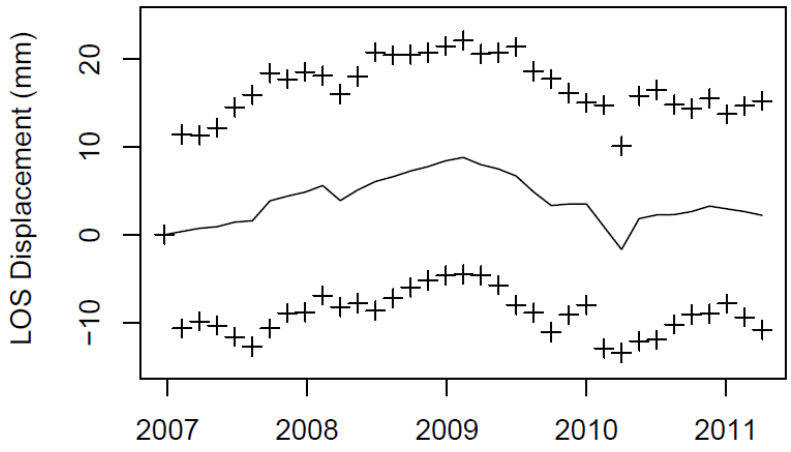

Figure 20 – Correction time series for the reference point effect (line); the crosses represent the average time series plus and minus one standard deviation.

The corrected displacement time series were then clustered following three different aggregation methods (Ward method, complete linkage and single linkage), with the respective

dendrograms (tree chart of the linkage distances showing how the PSs were aggregated with each other) presented in Figure 21.

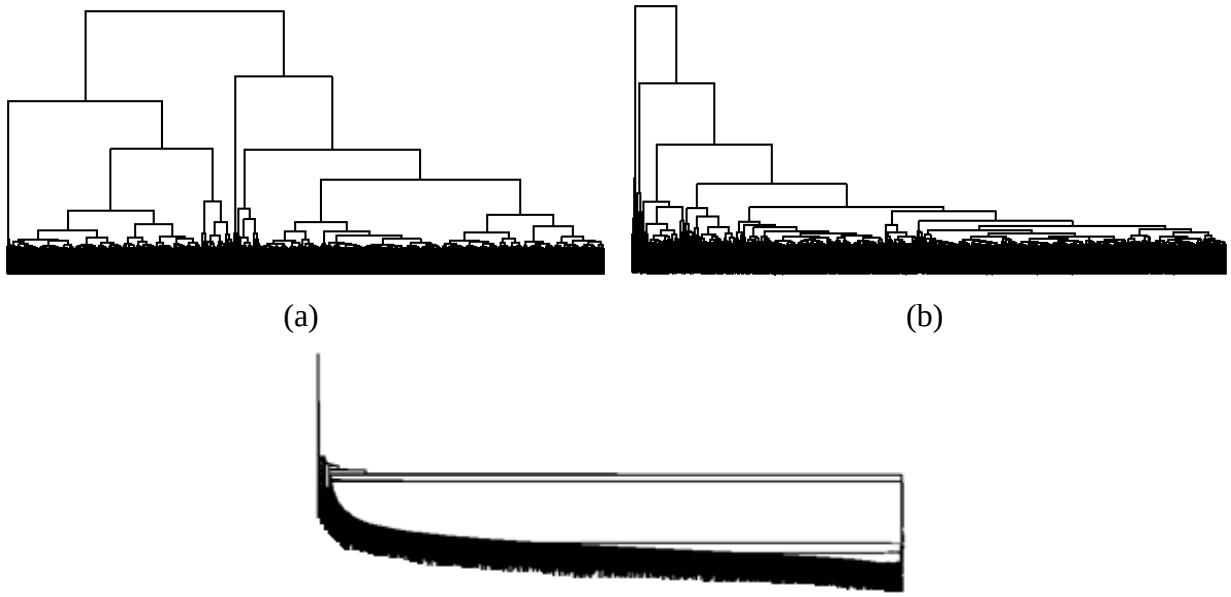

(a) (b)

(c)

Figure 21 – Dendrograms for Ward method (a), complete linkage (b) and single linkage (c).

The three aggregation methods led to distinct solutions. Ward method built two large clusters, each of them divided into two other clusters: a small one, with few PSs, and a large one, containing the remaining points. Complete linkage formed a progressively growing cluster, where smaller sets of PSs were aggregated into the main cluster until they formed a single group. A similar pattern was found for single linkage, where the dimension of the clusters being aggregated in each iteration was even smaller than on complete linkage, often being constituted by single PSs. The three strategies automatically suggested a number of clusters to be used in the analysis. Ward method proposed four clusters, complete linkage led to three and single linkage to two. Solutions with manually selected number of clusters were also analysed and will be presented in section 3.4.1.

Two additional data were included in raster files to aid the cluster interpretation: slope inclination and curvature. The two information sources were built in GIS software through the EU-DEM. Slope inclination was provided in degrees and attributed to each raster pixel the largest inclination among that pixel and its adjacent neighbours. Curvature was determined through the second derivative of the surface, based on a 3 x 3 pixel neighbourhood. This procedure was executed in ArcGIS® software, which attributed negative curvature values to convex surfaces and positive values to concave ones.

The mentioned strategy enabled the achievement of displacement time series representative of each cluster and cluster centroids, which can be used in the identification of eventual

anomalies on the slope behaviour. Parameters used in clustering processing are presented in Annex A.1 Table 17.

3.3.2 Lisbon Downtown

3.3.2.1 Description of study area

The city of Lisbon, in Portugal, is located at the right bank of Tagus River, 15 km east of the river mouth at the Atlantic Ocean. The municipality spans an area of 100 km^2. There are 0.5 million people living in the city, but 2.8 million inhabit its metropolitan area, with a large number of daily commutations to and from the city. The Downtown area is an important government, business and touristic centre. It is located close to the river and natural disasters have affected it in the past. In 1775, an Mw 8.7 earthquake with epicentre southwest of Portugal and the subsequent tsunami caused severe damage at the area, requiring its reconstruction. A new urban organization and building type emerged in order to mitigate the effects of future disasters. The streets became larger than before, perpendicular to each other and oriented towards the river (Figure 22). The buildings, called Pombalinos, have wooden structures to increase their flexibility and resistance to earthquakes. Since 1956, LNEC's AGU performs high-precision geometric levelling along the west wing building of Praça do Comércio (large square close to the river at Figure 22). They found a progressive settlement towards the river, which reached more than 15 cm by 2017 at the benchmark closest to the water line (LNEC, 2017a).

Figure 22 – Orthophoto of Lisbon Downtown, provided by the General Directorate of the Territory through the Geographic Information National System (GINS). Coordinate grid in WGS84.

The Downtown is located at the junction point of two old streams, which are now piped, and it was reconstructed over alluvial soil (Quaternary period) formed by the sediments transported by those streams and debris from the buildings destroyed during the earthquake. The area is flanked by geological formations from Miocene epoch (Neogene period), with main lithologies being sand, limestone and clay. To the west and north of the alluvial soil is the formation “Areolas de Avenida da Estefânia”, with fine and clayey sand, claystone and some bio-calcarenite stone. Smaller areas formed by “Calcários de Entrecampos” (bio-calcarenite stone) and “Argilas de Prazeres” (clay and marl) are also present in the area west of the alluvial soil. To the east of the alluvial soil, there is “Areias com placuna miocénica”, formed by sand, pebbles, sandy clay and other elements, which is surrounded by “Calcários de Casal Vistoso” (limestone rich in organic matter), “Areias de Quinta do Bacalhau” (deposited sand), “Argilas de Prazeres” and “Calcários de Entrecampos” (Figure 23).

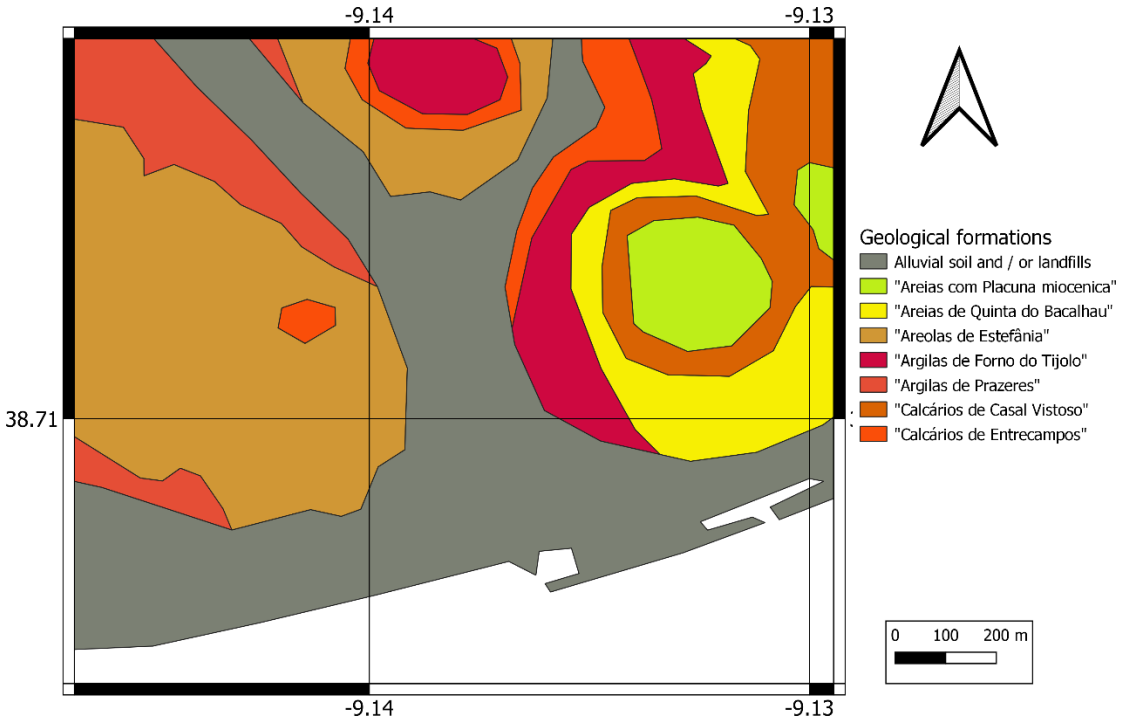

Figure 23 – Manual digitalization of the geological formations at the Downtown area, from the geological map by the National Laboratory for Energy and Geology, at 1:50000 scale. Coordinate grid in WGS84.

3.3.2.2 PSI processing

The PSI analysis considered part of Lisbon metropolitan area, including the whole Lisbon municipality and parts of the neighbour municipalities of Loures, Odivelas, Amadora, Sintra and Oeiras, spanning an area of 16 km x 16 km. The goal was to achieve a displacement map for this area, where smaller regions were then analysed using the method proposed for RADAR interpretation of displacement time series.

This study used SAR images from the C-SAR system on board of Sentinel-1 from ESA. These are images acquired in microwave C-band, with a centre frequency of 5.405 GHz, corresponding to a wavelength of, approximately, 55 mm. The scenes are in Interferometric Wide Swath (IW) imaging mode and are acquired using TOPSAR, in which a strip of 250 km is imaged, divided into three subswaths, through successive bursts resulting from the steering of the antenna in both elevation and azimuth directions (ESA, 2020). The image nominal spatial resolution is of 20 m in azimuth and of 5 m in slant range. The time interval for the study spaned three years, from March 2015 to February 2018. In order to assure a regular acquisition frequency in time (and due to computational constraints), only scenes from Sentinel-1A were considered. The temporal resolution was 12 days. The orbits had accuracies of 2 cm to 3 cm at radial and cross-track directions and of 5 cm at along-track direction (Sandwell *et al.*, 2016). Two datasets were considered (Figure 24). The first one was from the ascending pass of the satellite with the relative orbit 45, subswath 2. Eighty-nine scenes composed the dataset, with only three gaps in the acquisition time series. The second dataset was from the descending pass with relative orbit 125, subswath 1, which contained 86 images, from 92 that were expected during the three years of the study. The images were in SLC format.

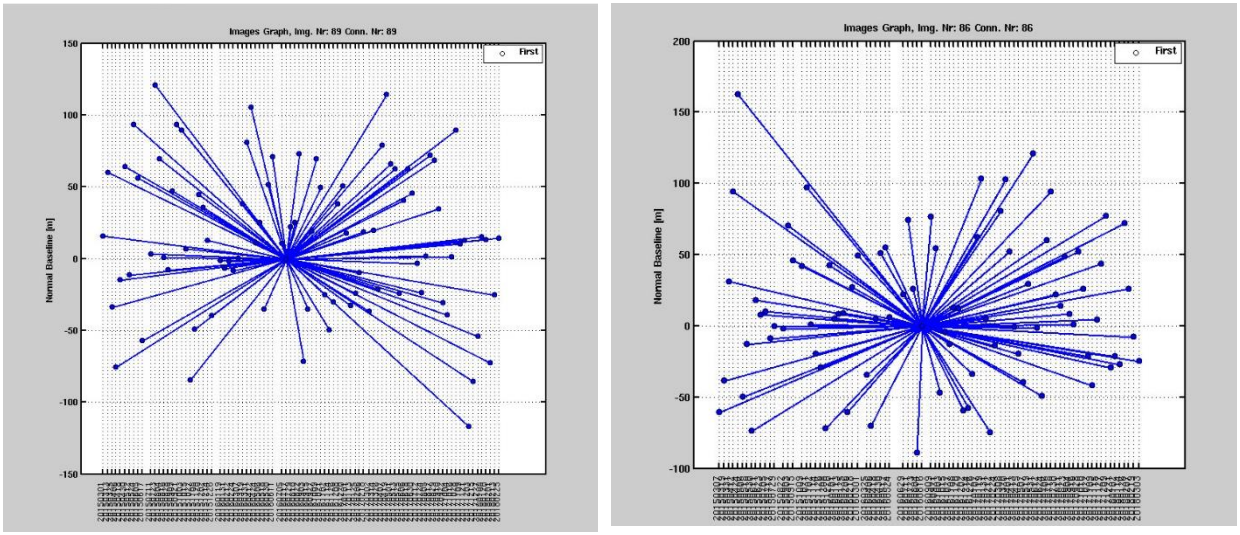

(a) (b)

Figure 24 – Distribution of normal and temporal baselines for (a) ascending and (b) descending passes for the city of Lisbon.

Altitude data was from the EU-DEM, with a spatial resolution of 25 m and vertical accuracy of 7 m.

PSI processing was performed, independently, for each dataset using SARPROZ© software. The images from July 17, 2016 and August 16, 2016 were the master images for the ascending and descending datasets, respectively. Slave images from each dataset were coregistered with

respect to their corresponding master and a GCP, manually selected, ensured the alignment between the SAR images and the DEM. Flat earth and topographic components of phase were removed through orbits and the DEM. APS was estimated for selected points with stable amplitude, interpolated and removed from all pixels. For residual height and movement estimation for each point, the non-linear displacement model was used, similar to Odelouca case study, as the monitored structures (mainly buildings) were expected to have non-linear responses to certain loads (e.g. temperature). Residual height, a displacement time series and cumulative displacement during the study time interval were determined for each scatterer. Scatterers with temporal coherence above 0.9 were considered as PSs.

Displacements and residual heights were determined with respect to reference points, which differed for each dataset. The reference points were distanced 2 km from each other, but they were both located at areas considered stable.

3.3.2.3 Identification of PSs on structures

In urban areas, there are many objects which keep their reflective behaviour stable to SAR signal, thus being potential PSs. Besides structures, other elements such as lampposts or advertising signs can also originate PSs. As this study focussed on the use of SAR interferometry for structure monitoring, the identification of the PSs located on the objects of interest was required. For that, an orthophotograph was classified, following an Object-Based Image Analysis (OBIA) approach, in which structures were separated from streets, squares and vegetated areas, where the unwanted elements were most likely located.

This step was performed only for Lisbon Downtown, at an area of 1 km x 1 km. The orthophotograph had a spatial resolution of 50 cm and it was provided by the Portuguese General Directorate of the Territory. The optical data were from 2004 – 2006, around 10 years older than the SAR data. Despite some changes between the acquisition dates of optical and SAR images, especially close to the river where the subway line expansion was on going at the acquisition time of the optical data, the core of the Downtown did not suffer many changes between the two epochs. Thus, the area of the subway construction works was excluded from the analysis and the orthophotograph was used as a source for structure location. Orfeo ToolBox[11] was used to perform the OBIA approach. The Large Scale Mean Shift algorithm segmented the image into variable dimension objects, which became the unit for analysis, instead of individual pixels. The level of required smoothing in each object, the accepted distance between spectral signatures of different

[11] https://www.orfeo-toolbox.org/

pixels and the minimum acceptable size for an object were criteria used to perform the segmentation. A vector layer with the object delimitation was achieved, for which radiometric and shape indices to be used in classification were defined. For each object, the mean and variance of the radiometric levels in the red, green and blue bands were computed during the segmentation procedure. Additional radiometric indices, computed in QGIS[12], were included, such as brightness and the proportion of red, green and blue in each object (ratio between the digital number of a band and the sum of the digital numbers from the three bands). Shape parametres were the object area, perimeter and their ratio. The segmentation result and a map of proportion of red for each object are presented in Figure 25.

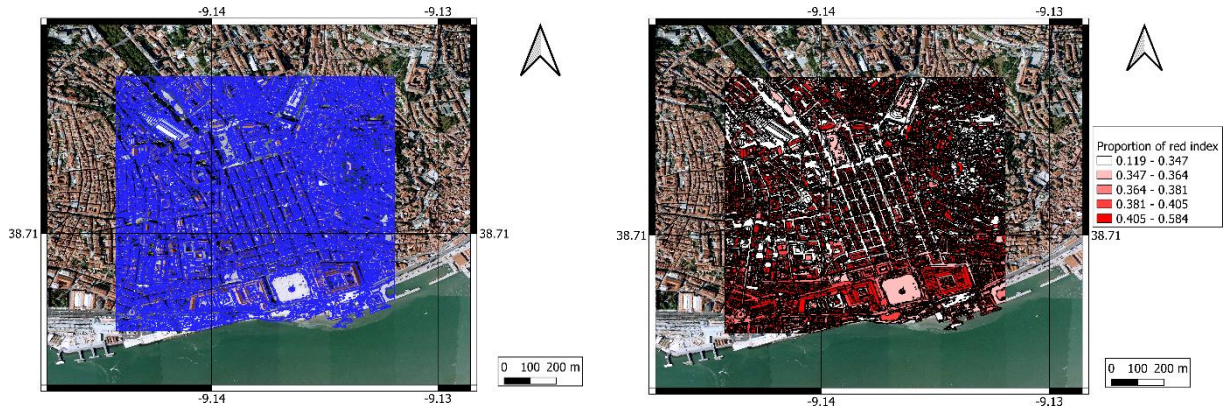

(a) (b)

Figure 25 – Segmentation result (a) and map of proportion of red (b).

The image was classified using a supervised approach. Six classes composed the classification nomenclature: four types of structures – red roofs with small area, red roofs with large area, dark roofs and bright roofs – squares and roads. The variables used for the classification for each object were their red and blue average digital numbers, the variance of their red digital numbers, indexes of red, green and blue proportions, brightness (the average of the three bands), object area, perimeter and the ratio between area and perimeter. Training and validation samples were manually selected and a classification model was defined from the training dataset (Figure 26). Orfeo Toolbox performed a classification of the validation dataset using the model. From the comparison of the result with the classes manually attributed, it provided a confusion matrix. Table 2 presents the confusion matrix, after aggregating the six classes into structures and non-structures.

From the 844 objects in the validation dataset, 817 were correctly classified, resulting in a global accuracy[13] of 97%. The producer's accuracy[14] for the structure class was of 99.5%, while it was only

[12] https://qgis.org/en/site/
[13] Percentage of correctly classified objects at all classes.
[14] Probability of an object from a certain class to be correctly classified (Zanotta *et al.*, 2019).

36.1% for non-structures. The user's accuracy[15] for the structure class was 97.2% and it was 76.5% for the non-structures. Cohen's Kappa index evaluated the overall classification accuracy considering also the proportion of the objects being correctly classified by chance (Cohen, 1960) and in this case its value was 0.97. As both global accuracy and Cohen's Kappa were values close to 1, the classification model was considered acceptable and it was used to classify the whole segmented image. The classification algorithm was the k-Nearest Neighbour (k-NN) (Zouhal and Denoeux, 1998), which is a supervised machine learning algorithm that compares the feature vector (vector containing the values of the variables selected for the classification) of each object to classify to the feature vectores of the objects in the training dataset. The algorithm considers the k training objects with the closest feature vectors to that of the object to classify as neighbours. The object to classify was attributed the most common class among its neighbours. In this case, it used 32 neighbours. The classification map passed an edition phase to improve the quality (Figure 27).

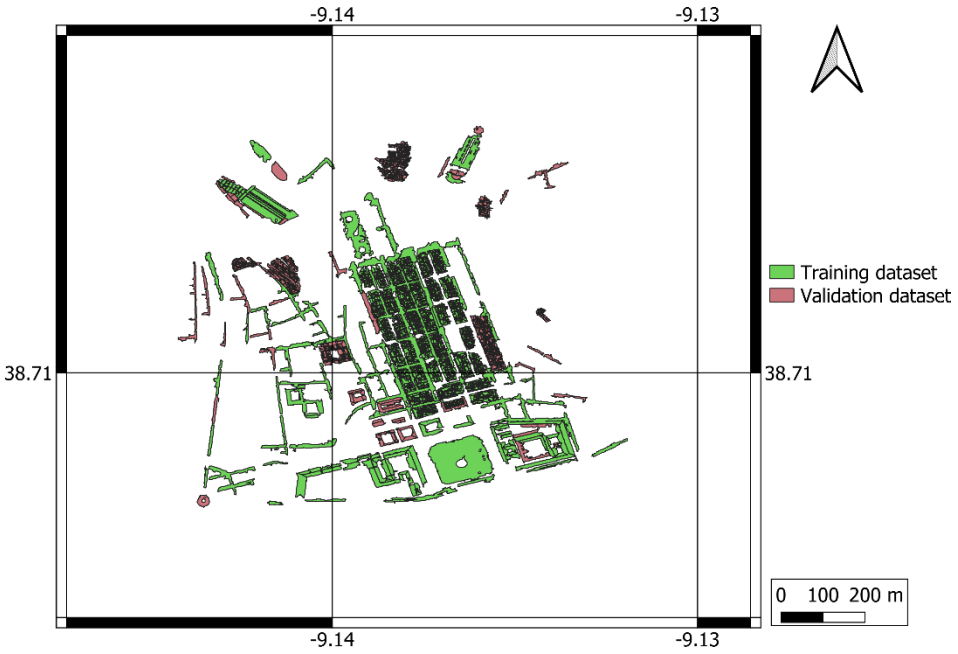

Figure 26 – Training and validation datasets for the supervised classification. Coordinate grid in WGS84.

Table 2 – Confusion matrix for the supervised classification.

		Classification	
		Structure	Non-structure
Ground truth	Structure	804	4
	Non-structure	23	13

[15] Probability of objects classified in a certain class to actually belong to it (Zanotta *et al.*, 2019).

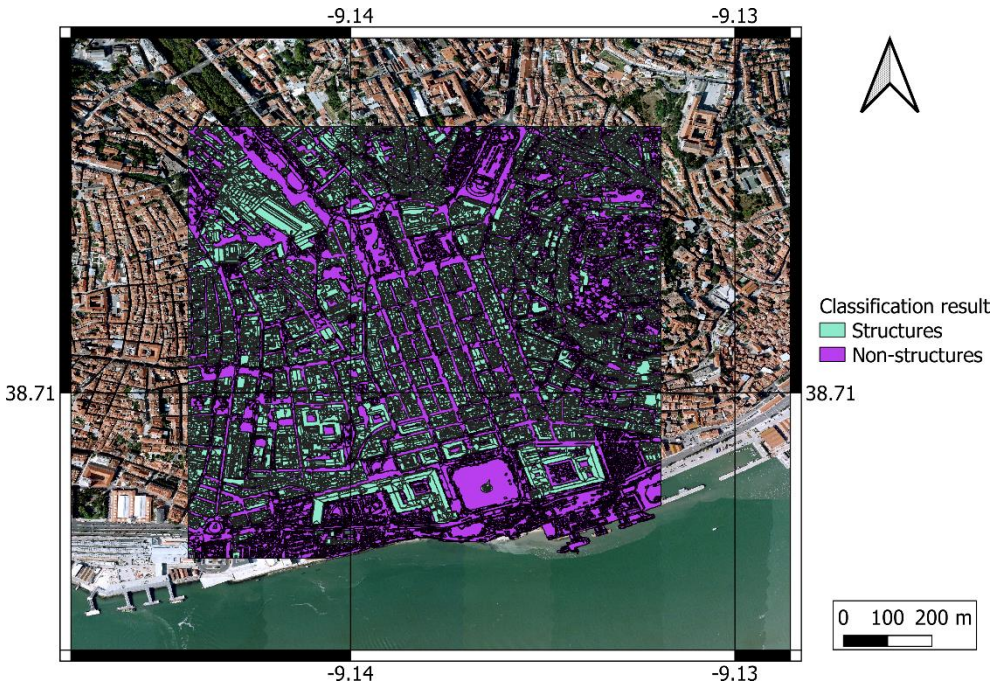

Figure 27 – Classification map after manual editing. Coordinate grid in WGS84.

PSs located on structure or on non-structure elements were distinguished through their superposition with objects of the corresponding classes. As residual height provides relative heights between PSs, this variable was inspected for both classes, in order to verify if it could provide a way to separate them from each other, without the need to perform the OBIA classification. Figure 28 presents the histograms of residual heights for the two classes of PSs, for ascending and descending geometries together. Both structure and non-structure PSs occupied the same residual height classes, not being possible to identify a threshold to separate them. This may happen because non-structure PSs were not only located on the ground, they might also be on high objects, such as lampposts. There were some differences between the classes, though. First, there were more PSs located on structures than on non-structures. Second, there was a shift on the variable histogram modes: while the mode for PSs located on structures was 5 m below the reference height surface, the mode for PSs located on non-structures was 13 m below that surface. Third, while the histogram for non-structure PSs showed a symmetry, the histogram for structure PSs was asymmetric, presenting a tail to the right.

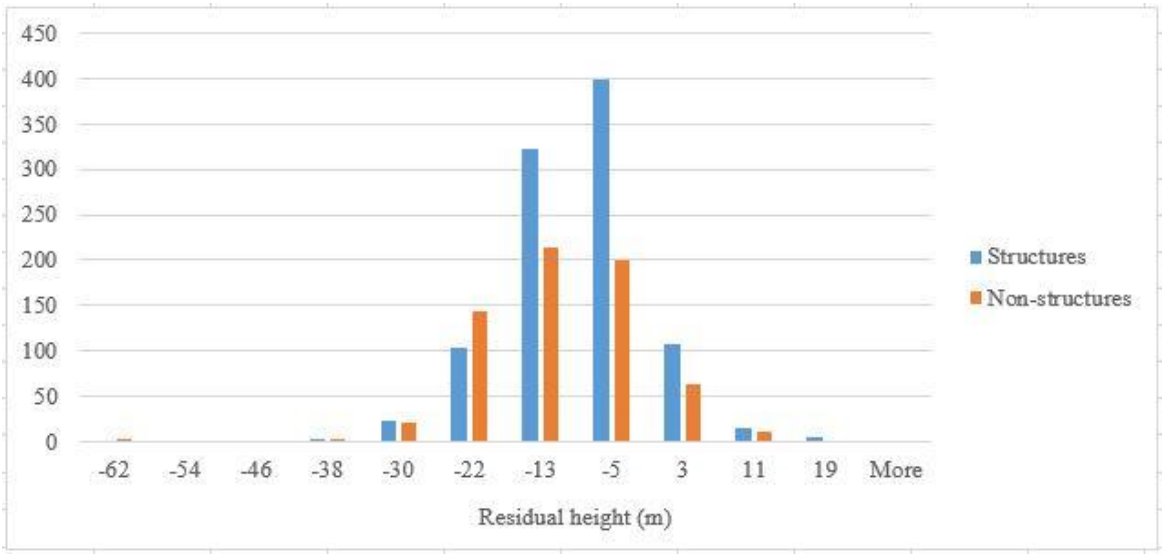

Figure 28 – Histograms of residual height, in metres, for PSs on structures and PSs on non-structures.

3.3.2.4 Cluster analysis

Cluster analysis was performed on the PSs associated to structures in the previous section, analysing the ascending and descending datasets together. The PSs to be included were selected by their temporal coherence (larger or equal to 0.9) and by the coordinates of a rectangular area containing the ROI. The reference point effect was determined and removed from the displacement time series of each acquisition geometry. Figure 29 shows the average displacement time series of the PSs considered stable and the corresponding standard deviation for both passes. The displacement time series for all PSs considered stable in each pass are presented in Annex A.1 Figure 134. Each geometry presented a distinct behaviour, with oscillations reaching a maximum range of 4 mm at both passes, which might result from displacement at the reference points or residual atmospheric effects.

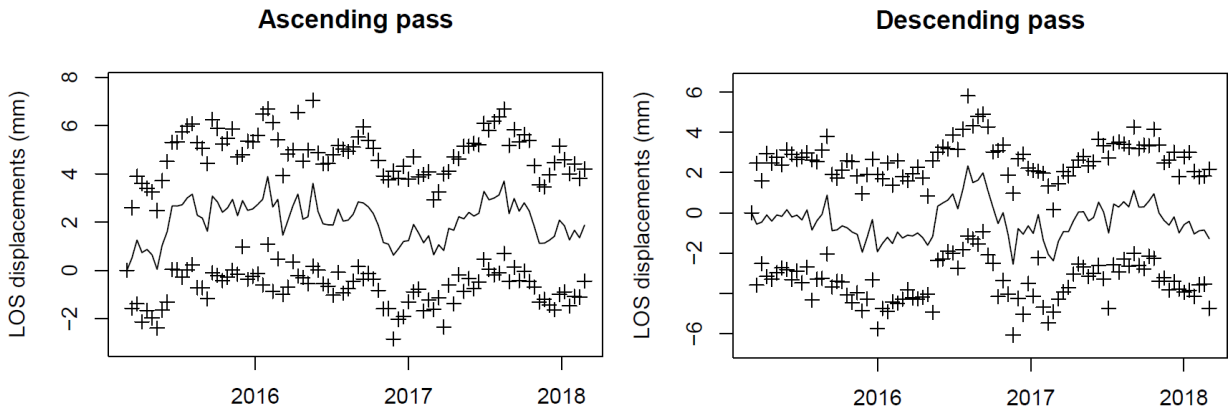

Figure 29 – Displacement time series corresponding to the reference point effect for (a) the ascending pass and (b) for the descending pass (solid line) plus and minus one standard deviation (crosses).

Displacements from ascending and descending passes were merged into vertical and horizontal displacements. As there was no previous knowledge regarding dominant directions for horizontal displacements at the ROI, the east – west direction was selected, since it is the direction at the horizontal plane along which LOS is more sensitive (Chapter 5). Displacement time series of both vertical and east – west directions were considered simultaneously for the cluster analysis. Complete linkage was used as aggregation method. The proposed algorithm identified an automatic solution for the problem of defining the number of clusters, which corresponded to the number of clusters, n, with the maximum relative linkage distance with respect to the previous solution with number of clusters n+1. In this case, the automatic solution led to the creation of three clusters, but the analysis of the dendrogram (Figure 30a) revealed that the largest cluster still presented PSs with heterogeneous behaviours, as large steps in linkage distance separated clusters aggregated in previous steps. Therefore, the 10-cluster solution was manually selected, as it corresponded to a local maximum in relative linkage distances (Figure 30b). The new achieved clusters were formed by PSs with homogeneous behaviour, as there were not large steps in linkage distance between clusters visible in the dendrogram. Thus, this solution was accepted.

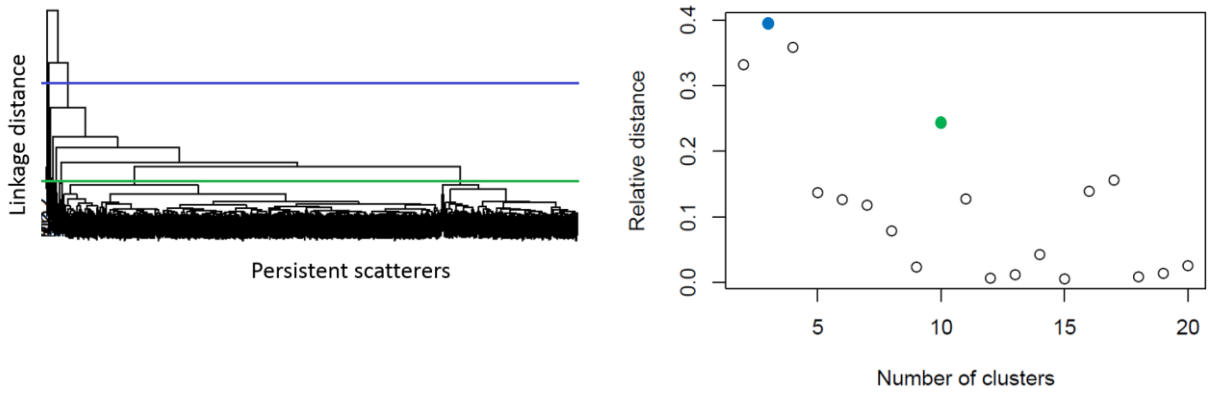

(a) (b)

Figure 30 – Dendrogram for PS aggregation, where the blue horizontal line corresponds to the automatic solution and the green line is the manually selected solution (a); chart of the relative linkage distances as a function of the number of clusters, with the blue circle being the automatic solution and the green circle being the manually selected one (b).

In order to aid the cluster interpretation, additional information was included through raster images and centroids of those variables were computed for each cluster. Five variables were considered for this analysis. Slope and curvature were used to assess the susceptibility to landslide occurrence on the hillsides that flank the Downtown. These images were built from the EU-DEM in a GIS software. The three remaining rasters were images of distance to elements that may have some influence on structure displacements: geological faults, subway lines and the Tagus river.

The distance images were created at a GIS software, with the same spatial resolution of the DEM, by attributing each pixel the Euclidean distance between that pixel and the considered elements.

The above procedure enabled the construction of displacement time series representative of each cluster and cluster centroids for variables achieved through the PSI processing and for the additional ones. Parameters used in clustering processing are presented in Annex A.1 Table 18.

3.4 Results

3.4.1 Odelouca slopes

3.4.1.1. This section presents the results achieved through PSI processing and cluster analysis (1D version) for the slopes around Odelouca reservoir during its first impoundment. A total of 7949 PSs were achieved inside the ROI (Figure 31). Positive displacement values correspond to displacements along LOS towards the sensor and negative values are LOS displacements away from it. The figure shows some PSs apparently located on the water, but that is due to the different acquisition dates of the data: SAR images are from 2006 to 2011, before the conclusion of the reservoir first impoundment, and the optical image is from 2020.

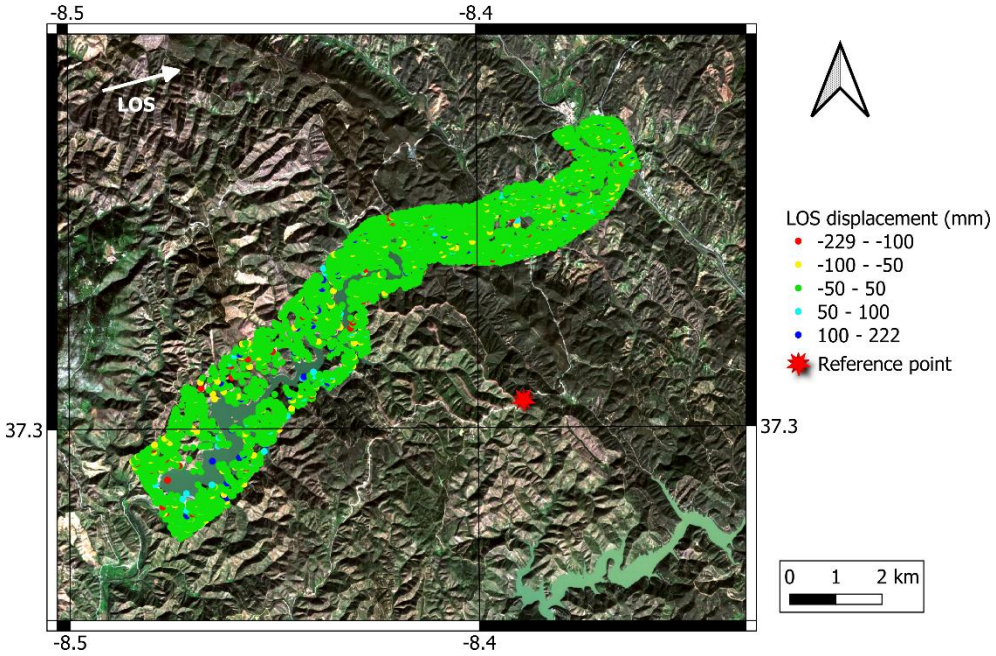

Figure 31 – Cumulative displacement for PSs on Odelouca slopes. Optical image is from Sentinel-2, acquired in February 2020. Coordinate grid in WGS84.

The cumulative displacement during the time interval of the analysis (approximately 4.5 years) varied between 228.8 mm away from the sensor and 221.9 mm towards it. However, 97.5% of the PSs presented cumulative displacement between 78.5 mm away from the sensor and 71.7 mm

towards it. Some PSs with cumulative displacement at centimetre-level and close to the water reservoir were identified, which might be a sign of slope instability. Thus, their displacement time series must be inspected in order to verify how those scatterers behaved during the study time interval: whether their movement has changed after the beginning of the first impoundment and if they were still moving by the end of the study time interval.

3.4.1.2. The identification of spatio-temporal patterns in the data was executed through the cluster analysis, where the performances of the three cluster aggregation methods were evaluated. The Ward method led to the construction of four clusters, which were spread throughout the ROI. Cluster 1 was predominant at the southwest of the ROI, closer to the dam, and cluster 2 was more concentrated at the northeast, i.e., farther from it. Clusters 3 and 4 were equally spread throughout the ROI (Figure 32).

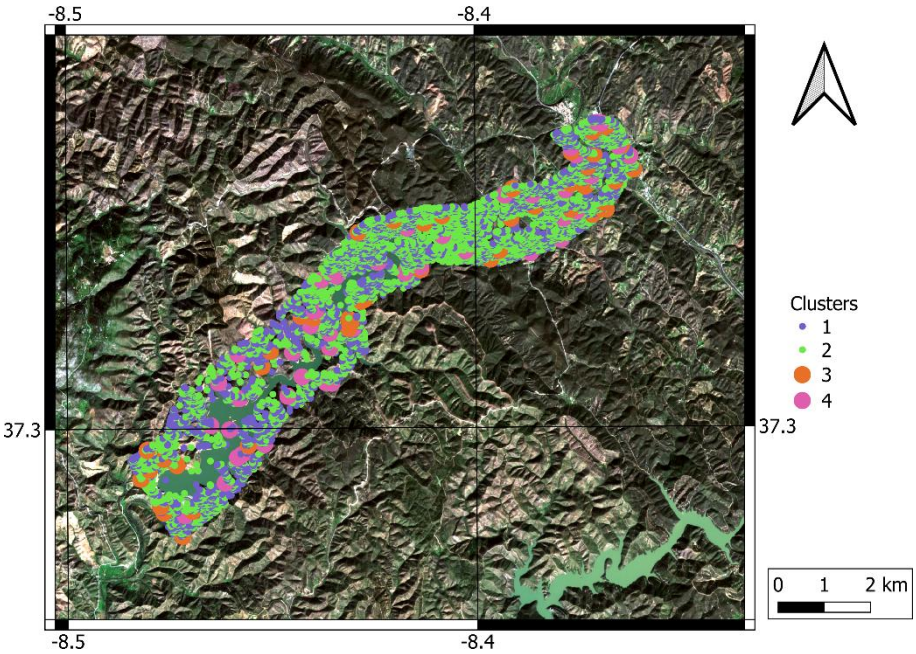

Figure 32 – Automatic cluster solution achieved through Ward method for Odelouca slopes. Coordinate grid in WGS84.

Figure 33 presents the displacement time series representative of each cluster obtained from the Ward method and Table 3 shows the corresponding centroids. Cluster 1 was the second most frequent cluster in the ROI and, in average, it moved away from the sensor. Its behaviour was almost stable until 2009, when it started moving away from the sensor a few months before the beginning of the first impoundment. Between February 2009 and July 2010, cluster 1 moved away from the sensor 18 mm, when it became stable until the end of the study time interval. Movement away from the sensor is compatible to subsidence, which has been reported in literature to affect the neighbourhood of water reservoirs (Saleh *et al.*, 2018). The displacements at Odelouca started in March 2009, when the construction of the dam body was finished (Rodrigues, 2013), and may

be due to the interaction between accumulated water and the riverbed. The hypothesis of the displacement being caused by the water influence is reinforced by the stronger presence of this cluster at the region closer to the dam, where the water started accumulating.

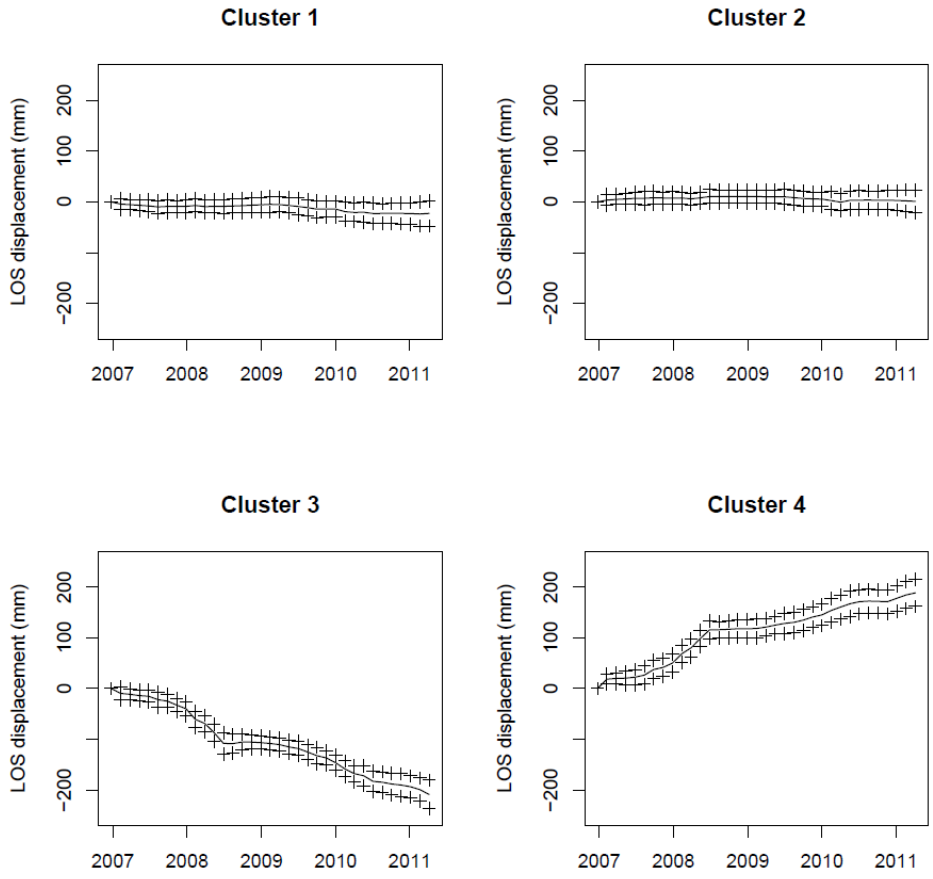

Figure 33 – Displacement time series representative of the clusters achieved for Odelouca slopes through the Ward method; crosses are the average displacement time series plus and minus one standard deviation.

Cluster 2 was the most frequent cluster in the ROI, containing more than 60% of the PSs. This cluster also presented displacement away from the sensor; however, its duration and magnitude were shorter than at cluster 1. Cluster 2 moved away from the sensor 11 mm, in average, between July 2009 and April 2010, when the ground recovered its original position, resulting in a cumulative displacement centroid close to zero (Table 3). Similar to cluster 1, that behaviour may be related to subsidence caused by the water weight. However, perhaps due to the larger average distance to the water storage place, that influence was smaller for cluster 2 than for cluster 1, allowing the ground recovery.

Clusters 3 and 4 together contained 1.2% of PSs at the ROI. Both clusters presented average cumulative displacement at the decimetre-level, in opposing directions, with cluster 3 moving away from the sensor and cluster 4 moving towards it. The large observed displacements and the

large difference between the residual height centroids for these two clusters and for clusters 1 and 2 (Table 3) suggested the results from both clusters might be affected by unwrapping errors. This issue will be further addressed in section 3.5.

Table 3 – Percentage of PSs in each cluster and centroids achieved through the Ward method for Odelouca slopes.

Cluster	Percentage of PSs (%)	LOS cumulative displacement (mm)	Altitude (m)	Residual height (m)	Slope inclination (º)	Curvature (m^{-1})
1	37.4	-22.7	128	-4	10.7	0.037
2	61.4	0.3	126	-5	10.2	0.003
3	0.6	-188.5	137	8	11.1	0.033
4	0.6	171.8	111	-15	10.7	-0.009

Regarding the centroids of the remaining variables (Table 3), clusters 1 and 2 were located at close average altitudes. Cluster 3 presented the largest average altitude, while cluster 4 had the lowest, but this might be a consequence of unwrapping errors.

According to Rosi *et al.* (2018), landslides tend to occur for slope inclinations between 10º and 15º and at slightly concave surfaces. In average, all clusters presented slope inclinations above 10º and the boxplots of slope inclination for each cluster (Annex A.1 Figure 135) show that approximately 50% of the PSs in each group were located on surfaces with slope inclinations above that threshold. Clusters 1, 2 and 3 presented positive average curvatures, i.e., they were mainly located on concave surfaces; while cluster 4, with negative average curvature, was mostly at convex surfaces. Nevertheless, the boxplots of curvature showed that also around 50% of the PSs in each cluster had positive curvature (Annex A.1 Figure 136). There were 1906 PSs (24% of all points) which fulfilled both criteria, i.e., they were placed at locations with slope inclinations above 10º and positive curvature, meaning that they were located at areas more susceptible to landslide occurrence than the remaining PSs (Figure 34). Most of these PSs belonged to cluster 2 (57.1%) and to cluster 1 (41.7%), while clusters 3 and 4 contained 0.6% of these points each. Displacement time series representative of clusters 1 and 2 did not present signs of slope instability after July 2010. Thus, although these clusters contained many PSs on surfaces with geometric properties that turn them prone to landslide occurrence, the displacement time series did not show signs of ground instability by the end of the time interval considered for the analysis. As displacement time series of PSs from clusters 3 and 4 might be affected by unwrapping errors, the results for these clusters were inconclusive.

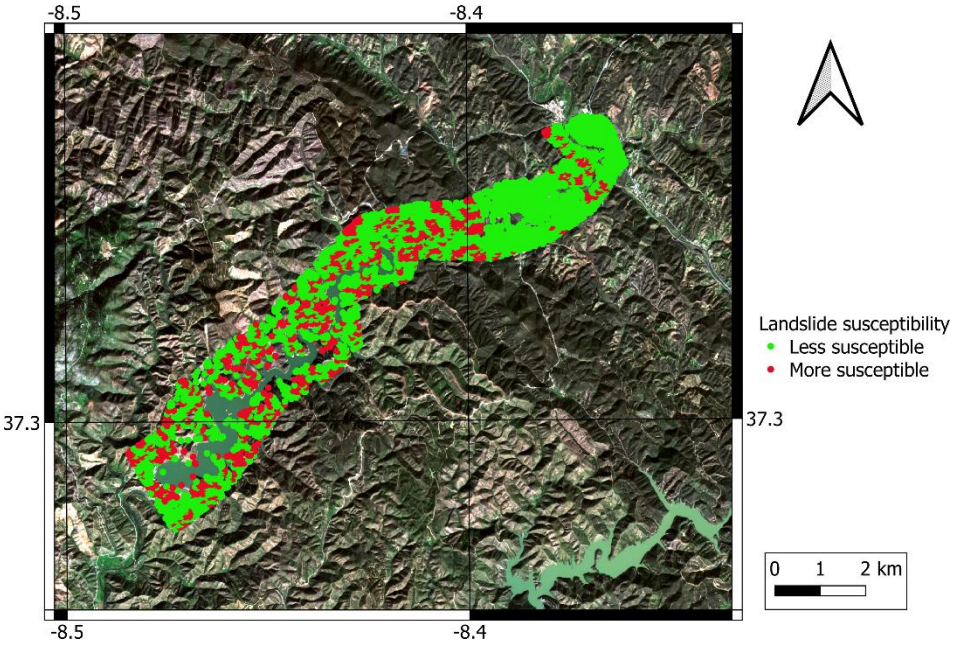

Figure 34 – Identification of PSs with different degrees of susceptibility to landslide occurrence for Odelouca slopes. Coordinate grid in WGS84.

Complete linkage led to a solution formed by three clusters: a large cluster with almost all PSs (98.2%) and two small clusters (Figure 35 and Table 4). There was similarity between the clusters achieved through the Ward method and complete linkage. Cluster 1 from complete linkage contained, approximately, the PSs organized into clusters 1 and 2 by the Ward method. This group moved 12.5 mm away from the sensor, in average, beginning in March 2009 until the end of the time interval of the study (Figure 36).

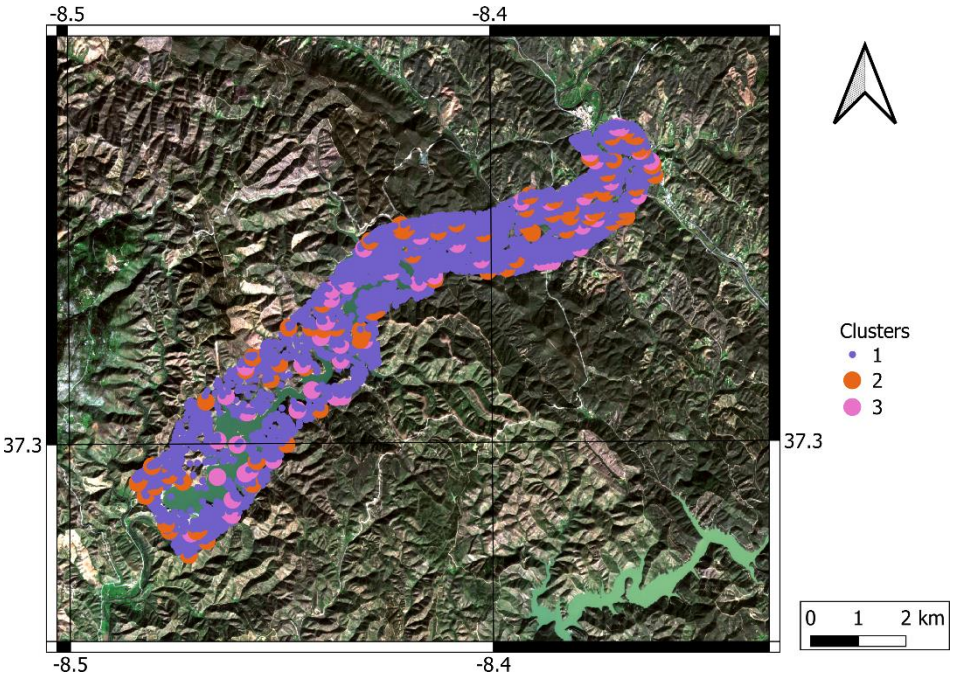

Figure 35 – Automatic cluster solution achieved through complete linkage for Odelouca slopes. Coordinate grid in WGS84.

Table 4 – Percentage of PSs in each cluster and centroids achieved through complete linkage for Odelouca slopes.

Cluster	Percentage of PSs (%)	LOS cumulative displacement (mm)	Altitude (m)	Residual height (m)	Slope (º)	Curvature (m^{-1})
1	98.2	-8.1	127	-5	10.4	0.016
2	1.0	-150.6	138	4	10.2	0.048
3	0.7	162.2	111	-14	10.8	-0.041

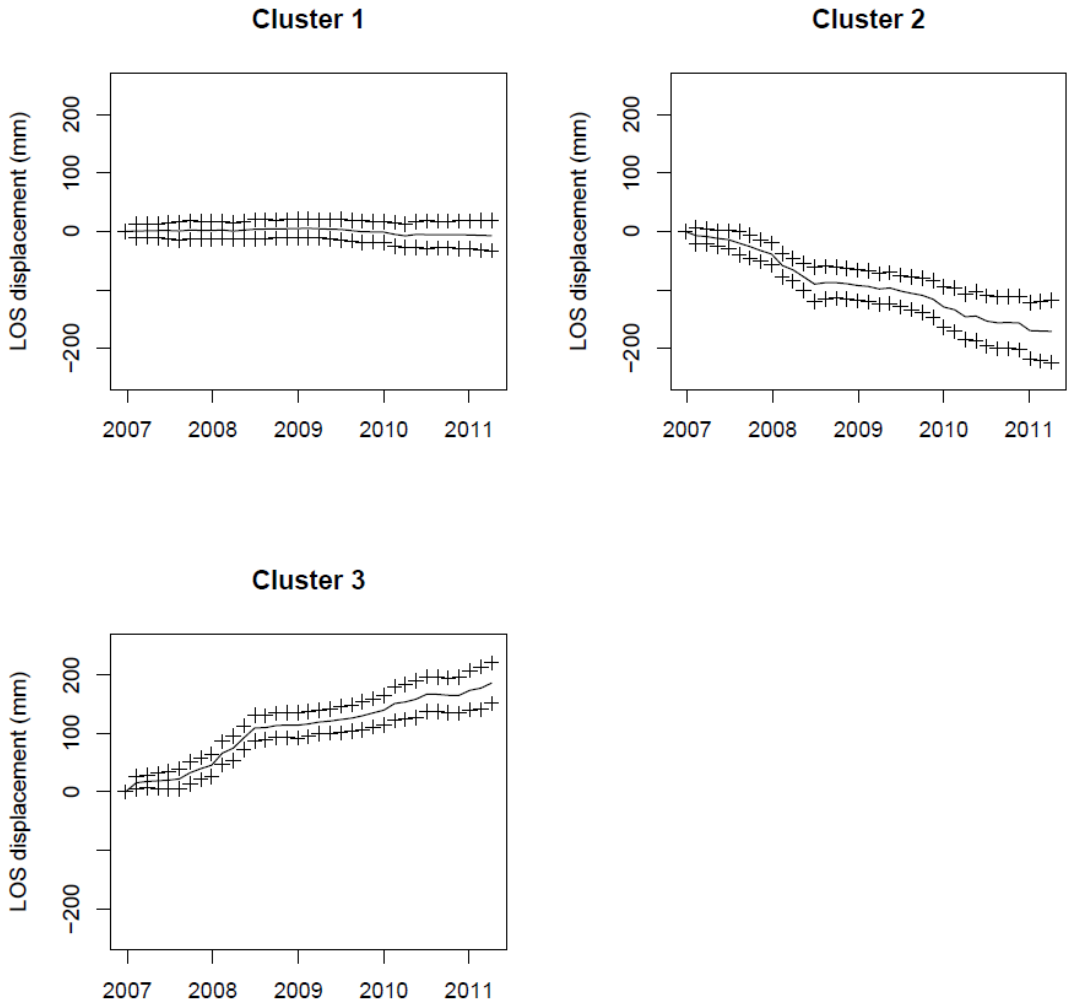

Figure 36 – Displacement time series representative of the clusters achieved through complete linkage for Odelouca slopes; crosses are the average displacement time series plus and minus one standard deviation.

There was also a resemblance between cluster 3 from Ward solution and cluster 2 from complete linkage and between cluster 4 from Ward method and cluster 3 from complete linkage. Given the similarity of the displacement time series representative of each cluster and the extreme residual height centroids, clusters 2 and 3 from complete linkage solution might also be formed by PSs affected by unwrapping errors, isolating these points from the remaining ones. The main

difference between the clusters from the Ward and from the complete linkage solutions was that clusters 2 and 3 from the complete linkage contained more PSs than the corresponding clusters in Ward method. Thus, complete linkage was more sensitive to the presence of unwrapping errors than the Ward method. The centroids for altitude, slope inclination and curvature were also similar to those of the corresponding clusters from Ward method.

The automatic solution of single linkage built two clusters, one of them containing 99.97% of the points and the other one formed by only two PSs (Figure 37 and Table 5). Cluster 1 presented a similar behaviour to clusters 1 and 2 from Ward method and to cluster 1 from complete linkage, moving away from the sensor 12.6 mm, beginning in March 2009 (Figure 38). Its average residual height was similar to those from the corresponding clusters in the previous clustering solutions, average slope was above 10º and curvature was positive.

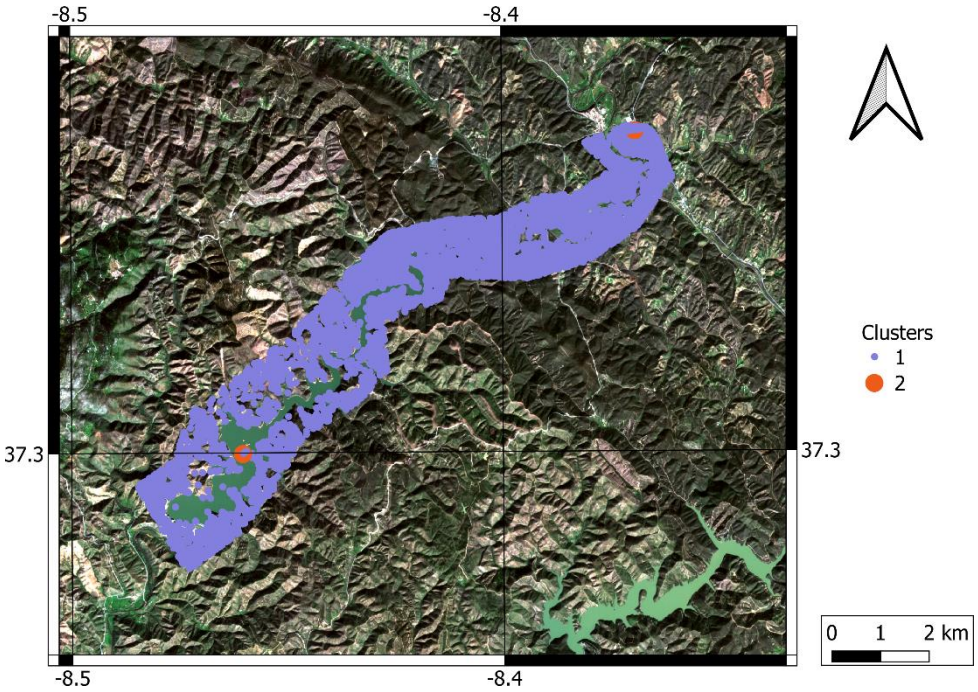

Figure 37 – Automatic cluster solution achieved through single linkage for Odelouca slopes. Coordinate grid in WGS84.

Table 5 – Percentage of PSs in each cluster and centroids achieved through single linkage for Odelouca slopes.

Cluster	Percentage of PSs (%)	LOS cumulative displacement (mm)	Altitude (m)	Residual height (m)	Slope (º)	Curvature (m^{-1})
1	99.97	-8.4	127	-5	10.4	0.016
2	0.03	218.0	70	-20	2.8	-0.058

The two PSs in cluster 2 were isolated and distant from each other (Figure 37). The cluster average altitude was lower than that of cluster 1 and the PSs were located on a convex and almost

flat surface; thus, with small susceptibility to landslide occurrence. The two PSs in cluster 2 presented large cumulative displacements towards the sensor during the time interval of the study. The behaviour of this cluster was similar to those of cluster 4 from Ward method and cluster 3 from complete linkage. Therefore, the displacements of these two PSs might be affected by unwrapping errors. From the analysis of the other clustering solutions, it was known that there were more PSs affected by unwrapping errors. However, single linkage was not able to isolate them and they were included in cluster 1, revealing low sensitivity of this aggregation method to detect this type of errors, at least for clustering solutions with a small number of clusters.

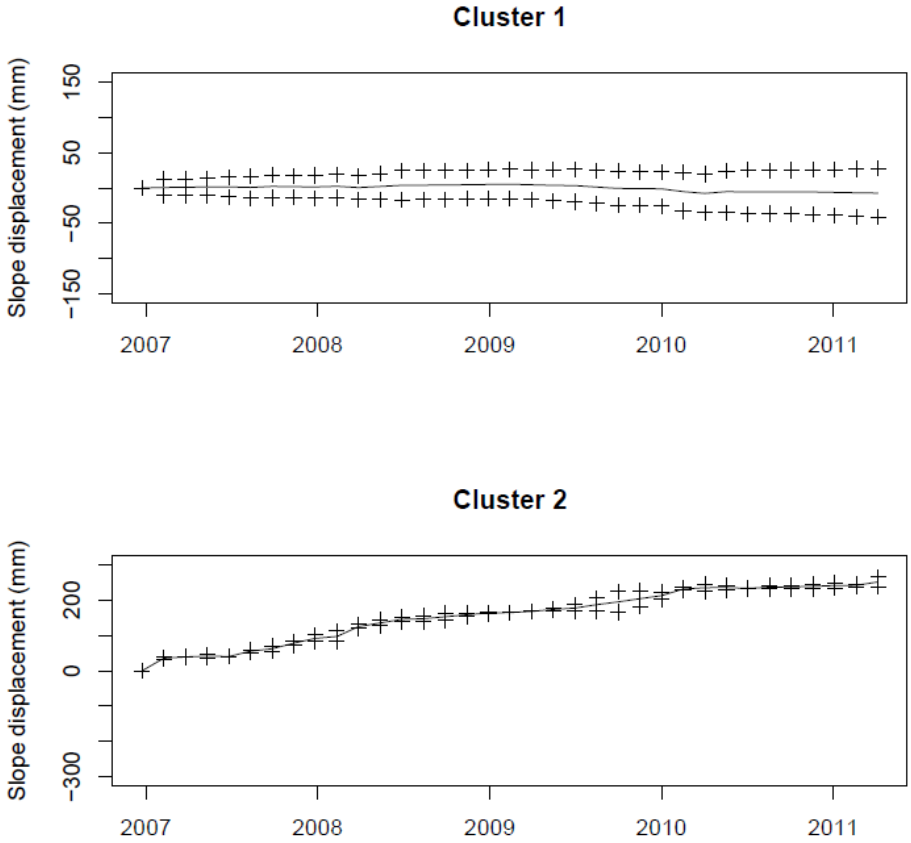

Figure 38 – Displacement time series representative of the clusters achieved through single linkage; crosses are the average displacement time series plus and minus one standard deviation.

All clusters from all solutions presented increasing displacement standard deviation with time (Figure 33, 36 and 38), except cluster 2 from single linkage, which was formed only by two points with similar behaviour. The increase in standard deviation with time reflected a larger detachment among the PSs' displacements as time passed.

3.4.1.3. From the above results achieved through the different aggregation methods, it was verified that the automatic solutions were capable of isolating PSs with time series affected by unwrapping errors, although the degree of that detection varied with the aggregation method. On the other hand, only Ward method was able to detect two distinct behaviour patterns at the slopes,

while complete and single linkages included all the non-erroneous PSs in a single cluster. In order to identify eventual slope instability signs, it was necessary to increase the detail of the analysis by further dividing those major clusters into smaller ones.

As complete linkage was the method with larger sensitivity to the detection of displacement time series affected by unwrapping errors, this aggregation method was selected to deepen the analysis. The chart of relative linkage distances was inspected and a new number of clusters was manually selected, corresponding to a local maximum (Figure 39). Seven clusters were considered for the slope stability analysis.

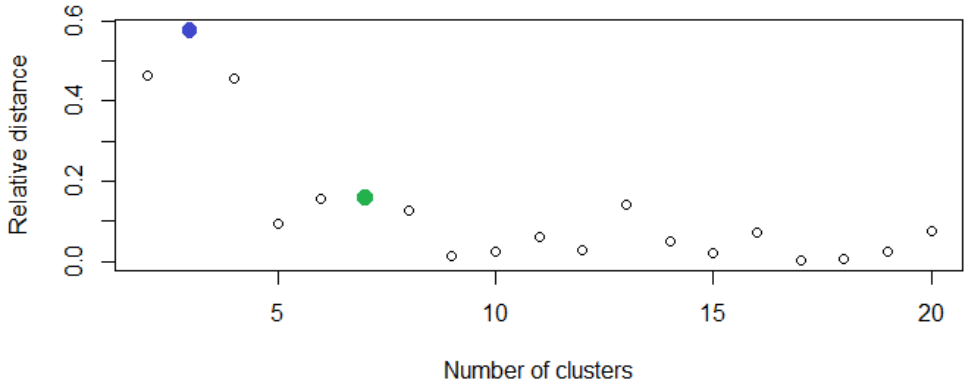

Figure 39 – Chart of relative linkage distance as a function of the number of clusters for the Odelouca reservoir slopes; blue dot corresponds to the automatic solution and the green dot is the manually selected one.

The seven clusters were spread throughout the ROI (Figure 40). The displacement time series representative of each cluster showed that this solution identified three clusters with PSs possibly affected by unwrapping errors: cluster 2 with points moving away from the sensor and clusters 6 and 7 with PSs moving towards the sensor (Figure 41). The behaviour of these clusters was similar to those from previous solutions, with the cluster of anomalous PSs moving towards the sensor being divided in two. The main difference between clusters 6 and 7 was that cluster 6 presented smaller magnitude displacements. For this clustering solution, the cluster centroids for residual heights were also evaluated and it was observed that clusters 2, 6 and 7 presented residual height centroids distinct from the remaining clusters (Table 6 and Annex A.1 Figure 137). Residual height is the correction of the PS altitude with respect to the DEM used in PSI processing. As the seven clusters were spread uniformly throughout the ROI, it would be expectable that the centroid for residual height would be similar for all clusters, which was verified for clusters 1, 3, 4 and 5. The extreme values presented by clusters 2, 6 and 7 reinforced the hypothesis that the PSs in these clusters might be affected by unwrapping errors. The errors may have led to an incorrect determination of the residual heights, and, consequently, of the PSs' altitudes. This may be the

reason why, for all clustering solutions, the clusters with PSs possibly affected by unwrapping errors presented extreme values of altitude centroids.

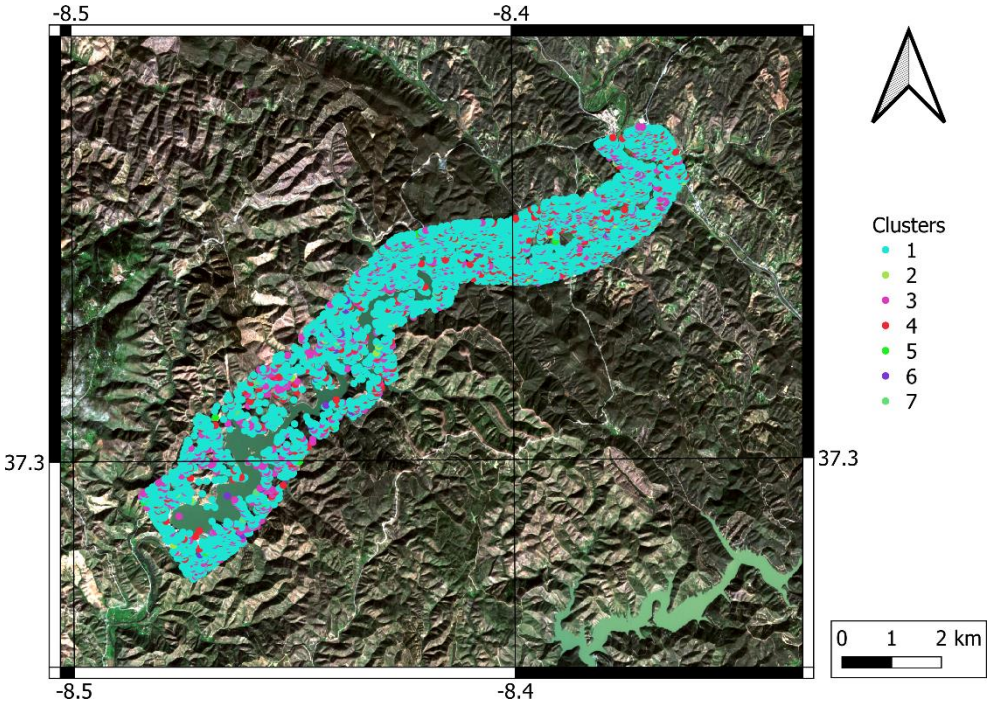

Figure 40 – Cluster solution achieved through manual selection of number of clusters for complete linkage at Odelouca slopes. Coordinate grid in WGS84.

The evaluation of slope stability was performed for clusters 1, 3, 4 and 5. Cluster 1 was the most frequent cluster in the ROI, with more than 80% of the PSs. This cluster presented low displacement magnitudes during the time interval of the study. Movement away from the sensor was observed starting in March 2009, which reached its maximum in April 2010 (7.3 mm) and after that became stable until the end of the study time interval. Similar to the clusters analysed at the previous solutions, the observed displacements might be due to subsidence caused by the water weight.

According to Colesanti *et al.* (2003), dispersion of a single displacement measurement at a PS ($\hat{\sigma}_{\text{displacement}}$) can be estimated through Equation (20):

$$\hat{\sigma}_{\text{displacement}} = \frac{\lambda}{4\pi}\sqrt{-2\ln|\hat{\gamma}|} \tag{20}$$

where λ is the SAR signal wavelength and $|\hat{\gamma}|$ is the estimated absolute value of temporal coherence. For a PS achieved through PALSAR-1 images, with a wavelength of 229 mm, and coherence of 0.90, which was the minimum accepted for this study, displacement dispersion is of 8.4 mm. Therefore, it was not reasonable to consider that displacements with the observed magnitude were actual movement. On the other hand, the displacement time series representative of each cluster resulted from the average displacement time series of all PSs forming the cluster;

thus, there might be points with magnitude displacements above the displacement dispersion and the analysis must be performed carefully.

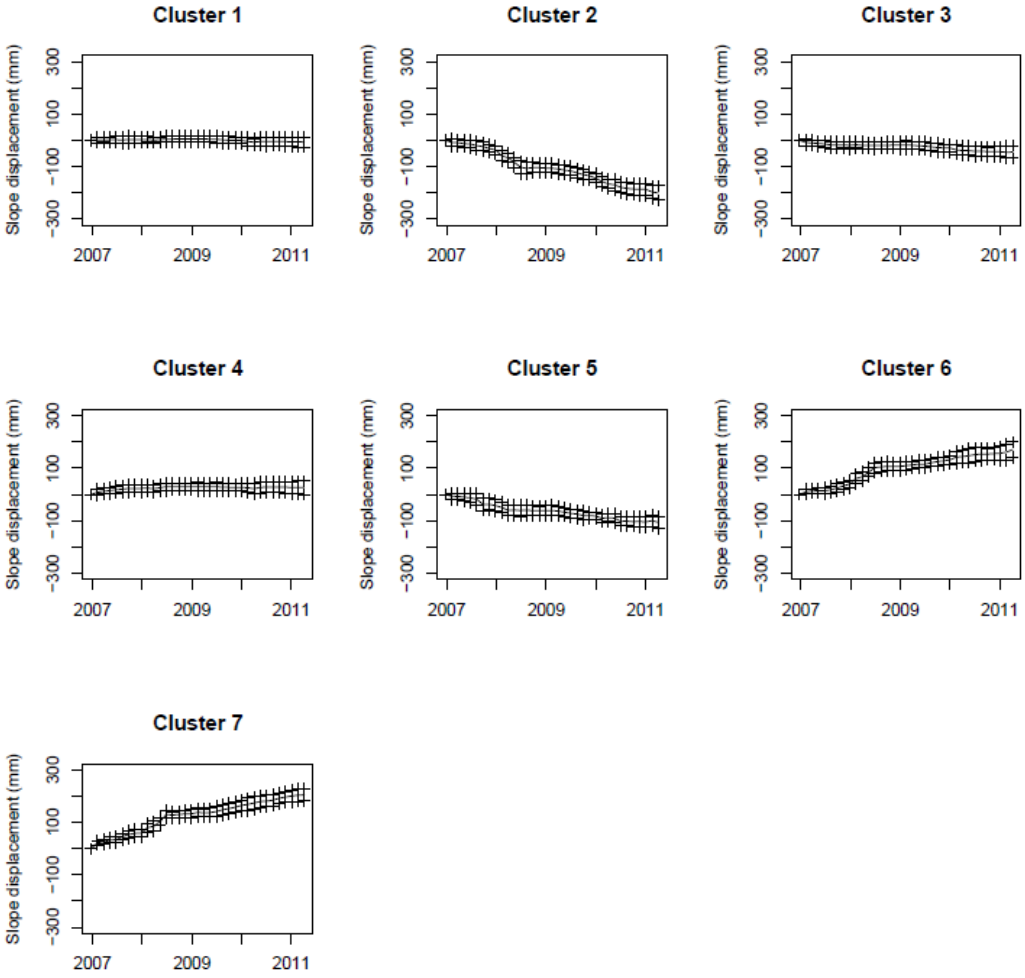

Figure 41 – Displacement time series representative of the clusters achieved through complete linkage with manual selection of the number of clusters for Odelouca slopes; crosses are the average displacement time series plus and minus one standard deviation.

Table 6 – Percentage of PSs in each cluster and centroids achieved through complete linkage for manual solution at Odelouca slopes.

Cluster	Percentage of PSs (%)	LOS cumulative displacement (mm)	Altitude (m)	Residual height (m)	Slope (º)	Curvature (m^{-1})
1	82.7	-7.4	127	-5	10.4	0.013
2	0.6	-187.5	139	8	11.1	0.031
3	8.5	-39.7	131	-4	10.8	0.053
4	7.1	22.1	125	-6	9.0	0.010
5	0.4	-97.3	137	-3	8.9	0.073
6	0.5	151.0	111	-14	10.9	-0.101
7	0.2	184.7	111	-14	10.7	0.080

Cluster 3 was spread throughout the ROI and, in average, it moved around 4 cm away from the sensor during the time interval of the study. Part of the movement, with magnitude of 2 cm, occurred between December 2006 and August 2007. At that time, it stabilized until March 2009, when it began to move away from the sensor once again, reaching 26.7 mm by the end of the time interval of the study. As only the possible effects of the reservoir first impoundment on the slopes were being evaluated in this research, the causes for the first period of movement were not analysed. The movement in the second period was probably caused by the water weight, similarly to what was discussed for the other clustering solutions.

Cluster 4 was the only cluster presenting average displacement towards the sensor during the time interval of the study. This behaviour might be explained by groud uplift due to water infiltration or it might correspond to horizontal displacement from east to west. Using images from a single acquisition geometry, it was not possible to identify the displacement direction. Between July 2009 and April 2010, the cluster moved away from the sensor, similar to the other groups, possibly due to the water weight. In May 2010, cluster 4 recovered from the displacement away from the sensor and kept a stable behaviour until the end of the study. The cluster contained 7.1% of the PSs and it was not uniformly distributed along the ROI, as it had a larger number of points concentrated at the region farther away from the dam and from the stored water (Figure 42). That might be the reason why the movement away from the sensor occurred later than in other clusters, similar to cluster 2 from Ward method, as the larger distance to the stored water might have led most PSs in the cluster to be affected later.

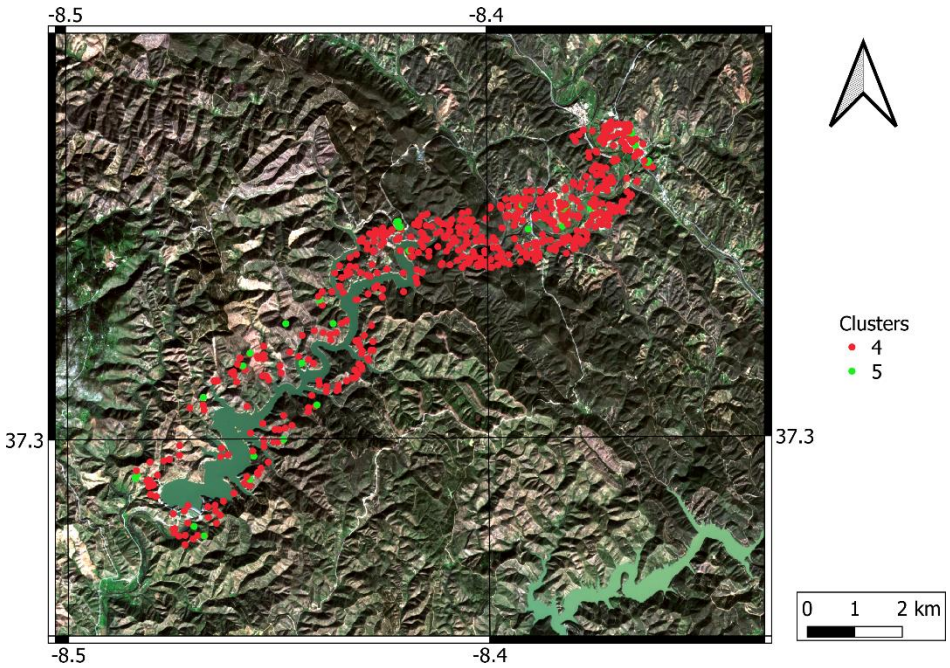

Figure 42 – Location of clusters 4 and 5 achieved through the solution with manually selected number of clusters using complete linkage for Odelouca slopes. Coordinate grid in WGS84.

Cluster 5 contained 0.4% of the PSs, equally spread throughout the ROI (Figure 42). The cluster moved almost 10 cm away from the sensor, presenting distinct displacement rates along time. After a first phase of displacement away from the sensor finished by March 2008, the cluster remained stable and one year later, possibly under the influence of the reservoir water, it started moving away from the sensor again until July 2010. Around that time, it stabilized until the end of the time interval of the study. The first period of movement was not further analysed, as it occurred much earlier than the first impoundment. The second period was possibly related to the effect of the water weight.

Figure 43 presents the displacement time series representative of clusters 1, 3, 4 and 5 compared to the water level at the reservoir. Water level data were only available after December 2009[16], when the first impoundment began; thus, it was not possible to verify whether the displacements observed in March that year were related to changes in the water level or not. There was an increase in the water level of almost 12 m during December 2010, but there were not large changes on the clusters' behaviour around that time. The dataset contained only two images acquired after the rise in the water level. The slopes may have taken some time to respond to the water load and the displacements induced by the water weight occurred later, when there were no images available. From the existing data, only movement away from the sensor with magnitude below 3 mm was detected after the rise in the water level, which was lower than the displacement dispersion of 8.4 mm for each individual PS.

In summary, several PSs were identified on the slopes around Odelouca reservoir, which were located at areas prone to landslide occurrence (slope inclination above 10º and concave surfaces). Displacement time series representative of each cluster, which were not affected by unwrapping errors, displayed movement away from the sensor during some months. For clusters closer to the dam, that behaviour was observed to begin in March 2009 (when the construction of the dam body was finished). For clusters with PSs concentrated far from the dam, that behaviour began later, in July 2009. All clusters' behaviour stabilized around July 2010, when the water level did not present large variations for some months. The observed movement away from the sensor might have reflected the occurrence of subsidence, perhaps due to the stored water weight. A rise of almost 12 m in the water level did not cause significative changes on the clusters behaviour during the study time interval. It was possible the slopes needed some time to respond to the load and that its effect had occurred only after the considered time interval, when there were no SAR images available.

[16] Data retrieved from the Hydric Resources National Information System (https://snirh.apambiente.pt/)

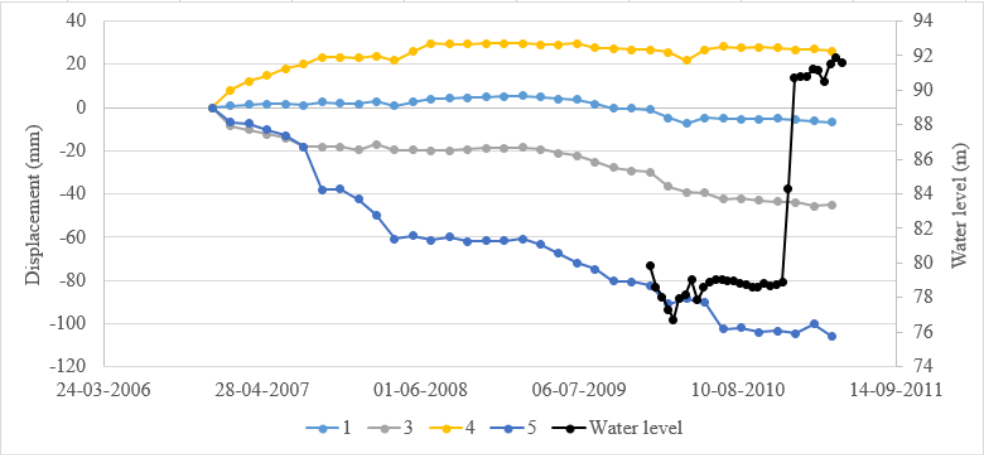

Figure 43 – Comparison of displacement time series representative of clusters 1, 3, 4 and 5 with the water level at the reservoir.

3.4.2 Lisbon Downtown

3.4.2.1. Tens of thousands of PSs were detected at the 16 km x 16 km ROI considered for the PSI processing at part of Lisbon metropolitan area. The analysis of the dataset from the ascending pass detected 87731 PSs, while the descending one led to 90968 points, resulting at a PS density around 350 PS/km^2 for each dataset. The cumulative displacement maps are shown in Annex A.1 Figure 138 and Figure 139. Most of the ROI presented cumulative displacements with magnitude below 10 mm during the three years of the analysis, for both acquisition geometries, with some localized areas presenting displacement away or towards the sensor.

The focus of this study was the analysis of displacements on PSs located on structures at the Downtown. After combining ascending and descending data, 974 PSs were achieved at the ROI, with vertical and east – west displacements determined every 12 days. Figure 44 and 45 display the cumulative vertical and horizontal displacement at the Downtown, respectively. For vertical displacements, positive values corresponded to uplift, while negative ones were associated to settlements. For horizontal displacements, positive values were displacement towards east and negative ones were movement towards west. At the ROI, vertical displacement varied between an uplift of 28.9 mm to a settlement of 35.6 mm, while east-west displacement ranged from 46.9 mm towards east to 24.5 mm towards west.

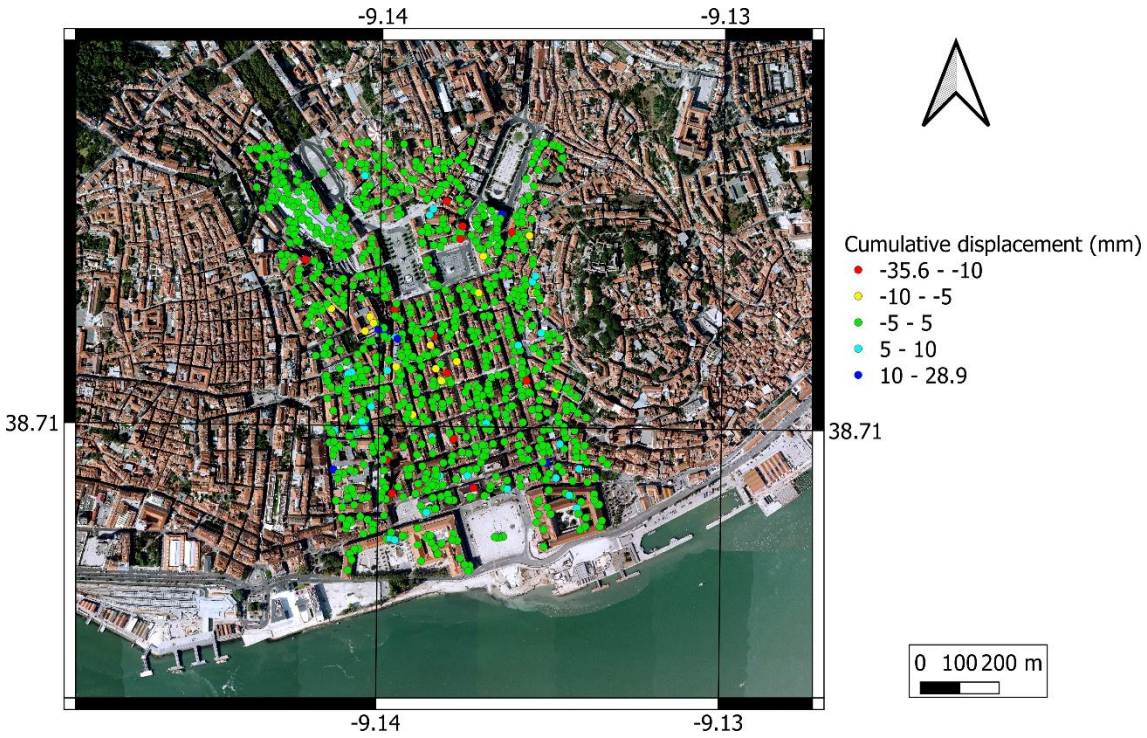

Figure 44 – Cumulative vertical displacement between March 2015 and February 2018 at Lisbon Downtown. Coordinate grid in WGS84.

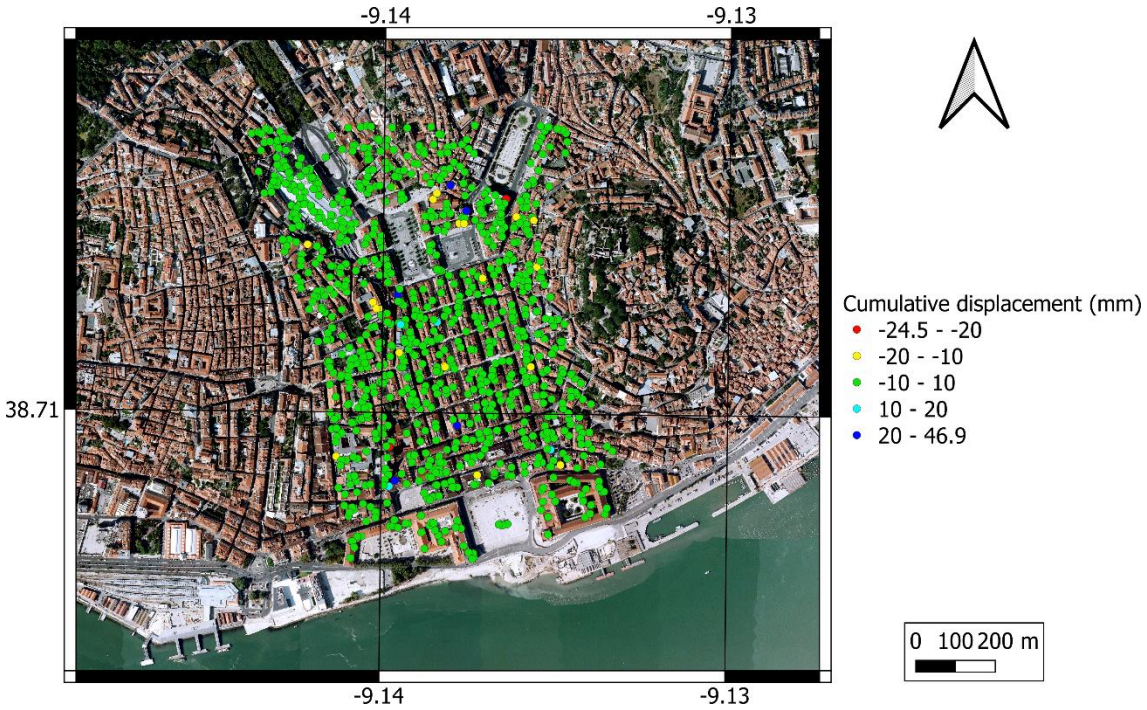

Figure 45 – Cumulative horizontal displacement between March 2015 and February 2018 at Lisbon Downtown. Coordinate grid in WGS84.

3.4.2.2. The PSs were aggregated based on both vertical and east – west displacement time series, resulting in the identification of 10 clusters of distinct behaviour (Figure 46). Cluster 1 contained 71.0% of the PSs at the ROI (Table 7), being spread throughout the whole region being analysed. Cluster 3 held the second largest cluster at the ROI, with 25.7 % of the PSs, and it was

also represented at the entire study area. The remaining clusters were formed by small numbers of PSs, varying from 0.1% to 0.9% of the total number of points.

Figure 46 – PSs aggregated into the 10-cluster solution for Lisbon Downtown. Coordinate grid in WGS84.

Table 7 presents the centroids of the considered variables for all the clusters. Clusters 1 and 3 had cumulative vertical displacements, in average, close to zero; therefore, PSI did not detect signs of vertical movement for most of the ROI. Clusters 4, 6, 7 and 8 settled from a minimum of 9.2 mm to a maximum of 35.6 mm during the three years of the study. However, clusters 2, 5, 9 and 10 presented uplift ranging values between 6.9 mm and 28.9 mm.

Regarding the cumulative horizontal displacements, in average, only cluster 3 presented a cumulative east – west displacement close to zero during the three years of the analysis. Clusters 1, 2, 5 and 7 moved towards west, with cluster 1 showing the lowest magnitude displacement (2.8 mm). Clusters 2, 7 and 5 presented increasing displacement towards west, with the last cluster reaching more than 20 mm. On the other hand, clusters 4, 6, 8, 9 and 10 moved towards east, all of them presenting cumulative displacements above 10 mm.

Table 7 – Relative number of PSs in each cluster and centroids for the 10-cluster solution, considering variables achieved through the PSI processing and from the additional raster files for Lisbon Downtown.

Cluster	Relative number of PSs (%)	Vertical displacement (mm)	East – west displacement (mm)	Slope (º)	Curvature (m^{-1})	Distance to faults (m)	Distance to subway (m)	Distance to river (m)
1	71.0	0.2	-2.8	6.0	-0.04	674	132	588
2	0.9	6.9	-7.5	6.4	-0.14	630	73	382
3	25.7	1.2	0.7	6.4	-0.02	810	104	737
4	0.2	-21.9	31.6	10.0	0.81	723	30	469
5	0.3	14.2	-21.2	6.5	1.05	772	47	635
6	0.6	-9.2	10.5	5.2	-0.63	687	157	656
7	0.7	-10.2	-16.0	8.4	0.29	685	127	565
8	0.1	-35.6	46.9	12.8	2.12	768	40	885
9	0.3	12.1	10.8	8.6	0.25	601	92	526
10	0.1	28.9	31.1	7.0	0.18	684	20	337

Although the Downtown is a flat area, the hillsides at its flank reach inclinations of 26º at some locations of the ROI. The centroids for slope inclination and curvature were evaluated to verify if any of the identified clusters was located at landslide prone areas, according to the criteria in Rosi *et al.* (2018). The centroid for slope inclination showed that only clusters 4 and 8 presented an average value above the threshold of 10º. Furthermore, those clusters were also located on concave surfaces. The structures with PSs belonging to these two clusters were those more prone to be affected by eventual slope movement.

The analysis of the centroids for the three distance variables revealed that all clusters were closer to the subway line than to faults or the river, in average (Annex A.1 Figure 140). Clusters 2, 4, 5, 8, 9, and 10 had average distance to the subway line lower than 100 m. Comparing the locations of the PSs in these clusters with respect to the subway line, it was clear that all clusters had PSs on buildings flanking the underground structure (Figure 47). Cluster 5 and 8 had PSs near the subway green line, between Martim Moniz and Rossio stations. This is one of the oldest segments of the line, built in the 1960s (Metropolitano de Lisboa E.P.E, 2018). Other clusters were located along the blue line, between Restauradores and Terreiro do Paço stations. The segment between Restauradores and Baixa/Chiado started to be operated in 1998 and it was expanded to Terreiro do Paço, being concluded in 2007. An accident occurred during this last expansion, in 2000, when there was the flooding of a tunnel during the construction works (Ribeiro, 2000). Nevertheless, the construction of these segments of the subway line were concluded several years before the time interval of the analysis (2015 – 2018); thus, it was not likely that there was some relationship between the observed displacements and the construction works. A study performed by LNEC's Building Department analysed vibrations at a building over the subway line and close to the building with a PS in cluster 10 and concluded subway vibrations were not affecting the structure (LNEC, 2020). Therefore, it was not likely that the displacement anomalies at these clusters were caused by vibrations due to the trains' passages. On the other hand, these clusters were mostly located on the hillsides that flank the Downtown, on steep slopes and concave surfaces (Table 7); thus, susceptible to ground movement (Rosi *et al.*, 2018), which might be the cause for the observed displacements at the buildings.

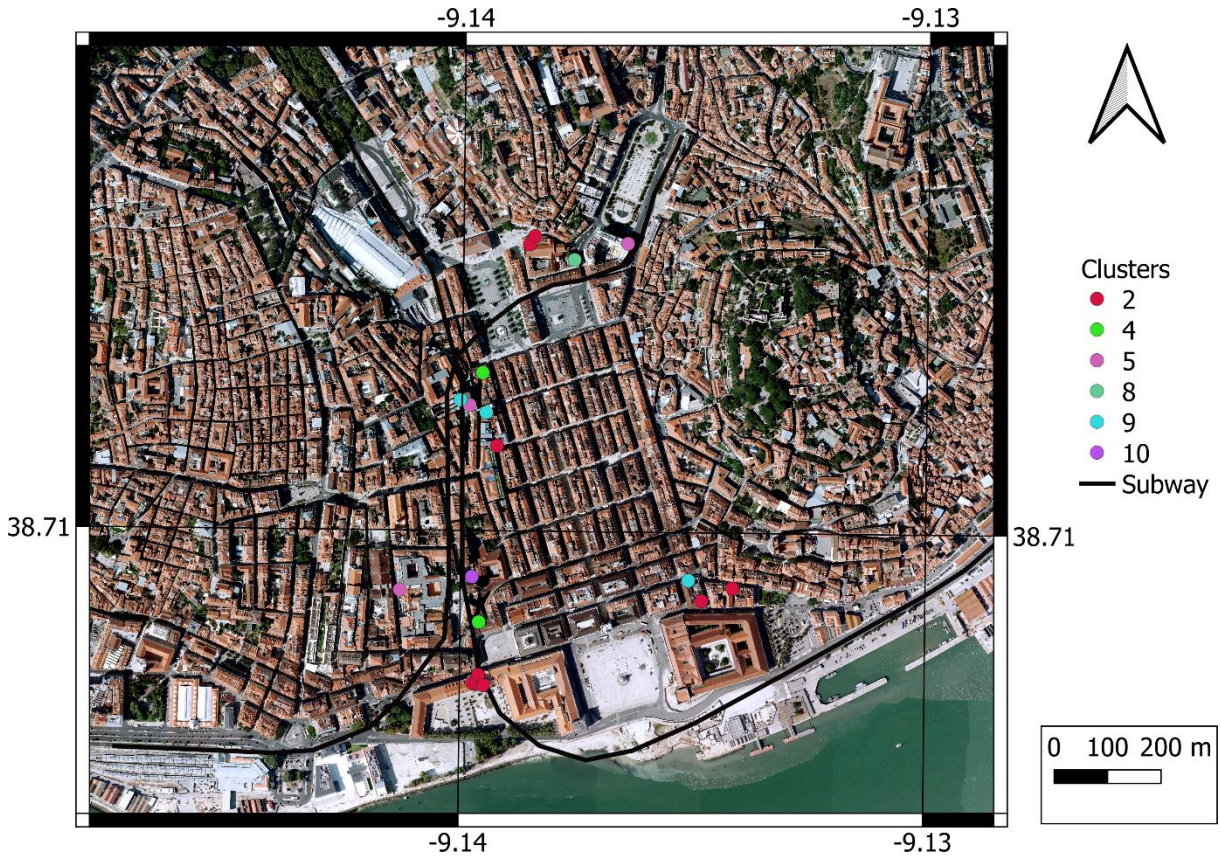

Figure 47 – Position of the PSs belonging to the clusters with centroid for distance to subway lower than 100 m and the location of the subway line. Coordinate grid in WGS84.

3.4.2.3. The displacement time series representative of each cluster provided information regarding the cluster behaviour along the time interval of the analysis. Cluster 1 represented the most frequent behaviour at the ROI, located at both the Downtown and at the flanking hillsides. This cluster was the one with the lowest cumulative vertical displacement and the time series representative of its vertical behaviour was the closest to zero among the ten clusters, presenting oscillations of a few millimetres around this value (Figure 48). Regarding the east – west displacement, this cluster moved some millimetres towards west until January 2016, when it slightly recovered and stabilized around 2 mm to the west of the original position. Standard deviation of displacements inside the cluster were similar for all dates, for both vertical and horizontal time series, as represented by the symbol '+' in Figure 48.

According to Sun (1997), the changes in estuary water level caused by tides influence the ground vertical behaviour at land, due to variations of water infiltration – tidal loading. As cluster 1 vertical displacement time series seemed unaffected by any trends and it covered most of the ROI, its representative vertical displacement time series was inspected in order to verify the presence of tidal effects on the structure behaviour. Tidal heights were available from the Lisbon tide gauge, located 1 km away from the ROI (Antunes, 2007). Hourly observations were

considered for the analysis during the three years of the study. In order to compare the frequencies present at both the tidal heights and the vertical displacement time series representative of cluster 1, spectral densities were determined for each time series (Figure 49). Tidal height frequencies were analysed only for the frequency range common with the displacements (below 15 year^{-1}). For the considered frequencies, tidal heights time series presented a single peak at frequency 0.974 year^{-1}. The largest peak for the vertical displacements time serie spectral density occurred at frequency 1 year^{-1}. Smaller peaks were visible for frequencies 2 year^{-1} and 3 year^{-1}. Thus, both time series presented peaks of spectral density for frequencies around 1 year^{-1}. This suggested that there might be some tidal influence on the structure behaviour. Nevertheless, there are other variables capable of influencing structure behaviour that also present an annual period, such as temperature, whose possible influence was evaluated.

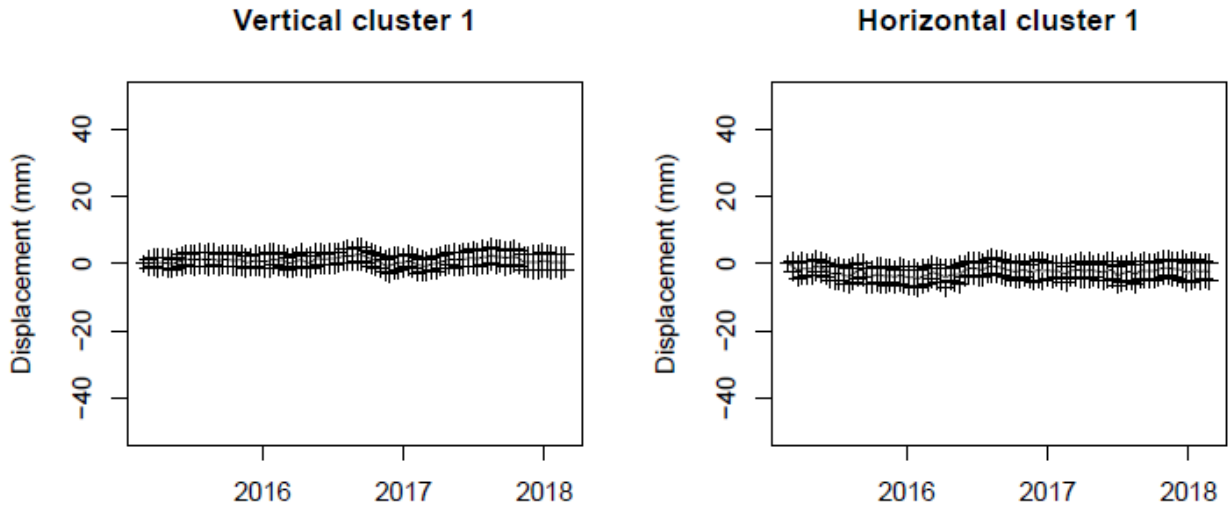

Figure 48 – Vertical and horizontal displacement time series representative of cluster 1 (black line) for Lisbon Downtown; crosses are displacement plus and minus one standard deviation.

The tidal height data were band-pass filtered to isolate the frequency component corresponding to 0.974 year^{-1}. A band width of 0.01 year^{-1} was considered. The filter was applied at TSOFT software, developed at the Royal Observatory of Belgium (Van Camp and Vauterin, 2005). Monthly temperature data at Lisbon airport were also collected from Meteored (2020).

The vertical displacement time series representative of cluster 1 was compared to the filtered tidal heights and to the temperature data (Figure 50). It was verified that the maximum tidal height (at the considered frequency) occurred in October / November and the minimum was in April / May, after the extreme uplift and settlement occurrence. Therefore, tidal heights might not be the cause for the observed seasonal displacements. On the other hand, maximum temperature was observed in July / August and the minimum in January / February, slightly before the displacement extreme values. Thus, it was more likely that the observed vertical displacements were structures'

responses to the changes of air temperature than to tidal heights. The delay of displacements with respect to temperature might be due to the time the structures take to adapt to the new temperature conditions (thermal inertia) and to temperature differences between the airport and the Downtown (approximately 6.5 km away from each other).

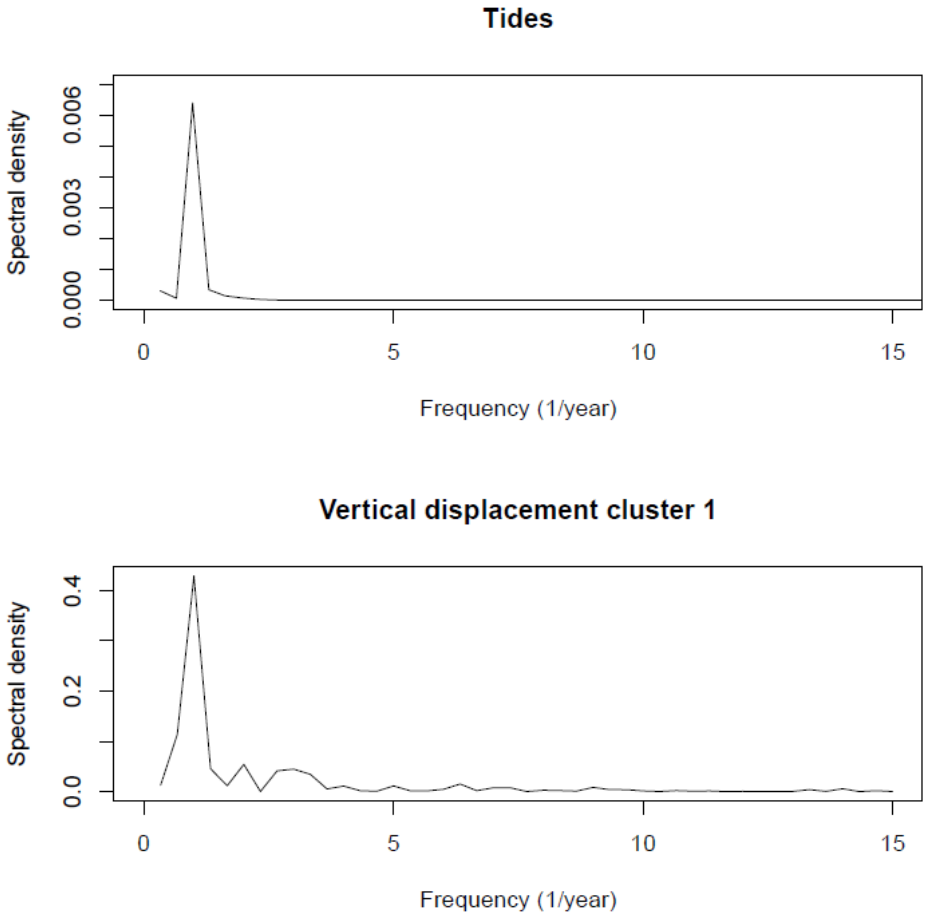

Figure 49 – Spectral density charts for tidal height and vertical displacement time series representative of cluster 1.

The decomposition of the vertical displacement time series representative of cluster 1 was performed, following the method STL as in Cleveland *et al.* (1990). The time series was decomposed into seasonal, trend and remainder components (Figure 51). Iterative detrending and smoothing operations enabled the separation of the three components. The remainder was tested for normality through a Shapiro-Wilk test, for a level of significance of 0.05, and the null hypothesis of the remainder following a normal distribution was accepted. The decomposition showed the data were affected by a seasonal component, which reached its maximum uplift in August and maximum settlement in March.

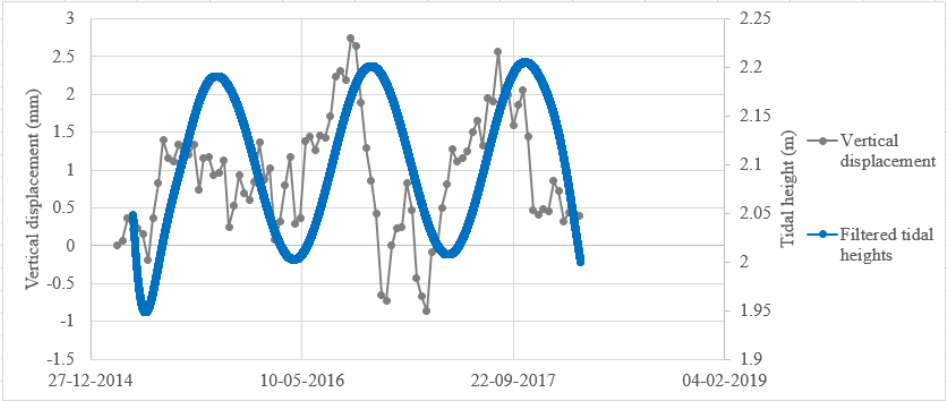

(a)

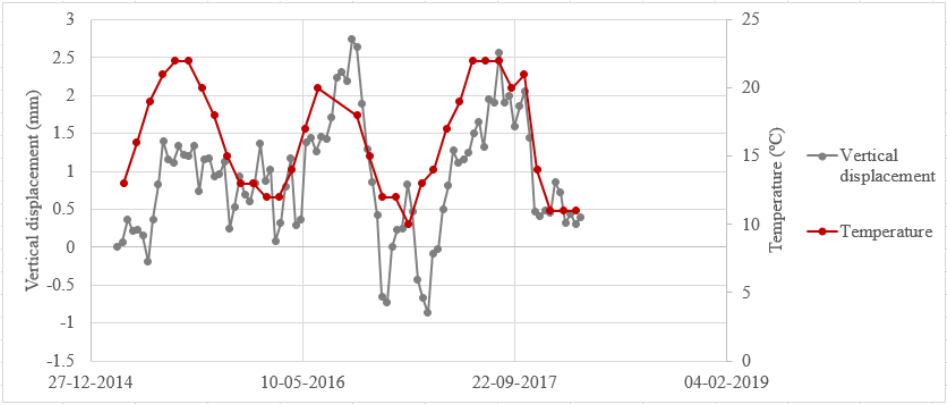

(b)

Figure 50 – Comparison of the vertical displacement time series representative of cluster 1 with (a) the filtered tidal heights and (b) the monthly temperature.

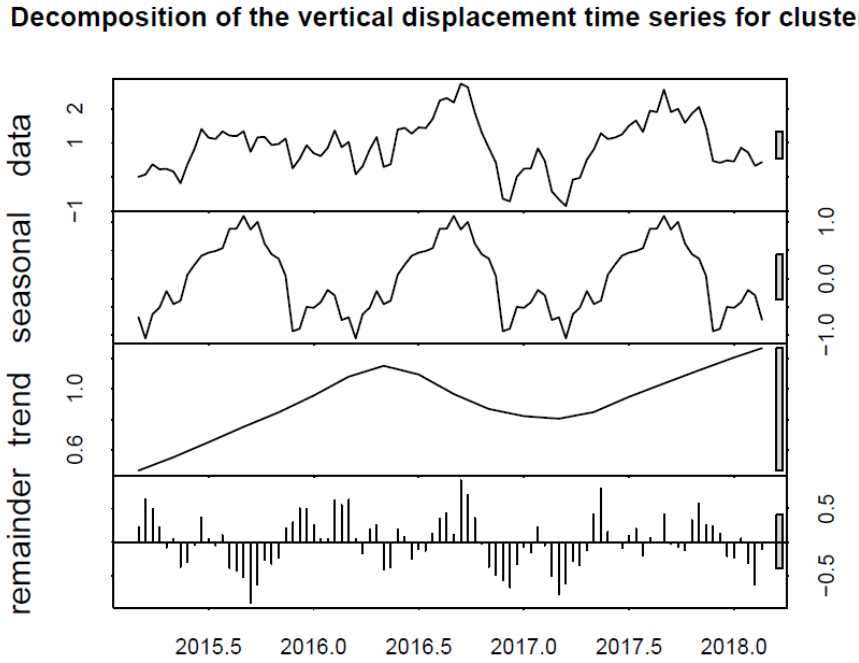

Figure 51 – Decomposition of the vertical displacement time series representative of cluster 1 based on STL method; from top to bottom: original data, seasonal component, trend component and residuals.

The trend component presented a cumulative uplift of 0.8 mm during the three years of the analysis, which could be considered negligible. The decomposition of the horizontal displacement time series for cluster 1 (Annex A.1 Figure 141) displayed a submillimetric seasonal component and the trend showed a cumulative displacement of 0.5 mm. The remainder followed a normal distribution. Therefore, there were no meaningful horizontal displacements at this cluster.

Cluster 2 was one of the clusters with PSs close to the subway lines. The displacement time series representative of this cluster confirmed the cumulative displacements presented in Table 7, with its PSs moving up and towards west during the study (Figure 52). The standard deviations were similar for all epochs for the horizontal displacement component, but for the vertical displacements, there was a time interval of 48 days by the end of 2015 when it was larger than for the remaining time. This meant that there was more variability in the vertical displacements of the PSs during that period. Besides, the larger standard deviation for the horizontal time series showed the cluster admited more variability in the horizontal component than in the vertical one. The vertical displacements in this cluster were characterised by a seasonal component with an amplitude of 2 mm, annual period, with maximum uplift in summer and maximum settlement in winter, compatible with thermal expansion. The cluster trend showed an average uplift of 6 mm, with a decrease in rate starting in the summer of 2016. Horizontal behaviour displayed a submillimetric seasonal component and the trend showed movement towards west of around 6 mm until 2017, when an inversion started to occur. The results of the decomposition were presented for both displacement components in Annex A.1 Figure 142 and Figure 143. The remainder followed a normal distribution for both cases. The combined vertical and horizontal displacements suggested the PSs might be located on tilting objects. These objects can be the buildings, but the hypothesis of the reflective points being located on elements on their roofs, such as skylights, cannot be discarded. Displacement rates decreased along time for both vertical and horizontal components, meaning the PSs were starting to stabilize.

Similar to cluster 1, cluster 3 also contained a large number of PSs (25.7%) and it was spread throughout the ROI. The behaviour of cluster 3 was similar to that of cluster 1. The STL decomposition of cluster 3 presented a seasonal component in the vertical displacement time series with amplitude of 1 mm, annual period, maximum uplift in summer and settlement in winter. Its trend component showed an average uplift of 1 mm, only slightly larger than that of cluster 1. Regarding the horizontal behaviour, the seasonal component was submillimetric and its trend oscillated towards east and west along the time interval of the analysis, reaching a cumulative displacement of 1 mm towards east. The difference in cumulative uplift and cumulative displacement towards east, despite having small magnitudes, were the major distinctions between

the two clusters and may have been the causes for the split of a larger cluster into these two. The remainder of the decomposition followed a normal distribution and the results from this operation are in Annex A.1 Figure 144 and Figure 145. The standard deviations of vertical and horizontal displacement time series were homogeneous along the time interval of the study (Figure 53).

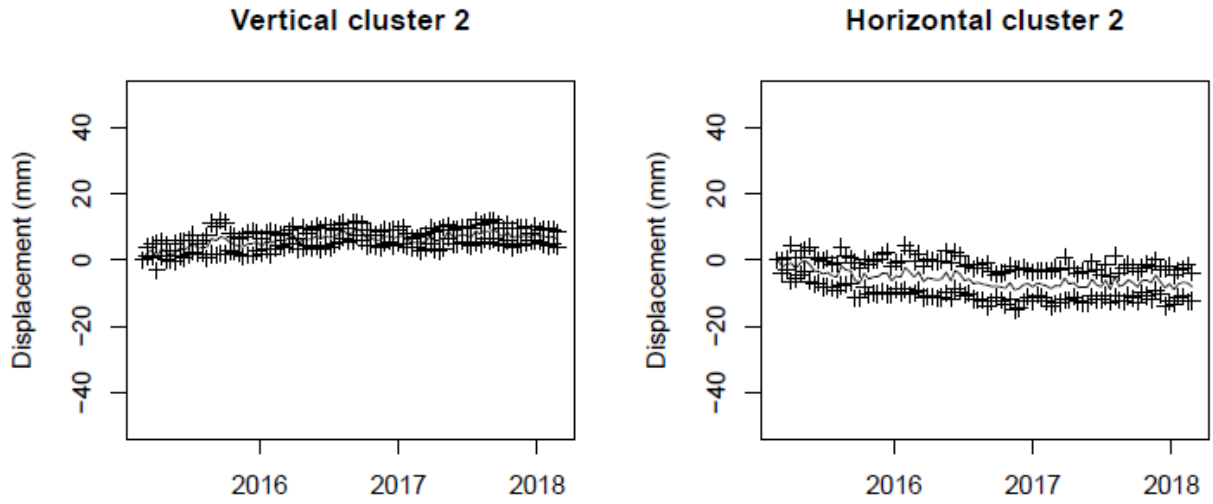

Figure 52 – Vertical and horizontal displacement time series representative of cluster 2 (black line) for Lisbon Downtown; crosses are displacement plus and minus one standard deviation.

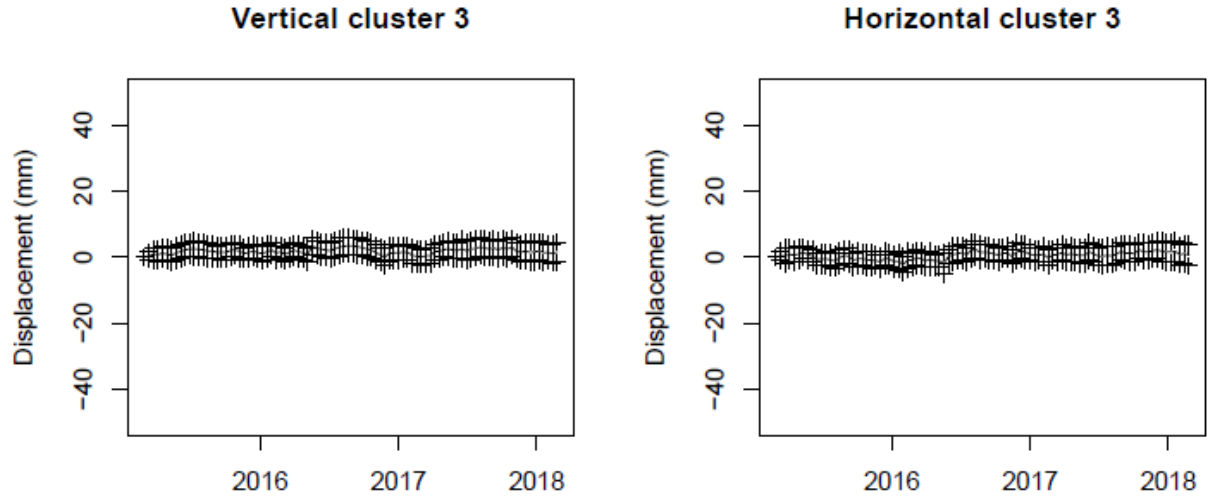

Figure 53 – Vertical and horizontal displacement time series representative of cluster 3 (black line) for Lisbon Downtown; crosses are displacement plus and minus one standard deviation.

Cluster 4 was formed by two PSs close to the subway blue line. These points settled around 2 cm, with a larger rate during 2015 than at the later years (Figure 54). The cluster also presented horizontal displacements at the centimetre-level, having moved around 3 cm towards east. Similar to the vertical displacements, the horizontal displacement rate during 2015 was larger than at the other years. The data showed the PSs on this cluster tilted a few centimetres; however, it was possible the measurement point did not reflect the building behaviour, but that of elements located

on its roof, such as chimneys or ventilation systems (Figure 55). Nevertheless, both vertical and horizontal displacements started to stabilize in 2016. The STL decomposition of the representative displacement time series for cluster 4 did not lead to a remainder following a normal distribution; thus, seasonal and trend components were not analysed. This cluster presented variable displacement standard deviation along the time interval of the analysis. For the vertical component, displacement variability reached a maximum of 10 mm in January 2016, while for the horizontal component, it took the maximum value of 16.4 mm for the same epoch. The horizontal displacement time series representative of cluster 4 presented larger standard deviations than the vertical one for almost all epochs, meaning the PSs in cluster 4 have more variability in the horizontal displacements than on the vertical ones.

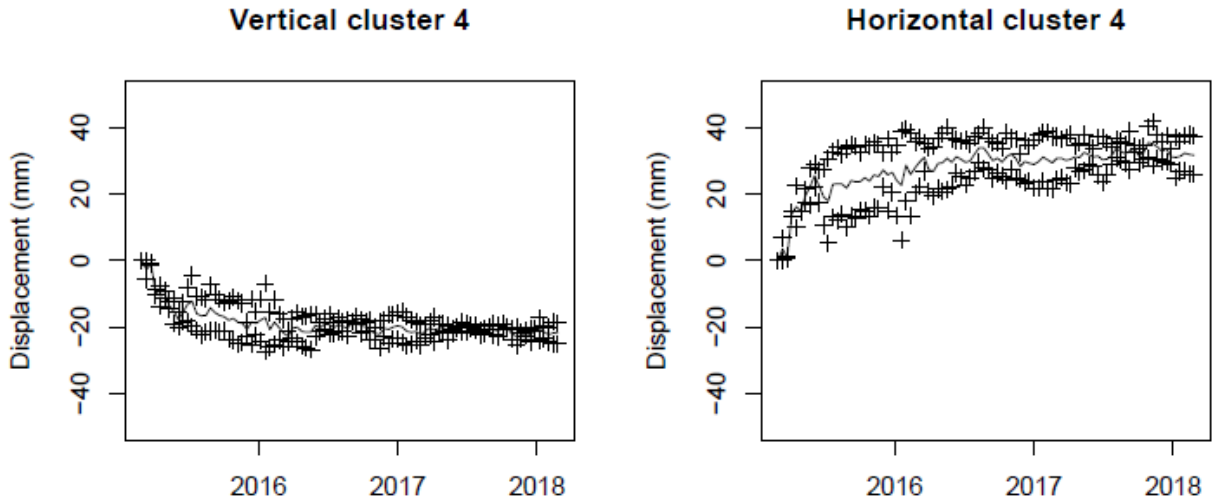

Figure 54 – Vertical and horizontal displacement time series representative of cluster 4 (black line) for Lisbon Downtown; crosses are displacement plus and minus one standard deviation.

Figure 55 – Objects on the roof of a building where a PS from cluster 4 was located; photo from August 2019.

Cluster 5 contained three PSs, relatively close to the subway lines. The cluster presented centimetre-level displacements, having moved up and towards west (Figure 56). There was larger displacement variability in the cluster between April 2015 and November 2016, with the vertical displacements presenting standard deviations around 7 mm and horizontal displacements with standard deviations around 10 mm. After that time interval, standard deviation of vertical displacements decreased to 3 mm and that of horizontal displacements to 4 mm. Thus, this cluster admited more behaviour variability during the first years of the analysis and, after November 2016, the behaviour of the PSs in the cluster became more similar. The remainder of the STL decomposition followed a normal distribution; therefore, the decomposition results could be evaluated (Annex A.1 Figure 146 and Figure 147). Oscillations with a range of 3.5 mm, but without a clear period, were observed for the seasonal component of the vertical displacement time series representative of the cluster. The data showed an uplift of 16 mm during the three years, with a deceleration starting in 2017. Regarding the horizontal displacements, the seasonal component revealed oscillations with a range of 5 mm, without a clear period. The trend displayed movement towards west until May 2017, reaching a magnitude of 15 mm. After May 2017, the cluster presented a stable horizontal trend.

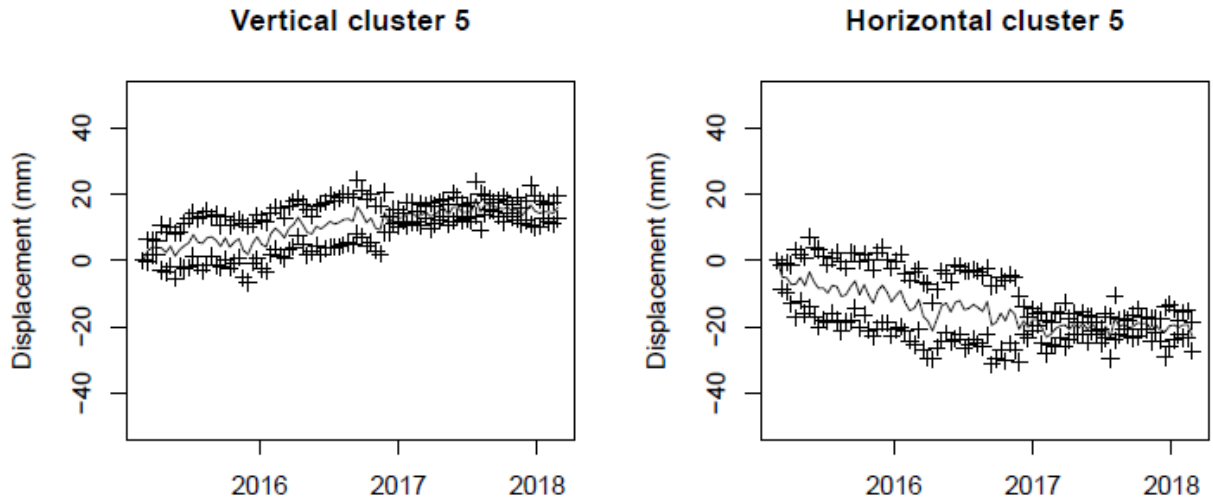

Figure 56 – Vertical and horizontal displacement time series representative of cluster 5 (black line) for Lisbon Downtown; crosses are displacement plus and minus one standard deviation.

Cluster 6 presented settlements and horizontal displacement towards east (Figure 57). Both vertical and horizontal displacement time series representative of this cluster showed an increase in the standard deviations after January 2017, leading to a larger variability of the displacements admitted into this cluster after that date. The seasonal component of the vertical displacement showed an annual period with a range of values of 3.5 mm, maximum uplift in summer and maximum settlement in winter, compatible with thermal expansion. The trend displayed a

settlement of 8 mm, stronger during the first years of the analysis, which tended to stabilize starting in 2017. Horizontal displacement presented a seasonal component without a clear period and the trend displayed 10 mm of movement towards east, also during the first years of the considered time interval. This behaviour stoped in the beginning of 2017. The remainder of the STL decomposition followed a normal distribution. The results from the decomposition are presented in Annex A.1 Figure 148 and Figure 149.

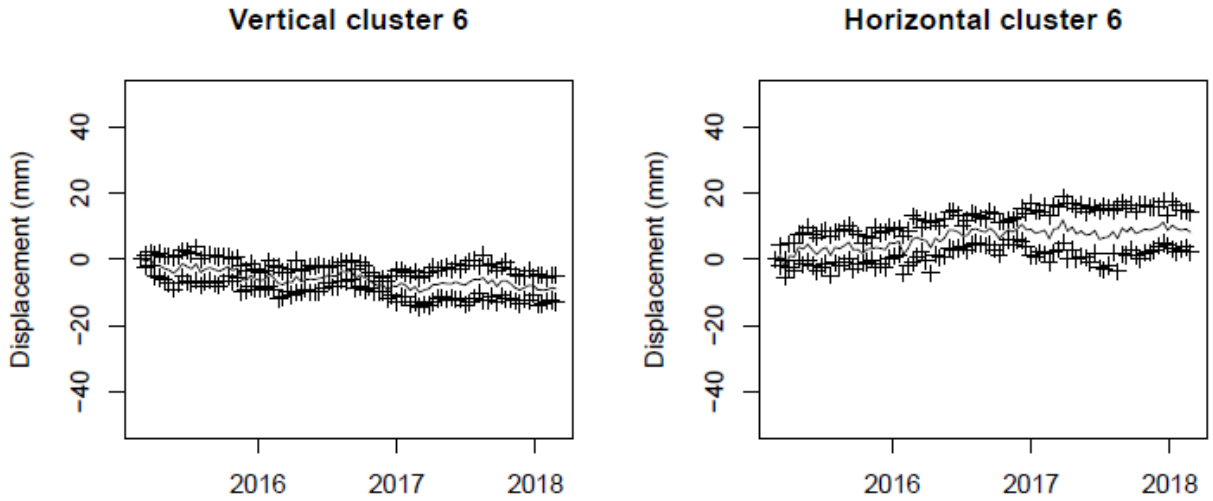

Figure 57 – Vertical and horizontal displacement time series representative of cluster 6 (black line) for Lisbon Downtown; crosses are displacement plus and minus one standard deviation.

Cluster 7 settled and moved towards west during the time interval of the study (Figure 58). The standard deviation was slightly larger during 2015. Vertical displacement showed a seasonal component with 2 mm of amplitude, annual period, with maximum uplift in summer and maximum settlement in winter, compatible with thermal expansion. The cluster settled 8 mm during 2015 and then became stable. Regarding the horizontal displacement, a seasonal behaviour with annual period, 2 mm amplitude, moving east in summer and west in winter was present. This behaviour was superimposed on a trend of displacement towards west during 2015, which then stabilized. Remainder followed a normal distribution and the results of decomposition are in Annex A.1 Figure 150 and Figure 151.

Cluster 6 and 7 had a spatial distribution distinct from that of other clusters. Most of their PSs formed an alignment along the west-northwest – east-southeast direction (Figure 59), which suggested the two clusters might be related. However, distinctive geological or underground features at that area, which could aid in the clusters interpretation, were not found. Besides, the analysis of the displacement time series representative of each cluster revealed different behaviour in time: horizontal displacement in opposite directions and stabilization processes beginning one year apart. Therefore, there was no evidence that the clusters might be related to each other.

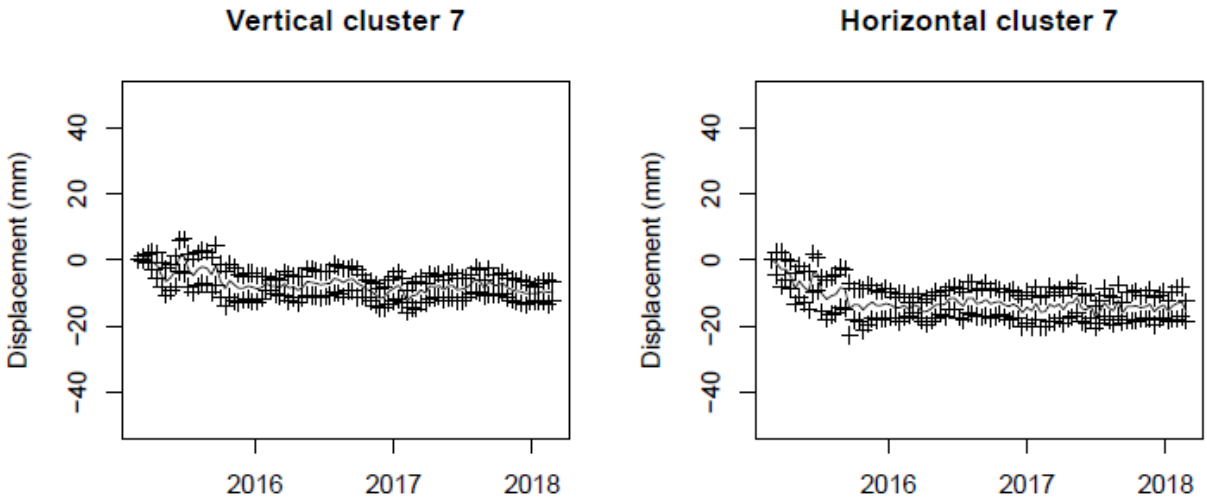

Figure 58 – Vertical and horizontal displacement time series representative of cluster 7 (black line) for Lisbon Downtown; crosses are displacement plus and minus one standard deviation.

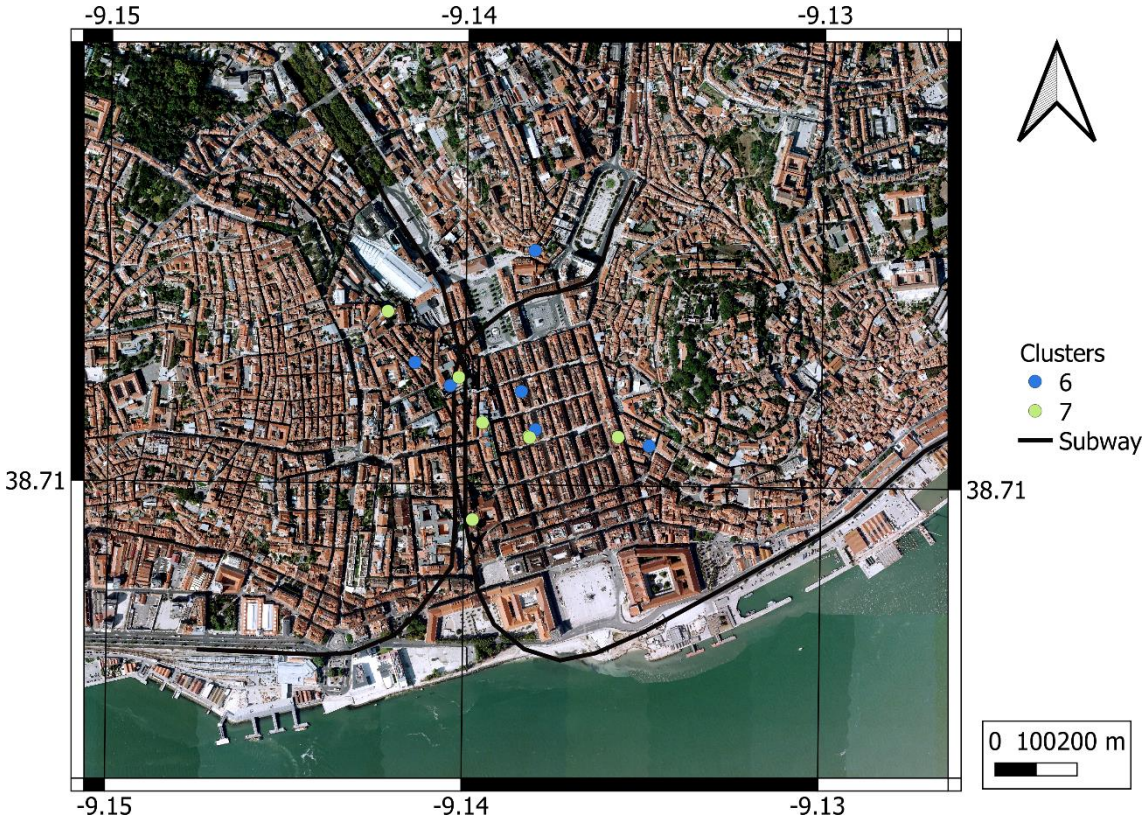

Figure 59 – Location of clusters 6 and 7. Coordinate grid in WGS84.

Cluster 8 was formed by a single PS, which settled and moved towards east (Figure 60). The STL decomposition (with remainder following a normal distribution) showed the point had a seasonal component with annual period, amplitude of 4 mm, reaching the maximum uplift in summer and the maximum settlement in winter, compatible to thermal expansion. The point settled 30 mm until the summer of 2016, when it stabilized. The horizontal displacements also presented a seasonal component with annual period and amplitude of 4 mm, which reached its maximum

displacement towards east in winter and maximum displacement towards west in summer. The trend displayed a movement of 40 mm towards east, with a rate that started decreasing in 2016, until stabilization (Annex A.1 Figure 152 and Figure 153). The PS in this cluster was located at a roof, near a skylight.

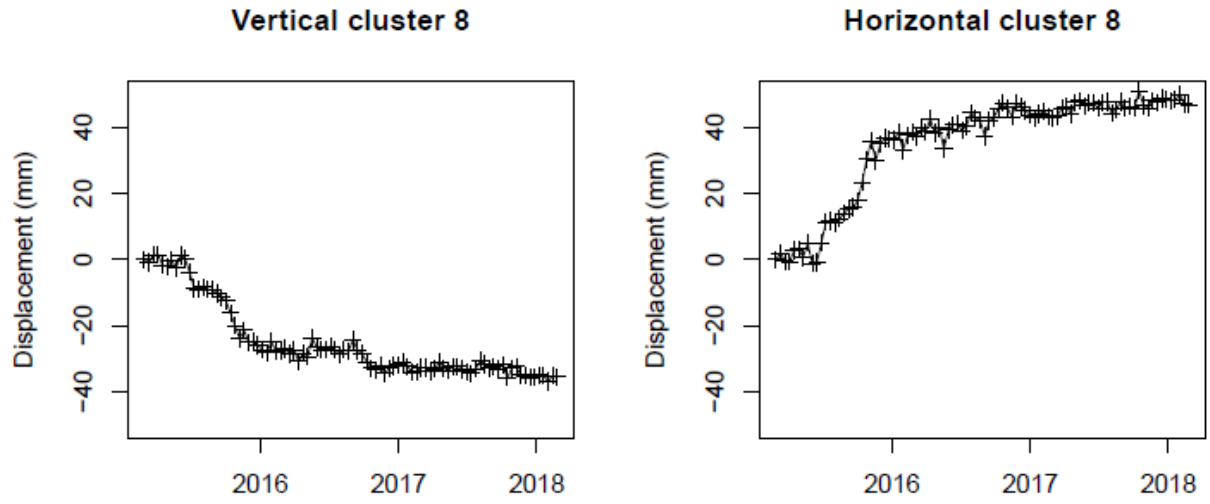

Figure 60 – Vertical and horizontal displacement time series representative of cluster 8 (black line) for Lisbon Downtown; crosses are displacement plus and minus one standard deviation.

Cluster 9 contained three PSs, which moved up and towards east during the three years of the study (Figure 61). Standard deviation was larger for some epochs between March and June 2015. For most epochs, the cluster had more variability in the horizontal displacements than in the vertical ones. The decomposition of the vertical displacement time series representative of the cluster did not lead to a remainder following a normal distribution; thus, seasonal and trend components were not analysed. The cluster presented uplift with a magnitude of 14 mm until May 2015 (corresponding to the interval with larger variability of displacements inside the cluster), when it started to settle and stabilized around 12 mm. The decomposition of the horizontal displacement time series led to a remainder with normal distribution; thus, its results could be evaluated (Annex A.1 Figure 154). A clear period was not found for the seasonal component and the trend presented 6 mm of displacement towards east, when it inverted the movement direction and started going west. One of the PSs in this cluster was located at one of the arches of Carmo Convent, built in the 14th century and partially destroyed during the 1755 earthquake. The other two PSs were on roofs of Pombalino buildings (Figure 62).

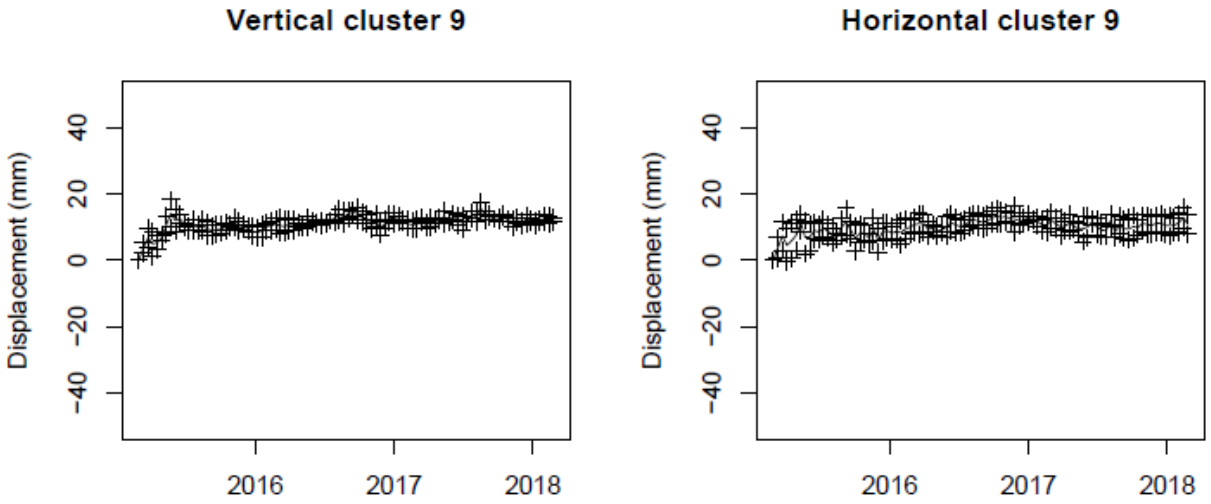

Figure 61 – Vertical and horizontal displacement time series representative of cluster 9 (black line) for Lisbon Downtown; crosses are displacement plus and minus one standard deviation.

(a) (b)

Figure 62 – Carmo Convent (a) and Pombalino building (b), where PSs from cluster 9 were located; photos from August 2019.

Cluster 10 was formed by a single PS located on a roof and close to a PS from cluster 7. Neither the vertical nor the horizontal displacement time series representative of each cluster led to an STL decomposition with remainder normally distributed; thus, seasonal and trend components were not analysed. The point moved up around 30 mm and another 30 mm towards east during 2015 and then stabilized (Figure 63). The proximity between this point and the PS in cluster 7 may be cause for some concern, as these clusters had distinct behaviour (cluster 7 moved down and towards west). The opposite behaviour from the two PSs may indicate the presence of some damage. However, both clusters stabilized by the beginning of 2016.

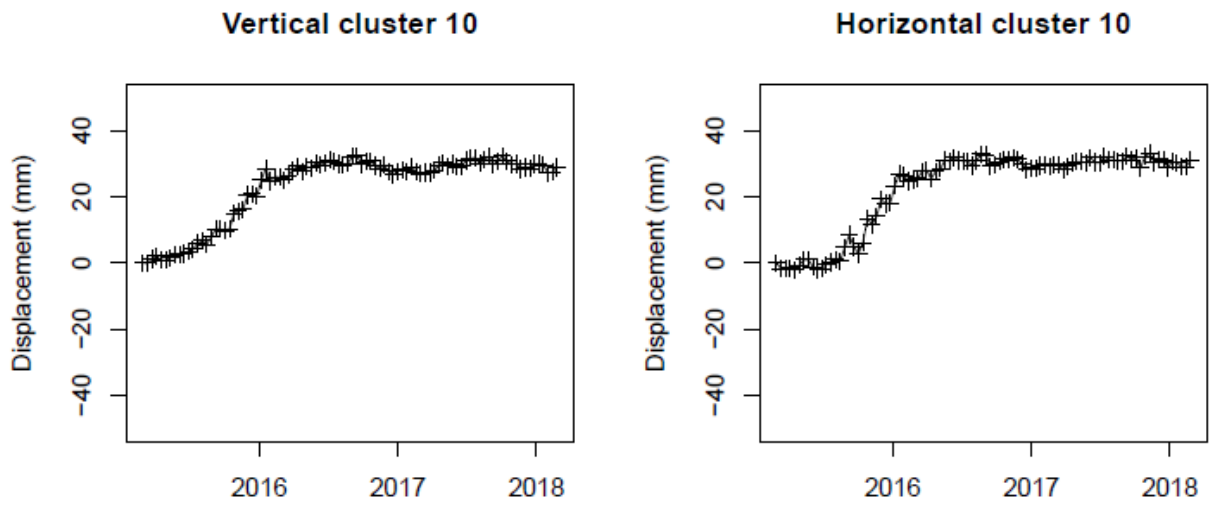

Figure 63 – Vertical and horizontal displacement time series representative of cluster 10 (black line) for Lisbon Downtown; crosses are displacement plus and minus one standard deviation.

Table 8 summarizes the results from the cluster analysis. All clusters presented distinct behaviour among each other, with the main distinctive features being displacement direction, magnitude and the epoch when they started to stabilize. By the end of the time interval of the study, all clusters presented stable behaviour.

An evaluation of differential displacements at building block-level was performed using the cluster information (Figure 64). It was considered that building blocks with PSs from distinct clusters could have differential displacements, being a sign of possible damage. A code was attributed to each block, considering the different behaviour of the represented clusters. Code 0 was set to building blocks containing PSs of a unique cluster. Code 1 was attributed to blocks displaying PSs from both clusters 1 and 3, which presented similar behaviour. Code 2 was given to the blocks containing PSs from more than one cluster and in which at least one of those clusters was cluster 2, 4, 5, 6, 7, 8, 9 or 10. The building blocks were identified through the merging operation of adjacent structure objects achieved through OBIA in section 3.3.2.3.

Table 8 – Summary of the cluster analysis.

	Vertical						Horizontal					
	Movement direction			Magnitude		Stable by 2018	Movement direction			Magnitude		Stable by 2018
Cluster	Uplift	Settlement	None	Millimetre	Centimetre		East	West	None	Millimetre	Centimetre	
1			X	X		X		X		X		X
2	X			X		X		X		X		X
3			X	X		X			X	X		X
4		X			X	X	X				X	X
5	X				X	X		X			X	X
6		X		X		X	X				X	X
7		X			X	X		X			X	X
8		X			X	X	X				X	X
9	X				X	X	X				X	X
10	X				X	X	X				X	X

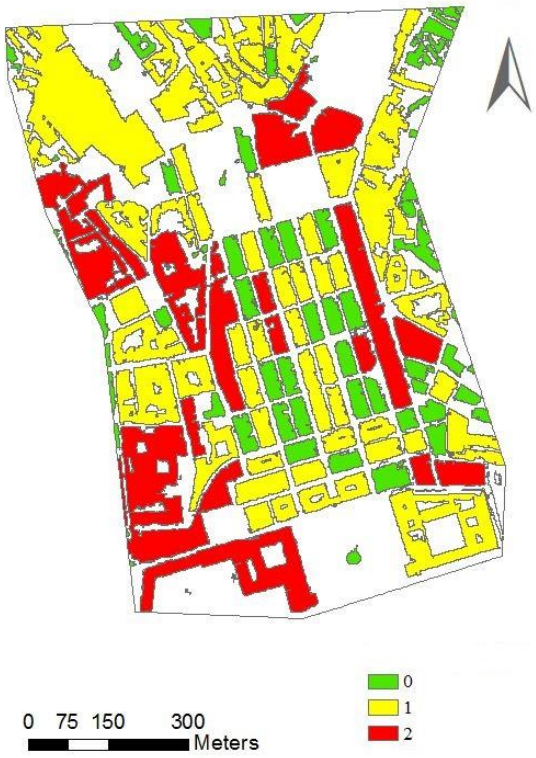

Figure 64 – Code map for differential displacements of building blocks at Lisbon Downtown, based on cluster results.

3.5 Discussion

This section presents a discussion of several topics regarding the method for RADAR interpretation proposed in this Chapter, based on the results presented in the previous section.

3.5.1. PSI technique enabled the identification of several PSs on both types of studied structures. Although C-band SAR images are freely available worldwide through Copernicus programme, for vegetated areas such as the slopes around Odelouca reservoir, the usage of L-band data is advantageous (Shi *et al.*, 2019), due to its capability to pass through foliage and to be reflectd by elements which move together with the slope, such as rocks. Despite the vegetation cover of the ROI at Odelouca, several PSs were detected on the slopes, providing a density measurement of 346 PSs/km^2. However, some PS gaps were detected at shadow areas to the SAR signal.

3.5.2. The number of images and distribution of normal and temporal baselines were also important for the results' quality. According to Benoit *et al.* (2020), unwrapping errors tend to occur at areas with alterations in scattering properties caused by vegetation, humidity, anthropic activities, strong relief or fast deformation. Large temporal and normal baselines also contribute to low spatial coherence, which may also lead to unwrapping errors. For the slopes case study, the number of images was small, there were many gaps in the acquisition time series, some temporal

baselines spanned more than three years and there were normal baselines around 3000 m (Figure 19), which may have contributed to the occurrence of the detected unwrapping errors.

On the other hand, Sentinel-1 datasets for Lisbon Downtown had a regular acquisition frequency, with few gaps in the time series, maximum temporal baselines around 1.5 years (at an area with small decorrelation) and normal baselines below 200 m. Unwrapping errors were not detected; however, the fact that the Downtown is mostly flat may also have contributed to their absence.

3.5.3. Sentinel-1 C-band data led to a similar PS density for Lisbon metropolitan area, with around 350 PSs/km^2. The analysed area included large vegetated regions, such as Monsanto Forest Park, where PSs were not detected; thus, leading to the low achieved density. On the other hand, at the Downtown, the combined ascending and descending datasets restricted to structures originated a density of 1200 PSs/km^2. All blocks of adjacent structures had at least one PS, which enabled the evaluation of differential displacements at block-level. Image properties also influenced the precision of the measured displacements. According to Equation (20), the dispersion of a displacement value at a certain epoch depends on the SAR signal wavelength and PS temporal coherence. In this study, only scatterers with coherence greater or equal to 0.9 (ranging from zero to one) were considered as PSs. Therefore, for PALSAR-1 ALOS-1 images, the maximum displacement dispersion at a certain epoch for a PS used in the study was 8.4 mm. On the other hand, for SAR-C Sentinel-1 data, that value was 2.0 mm. Thus, it was not reasonable to consider that displacements with magnitudes lower than these values were actual movement.

3.5.4. The method proposed to analyse PSI displacement time series was intended to be objective, independent of prior knowledge about the problem being studied and usable by InSAR non-experts. An unsupervised strategy for time series exploration, such as clustering, was appropriate for this purpose. Allied to a hierarchical procedure, in which the elements were progressively aggregated or separated given a dissimilarity measure, the method was objective, as an automatic selection of the number of clusters could be performed, without the user intervention.

Other clustering methods found in the literature, such as partitioning (Milone and Scepi, 2011), required the user to select the number of clusters. The solution presented to the problem was the application of the clustering procedure to a few pre-selected number of clusters and then choose one of the solutions, which turned the method subjective. In the method proposed in this study, a solution was always provided automatically, which ensured the data division into homogeneous clusters. However, the user had the freedom to select other numbers of clusters and to change the detail of the analysis, informed by auxiliary data provided by the tool. For example, at Odelouca case study, the automatic solution was able to separate PSs affected by unwrapping errors from regular PSs. This was an important result, as it increased the trust the user could have in the data

from the other clusters, where the errors were minimised or even removed. However, in order to detect possible signs of instability, which was the aim of the study, the scale of the analysis had to be increased into a more detailed one.

At the Downtown case study, clusters 1 and 3 were very similar to each other in both displacement time series and centroids, which showed the proposed method had high sensitivity to behaviour changes and that it was able to separate distinct clusters even when the difference between them was not much evident.

3.5.5. Three aggregation methods were tested at Odelouca slopes case study: single linkage, complete linkage and Ward method. Single linkage tended to add PSs to a main cluster one by one. Despite this large sensitivity to outlier presence, a large number of clusters would be required to detect all the PSs behaving distinctly from the more homogeneous clusters. The outliers may correspond to unwrapping errors or to signs of structure instability and must be separated from the other points and carefully analysed. Complete linkage and Ward method led to the inclusion of several wrongly-unwrapped PSs on the same clusters, which was a more efficient solution, as those points could be analysed together and separated from the regular PSs. Besides, other outliers, such as those reflecting signs of possible structure instability, could be detected more easily by using a lower number of clusters.

Complete linkage was found to be more sensitive to outlier presence than Ward method, as the first technique detected a larger number of PSs with unwrapping errors. Therefore, complete linkage provided a balance between building compact clusters and outlier detection, while Ward method privileged the construction of compact clusters over the outlier identification and included some of these deviant points into regular clusters.

3.5.6. The dissimilarity measure used to compare the time series was DTW. This is a shape-based and elastic distance measure, which uses only the displacement time series. Thus, *a priori* knowledge on the displacement cause was not required to apply the method. According to Romano and Scepi (2006), DTW is not an appropriate distance measure to compare InSAR displacement time series, due to the noise present in the data. A qualitative evaluation of the clustering quality using displacement time series without being pre-processed actually revealed many clustering errors. PSs spatially close and with similar displacements time series were aggregated into distinct clusters, while PSs far from each other and with different behaviour were attributed to the same group. In order to minimise those errors, the proposed method low-pass filtered the displacement time series with a moving average and DTW was applied on the filtered data instead. This operation was successful, as the visual inspection of the results for the same PSs showed the points were aggregated into the correct clusters afterwards. Despite performing DTW on the filtered data,

after the cluster definition, operations were executed on the original time series to avoid working with approximated data.

In this study, another limitation regarding DTW usage for InSAR displacement time series comparison was identified. The fact that DTW is an elastic distance measure may lead to the inclusion of PSs with displacement anomalies occurred at distinct epochs into the same cluster. In this study, this potential error source was minimised through the constraint of the DTW through a Sakoe Chiba band, which limited the epochs for which the comparison was performed. The strategy was successful, as at both case studies, different clusters were identified presenting similar behaviour occurring at different epochs.

It was also verified that DTW may not be appropriate to deal with long time series. If a pair of long displacement time series was similar for most of the epochs, presenting some eventual anomaly during a small number of dates that might cause a small change in the distance value and become unnoticed for the cluster construction. This limitation was already referred in the literature (Esling and Agon, 2012), where the authors state that compression-based distances might be the most appropriate to deal with long time series. The application of representation techniques, such as Piecewise Aggregate Approximation (Keogh *et al.*, 2001), which divides the time series into segments and considers the average value of each of them to represent it, could also be helpful to deal with long time series, as they reduce their dimension. The application of these techniques to InSAR displacement time series is an important issue, as the SAR image availability has increased significantly in the last years, especially with the contribution of Sentinel-1 data, and the analysis of long time series is becoming common. The usage of long SAR image time series is beneficial for PSI processing, as it allows a more precise determination of the parameters of interest. However, the small sensitivity to disturbances occurred at a small number of epochs may cause the late detection of anomalous behaviour. This limitation could be surpassed by dividing the long PSI displacement time series into smaller segments, in which short-duration anomalies would cause a larger difference in the distances among time series; thus, being more easily identified and aggregated into a separated cluster.

3.5.7. The quality of the results achieved through the RADAR interpretation method proposed in this thesis was evaluated through the comparison with one of the methods proposed in the literature: PS-Time, developed in Berti *et al.* (2013) and described in section 3.1.1 of this document. PS-Time performs a series of statistical tests until it classifies each PS in one of six pre-defined classes according to the point displacement time series (Figure 10). As PS-Time analyses a single displacement direction, the quality control was performed only for the LOS displacement time series from Odelouca slopes study case, in order to directly compare both results. PS-Time was applied to

the displacement time series after correction of reference point effect. The thresholds used for the statistical tests were 0.5 to test for linear correlation, 0.5 to evaluate quadratic regression and 1.0 for segmented regression. Figure 65 presents the spatial distribution of PS-Time classes. There were PSs attributed to all six classes, with class 0 (uncorrelated time series) being associated to 41.5% of the PSs. Classes 3 (bilinear) and 1 (linear) contained 24.1% and 20.6% of the points, respectively, being the second and third more frequent. Quadratic behaviour affected 10.5 % of the points and 3.3% of the PSs presented discontinuities in their displacement time series. From those, 1.4% kept velocity values before and after the discontinuity, while 1.9% suffered a change in displacement rate. All classes were equally distributed along the ROI.

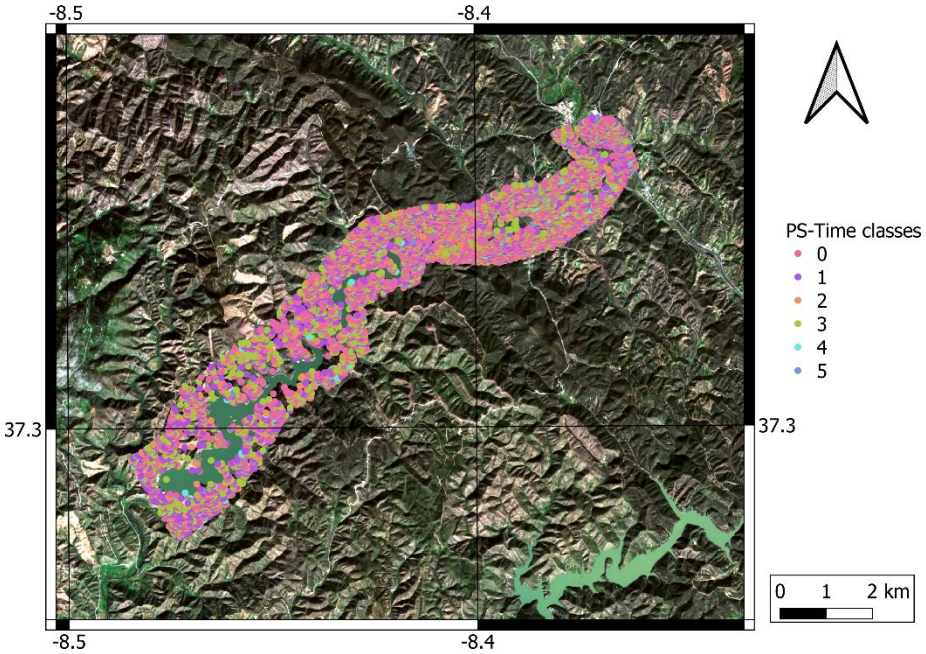

Figure 65 – Classification of the displacement time series according to PS-Time method. Coordinate grid in WGS84.

In this case study, PS-Time classes admited PSs with different behaviour. Each class included PSs moving both away and towards the sensor, showing superposition among classes. Besides, except for class 0, all other classes included PSs affected by unwrapping errors together with regular PSs (Figure 66), which made the performance of the algorithm proposed in this thesis more effective than PS-Time in this topic. The method proposed in this study is also more objective, as a solution was achieved automatically and information was provided to aid the user to select another adequate level of detail to the analysis, while PS-Time required a trial and error approach to identify the level of significance for the hypothesis tests that were performed.

Comparing the displacement time series of all PSs found at the ROI (Figure 67) and the displacement time series of the PSs in each cluster from the proposed method (Figure 68), it was arguable that a similar result could be achieved through a simpler method, such as the thresholding

of the PS cumulative displacements. Nevertheless, it was verified for both case studies from the present Chapter, that some of the clusters presented superposition of their PSs cumulative displacement values; thus, cumulative displacement was not the only used criterion. Due to the usage of the Sakoe Chiba band, the epochs of anomaly occurrence were also considered. Therefore, it was advantageous to apply the proposed method. Displacement time series of all PSs and of all PSs at each cluster at the Downtown are presented in Annex A.1 Figure 155 and Figure 156.

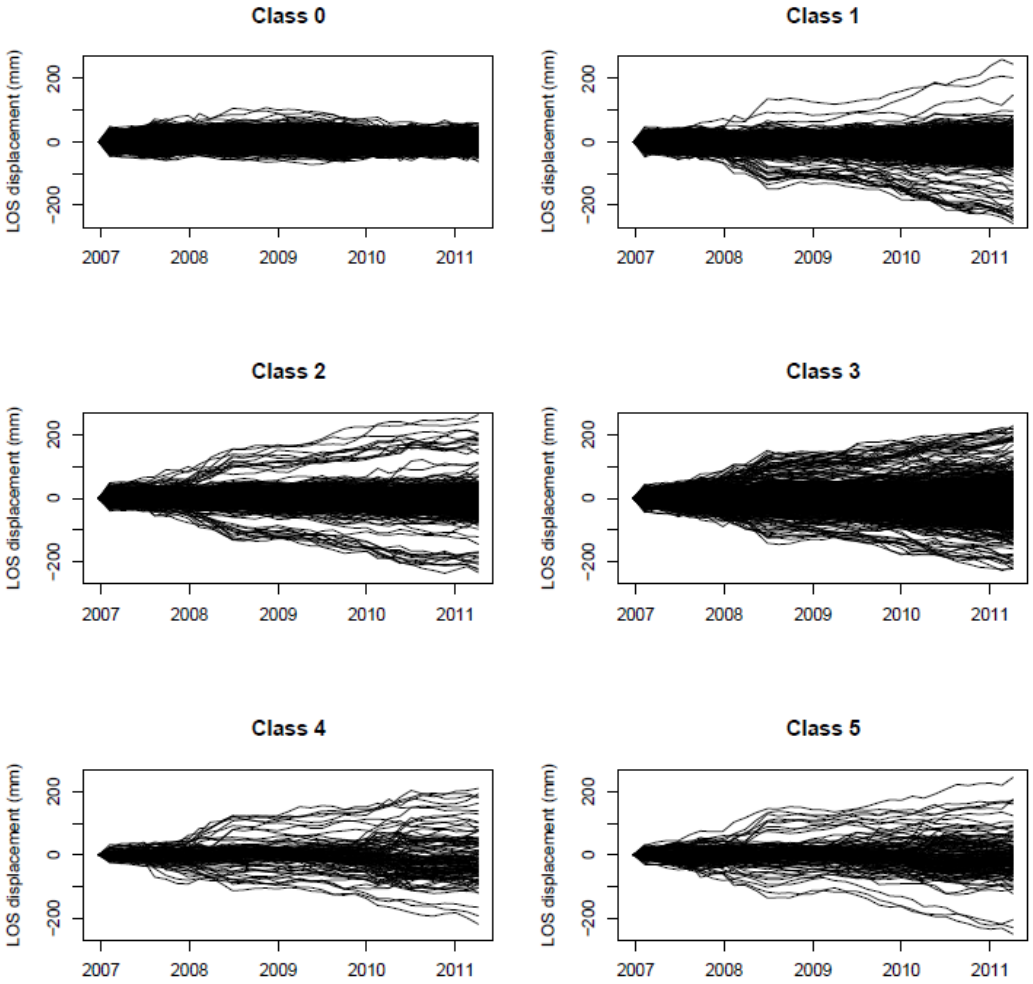

Figure 66 – Displacement time series of PSs in each class from PS-Time; class 0: uncorrelated; class 1: linear; class 2: quadratic; class 3: bilinear; class 4: discontinuous with constant velocity; class 5: discontinuous with variable velocity.

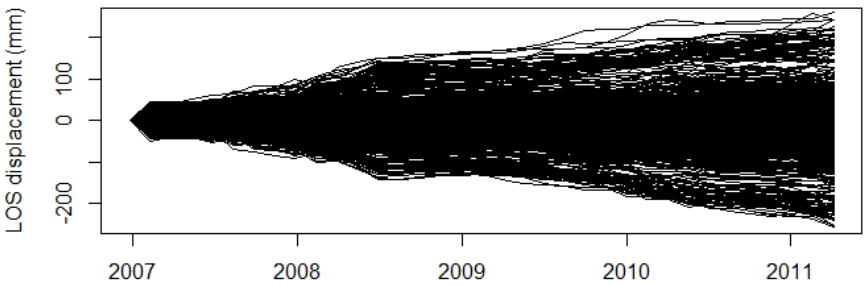

Figure 67 – Displacement time series of all PSs on Odelouca slopes.

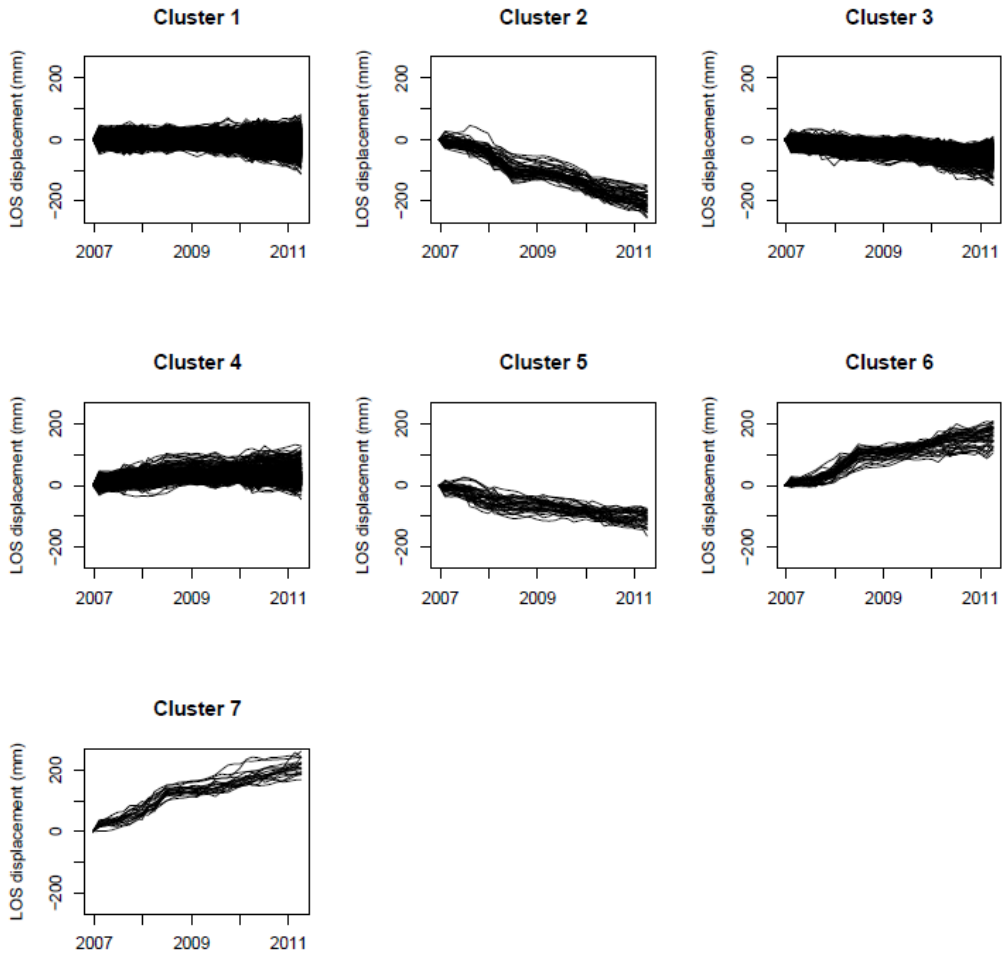

Figure 68 – Displacement time series of all PSs in each cluster, for the seven cluster solution using complete linkage for Odelouca slopes.

3.5.8. The proposed method provided measures that aided the interpretation of each cluster. These measures were average displacement time series representative of each cluster behaviour and centroids of variables computed during PSI processing or added as optional raster files. These data were accompanied by information about the variability inside each cluster, such as displacement standard deviation for each epoch at the representative time series or boxplots for the centroids. The average values were useful to identify the general behaviour trends for each group, but when interpreting the data, attention must be paid to the fact that the cluster may contain PSs whose behaviour deviates from the average values provided. For example, as seen at Odelouca study case, a cluster with curvature centroid below zero may still have a large number of PSs located on concave surfaces. The average data were useful to identify major trends in the clusters, to compare them among each other and to analyse their spatial and temporal behaviour, which may be helpful information when evaluating the need for sending a team to perform *in situ* field work.

3.5.9. Another relevant question for the application of the proposed method are the PSI reference points when two datasets are combined, as performed for the Downtown study case. The

reference point for each dataset was selected among the most stable PSs at the ROI. However, the two reference points were not coincident. At the Downtown case study, displacements from ascending and descending passes were referred to reference points separated by 2 km. Those points may have distinct physical natures, be located at elements with different behaviour and have relative displacements with respect to each other, which will affect the combined data. The applied procedure to estimate and remove the reference point movement and residual atmospheric artifacts minimised the differences between the reference points, but the ideal solution would be to have the same point as reference for both datasets. Such a goal could be achieved by using an artificial reflector capable to receive and transmit the SAR signal from both geometries, e.g. a compact active transponder (Mahapatra, 2015) or a bidirectional corner reflector like the one proposed in this thesis Chapter 5.

There is the risk that the method used for estimation and removal of reference point effect may remove displacement components of interest to the analysis from the displacement time series. If all analysed structures present similar responses to a certain load (e.g. the buildings at the Downtown are similar to each other), it will be possible for these responses to be included in the correction time series, being removed from all PSs. However, for these responses to be removed from the data, they will have to be present at a large number of PSs with low average velocities. In that case, they will not correspond to an anomaly at that ROI, whose identification is the goal of the presented analysis. If the anomaly is present only at a small number of PSs considered stable, their anomalous observations will be smoothed through the average with displacement time series from other PSs and the anomaly will not be removed from the PSs.

3.5.10. The major hindrance of the proposed method was the computational requirements. Hierarchical clustering and DTW both have quadratic complexity (Aghabozorgi *et al.*, 2015; Gold and Sharir, 2018); thus, the processing of large displacement time series is time consuming. Besides, the available memory also influences the maximum number of points to be analysed. In order to reduce processing time, the code for clustering operation was parallelized using R packages “parallel”, “foreach” and “doParallel” (Corporation and Weston, 2018; R Core Team, 2018). The case study of the Downtown considered 974 PSs, with two time series each, and observations at 92 epochs. The processing took 11 minutes at a laptop with 2.40 GHz CPU, 8 GB of RAM and four cores. Odelouca slopes case study, with 7949 PSs and 35 epochs each[17], was processed in Jupyter during 6 hours.

3.5.11. The RADAR interpretation method proposed in this thesis enabled the detection of behaviour patterns on both case studies and the identification of research questions specific for

[17] After linear interpolation in time to assure a regular observation frequency.

each situation. Displacement away from the sensor was found on Odelouca slopes compatible to subsidence caused by water load, similar to what was found in literature for other water reservoirs. From February 2009, when there was no sign of slope movement, to April 2011, when the last SAR image was acquired, LOS subsidence rate varied from 1.6 mm/year (at cluster 4) to 21.1 mm/year (at cluster 5). These values were larger than the 1 mm/year – 2 mm/year of subsidence rate found around lake Nasser, in Egypt (Saleh *et al.*, 2018), caused by the water load. To understand the difference in both values, it must be noted that the evaluation of displacement rates at both areas were performed at distinct phases of the structures' life cycles. LOS displacement rate at Odelouca was evaluated during the reservoir first impoundment, while the values presented for subsidence rate at lake Nasser were measured around 30 years after the Aswan High Dam construction and the impoundment of the respective reservoir, being expectable that the Egyptian lake shows lower values. The lithology of both areas was distinct, with slopes around lake Nasser being formed by granite, granitoids, gneisses, schists, sandstones, conglomerates and shales (ElKobtan *et al.*, 2016). At Odelouca, the main lithologies are shales and greywacks (section 3.3.1.1.). In particular, shales tend to suffer modifications when in contact with air and water: a rise in moisture may reduce the shear strength, originating cracks. The presence of those cracks increases the surface with which water can interact, thus enhancing the rock deformation and leading to landslide susceptibility (Walkinshaw and Santi, 1996). Therefore, it is expectable that reservoir banks composed of shale present a deformation behaviour due to their constant contact with water. The data from Odelouca presented a trend to stabilize after the initial phase of the impoundment.

A crucial point for the results' interpretation was the knowledge on the physical nature of the PSs. The aim of the study was to evaluate eventual contributions of PSI displacements to structure monitoring; thus, PSs located on structures were identified to be analysed separately from PSs on other objects, such as lampposts or fences. At the Downtown case study, an OBIA image classification was executed to distinguish between structure and non-structure elements and to associate the corresponding PSs to each class. PSs on structures were successfully isolated and their behaviour was evaluated through the clustering analysis proposed in this thesis. Nevertheless, a few PSs presenting anomalies in their displacement time series were located on building roofs close to skylights or ventilation systems. Thus, the observed displacements for those PSs may result from some instability of those elements instead of the buildings themselves.

Tidal loading was expected to exert some effect on the displacements of Downtown buildings, due to the ROI proximity to the river and to its geological properties. However, the frequency analysis of tidal heights at Lisbon port for the time interval of the study did not reveal signs of this

effect. According to Sun (1997), more than 80% of tidal height amplitude is due to diurnal and semidiurnal tides, with periods of 24 hours and 12 hours, respectively. For the same acquisition geometry, a new SAR image was acquired by Sentinel-1A every 12 days at the same hour. Therefore, to each SAR observation corresponded a similar tidal height and, consequently, a similar tidal load effect. For this reason, this effect was not identified on the PSI displacement time series.

A similar effect was found on GNSS data. Lima (2009) studied the effect of tidal loading for two GNSS bases in Lisbon region for observation sessions of distinct durations. For the same base, if the GNSS session lasted for less than 24 hours, the difference of tidal loading between the two points reached 10 mm. On the other hand, if the GNSS session was longer than 24 hours, the difference in tidal loading for the same two points was lower than 3 mm.

In the research for this thesis, ascending and descending data were combined, when images from the ascending pass were acquired around 6:35 pm and images from the descending pass were from 6:43 am. One could think that the combined data could detect the effect caused by the diurnal tide; however, that was not verified. Each SAR image geometry was processed individually and displacements were referred to a reference epoch, which coincided with an image acquisition of that geometry. Thus, the tidal load at the reference epoch was equal to the tidal load at the other image acquisition epochs and it was not detected for the individual geometries. Consequently, when the data from the two passes were combined, it was not detected neither.

Sun (1997) stated that tidal loading reduces its amplitude and presents a phase delay as it moves towards inland. Therefore, the tidal loading effect at reference point was lower (and occurred later) than at the Downtown. However, as the movement inland did not change angular velocity, tidal loading effect was not identified for the reference point neither (Figure 69).

The observed displacements at PSs on buildings at Lisbon Downtown were consistent with thermal expansion. Nevertheless, it must be noted that the displacements in the representative time series resulted from the average of displacements from structures with distinct properties and responses to temperature changes. Figure 70 presents the displacement time series for two PSs in cluster 1: one is on the roof of Rossio train station and the other is on the roof of a Pombalino building. Both presented oscillatory behaviour consistent with thermal expansion, but the effect has a larger magnitude at Rossio station, perhaps due to the different materials of the roofs.

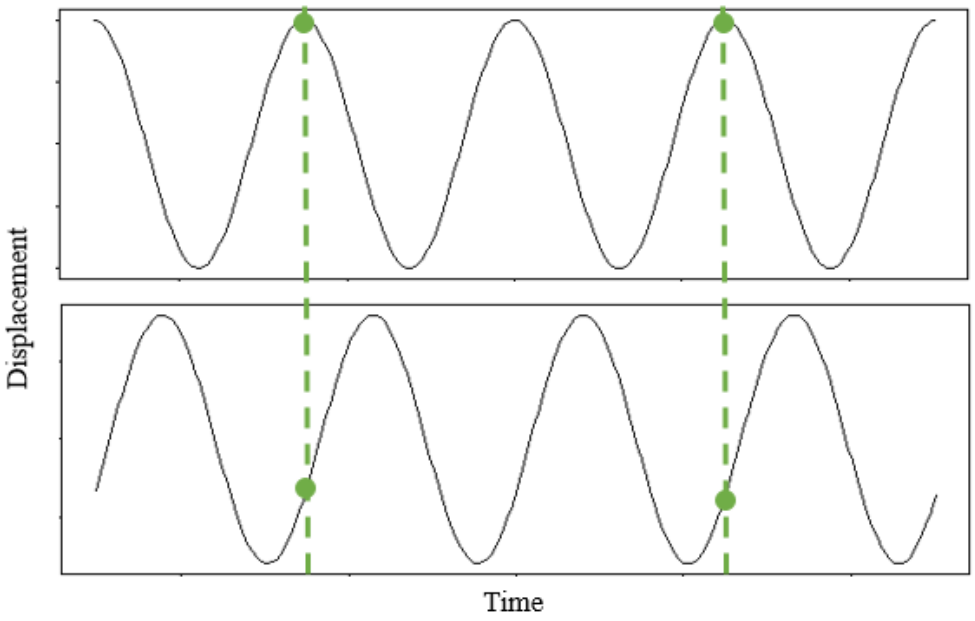

Figure 69 – Simulation of tidal loading effect at a PS in the Downtown (top) and at the reference point (bottom) with a delay with respect to the Downtown; green dashes represent the SAR observation epochs and the green circles correspond to the observed displacement component caused by tidal loading.

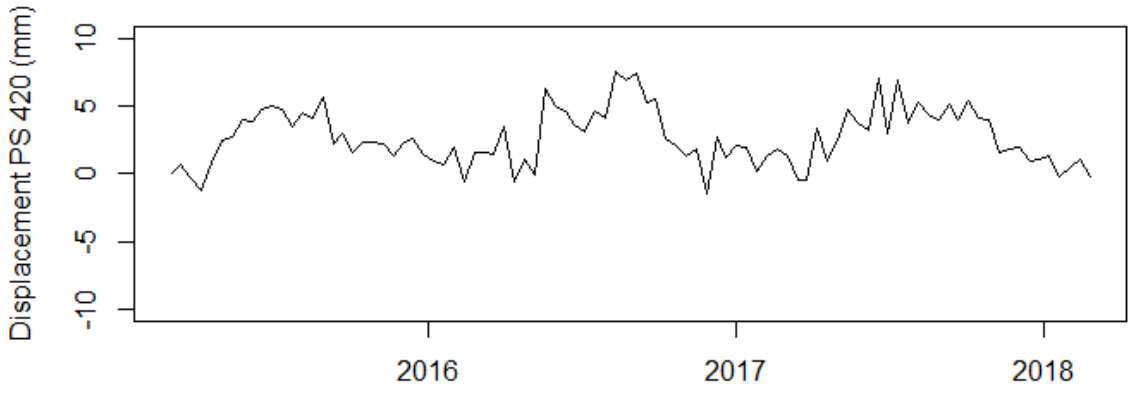

(a)

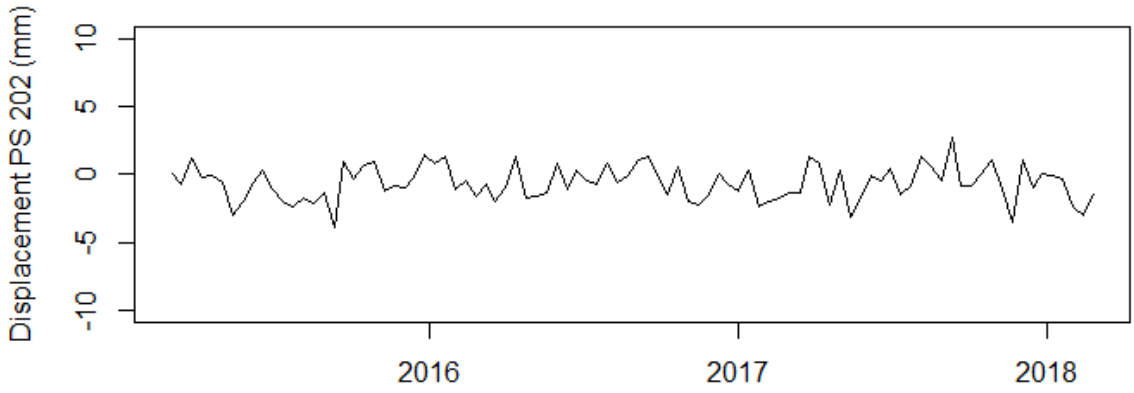

(b)

Figure 70 – Displacement time series of a PS on the roof of Rossio train station (a) and of a PS on the roof of a Pombalino building (b), both from cluster 1.

Studies by LNEC's AGU showed the west wing of Praça do Comércio, at the Downtown, has been settling at least since the 1950s (LNEC, 2017a). The settlements presented increasing magnitude towards the river, reaching its maximum value at the tower at the southernmost part of the building. Several PSs were identified on the building, including on the tower; however, those PSs were all included in cluster 1, which was the one with the most stable vertical behaviour. Levelling data along the building showed the closest benchmark to the river settled 2.3 mm between September 2015 and September 2017 with respect to a benchmark at the northernmost part of the building (LNEC, 2017a). In case the settlement rate was constant during the three years of this study, the point may have settled around 3.4 mm, which was consistent with the point inclusion in cluster 1, in case there were no relative displacements between the levelling and the PSI reference points. As there were no PSs near the levelling reference point, it was not possible to verify the existence of relative displacements between them.

3.6 Conclusions

In this Chapter, a method to automatically identify distinct displacement patterns on structures, based on PSI displacement time series, was proposed and its efficiency was evaluated for anomaly detection at both geotechnical and civil structures. The method proved to be independent of prior knowledge about the problem being evaluated, relying only on the displacement time series achieved through the PSI processing. However, the optional inclusion of additional information describing the ROI was helpful to the results' interpretation, providing clues about the potential causes of the detected behaviour anomalies. The usage of an unsupervised method for time series analysis like clustering, allied to a hierarchical aggregation strategy, led to an objective evaluation of the displacement time series. Although an automatic clustering solution was always provided, which presented the distinction of important patterns, e.g. between regular PSs and those affected by unwrapping errors, it was verified that the automatic solution may not conduct to the isolation of the eventual anomalies. In those situations, an increase in the number of clusters to be analysed, informed by data as linkage distances and dendrograms, enabled the detection of the wanted patterns. Complete linkage proved to be an adequate choice for aggregation method, as it enabled the construction of compact clusters, yet being sensitive to outlier detection. DTW may not be the optimal choice for dissimilarity measure for time series as long and noisy as those typically achieved through PSI; however, the pre-processing and the parameter choices executed minimised the limitations of the technique and led to its successful application for two case studies of distinct natures. The whole procedure was integrated at a computer tool, developed in R, and expert knowledge on InSAR or time series analysis was not required to operate it. The tool may be useful

for decision-makers in charge of monitoring of large urban or rural areas. The issue of early-warnings using the tool needs to be carefully managed, perhaps requiring the analysis of smaller segments of the original displacement time series. The spatio-temporal information of the anomalies provided by the tool may help the planning of other monitoring activities, such as visual inspections or *in situ* measurements. Computational requirements may be a hindrance for the processing of large numbers of PSs, but the growing access to on-line platforms, such as Jupyter, may solve this issue, as done in this research.

The proposed RADAR interpretation method successfully detected distinct structure behaviour for this Chapter case studies. At Odelouca slopes, the method detected movement away from the sensor, which may correspond to subsidence due to the load associated to the weight of the stored water. Those displacements began in March 2009, before the official start of the reservoir first impoundment in December that year, but right after the end of the dam body construction, when some water may have started accumulating. The clusters also revealed the eventual subsidence affected different regions of the ROI at different epochs, with the phenomenon evolving from southwest to northeast, accompanying the water route. At Lisbon Downtown, centimetre-level displacements were detected on buildings on the neighbourhood of the subway line and on steep slopes. Nevertheless, by the end of the considered time interval, in February 2018, there were no more signs of anomalous displacements.

In conclusion, the method proposed for RADAR interpretation of PSI displacement time series was successfully used to identify behaviour patterns in both geotechnical and civil structures.

Chapter 4. Integration of InSAR displacements in structure monitoring systems

This chapter proposes an adaptation of the Method of Variation of Coordinates (MVC) to integrate InSAR displacements into an existing structure monitoring system. The strategy uses GNSS observations to constrain InSAR displacements along a network of object points located on both the structure and its surroundings. It enables displacement measurement at a large number of object points, which naturally exist in the terrain and do not need to be materialised, with the mitigation of some of the errors associated to InSAR observations and the determination of a posteriori variances for the adjusted displacements. The method is applied on the simultaneous monitoring of a concrete dam and its neighbour slopes.

4.1 Introduction

This section presents a literature review of studies that attempted to combine InSAR displacements with data from other techniques, in order to improve the monitoring capability of the considered techniques. Data from GNSS are often used in this type of studies, but other technologies are also employed, such as Light Detection And Ranging (LiDAR), classic surveying methods or photogrammetry (Muller *et al.*, 2015). According to Hu *et al.* (2014), the first study to consider the merging of InSAR and GNSS was Gudmundsson *et al.* (2002). They used four interferograms with a temporal baseline of one day obtained throughout one year and one GPS observation per year on several points of their ROI. Three-dimensional displacements for each pixel in the interferograms were initialized through the interpolation of east – west and north –

south GPS displacements and from the difference of two DEM (obtained from differential GPS). As displacement was assumed to be smooth in time, the initial displacements were scaled to the time interval of the interferogram with dates closer to those of the GPS observations. An optimization procedure based on the minimisation of energy functions was then applied. The optimized result for the first interferogram was then used as an initial approximation for the interferogram with the closest dates and the optimization was applied again. This procedure was repeated until all interferograms were optimized.

Other authors have also used the optimization of energy functions for this purpose. Catalão *et al.* (2011) proposed a method to merge vertical velocities derived from PSI with horizontal ones obtained from GPS. As there is a bias between PSI and GPS observations, they performed a calibration operation. The median vertical velocities of scatterers inside a 200 m neighbourhood of each GPS station and the vertical velocity from GPS were used to minimise a cost function from which the bias and differences in parameters of the ellipsoids used by both techniques were obtained. The bias was then applied to correct scatterers vertical velocities, while GPS horizontal ones were interpolated to each scatterer location. WRF[18] meteorological model was used to determine atmospheric phase delays for the dates of SAR image acquisitions, whose differences were removed from the interferograms.

Polcari *et al.* (2016) computed 3D velocity vectors derived from InSAR and GPS for the 2014 South Napa earthquake. A coseismic interferogram from Sentinel-1 images and observations from 142 GPS permanent stations were used. GPS velocities were interpolated for each scatterer through Kriging. Determining the 3D velocity vector for each pixel corresponded to find the velocity values that minimised a likelihood energy function, which depended on the interpolated GPS and on the InSAR LOS velocities. Displacement values were obtained from the velocities, whose uncertainties were 5.31 mm in north – south, 4.27 mm in east – west and 5.96 mm in the vertical components. This study was then improved in Polcari *et al.* (2017) in order to include results from POT and MAI (introduced in section 2.1). Horizontal displacements were firstly determined through POT and, although these were just approximated values, they were used to input constraints / barriers to the GPS displacements interpolation, in order to simulate discontinuities in the displacement field. InSAR, MAI and GPS observations were used to determine the 3D displacement values for each pixel through the minimisation of an energy function. Quality control was performed through the evaluation of residuals. The best fit was obtained for the vertical component with residuals of 2 cm. The second best was that of the north

[18] Weather Research and Forecasting Model https://www.mmm.ucar.edu/weather-research-and-forecasting-model

– south component with residuals varying from 2 cm to 5 cm. The worst component was east – west with residuals reaching 6 cm.

Chen *et al.* (2010) determined improved vertical velocities for a set of sparse points in Hong Kong area (Figure 71). They used tropospheric zenith wet delays (ZWD) at GPS stations to correct atmospheric effects in SAR interferograms. The differences in time of ZWD were removed from each interferogram after being projected into the SAR LOS. GPS stations and SAR scatterers were connected to each other through a Delaunay triangulation. For each connection between pairs of points and for each interferogram, differences of vertical velocity and of altitude correction between points were computed through the maximization of the temporal coherence. Weighted Least Squares (WLS) was used to determine vertical velocities and altitude corrections for each point from the differential values observed for each connection. Temporal coherence was used as a weight and GPS vertical velocities were used as constraints for the connections that have a GPS station in one of its ends.

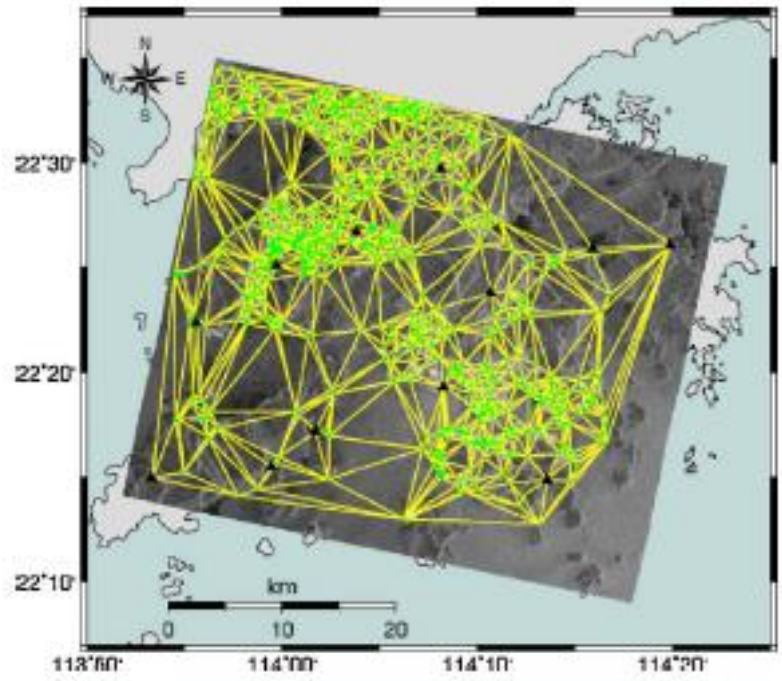

Figure 71 – Network of scatterers (green points) and GPS stations (black triangles) used in Chen *et al*. (2010).

In Guglielmino *et al.* (2011), the Simultaneous and Integrated Strain Tensor Estimation from Geodetic and Satellite Deformation Measurements (SISTEM) method to derive 3D displacement from DInSAR and GPS was presented. This method used the elasticity theory to relate an InSAR displacement and the 3D displacements of nearby GPS stations to 3D strain, rigid body rotation tensors and the 3D displacements of the scatterer. This relation was described by a linear matrix equation that was solved using WLS. The weights of each connection / equation between the scatterer and the neighbour GPS stations were computed from a function of the distance between

them. Muller *et al.* (2015) performed an adaptation of the SISTEM method in order to include other geodetic techniques besides InSAR and GPS. The authors showed an example of application using InSAR, GPS and classic surveying methods. The measurements of all techniques were converted into the same local reference frame. GPS was used at the fiducial sites (the points forming the local reference frame) and performed the connection between different clusters of points observed from the other techniques. GPS, InSAR and tacheometric measurements were all determined for each observation epoch, from which displacement time series were computed and velocities obtained. The SISTEM approach was then used to integrate the data.

Application of these combination methods to SHM is not often found in the literature. The only study identified was performed by Tapete *et al.* (2015). The authors used RTK GPS measurements for height determination on linear structures, such as aqueducts, and on the ground. Those data were utilized to determine the correct location on the structures of PSs and DSs used for displacement analysis (Figure 72), by the comparison of the heights observed for all points through both techniques, which enabled a better interpretation of the displacements and of the structure behaviour.

Figure 72 – Improved location of PSs (circles) and DSs (squares) on an aqueduct aided by RTK GPS observations; colours correspond to LOS velocity (Tapete *et al.*, 2015).

Interpolation has often been used for data integration. Hu *et al.* (2016) merged InSAR velocities from ascending and descending geometries with interpolated horizontal velocities from continuous GPS. Kriging was used to interpolate the data and WLS to perform the combination, achieving 3D displacements.

Farolfi, Bianchini, *et al.* (2019) merged vertical velocities from GNSS and InSAR in order to obtain an accurate vertical velocity map for all scatterer positions. Ascending and descending passes from Envisat were combined to obtain vertical and east – west velocity components. The velocities of scatterers within a certain neighbourhood of the GNSS stations were interpolated to

the GNSS station location. For each station, a correction value computed from the difference between the GNSS and the scatterer-interpolated vertical velocity was determined and a correction map for the whole study area was obtained from interpolation. That correction was then added to the vertical velocity of all scatterers. The results showed a good agreement between GNSS and corrected scatterer values, with velocities more accurate than those obtained only from InSAR. In Farolfi, Piombino, *et al.* (2019), this study was adapted to national scale and to consider also the east – west component of displacement.

Van Leijen *et al.* (2017) proposed the Connecting Undifferenced Points in Deformation Observations (CUPiDO), a system that intended to integrate data from several techniques: InSAR, GPS and levelling. As all techniques had different characteristics, such as measurement direction, reference points, geodetic data or uncertainties, the method used double-differences, both in space and in time, for all of them, which were then analysed together. This paper only presented an example of integration between GPS and levelling, but it is being adapted to include InSAR measurements as well.

Other authors tried to achieve 3D displacements using SAR data alone. Fuhrmann and Garthwaite (2019) attempted a WLS approach to combine LOS velocities from multiple distinct geometries to achieve 3D displacements; however, besides requiring a minimum of three acquisition geometries, the north – south velocity component was not accurately determined and its magnitude influenced the errors of vertical and east – west components.

SAR artificial reflectors have been combined with GPS to perform the merging of the data. Zhu *et al.* (2014) used triangular trihedral Corner Reflectors (CRs) for X-band to monitor displacements along a slope. GPS observations at the CRs' locations were used to compute the points' height and tropospheric correction. Those data were then used to improve the InSAR processing for the CR. GPS horizontal displacements combined with the LOS displacements from InSAR at the CR enabled the determination of vertical displacements. The three-dimensional displacements were projected onto the slope direction, in which an accuracy of 1.89 mm and a precision of 1.1 mm were achieved for the measurements.

Komac *et al.* (2015) presented a device named I2GPS which consisted of a Compact Active Transponder (CAT) together with a GNSS antenna (Figure 73). The equipment enabled the determination of improved 3D displacements for its installation location with reference to a global reference frame (e.g. ITRF2008) and the resolution of InSAR ambiguities for nearby artificial reflectors. In order to determine InSAR displacements with respect to the reference frame for all scatterers, if there was an I2GPS in the network, it was only required that GNSS LOS displacement at the I2GPS location was added to the scatterers displacement. In case there were more than one

I2GPS, an adjustment was required. Quality control was performed through the determination of the daily station repeatability, i.e. the RMSE of the station coordinates, after removing a linear trend from it. For the horizontal components, a repeatability of 2 mm to 3 mm was achieved, while 5 mm to 7 mm were obtained for the vertical direction.

Figure 73 – I2GPS unit (Mahapatra *et al.*, 2018).

Table 9 shows a summary of the procedures followed by each presented study in order to merge data obtained from InSAR and other techniques. Uncertainty measurements are presented for each case, although they are not comparable to each other as different techniques, goals and measurements have been applied. Some of the studies were focused on merging data from distinct methods in order to determine more accurate displacements along a single direction of interest to the problem under analysis, such as vertical direction, SAR LOS or a slope, but there was also interest in obtaining 3D displacements. Many studies were related to geodynamic problems, for example deformation caused by earthquakes, volcanic eruptions or tectonics, for which displacements in the order of centimetres were observed and, therefore, centimetric-level uncertainty might be acceptable. Although most strategies achieved millimetre uncertainties, there were few applications to SHM. Several strategies required a smooth displacement constraint to be used, which would make difficult its application to the simultaneous monitoring of structures and its surroundings.

Table 9 – Comparison of InSAR and GNSS merging strategies and of obtained uncertainties for different studies.

Study	InSAR technique	GNSS technique	Studied problem	Uncertainty				Strategy
				E - W	N - S	V	Other direction	
Gudmundsson *et al.* (2002)	DInSAR	Repeated GPS	Ice surface motion	14% *[1]	16% *[1]	25% *[1]	-	GPS 3D displacements were interpolated for each interferogram pixel and an optimization procedure was applied based on energy functions.
Chen *et al.* (2010)	MT-InSAR	Continuous GPS	Urban subsidence	-	-	0,15 - 0,69 mm/yr *[2]	-	Use of GPS-derived ZWD to correct atmospheric effects in InSAR. Performed WLS to determine vertical velocities using GPS observations as constraints.
Catalão *et al.* (2011)	PSI	Repeated GPS	Tectonics	-	-	1,5 - 1,6 mm/yr *[3]	-	Merge of vertical PSI velocity with horizontal GPS ones. Use of WRF meteorological data to correct vertical velocities.
Guglielmino *et al.* (2011)	DInSAR	Continuous GPS + Repeated GPS	Volcano	4 - 5 mm *[2]	4 - 5 mm *[2]	4 - 5 mm *[2]	-	SISTEM: used WLS to combine InSAR and GPS displacements with strain and rigid body rotation.
Zhu *et al.* (2014)	CRInSAR	Repeated GPS	Landslide	-	-	-	1,89 mm *[2]	Used altitude and atmospheric corrections from GPS to improve the InSAR processing at corner reflectors.
Muller *et al.* (2015)	SBAS	Repeated GPS	Volcano	-	-	-	25 mm/yr *[2]	Adaptation of Guglielmino *et al*. (2011) to include other techniques.
Komac *et al.* (2015)	CAT	Continuous GPS	Landslide	2 - 3 mm *[4]	2 - 3 mm *[4]	5 - 7 mm *[4]	-	Use of I2GPS units: a device that includes a CAT and a GNSS antenna.
Tapete *et al.* (2015)	SqueeSAR	RTK GPS	SHM			0.97 *[5]		Improve of PS and DS location through comparison to RTK GPS heights.

Study	InSAR technique	GNSS technique	Studied problem	Uncertainty				Strategy
				E - W	N - S	V	Other direction	
Hu *et al.* (2016)	SBAS	Continuous GPS	Tectonics and anthropogenic activities	0,9 mm/yr *2	1,5 mm/yr *2	2,4 mm/yr *2	-	Merge of InSAR data from two acquisition geometries with interpolated horizontal GPS velocities.
Polcari *et al.* (2016)	DInSAR	Continuous GPS	Earthquake	4,27 mm/yr *6	5,31 mm/yr *6	5,96 mm/yr *6	-	Minimised a likelihood energy function to merge InSAR velocities with interpolated 3D GPS ones.
Polcari *et al.* (2017)	DInSAR	Continuous GPS	Earthquake	6 cm *7	2 - 5 cm *7	2 cm *7	-	Use of POT to determine approximated displacements that were used to constraint GPS interpolation. Bayesian statistical approach was used to merge the GPS, MAI and the InSAR data.
Farolfi, Bianchini, *et al*. (2019)	PSI	Continuous GPS	Urban subsidence	-	-	0,95 *8	-	Determined a correction for InSAR vertical velocities based on the difference between GNSS and interpolated InSAR vertical observations.
Farolfi, Piombino, *et al*. (2019)	PSI	Continuous GPS	National scale displacements	0,94 *8	-	0,95 *8	-	Similar to the previous one, but considered east – west displacements.
Fuhrmann and Garthwaite (2019)	SBAS	-	Crustal deformation and simulated data	0.33 – 0.53 mm/yr *9	3.21 – 4.60 mm/yr *9	0.20 – 0.63 mm/yr *9	-	Combination of multi-geometry InSAR displacements through WLS

*1 Relative error
*2 RMSE
*3 Velocity interquartile range
*4 Daily station repeatability
*5 Coefficient of determination between PS+DS and GPS heights
*6 Standard deviation
*7 Residuals
*8 Correlation coefficient between corrected and GNSS velocities
*9 Mean absolute difference between computed and simulated velocities

4.2 Methods

In this section, a method for integration of InSAR and GNSS data is proposed, with the aim of including InSAR data into structure monitoring systems; thus, contributing to the operationalisation of the usage of this type of data for SHM.

The idea behind the proposed strategy is the extension of a previously existing GNSS-based structure monitoring sub-system through the inclusion of observed InSAR displacements, in order to increase the monitored area to the structure surroundings. Although critical infrastructures, e.g., dams or bridges, may be subjected to periodic monitoring through visual inspections, embedded equipment or geodetic techniques, the structure surroundings are not monitored so often through these methods, despite the importance of their stability to the structure safety conditions. The lack of monitoring at these elements may be due to the high costs associated to the surveying of such large areas, which makes InSAR a promising choice to fill this gap.

The proposed method intends to combine GNSS data from permanent stations with InSAR displacements achieved through PSI. GNSS displacements are used to constrain the PSI measurements. The combination is performed using MVC, which is a widely used technique in traditional geodetic surveys. It relates variations of the observations between two points in two epochs with the variations of those points' coordinates between the same epochs, i.e. the points' displacements, by performing an adjustment through least-squares approach (Mittermayer, 1972; LNEC, 2001, 2013; Casaca *et al.*, 2015).

In traditional geodetic surveys, MVC is applied to networks connecting points (vertices) on locations of interest. Those networks can be unidimensional, bidimensional or three-dimensional, depending on the considered type of data. Unidimensional networks are usually utilized for altimetric data, bidimensional for planimetric and three-dimensional networks deal with both altimetric and planimetric data together. Observations are affected by systematic and random errors, whether they are height differences, distances or bearings, for example. Errors can be inherent to the equipment, influenced by the environmental conditions during the observation, such as temperature or humidity, or by the operator. The equipment manufacturer usually provides information on the uncertainty associated to the observations, which can be considered as *a priori* uncertainty. The redundant observation of each vertex at the network enables part of the observations affected by errors to go to the adjustment residuals, which allows the determination of *a posteriori* uncertainties.

In this thesis, the MVC was adapted to adjust a network of GNSS stations and PSs. The proposed method considers a unidimensional network, where the three-dimensional GNSS displacements d_E, d_N, d_V (east – west, north – south and vertical components, respectively) are converted to SAR LOS direction following Equation (11) from section 3.2 and adjusted together with PSI measurements.

Let us define a unidimensional reference system, with origin at one of the network vertices, P_{ref}, LOS direction and values increasing from the ground to the SAR sensor. A vertex in the network has a coordinate L in that reference system, which is the orthogonal projection of that vertex into the defined reference system.

The proposed method is intended to be performed fully remotely and automatically, for any geographic location and for any study object, which imposes some constraints on the network design. The variables to observe for each network connection have to be achieved remotely, which eliminates common variables such as distances between the vertices. The observations between the netweork vertices are the double-differences between the L coordinates of pairs of vertices and between two epochs, which are determined according to Equation (21):

$$y = \left(L_p^i - L_q^i\right) - \left(L_p^j - L_q^j\right) \tag{21}$$

where y is the vector of observation differences, L_p^i and L_p^j are the coordinates of vertex p at epochs i and j, respectively, and L_q^i and L_q^j are the coordinates of vertex q at epochs i and j, respectively. The epochs for analysis are those of the SAR image acquisitions, with j being the reference epoch of PSI processing and also for the new method. Epoch i is any SAR image acquisition epoch, except the reference one. The terms in Equation (21) can be reorganised and it is verified that the observation differences correspond to the LOS relative displacements between vertices p and q, as in Equation (22):

$$y = \left(L_p^i - L_q^i\right) - \left(L_p^j - L_q^j\right) = \left(L_p^i - L_p^j\right) - \left(L_q^i - L_q^j\right) = d_p^{LOS} - d_q^{LOS} \tag{22}$$

where d_p^{LOS} is LOS displacement for vertex p and d_q^{LOS} is LOS displacement for vertex q between epochs i and j. This vector has as many rows as the number of connections in the network. The vector of vertex coordinate differences between epochs i and j, x, is given by Equation (23):

$$x = \begin{bmatrix} \dots \\ L_p^i - L_p^j \\ \dots \end{bmatrix} \tag{23}$$

with L_p^i and L_p^j being defined as for Equation (21). Each row in vector x is the wanted displacement for the corresponding vertex and the vector has as many rows as vertices in the network. The design matrix, A, reflects the network configuration. In order to be automatically

applicable at any situation, a Delaunay triangulation is used to connect the vertices due to its simplicity and availability on most programming packages. The design matrix is defined as in Equation (24):

$$A \cdot x = y \tag{24}$$

with x and y as previously defined in Equations (21) and (23). Matrix A has as many rows as observations, i.e., network connections defined through the Delaunay triangulation, and as many columns as vertices in the network. The matrix entries are filled with zeros, except for those corresponding to the starting and ending vertices of a certain connection, which are set to 1 and to -1, respectively. As exemplified in Equation (25), the row corresponding to the connection that starts at vertex p and ends at vertex q is filled with zeros except for the column corresponding to vertex p, which is set to 1, and the column corresponding to vertex q, which is set to -1:

$$A = \begin{matrix} & & & & p & & & & q & & \\ \begin{bmatrix} \cdots & \cdots & \cdots & \cdots & \cdots & \cdots & \cdots & \cdots & \cdots \\ 0 & \cdots & 1 & \cdots & 0 & \cdots & -1 & \cdots & 0 \\ \cdots & \cdots & \cdots & \cdots & \cdots & \cdots & \cdots & \cdots & \cdots \end{bmatrix} \end{matrix} \tag{25}$$

In order to constraint the vertices' displacements, GNSS measurements are introduced into the adjustment. The procedure requires the existence of two PSs coincident or close to two GNSS antennas. The constraint is introduced by setting the double-difference of L coordinates, i.e. the relative LOS displacements, of the PS pair equal to the double-difference of L coordinates of the GNSS antennas' pair. This is performed by adding a row to the design matrix at Equation (25), where the value 1 is attributed to the column corresponding to one of the PSs in the pair, the value -1 is set to the column of the other PS and the remaining columns present the value zero. Furthermore, a row is also added to vector y, in Equation (21), containing the relative LOS displacement between the GNSS antennas' pair, for the epoch under analysis.

The design matrix has a rank defect of one; therefore, at least one of the vertices in the network must be considered fixed or with known displacements, in order to solve the system of observation equations. Those vertices form the local reference frame of the network and the vertices' adjusted displacements are computed with respect to them. It is useful to select the vertex which is the origin of the reference system to be part of the local reference frame, as its coordinates are known (and equal to zero) at all epochs. The definition of the local reference frame is executed through matrix C, with as many rows as points in the local reference frame and as many columns as vertices in the network. The matrix is filled with zeros, except for the entries corresponding to the points in the local reference frame, which are set to 1. Equation (26) exemplifies matrix C for two vertices, s and t, to form the local reference frame:

$$C = \begin{bmatrix} & & s & & & & t & & \\ 0 & \dots & 1 & \dots & 0 & \dots & 0 & \dots & 0 \\ 0 & \dots & 0 & \dots & 0 & \dots & 1 & \dots & 0 \end{bmatrix} \quad (26)$$

The known displacements of the points in the local reference frame are defined in vector d, with as many rows as points in the local reference frame (Equation 27):

$$d = \begin{bmatrix} d_s^{LOS} \\ d_t^{LOS} \end{bmatrix} \quad (27)$$

where d_s^{LOS} is LOS displacement at point s and d_t^{LOS} is LOS displacement at point t, between epochs i and j.

Besides the deterministic component of the model, there is also a stochastic one and the observations are characterized through a covariance matrix. The matrix diagonal is filled with the *a priori* variances of the observed double-differences. Let us assume the PSI and GNSS displacements at a certain epoch follow a normal distribution (Colesanti *et al.*, 2003; Leick, 2004) and σ_p^2 and σ_q^2 are the variances of displacements of vertices p and q, respectively. Thus, given the definition of double-differences in Equation (22), the *a priori* variance for the double-difference between vertices p and q for epochs i and j (σ_{pq}^2) is determined by Equation (28).

$$\sigma_{pq}^2 = \left(\frac{\partial y}{\partial d_p^{LOS}}\right)^2 \cdot \sigma_p^2 + \left(\frac{\partial y}{\partial d_q^{LOS}}\right)^2 \cdot \sigma_q^2 = \sigma_p^2 + \sigma_q^2 \quad (28)$$

The determination of the variances of displacements of vertices p and q is performed according to the vertex nature. If it is a PS, the variance is calculated through Equation (20) in section 3.4.1. If it is a GNSS antenna, the variance is achieved from the GNSS processing. The covariances in the matrix are assumed to be zero.

The local reference frame also is attributed a stochastic component, which consists on a covariance matrix of the displacements at the points in the local reference frame. The matrix diagonal is attributed the variances of the points' displacements, which can be determined from Equation (20) or from the GNSS processing, if the points are PSs or GNSS antennas, respectively. However, the points' variances may be a value reflecting the confidence of the user in the points' stability. Thus, if there is a great confidence that the point is fixed, e.g., the point is a GNSS antenna installed at a carefully built pillar and at a stable location, a small variance can be attributed. Otherwise, if there are some concerns regarding the point stability, a larger variance must be considered. Covariances are assumed to be zero.

Let P be the inverse of the covariance matrix of the observations and Q be the inverse of the covariance matrix of the local reference frame. The adjusted displacements along LOS, $\hat{x}$, are achieved through Equation (29):

$$\hat{x} = (A^T P A + C^T Q C)^{-1}(A^T P y + C^T Q d) \quad (29)$$

where A, P, C, Q, y and d are the matrices and vectors previously defined and T is matrix transpose. Displacement variances are the diagonal elements of covariance matrix Σ_x defined in Equation (30):

$$\Sigma_x = (A^T P A + C^T Q C)^{-1} \quad (30)$$

This procedure is performed iteratively for all SAR image acquisition epochs, except the reference one, and it provides adjusted displacement values for all vertices in the network and their respective *a posteriori* variances.

For a geodetic network to be admissible, it must fulfil precision and robustness criteria (LNEC, 2001). Precision evaluation for unidimensional networks is performed through error intervals, which depend on the distribution of displacement errors for each network vertex, independently of the other vertices. The error interval is defined, for a certain level of significance, α, as the interval]-q, +q] for which the probability of the displacement error to be inside it is (1-α), as in Equation (31), adapted from LNEC (2001):

$$P(-q < N(0, \sigma_L^2) \leq +q) = 1 - \alpha \quad (31)$$

where P is probability, q is the quantile of probability $\left(1 - \frac{\alpha}{2}\right)$, $N(0, \sigma_L^2)$ is the normal distribution of the displacement error with zero mean and variance equal to the variance of the vertex L coordinate. LOS displacement between epochs i and j at a vertex p (d_p^{LOS}) is written as in Equation (32):

$$d_p^{LOS} = L_p^i - L_p^j \quad (32)$$

where L_p^i and L_p^j are the L coordinates of vertex p in epochs i and j, respectively. From the law of variance-covariance propagation, assuming L_p^i and L_p^j follow normal distributions and that the variance of L coordinate at vertex p is equal for all epochs, the variance of adjusted LOS displacement $\left(\sigma_{d_p^{Los}}^2\right)$ is given by Equation (33):

$$\sigma_{d_p^{Los}}^2 = \left(\frac{\partial d_p^{LOS}}{\partial L_p^i}\right)^2 \cdot \sigma_{L_p^i}^2 + \left(\frac{\partial d_p^{LOS}}{\partial L_p^j}\right)^2 \cdot \sigma_{L_p^j}^2 = 2 \cdot \sigma_{L_p}^2 \quad (33)$$

with $\sigma_{L_p^i}^2$ and $\sigma_{L_p^j}^2$ being the variances of L coordinates at epoch i and j, respectively, and $\sigma_{L_p}^2$ being the variance of L coordinate at any epoch. As $\sigma_{d_p^{Los}}^2$ is known for all vertices from the network adjustment, the variance of the L coordinate can be computed through Equation (34):

$$\sigma_{L_p}^2 = \frac{1}{2} \cdot \sigma_{d_p^{Los}}^2 \quad (34)$$

The amplitude of the error interval (q) is then compared to a tolerance value, defined by the user. The network fulfils the precision requirements if the amplitude of the error interval is lower than the tolerance value for all vertices.

The robustness analysis evaluates the capability of the network to detect systematic and gross errors at the observations and to send them to the adjustment residuals. A network robustness is assessed through the local redundancy numbers, associated to each observation (L coordinate double-difference). Let A* be the matrix which results from adding the rows from matrix C to matrix A, as in Equation (35):

$$A^* = \begin{bmatrix} A \\ C \end{bmatrix} \tag{35}$$

P* is the inverse matrix of the observations covariance matrix, which results from adding a block with the local reference frame covariance matrix (Q) to the original observations covariance matrix (P), as in Equation (36):

$$P^* = \begin{bmatrix} \ddots & 0 & 0 & & & \\ 0 & \sigma^2_{pq} & 0 & & 0 & \\ 0 & 0 & \ddots & & & \\ & & & \sigma^2_{d_s^{Los}} & 0 & 0 \\ & 0 & & 0 & \ddots & 0 \\ & & & 0 & 0 & \sigma^2_{d_t^{Los}} \end{bmatrix}^{-1} \tag{36}$$

where σ^2_{pq} is the *a priori* variance of the double-difference observed between vertices p and q, as in Equation (28), $\sigma^2_{d_s^{Los}}$ and $\sigma^2_{d_t^{Los}}$ are the variances of the LOS displacements at the vertices s and t, respectively, that form the local reference frame. C^{*-1} is the variance matrix of the error vector and it is determined through Equation (37):

$$C^{*-1} = A^{*T} \cdot P^* \cdot A^* \tag{37}$$

The above mentioned matrices are used to define matrix U as in Equation (38):

$$U = A^* \cdot C^{*-1} \cdot A^{*T} \cdot P^* \tag{38}$$

Local redundancy numbers are the elements in the diagonal of matrix I – U, where I is the identity matrix. A network is admissible regarding robustness when the average of local redundancy numbers is above a threshold, e.g., 0.60, and its standard deviation is below another threshold (0.10). If a network is admissible regarding robustness, the quality of the observations can be evaluated to verify the presence of gross or other unexpected errors. The quality control is performed through a hypothesis test, based on the adjustment residuals (LNEC, 2001), which are determined through Equation (39):

$$\delta = A^* \cdot \hat{x} - y^* \tag{39}$$

where δ are the residuals, A^* is as defined in Equation (35), $\hat{x}$ is as defined in Equation (29) and y^* is the vector of observation differences after adding lines corresponding to the known displacements of the vertices in the local reference frame. The test statistic, v, is computed through Equation (40), with δ and P^* as defined in Equations (39) and (36), respectively, and T being the transpose.

$$v = \delta^T \cdot P^* \cdot \delta \tag{40}$$

The test statistic follows a central qui-squared with degrees of freedom equal to the difference between the number of observations (including the local reference frame) – m – and the number of vertices – n. Let the null hypothesis H_0 be: "The observations fulfil the quality criteria" against the alternative hypothesis H_A: "The observations are affected by gross or unexpected systematic errors". The null hypothesis is accepted, for a level of significance, α, if the value of the test statistic is inside an acceptance region, which corresponds to the interval [0,q], where q is the quantile of probability (1 – α) of a central qui-squared with (m – n) degrees of freedom. On the other hand, H_0 is rejected and H_A is accepted in case the test statistic belongs to the interval]q,+∞[.

4.3 Application to case study

4.3.1 Description of study area

The method proposed in section 4.2 was tested for displacement measurement at Baixo Sabor dam and the slopes around its reservoir, located in Torre de Moncorvo municipality, Bragança district, in the northeast of Portugal. This dam was chosen as case study because its geodetic monitoring system includes a GNSS monitoring sub-system, which makes it appropriate for the implementation of the proposed strategy.

Baixo Sabor is a concrete arch dam, located at Sabor River, which is a tributary of Douro River (Figure 74). The dam is 123 m high above its foundation and its crest is 505 m long (LNEC, 2017b). Baixo Sabor dam is part of Baixo Sabor hydroelectric scheme, which also includes Feiticeiro dam, located 9 km downstream of Baixo Sabor. The scheme is expected to produce an average of 444 GWh of energy per year. Baixo Sabor reservoir alone can store a volume of 630 hm^3 and occupies an area of 2820 ha, when it reaches its full storage level (Grupo Cimpor, 2020).

Figure 74 – Baixo Sabor concrete arch dam (LNEC, 2017b).

Baixo Sabor dam is operating since 2016. Being a recently built dam, it is regularly monitored through embedded equipment. The geodetic monitoring system is composed by three parts. The altimetric monitoring sub-system considers five precision levelling lines, one on the dam crest and the remaining ones at the visiting galleries. The planimetric monitoring sub-system is formed by three traverses at visiting galleries. The number of object points in each levelling line / traverse varies with the crest / visiting gallery extension and the reference points are located at rock massifs (LNEC, 2016). Finally, the GNSS monitoring sub-system comprises three GNSS antennas on the dam crest and a reference antenna at a stable location on the banks (Figure 75). Displacements at the dam antennas are computed with respect to the reference one, in relative mode. The GNSS equipment is formed by Leica GMX902 GNSS receivers, which operate together with GNSS Leica AR20 antennas equipped with conic protections. The three crest antennas are located close to plumb lines (named FP), with one of the antennas being close to the crest centre (FP3M) and the other two being one at the structure left side (FP2M) and the other at the right side (FP4M). The two lateral antennas are installed on pillars built on purpose, while the central one is on the cover of the floodgate control building. The reference antenna (REFM) is installed on the right bank, on a pillar purposefully built. The reference antenna is located around 500 m away from the dam at an altitude 270 m higher than the dam crest, as this structure was required to be located at a stable location and with good visibility to the satellites (LNEC, 2017b). Data from all GNSS stations are collected and processed automatically. The used software is Spider, from Leica Geosystems, and hourly solutions are continuously

computed, being low-pass filtered with a moving average in order to reduce displacement uncertainty while keeping the large observation frequency (LNEC, 2018).

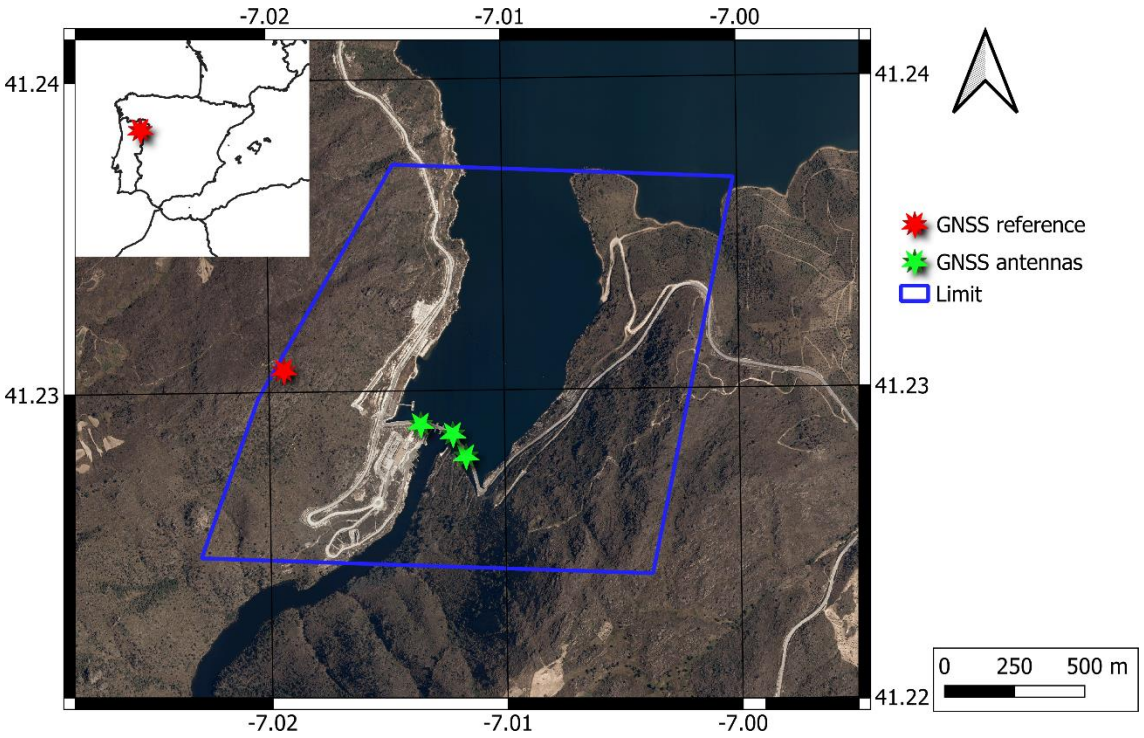

Figure 75 – Location of GNSS antennas on the dam and its vicinity; blue polygon identifies the area for analysis. Background images are optical orthophotographs (2018) provided by the Portuguese General Directorate of the Territory through GINS. Coordinate grid in WGS84.

The ROI for the method application is a neighbourhood of the dam with an area of 2 km^2, which includes the GNSS reference antenna and the slopes facing the reservoir. The main lithology inside the ROI is granite, from three distinct types: Granite of Estevais – Cabanas de Baixo, Granite of Amêdo – Estação de Larinho and Granite of Zêdes – Cabeça Boa – Especiarias. Desejosa Formation, composed by phyllites interbedded with metagraywackes and meta-quartz wackes, is also represented. Furthermore, there are also some veins of quartz and aplite (Figure 76). Slope inclinations are large, between 30º and 40º and the valley is asymmetric, suggesting the occurrence of rockslides of granite blocks at the left bank in the past (Sousa, 2011).

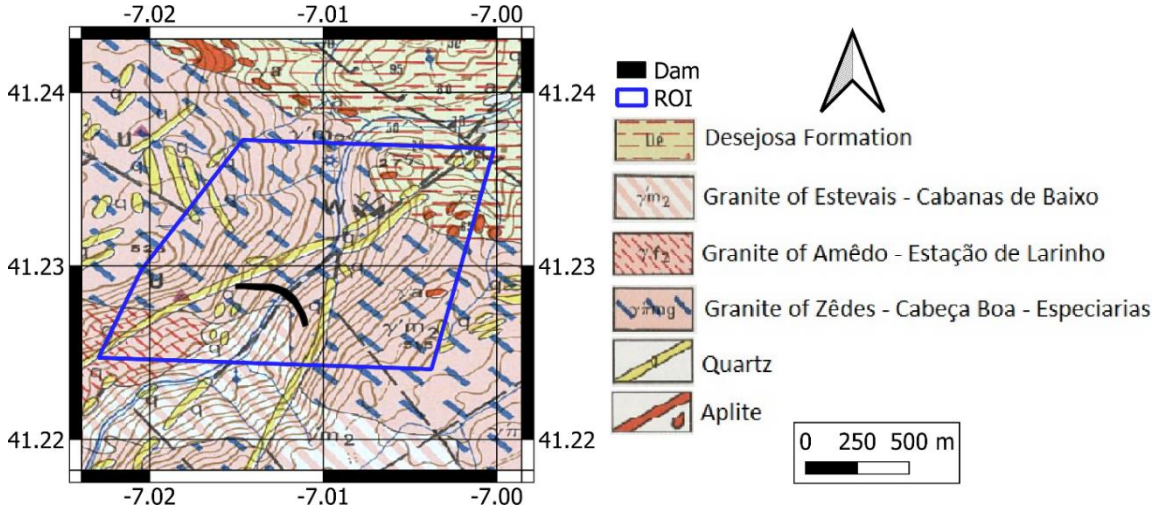

Figure 76 – Map of the geological formations at Baixo Sabor ROI, from the geological map by the National Laboratory for Energy and Geology, at 1:50000 scale. Coordinate grid in WGS84.

4.3.2 PSI processing

The time interval considered in this study were the two first years of operation of the GNSS monitoring sub-system, between June 2016 and May 2018. During this time interval, the first impoundment of the reservoir was already concluded and there were only small magnitude cyclic variations in the water level.

The images used in the study were from SAR-C sensor on board of Sentinel-1A satellite, in IW swath mode, from the descending pass with relative orbit 52 and a revisit period of 12 days. The dataset presented a single gap on the image acquisition, which corresponded to 59 scenes available for the PSI processing (Figure 77). The ROI was located at subswath 2 and corresponded to an incidence angle of 38.3º. The satellite heading was of 191º. The scenes were provided in SLC format. The DEM used in the processing was the EU-DEM, like for the case studies evaluated in Chapter 3.

InSAR displacements for the study were computed through the PSI processing implemented in SARPROZ© software (Perissin *et al.*, 2011). An area of 14 km x 14 km, centred at the dam, was selected for the analysis and the scene acquired in June 7, 2017 was selected as master image, since it minimised normal and temporal baselines. Slave images were coregistered with respect to the master geometry. A GCP was manually chosen to align the SAR data with the DEM, which was used to remove flat Earth and topographic components of phase. Similar to the procedures followed in Chapter 3, APS was removed from phase, from which residual height and cumulative displacements were estimated for each candidate to PS, based on a non-linear displacement model. As the dam was expected to display seasonal displacements and the

slopes, in case of eventual instability, might present discontinuities in their displacement time series, the usage of a non-linear displacement model was more appropriate for the analysis than a linear one. Scatterers with temporal coherence greater or equal to 0.9 were considered as PSs. Displacements were referred to a reference point outside of the reservoir area of influence, located 3.7 km downstream of the dam. Displacement time series along LOS were achieved for all 59 epochs.

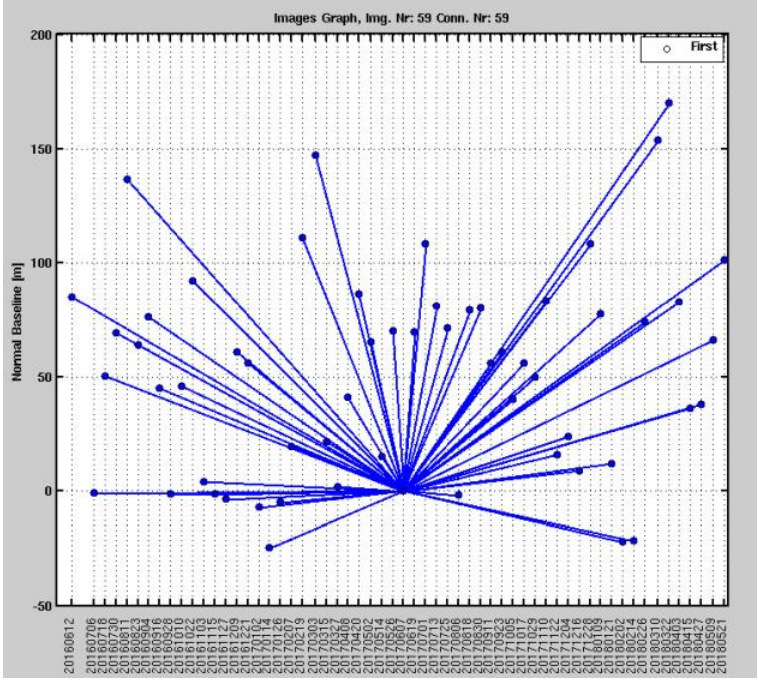

Figure 77 – Distribution of normal and temporal baselines for the SAR images available for Baixo Sabor ROI.

4.3.3 Network analysis

The network analysis proposed in section 4.2 was implemented in R software (R Core Team, 2018) and tested using the PSI displacements achieved through the procedure followed in the previous section. PSI displacements for each PS were determined for the 59 epochs of SAR image acquisition and the first observation epoch (June 12, 2016) was the reference epoch for both PSI and network analysis.

A reference in space for PSI processing was also defined. A PS located close to the GNSS reference antenna, with average velocity[19] close to zero and high temporal coherence was selected and its displacement time series was removed from the displacement time series of all PSs inside the ROI. Therefore, all PS displacements became relative to the reference PS (PS_{ref}),

[19] Absolute value of the trend of a linear model adjusted to the displacement observations.

where the absence of relative motion with respect to the reference GNSS antenna was assumed. This procedure also influenced the values of *a priori* variances of the PS displacements, as the displacement variance of PS_{ref} contributed to the other PSs' displacement variances. These were determined through Equation (28) in section 4.2, where p was any PS considered for the analysis and q was PS_{ref}.

The GNSS reference antenna was selected to be the origin of the reference system defined in section 4.2, which implied that coordinate L of this point was zero for all SAR scenes' acquisition epochs to be analysed.

In this research, the minimum constraint solution was considered, in which the GNSS reference antenna was the single point at the local reference frame. The constraint introduced in the network by attributing a GNSS baseline to a pair of PSs located close to the GNSS antennas was added. PS_{ref} and a PS close to the GNSS antenna FP2M, at the left part of the dam crest, were selected as the PS pair and the relative displacements between the GNSS reference antenna and FP2M, after being filtered by a weekly moving average and projected to SAR LOS, were attributed to the PS pair.

These implementation choices were reflected in the definition of the matrices and vectors mentioned in section 4.2. Matrix C (Equation 26) was formed by a single row, filled with zeros, except for the entry corresponding to the GNSS antenna, which was set to 1. Vector d (Equation 27) turned into a scalar value corresponding to the displacement of the GNSS reference antenna for the epoch being analysed in that iteration. As the point was the origin of the reference system, this value was zero for all epochs. The covariance matrix of the local reference frame (Q^{-1}) turned into a scalar value, which corresponded to the variance of the displacement of the GNSS reference antenna. This value reflected the confidence the user had in the point stability. In this case, as the antenna was installed on a pillar purposefully built and located at a place considered stable by geotechnical experts, a small variance was attributed (0.01 mm^2). This variance was also considered for determining the variances of the double-differences in which the GNSS reference antenna was at one of the connections' extremities in order to build the covariance matrix of the observations.

This procedure was performed iteratively for 58 SAR image acquisition epochs and enabled the determination of adjusted LOS displacement time series for all network vertices and their respective variances.

The precision analysis of the network required the definition of a tolerance value to compare to the amplitude of the error interval. A tolerance of 4.0 mm was considered. A level of significance of 0.05 was used.

4.3.4 Displacement analysis

The adjusted displacements and respective variances can be used to retrieve information on the dam and slope behaviour. In the case of the dam, it is usual to consider three directions of interest for displacement monitoring: vertical, radial (perpendicular to the dam surface) and tangential (tangent to the dam surface). However, a single SAR geometry like the one used in this study (descending pass) does not enable the determination of three-dimensional displacements. Therefore, a sensitivity analysis of the LOS direction with respect to the directions of interest for the dam monitoring may be useful in order to improve the interpretation of the LOS adjusted displacements.

In this research, positive vertical displacement corresponded to upward movement, positive radial displacement was movement towards upstream and positive tangential displacement was movement from the right to the left bank. Sensitivities were determined through the partial derivatives of LOS displacement with respect to displacements along the directions of interest. Let θ be the incidence angle, α_h be the satellite heading, λ be the azimuth of the direction perpendicular to the direction of interest on the horizontal plane, δ be the azimuth of the tangential direction at a certain point on the dam, d_{LOS} be the adjusted LOS displacement, d_H be the horizontal component of displacement along a direction of interest, d_v, d_r and d_t be the vertical, radial and tangential displacement components, respectively. According to Dentz *et al.* (2006), displacement along a direction of interest at the horizontal plane can be related to Easting, d_E, and Northing, d_N, displacement components through Equations (41) and (42):

$$d_E = d_H \cdot \cos\lambda \tag{41}$$

$$d_N = -d_H \cdot \sin\lambda \tag{42}$$

Replacing Equations (41) and (42) in Equation (11) from section 3.2, Equation (43) was achieved, assuming all horizontal displacement occurred along the direction of interest on the horizontal plane:

$$d_{LOS} = d_v \cdot \cos\theta - d_H \cdot \sin\theta \cdot \cos(\lambda - \alpha_h) \tag{43}$$

If the direction of interest on the horizontal plane was the direction radial to the dam at a certain point in the structure, $\lambda = \delta - \pi$ and d_{LOS} was given by Equation (44):

$$d_{LOS} = d_v \cdot \cos\theta + d_r \cdot \sin\theta \cdot \cos(\delta - \alpha_h) \tag{44}$$

In case the direction of interest on the horizontal plane was the direction tangent to the dam at a certain point in the structure, $\lambda = \delta - \frac{\pi}{2}$ and d_{LOS} was given by Equation (45):

$$d_{LOS} = d_v \cdot \cos\theta - d_t \cdot \sin\theta \cdot \sin(\delta - \alpha_h) \tag{45}$$

Therefore, from the stated above, sensitivities to the directions of interest for dam monitoring were determined through Equations (46 – 48):

$$S_v = \frac{\partial d_{LOS}}{\partial d_v} = \cos\theta \tag{46}$$

$$S_r = \frac{\partial d_{LOS}}{\partial d_r} = \sin\theta \cdot \cos(\delta - \alpha_h) \tag{47}$$

$$S_t = \frac{\partial d_{LOS}}{\partial d_t} = -\sin\theta \cdot \sin(\delta - \alpha_h) \tag{48}$$

where S_v, S_r and S_t were the sensitivities of LOS direction to vertical, radial and tangential directions, respectively. This analysis was limited to PSs located on the dam crest, which were identified through their planimetric location on an optical satellite image and by applying a threshold on altitude.

Regarding the slopes' behaviour, it was assumed displacement occurred along the slope direction, which enabled the estimation of the displacement magnitude in that direction through a projection of LOS adjusted displacements. Let s_{un} be the unit vector of the slope direction and l_{un} be the unit vector of the LOS direction. Positive values of s_{un} were in the uphill direction and positive values of l_{un} were in the satellite direction. The vectors were defined as in Equations (49 – 50):

$$s_{un}=[-\cos(\varepsilon).\sin(\alpha)\ -\cos(\varepsilon).\cos(\alpha)\ \sin(\varepsilon)]^T \tag{49}$$

$$l_{un}=[-\sin(\theta).\cos(\alpha_h)\ \sin(\theta).\sin(\alpha_h)\ \cos(\theta)]^T \tag{50}$$

where ε was the slope inclination, α was the slope orientation, θ and α_h were defined as for Equation (43). Slope inclination and orientation could be determined from a DEM through a GIS software. In this case, ArcGIS© was used to compute the slope properties from the EU-DEM. Similar to Chapter 3, the slope attributed to a certain pixel was the largest slope observed between that pixel and its neighbours. Slope orientation was provided through an aspect image, which indicated each pixel orientation, increasing clockwise from the north. Displacement along the slope direction, d_{slope}, with positive values in the uphill direction, was determined through Equation (51), following Schlögel *et al.* (2015):

$$d_{slope} = \frac{d_{LOS}}{s_{un} \cdot l_{un}} \tag{51}$$

where d_{LOS} was as previously defined and the symbol $(\cdot)$ represented the inner product between two vectors. Assuming d_{LOS} followed a normal distribution (Colesanti *et al.*, 2003), the variance of displacement along the slope was determined from the variance of adjusted LOS displacements through the law of variance-covariance propagation, as in Equation (52):

$$\sigma^2_{d_{slope}} = \frac{\sigma^2_{d_{LOS}}}{(s_{un} \cdot l_{un})^2} \tag{52}$$

with $\sigma^2_{d_{slope}}$ being the variance of displacement along slope and $\sigma^2_{d_{LOS}}$ being the variance of displacement along LOS.

This procedure was repeated iteratively for all SAR acquisition epochs, except for the reference one (58 iterations), originating time series of displacement along the slope direction for each vertex in the network and the displacement variances.

The number of network vertices on the slopes might be large; thus, the visual inspection of the slope displacement time series might be subjective and time consuming. In order to better identify the behaviour patterns on the reservoir banks, the slope displacement time series were evaluated through the RADAR interpretation method proposed in Chapter 3. The 1D version of the algorithm was applied to the slope displacement time series, which were clustered using the complete linkage aggregation method.

4.4 Results

This section presents the results achieved through the application of the proposed network analysis to integrate PSI data into the GNSS monitoring sub-system for Baixo Sabor dam and surrounding slopes.

4.4.1. PSI processing enabled the detection of 24501 PSs, which resulted in a density of 125 PSs/km^2. There were gaps on the PS cover at water bodies and steep slopes, as can be observed in Annex A.2 Figure 157. Cumulative displacements varied from 80.2 mm away from the sensor to 51.3 mm towards it, with some PSs close to water reservoir presenting cumulative displacement in the order of centimetres. The reference point of the PSI processing was located 3.7 km downstream of the dam, being outside the reservoir area of influence.

4.4.2. The network analysis was restricted to a smaller region of interest, with an area of 2 km^2, which included the dam, the GNSS reference antenna and slopes facing the reservoir. There were 174 vertices in the network, from which 173 were PSs and one was the GNSS reference antenna (Figure 78). Cumulative displacement at the ROI ranged from 27.4 mm away from the sensor at the left bank to 33.1 mm towards it at the right one. The Delaunay triangulation enabled the connection of all vertices in the network, with each point belonging to at least three connections. A total of 508 double-differences were observed through this method.

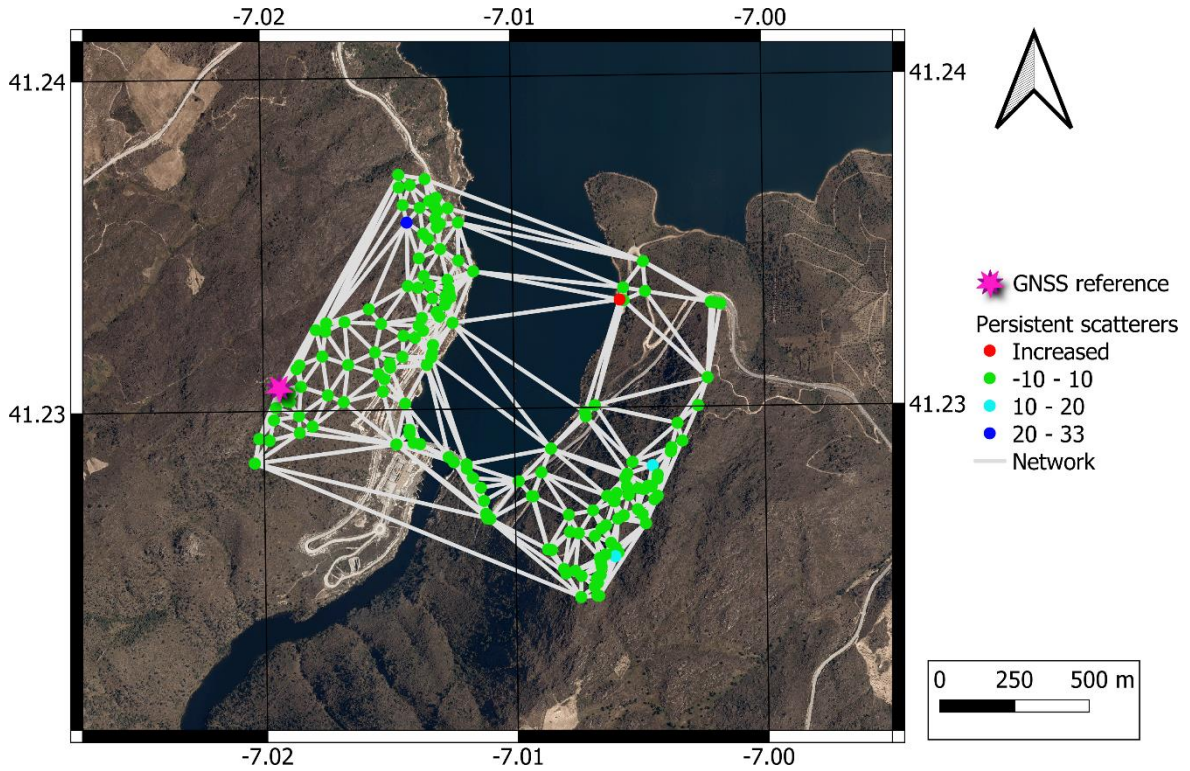

Figure 78 – LOS cumulative displacement before the adjustment for PSs in the network. Coordinate grid in WGS84.

Precision and robustness analysis were performed for the achieved network in order to verify if it complied with the requirements for network admissibility. The *a priori* LOS displacement variances were used to determine the L coordinate variances for each vertex, from which the quantile of probability 0.975 was computed for a normal distribution with zero mean and variance equal to the variance of the vertex L coordinate. The quantile corresponded to the amplitude of the error interval and it was represented for each vertex at Figure 79. The lowest amplitude of error interval was achieved for the GNSS reference antenna (0.1 mm) and those from the PSs varied from 1.9 mm to 3.3 mm. Therefore, there was a 0.95 probability of the displacement error being lower than 3.3 mm at all vertices. As all points presented amplitude of error interval below the selected tolerance of 4.0 mm, it was possible to conclude the network was admissible in terms of precision for that tolerance. The amplitudes of error interval for each vertex are in Annex A.2 Table 19.

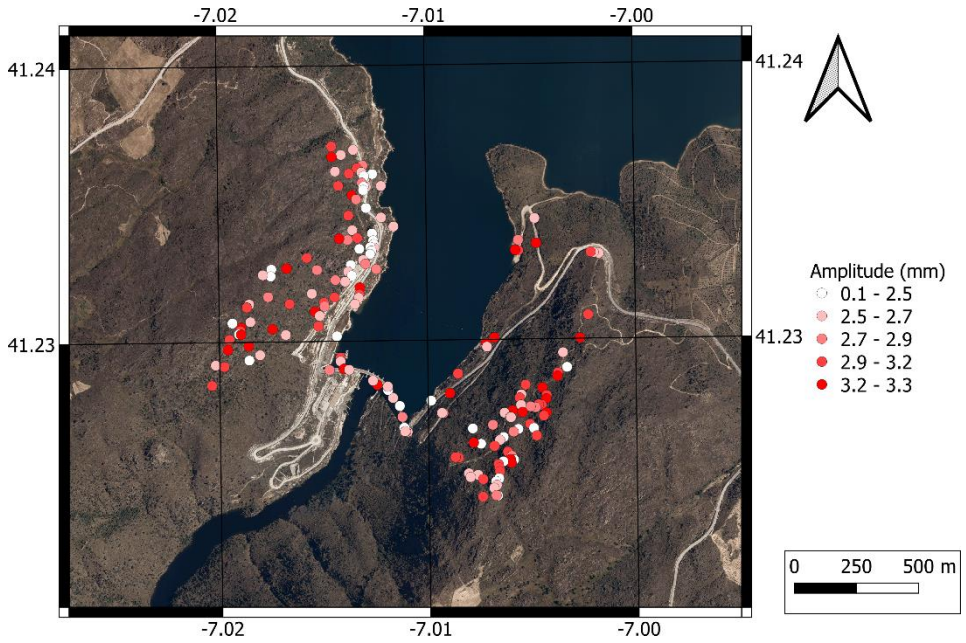

Figure 79 – Amplitude of error interval for precision analysis. Coordinate grid in WGS84.

Robustness analysis was executed based on the local redundancy numbers of each observation, which varied between 0.463 and 0.785. Figure 80 shows the local redundancy numbers were between 0.55 and 0.75, for most of the connections, with only four observations having local redundancy number below 0.5.

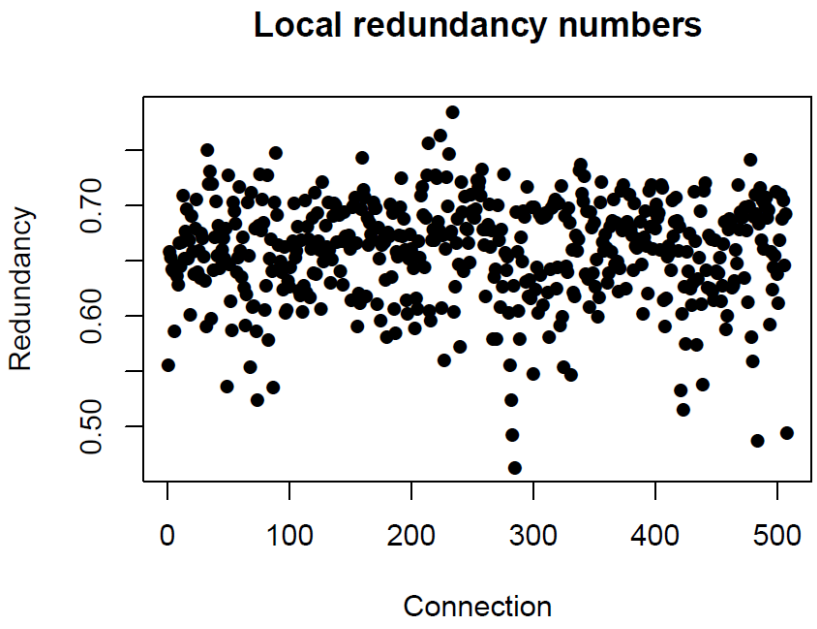

Figure 80 – Local redundancy numbers for each connection / observation in the network.

The connections with lower local redundancy numbers were located predominantly on the borders of the network (Figure 81), as usual in geodetic networks (Seemkooei, 2001). In case the observations were affected by unexpected errors, the displacement errors would probably

be concentrated in the vertices belonging to these connections. The average of local redundancy numbers was 0.66, above the threshold of 0.6, and their standard deviation was 0.05, below the threshold of 0.1. Therefore, the network fulfiled the robustness requirements and it was admissible in terms of both precision and robustness.

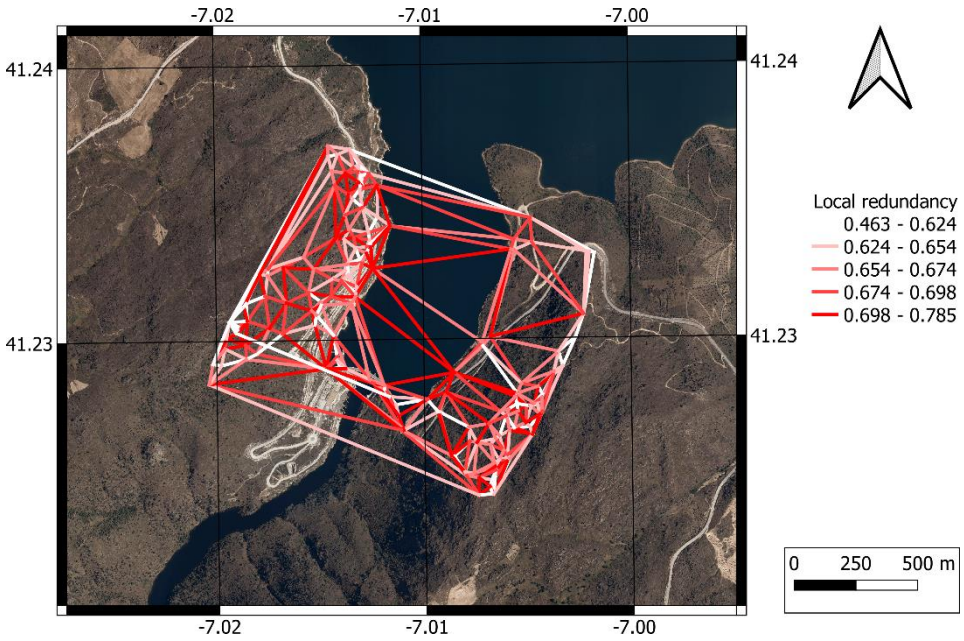

Figure 81 – Spatial distribution of the local redundancy numbers for each connection. Coordinate grid in WGS84.

As the network was robust, the quality control of the observations could be performed. The value of the quadratic form for each observation epoch is presented in Annex A.2 Table 20. The critical value considered for the analysis was the quantile of probability 0.95 of a central qui-squared with 335 degrees of freedom, which corresponds to 378.7. Values of the quadratic form were lower than the critical value at all observation epochs. Therefore, there were no gross errors at the observations and the network quality was assured.

4.4.3. After the verification of the network admissibility and of the observations' quality, the displacements achieved through the network adjustment were used for structure monitoring. There were 17 PSs on the dam crest (Figure 82). Except for a segment of approximately 100 m at the right side of the structure and close to the centre, there was a vertex around every 40 m. Cumulative displacement along LOS from original PSI technique varied between 7.2 mm away from the sensor and 5.7 mm towards it, with respect to PS_{ref} close to the GNSS reference antenna. After the network adjustment, cumulative LOS displacements presented values from 8.1 mm away from the sensor to 4.9 mm towards the sensor with respect to the GNSS reference antenna. Vertices at the dam central part tended to move away from the sensor during the two years of the

study, while vertices with displacements towards the sensor were mostly located close to the abutments. A VHR optical image from 2018 showed three vertices at the left bank abutment were PSs located on lamp posts; thus, the observed displacements did not reflect the structure behaviour and they were not further analysed.

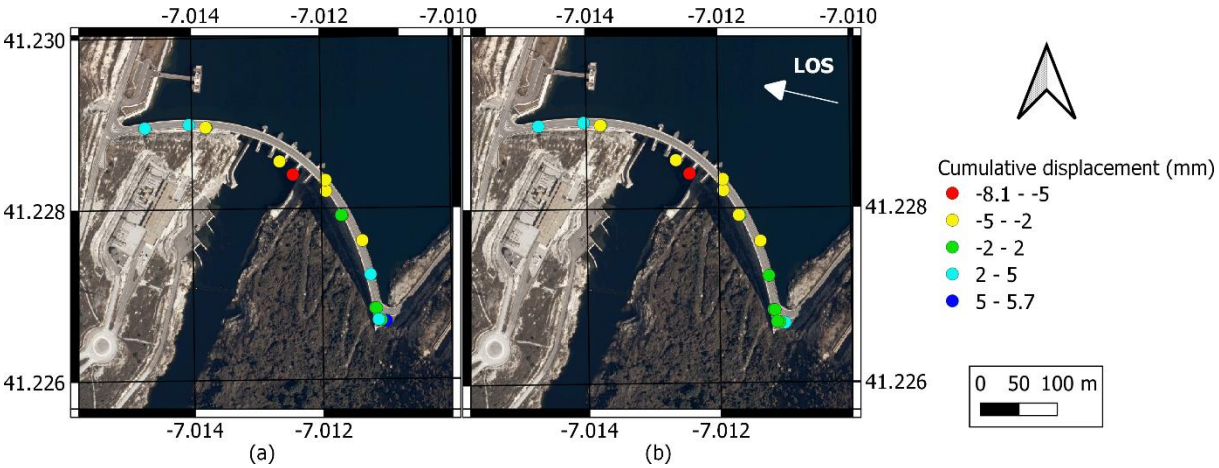

Figure 82 – Original PSI (a) and adjusted cumulative LOS displacements (b) for vertices on the dam crest. Coordinate grid in WGS84.

For a better understanding of the structure behaviour, the displacement time series of the vertices were analysed after being grouped according to their distance to the dam centre (Figure 83). The white rectangle represented zone 1, both yellow rectangles corresponded to zone 2 and both cyan rectangles presented zone 3. Vertices inside rectangles displaying the same colour were analysed together. The original LOS displacement time series are presented in Annex A.2 Figure 158 and the adjusted ones in Figure 84. The comparison between the original and the adjusted displacement time series showed that both results were similar; however, the adjusted time series were slightly noisier than the original ones, possibly due to the GNSS influence. This topic will be further addressed in section 4.5.

Zones 1 and 2 contained vertices presenting oscillations with annual period. The dam moved towards the sensor from spring to fall and away from it at the remaining part of the year. The amplitude of these oscillations was variable according to the vertices' location on the structure. While vertices in zone 1 presented an amplitude around 10 mm, for the vertices in zone 2, this parameter was of 8 mm. On the other hand, the vertices in zone 3 did not present strong oscillations, being mostly affected by noise.

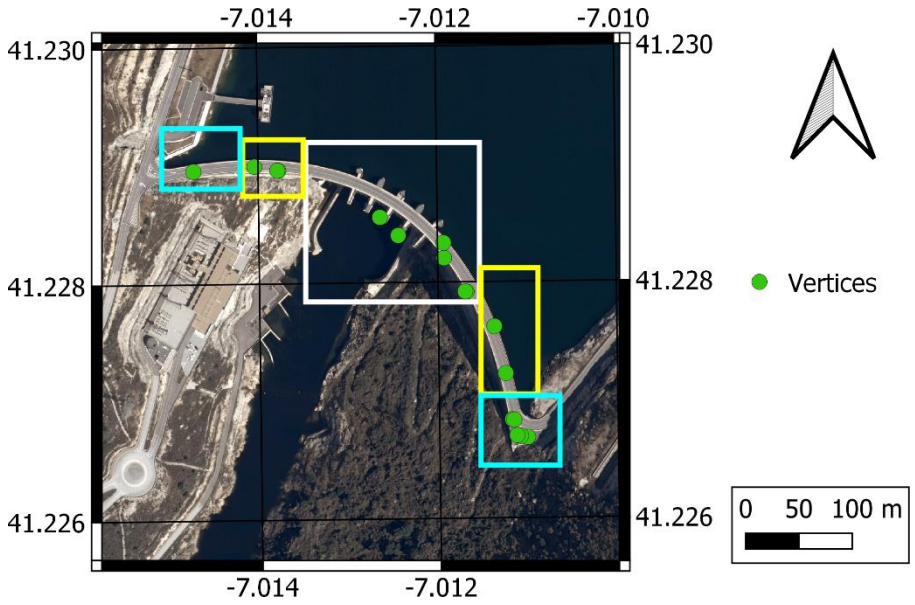

Figure 83 – Division of the dam crest into zones: zone 1 – white rectangle, zone 2 – yellow rectangles, zone 3 – cyan rectangles. Coordinate grid in WGS84.

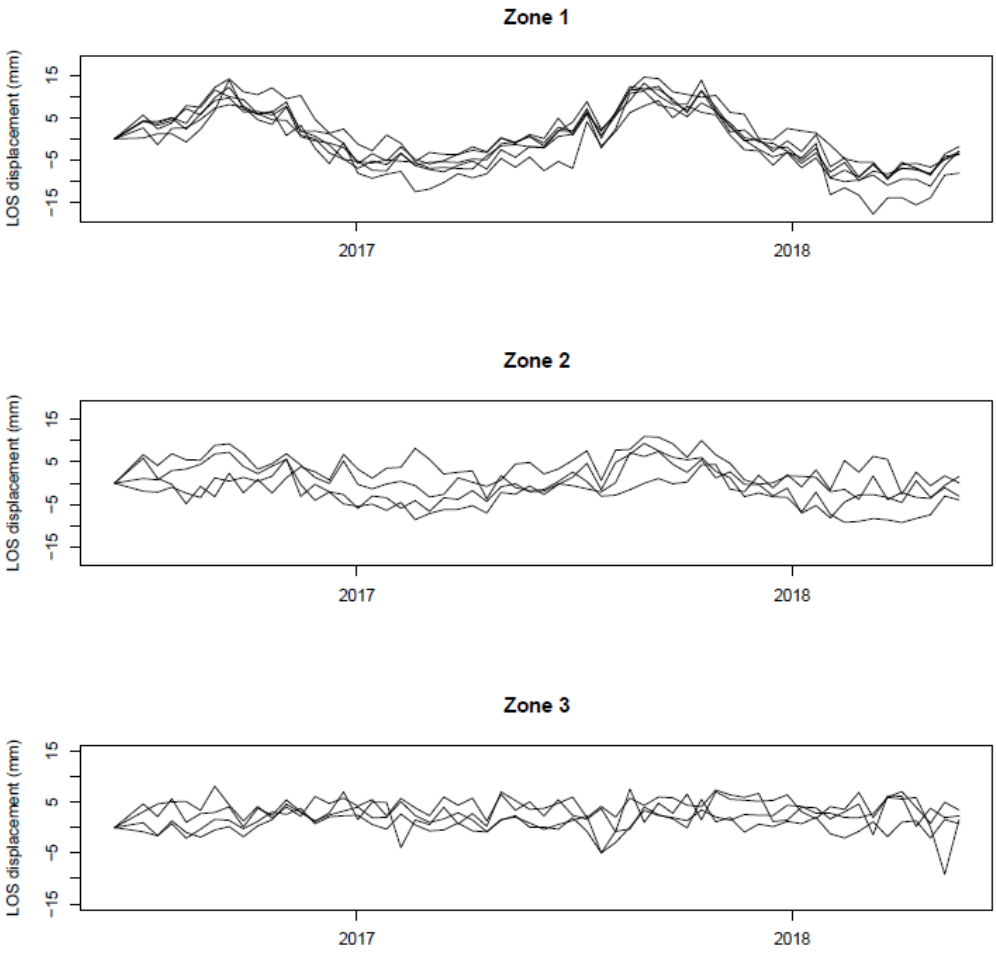

Figure 84 – Adjusted LOS displacement time series for the vertices on each zone.

Concrete dam behaviour is usually influenced by temperature and water loads. Figure 85 presents the evolution of air temperature and water level at the reservoir during the time interval

of the study. Portugal has a Mediterranean climate, with the summer being hot and dry, while winter is cold and wet. The highest temperatures are observed between July and September, while the lowest occur from December to February. At the time interval considered in this study, the first impoundment of the reservoir was already finished and only cyclic water level variations, of small amplitude, occurred. Comparing the time series from Figure 84 and Figure 85, a relationship between the seasonal displacements of vertices in zones 1 and 2 and air temperature was identified. A rise in the air temperature led to displacement towards the sensor, while a decrease in temperature conducted to displacement away from it. However, the change in displacement pattern occurred around two months after the change in the air temperature, which is known as thermal inertia and is due to the time the structure takes to react after the environmental change. This delay was according to the expected behaviour of the dam and it was also found while using other monitoring techniques, as it will be analysed later. For this particular time interval, the changes in water level did not seem to influence the dam behaviour, possibly because only small amplitude changes occurred.

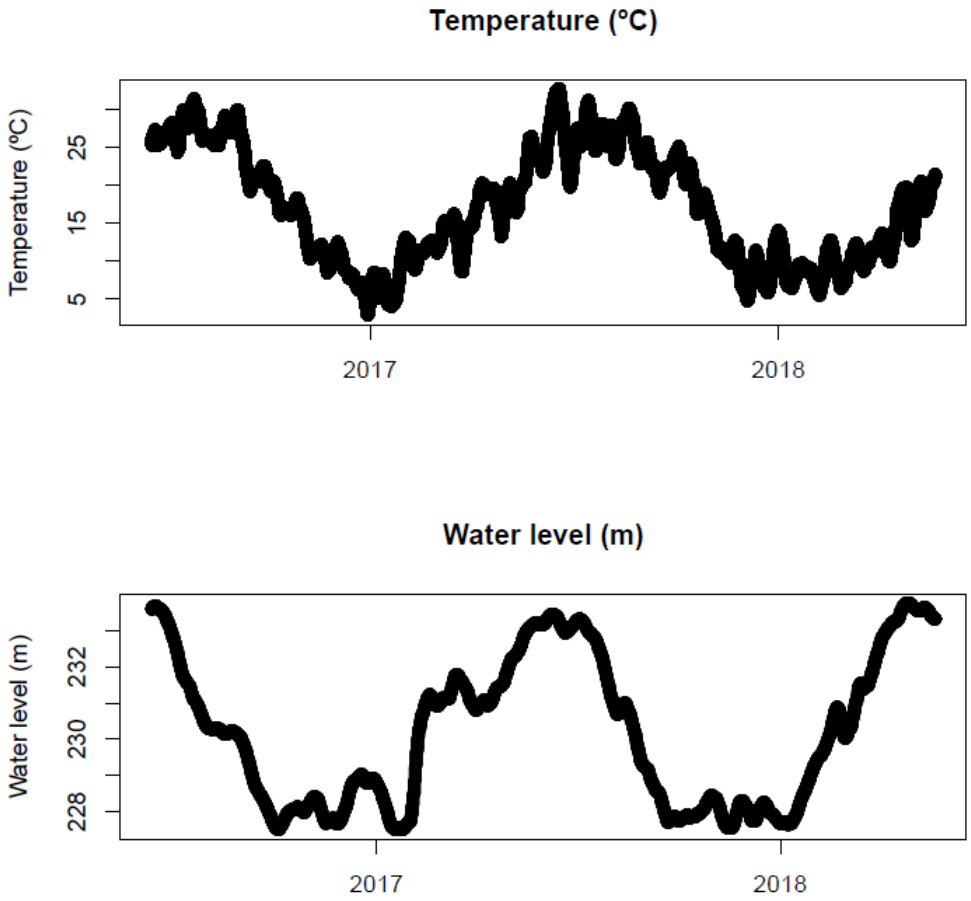

Figure 85 – Weekly moving averages of air temperature (top) and water level (bottom).

4.4.4. The adjusted LOS displacements did not enable the determination of displacements along the directions of interest for dam monitoring, but the sensitivity analysis of LOS direction with respect to the directions of interest aided in the data interpretation. Sensitivity to vertical displacements was homogeneous for the whole crest, as it depended only on the incidence angle, which could be considered constant for the dam extension. On the other hand, sensitivities to radial and tangential displacements were variable along the crest due to their relation to the azimuth of the direction of interest (Figure 86).

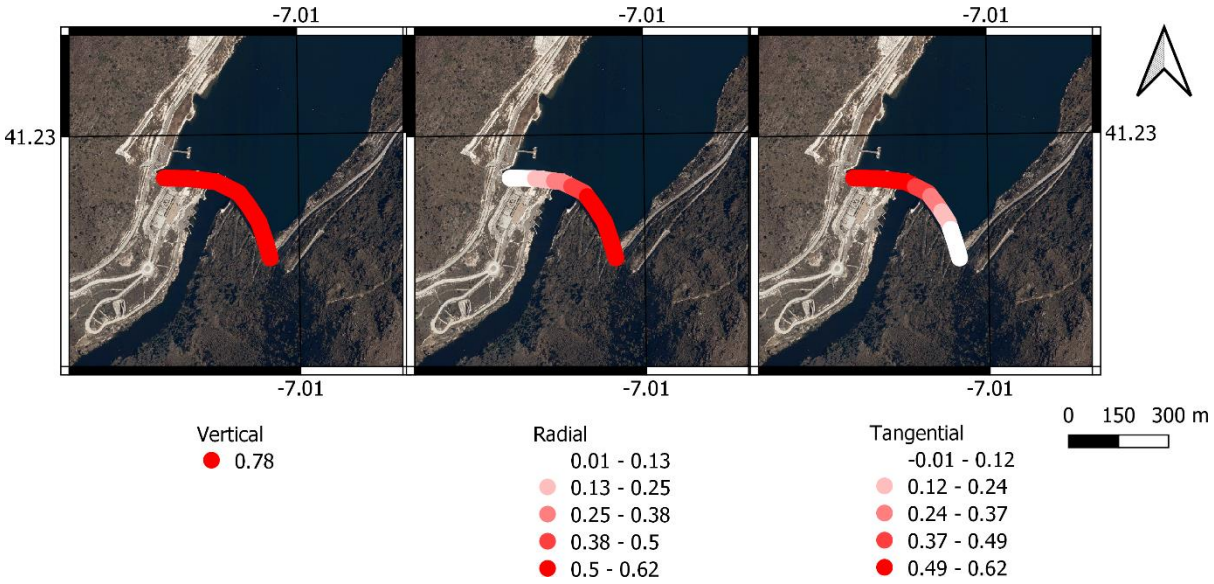

Figure 86 – Sensitivity of LOS adjusted displacements to displacements along the vertical (left), radial (centre) and tangential (right) directions of the dam. Coordinate grid in WGS84.

Sensitivity to vertical displacement presented a constant value of 0.8, which meant 1 mm of uplift at the dam was detected as 0.8 mm of displacement towards the sensor. Similarly, 1 mm of settlement corresponded to 0.8 mm of movement away from the sensor.

Sensitivity to radial displacement increased from the right bank to the left one. It was close to zero at the right bank abutment and it increased to 0.6 at the left bank abutment. The sensitivities were positive for the whole crest, which meant displacement in the upstream direction was detected as displacement towards the sensor and displacement in the downstream direction corresponded to displacement away from the sensor. Close to the right bank abutment, the sensitivity was close to zero, which meant that in case some behaviour anomaly in radial direction occurred at that area, this SAR geometry would not be able to detect it.

Sensitivity to tangential displacements had the opposite behaviour than sensitivity to radial ones. Sensitivity increased from the left bank abutment to the right one, where it reached a maximum sensitivity of 0.6. Sensitivity values were positive for almost the whole dam crest,

with only a small segment at the left bank abutment presenting negative values. For the crest extension with positive sensitivities, displacement from the right to the left bank was detected as movement towards the sensor and displacement from the left to the right bank was seen as movement away from it. At the segment with negative sensitivity, the displacement directions would be interpreted in the opposite way; however, the sensitivity magnitude was so low that, in practice, LOS displacements would not be able to detect any tangential displacement at that segment.

According to the performed sensitivity analysis, vertices in zones 1 and 2 were located at crest segments with larger sensitivity to vertical and radial displacements than to tangential displacements. Therefore, the seasonal behaviour presented in Figure 84, possibly influenced by temperature changes, might be a mixture of vertical and radial displacements. In case the detected displacement corresponded to vertical displacement, an increase in temperature would mean an uplift of the structure, while a decrease would correspond to a settlement. On the other hand, if the displacement occurred mainly in the radial direction, an increase in temperature would signify displacement towards upstream and a decrease would be movement towards downstream. According to the GNSS data, Baixo Sabor dam presented seasonal radial displacements with average amplitude around 15 mm (LNEC, 2017b), while vertical displacements did not show any clear pattern. Therefore, it was likely the seasonal displacements detected in LOS direction were mainly due to the projection of the radial displacements into the SAR geometry. In conclusion, the observed data were compatible to the dam thermal expansion.

4.4.5. The network analysis enabled the determination of *a posteriori* variances for the adjusted LOS displacements. The *a priori* standard deviations of the LOS displacements at vertices on the dam ranged from 1.5 mm to 2.4 mm. After the network adjustment, the *a posteriori* standard deviations were between 1.6 mm and 2.5 mm (Figure 87). Despite the increase in standard deviation at some vertices, there were also points where *a posteriori* standard deviation became lower than *a priori* one. Annex A.2 Table 21 displays *a priori* and *a posteriori* standard deviations for the vertices on the dam.

The displacements achieved through the network analysis were validated by comparing the adjusted displacements at a network vertex and the 3D GNSS displacements of a nearby GNSS antenna after filtered by a weekly moving average and projected to LOS (Figure 88). The points from both techniques showed similar seasonal behaviour. A Welch t test[20], which

[20] As Welch t test is extensively used in Chapter 5, it is further described there.

compares sample averages for samples with distinct variances, was used to compare the original PSI and the adjusted displacements to the GNSS data (Welch, 1938). The null hypothesis for this test was H_0: "The average value of the adjusted displacements was equivalent to the average value of the GNSS displacements" and was tested against the alternative hypothesis H_A: "The average value of the adjusted displacements was different from the average value of the GNSS displacements", to a level of significance of 0.05. The test statistic took the value of -0.0651 and it was compared to the critical value achieved from a t-Student with 59 degrees of freedom and a level of significance of 0.05, which presented the value 2.0010 and led to an acceptance region between -2.0010 and +2.0010. Threfore, as the test statistic was inside the acceptance region, the null hypothesis could be accepted and it was concluded that the average of the adjusted displacements could be considered equal to the average of the GNSS ones, to a level of significance of 0.05. The same test was executed to compare the original PSI displacements (after being referred to PS_{ref}) to the GNSS ones, where the test statistic took the value -3.0411. The acceptance region for the test was the same interval as in the previous test; thus, the test statistic was outside of it, leading to the rejection of the null hypothesis and acceptance of the alternative one. Therefore, the average value of the original PSI displacements cannot be considered equal to the average value of the GNSS displacements, to a level of significance of 0.05.

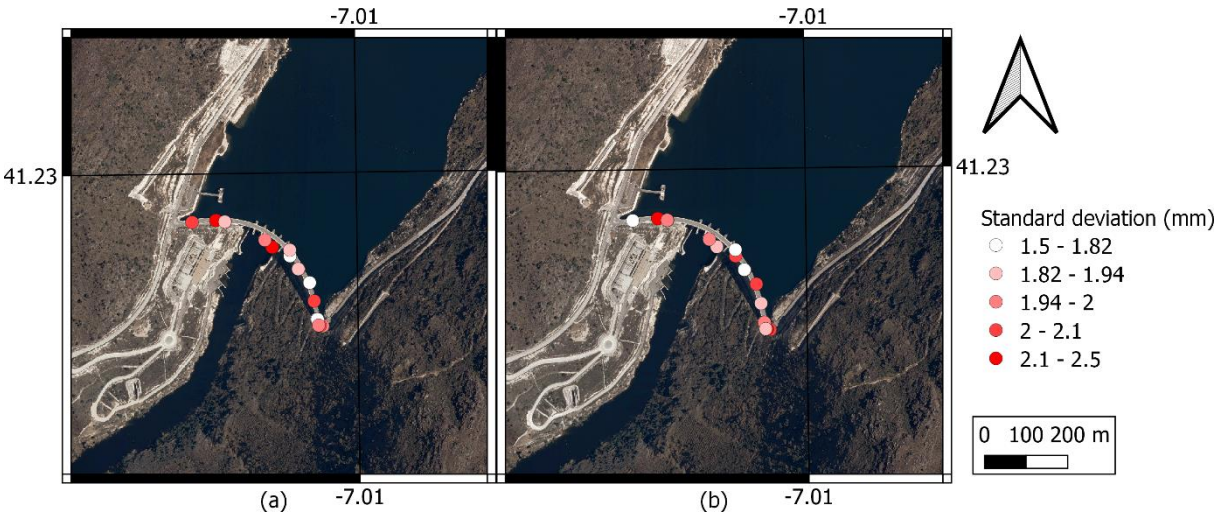

Figure 87 – *A priori* (a) and *a posteriori* (b) standard deviations of LOS displacements for vertices on the dam crest. Coordinate grid in WGS84.

The *a posteriori* standard deviation of the analysed network vertex was 2.0 mm. For the particular case of this dam, GNSS had an uncertainty of 0.4 mm at both radial and tangential directions and 7 mm at the vertical direction for daily solutions (LNEC, 2017b). The large magnitude of the vertical error of GNSS might be due to the altitude difference between the

reference antenna and the antennas on the dam crest (around 270 m), which corresponded to distinct atmospheric conditions at both points that perhaps were not correctly modelled by the commercial software used for the GNSS processing. The vertical error was then propagated to the LOS direction, resulting in an uncertainty of 5.5 mm.

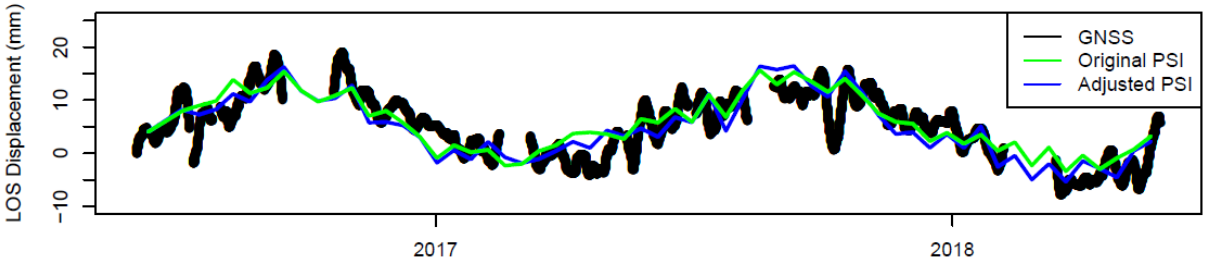

Figure 88 – LOS displacement time series of the original PSI, adjusted and GNSS LOS displacements. GNSS was filtered with a weekly moving average.

4.4.6. Regarding the slope monitoring, the network contained 157 vertices on the slopes inside the ROI, from which one was the GNSS reference antenna that formed the local reference frame. There were 83 vertices on the right bank and 74 on the left one. At the left bank, there was a gap in the point cover of the slope, due to the inexistence of PSs on that area, possibly because it might be in the shadow of the SAR signal.The original PSI displacements on the slope vertices ranged from 27.4 mm away from the sensor to 33.1 mm towards it. Despite these extreme values, occurred at single points, the remaining PSs presented cumulative displacements between 6.4 mm away from the sensor and 10.6 mm towards it. After the proposed network adjustment, the adjusted displacements varied from 27.9 mm away from the sensor and 32.8 mm towards it, with most points with adjusted cumulative LOS displacement between 7.1 mm away from the sensor and 10.0 mm towards it (Figure 89).

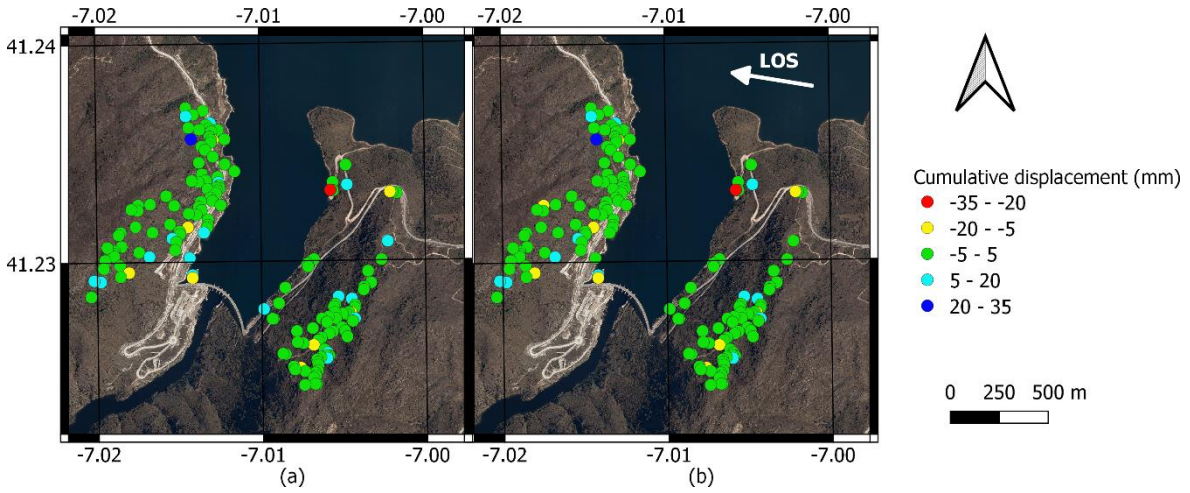

Figure 89 – *A priori* (a) and *a posteriori* (b) cumulative LOS displacement at vertices on the slopes. Coordinate grid in WGS84.

A posteriori variances for all vertices were also determined, which are presented in Annex A.2 Table 22. While the *a priori* standard deviations were equally distributed on the ROI, the *a posteriori* ones increased with the distance to the GNSS reference antenna until a maximum of 2.8 mm (Figure 90), similar to traditional geodetic monitoring systems when there is only one point in the local reference frame. This resulted in larger standard deviations at the left bank than at the right one.

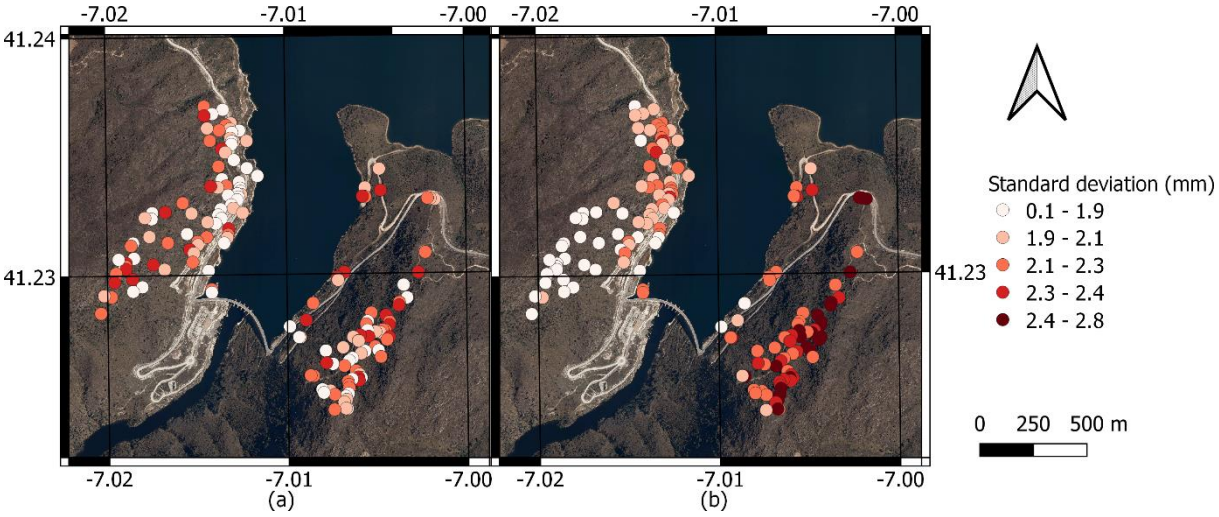

Figure 90 – *A priori* (a) and *a posteriori* (b) standard deviation of LOS displacements at network vertices on the slopes. Coordinate grid in WGS84.

Adjusted LOS displacements and the corresponding *a posteriori* variances were projected and propagated, respectively, into the slope direction of each vertex (Figure 91). The cumulative displacement along slope apparently ranged from 558.2 mm downhill to 918.6 mm uphill, with the largest values achieved for the right bank. Unlike the standard deviations of adjusted LOS displacements, standard deviations of displacements along the slope direction were larger at the right bank than at the left one and varyed between 0.3 mm and 479.8 mm (Figure 91). The large displacements along slope and respective standard deviations at the right bank resulted from the relationship between the LOS direction and the slope configuration at the points, as some combinations of slope inclination and orientation led to $s_{un} \cdot l_{un}$ values close to zero (Equations 51 and 52 in section 4.3.4), as seen in Figure 92. All points at the left bank presented values of $s_{un} \cdot l_{un}$ above 0.5, while points at the right bank tended to have negative values, with a few of them being close to zero. In order to avoid division by zero, a threshold was used to select the points to be further analysed. Only those presenting absolute value of $s_{un} \cdot l_{un}$ above 0.25 were considered for slope monitoring. This criterium led to the selection of 98 vertices located at both banks (Annex A.2 Figure 159).

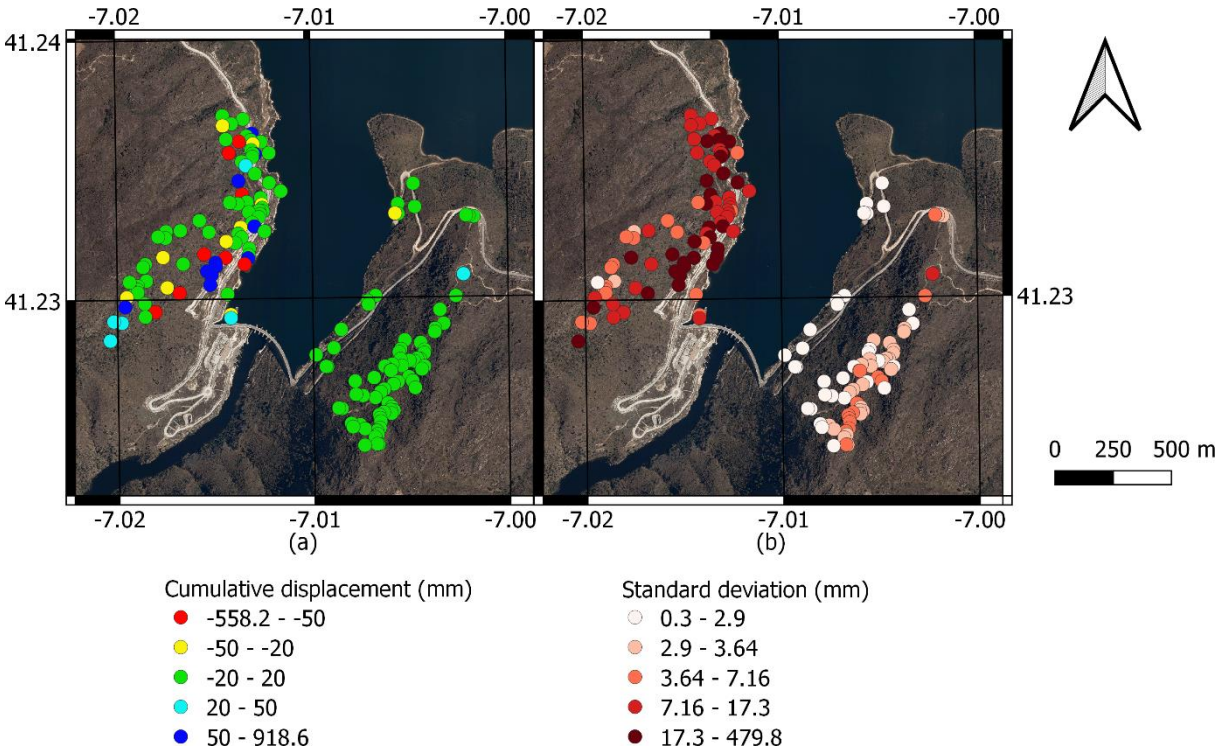

Figure 91 – Cumulative displacement along the slope direction (a) and standard deviation of displacement along the slope direction (b). Coordinate grid in WGS84.

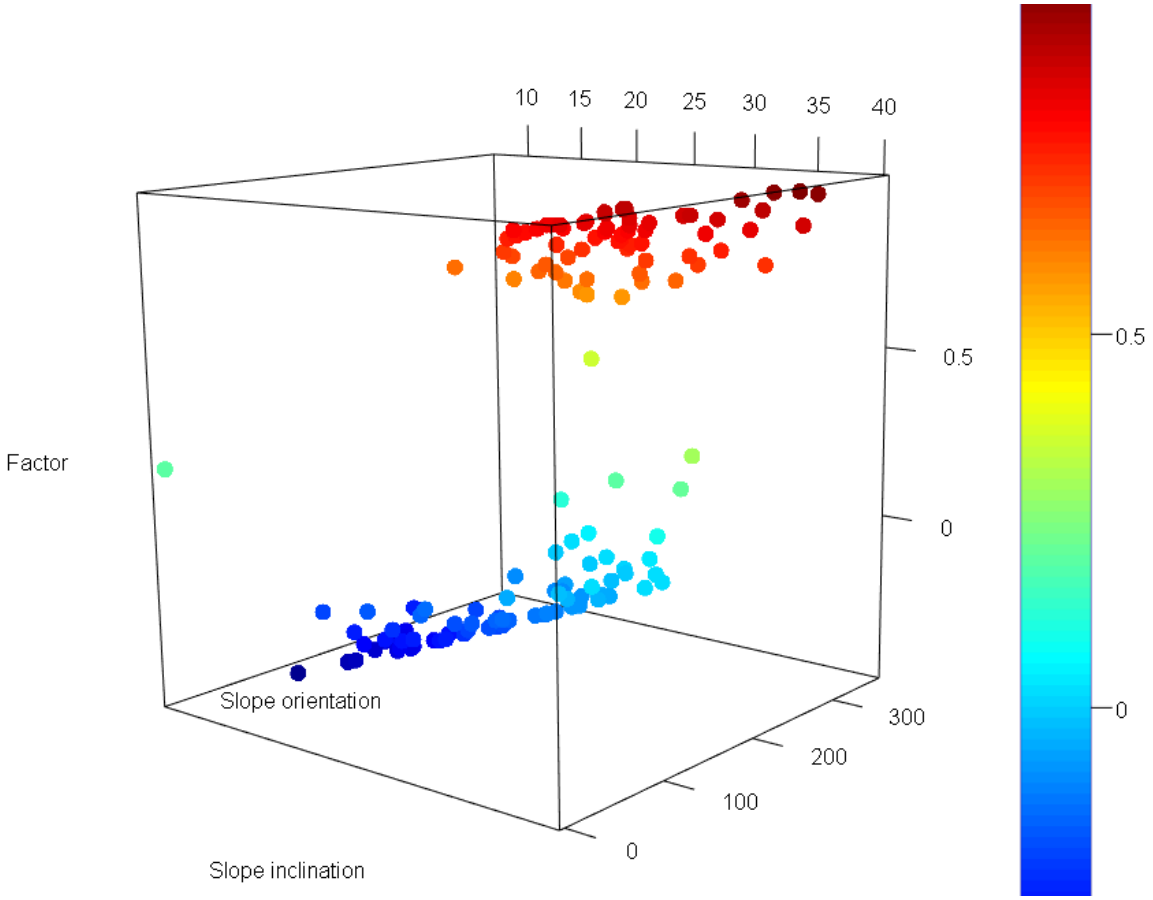

Figure 92 – Values of $s_{un} \cdot l_{un}$ (factor) as a function of slope inclination (°) and slope orientation (°).

The time series of displacement along the slope direction of the selected points were analysed through the RADAR interpretation method proposed in Chapter 3, using the parameters in Annex A.2 Table 23. The automatic solution provided by the algorithm consisted on two clusters, where one of them was composed by a single point. In order to identify distinct behaviour at the ROI, the scale of the analysis was increased and a solution with four clusters was manually selected.

Cluster 1 contained 80% of the points, which were spread throughout both banks (Figure 93). These points presented a stable behaviour during the time interval of the analysis, not showing large magnitude displacements (Figure 94). Therefore, a separated analysis for each bank was not performed.

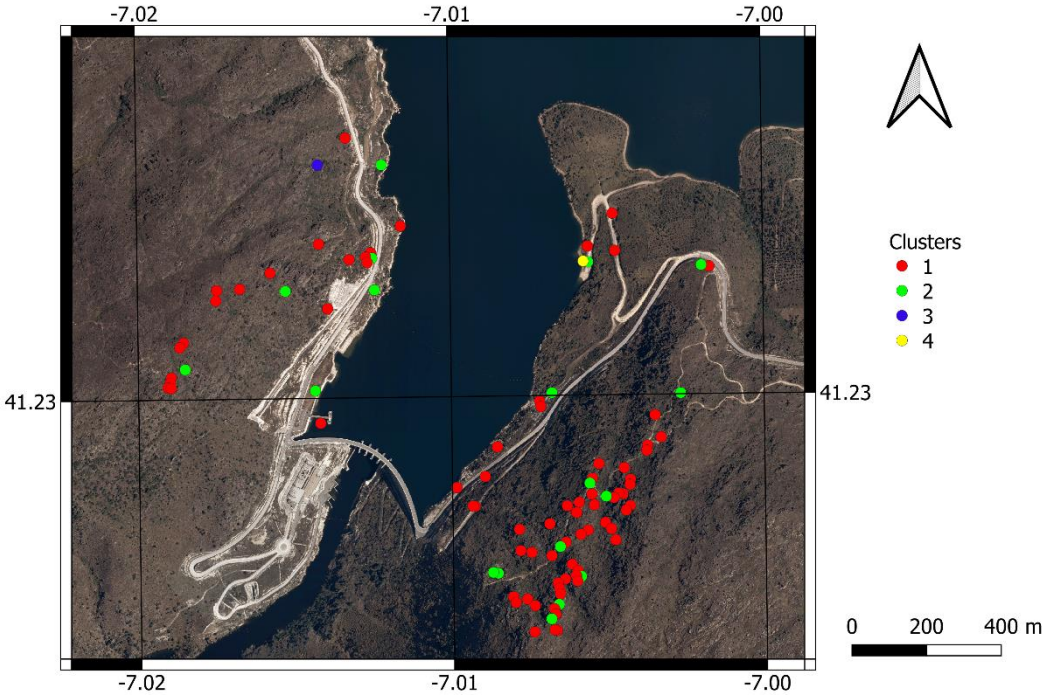

Figure 93 – Spatial distribution of the four clusters on the slopes. Coordinate grid in WGS84.

Cluster 2 was formed by 18% of the points and it was also represented at both banks. The representative time series presented downhill displacement during the first two months (around 5 mm) and it was inspected whether distinct behaviour occurred at each bank (Figure 95). The points at the left bank moved downhill until mid-July and then they stabilised around 4 mm away from the original position. On the other hand, the points at the right bank moved downhill around 10 mm by the end of September and then they stabilised. The average time series for the points at the right bank was noisier than for those at the left bank, possibly due to the smaller absolute values of $s_{un} \cdot l_{un}$ at that bank.

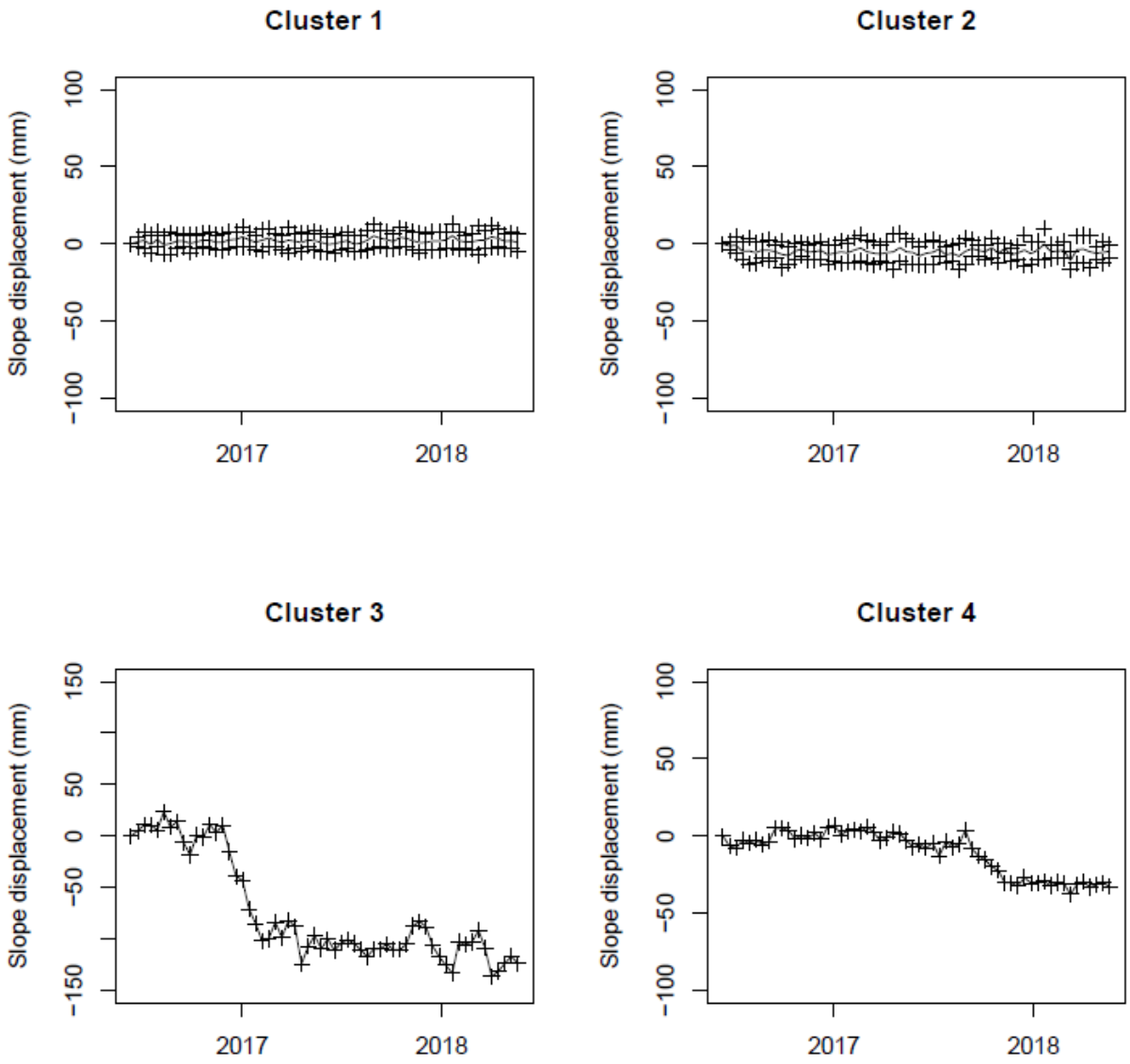

Figure 94 – Time series of displacement along the slope representative of each cluster; crosses are the average time series plus and minus one standard deviation.

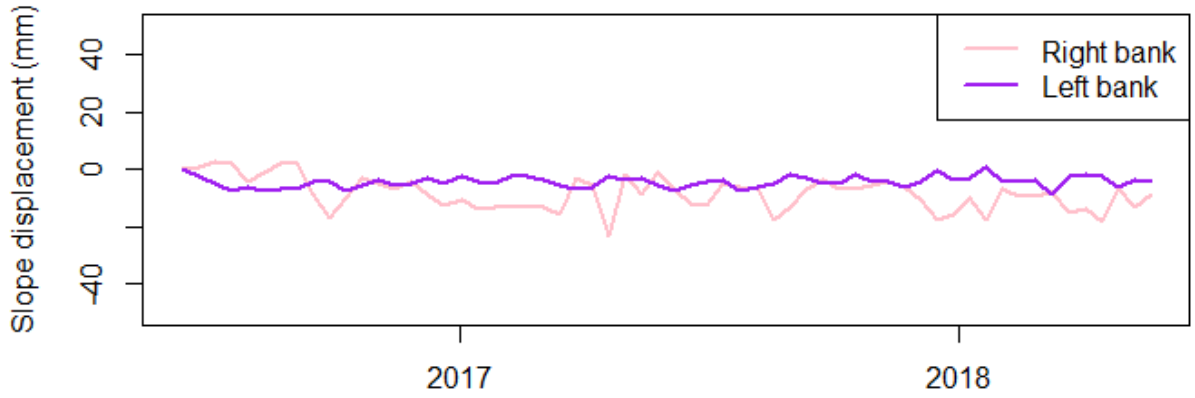

Figure 95 – Average displacement along the slope direction for points in cluster 2 at each bank.

Cluster 3 was an isolated point at the right bank, located far from the reservoir. This point presented downhill displacement between November 2016 and February 2017 with a

magnitude of 11 cm and then stabilized. The large achieved displacement might result from the small $s_{un} \cdot l_{un}$ value at the point's location (0.27), which was close to the selected threshold. Nevertheless, the method was able to identify a point with distinct behaviour and to isolate it for further analysis.

Cluster 4 was also composed by a single point. The point was located at the left bank and close to the reservoir. It moved downhill around 36 mm between August and December 2017 and then it stabilised until the end of the time interval of the study.

Clusters 2, 3 and 4 presented downhill displacements. Comparing the representative time series of the three clusters with the variation of the water level at the reservoir (Figure 85), it was verified the largest displacements occurred at periods when the water level was stable or decreasing. The fast decrease of the water level may pose a threat for the stability of low permeability slopes (Paronuzzi *et al.*, 2013), such as those composed of granite. Clusters 2 and 4 presented downhill displacements during the drawdown of the water level, with cluster 4 being the one with the largest probability of being affected by the load decrease, due to its proximity to the reservoir. The downhill movement of cluster 3 occurred during a period of very small variations on the water level and, as the cluster is far from the reservoir, it was not probable that the changes in water level were the cause for the displacements. By the end of the study time interval, in May 2018, the four analysed clusters presented stable behaviour.

4.5 Discussion

The present Chapter proposed a method for the integration of PSI observations on a geodetic monitoring sub-system based on GNSS and applied it to a concrete dam and the slopes around its water reservoir.

4.5.1. PSI and GNSS measurements were combined through a network, which was verified to be admissible in terms of precision and robustness. The network was admissible to precision for a tolerance of 4.0 mm and a level of significance of 0.05, which meant there was a probability of 0.95 that the displacement error at each point was below that tolerance. Regarding the robustness, the Delaunay network enabled enough redundancy to fulfil the requirements. This allowed the execution of the quality control of the observations, where it was verified that there were not unexpected errors.

The usage of double-differences between PSI and GNSS measurements as observations allowed the method to be performed fully remotely. Besides, it also enabled the mitigation or even the elimination of atmospheric residuals or of the reference point effect. The introduction

of GNSS double-differences into the network allowed the determination of adjusted LOS displacements, which proved to be closer to the GNSS measurements, considered as reference, than the original PSI observations. However, this strategy added some noise to the adjusted displacements, as, in this particular case study, the GNSS displacements along LOS direction presented more noise than the PSI measurements.

4.5.2. The local reference frame was defined using the minimum constraint solution, which consisted on the usage of a single point – the GNSS reference antenna. This led to the increase of *a posteriori* variance with the distance to the reference point. This limitation could be overcome recurring to a redundant local reference frame, with more than one reference point constraining the vertices' displacements. Those reference points should be installed at stable locations of the ROI (based on geotechnical experts' advice) and distributed in order to minimise *a posteriori* variances. This could be achieved by installing the benchmarks at the locations where larger *a posteriori* variances were obtained when using the minimum constraint solution.

These benchmarks may be any points with known LOS displacements that fulfil the previously mentioned requirements. GNSS antennas may be used, if available. However, the large costs associated and their difficult deployment can limit their usability. Artificial reflectors to SAR signal, either passive or active, may be acceptable alternatives. Passive reflectors are low cost and do not require electrical power. Their main limitations are the large dimensions, which may turn them difficult to install on difficult access locations, and their exposure to vandalism. The only additional equipment required would be a well-founded concrete block to be used as a support and to assure the stability of the installation. Maintenance would be required in order to remove leaves or other dirt. This question will be further addressed on Chapter 5. On the other hand, active reflectors, such as CAT, are small and easy to transport (Mahapatra, 2015). They require electrical power, which can be provided by a battery. Maintenance operations include battery recharge and verification of electrical components of the device. While a GNSS system cost several thousand euros, the expenses associated to artificial reflectors are in the order of hundreds of euros.

4.5.3. The proposed method enabled the determination of *a posteriori* variances for the displacements along LOS direction. In traditional geodetic techniques, *a priori* variances of the observations are based on indications from the equipment manufacturer. However, systematic and random errors during the observation procedure (related to the equipment, to environmental conditions or to the operator) affect the observations' quality (LNEC, 2001). Therefore, operating procedures that help to minimise the errors are designed. Redundant measurements

enable the determination of corrected observations and their corresponding *a posteriori* variances, which are then propagated to the parameters to be determined (the displacements), allowing the computation of their variances, as well.

In this study, *a priori* variances of the observations reflected the user confidence regarding the GNSS antenna stability, in case of points occupied by GNSS devices. For points corresponding to PSs, *a priori* variances depended on the PS temporal coherence. The redundant observation of each vertex at the network and the usage of double-differences as observations enabled the mitigation of some errors (atmospheric and reference point effects) and the determination of adjusted displacements and their respective variances.

4.5.4. The fact that the observations were performed exclusively along LOS was a limitation of the proposed method, especially relevant for eventual applications to SHM, where the directions of interest for the monitoring depend on the structure orientation. In the particular case study analysed in this Chapter, this limitation was attenuated by the execution of sensitivity analysis or the projection of the LOS displacements into probable movement directions.

The presence of noise in the data was another limitation of the method, as the noise might mask possible signs of behaviour anomalies. The configuration of the four GNSS antennas contributed to noise presence in the data. The large altitude difference between the reference antenna and the ones on the crest hindered the determination of the displacement vertical component due to atmospheric differences. This might not be a problem for the usual dam monitoring using this technique, as only horizontal displacements were sought (being determined with sub-millimetric precision). However, the GNSS observations projected into LOS direction were affected by the uncertainty on the vertical displacement component. As LOS double-differences were used to constrain the network adjustment, the noise in the data propagated throughout the network, affecting the adjusted displacements. This problem might be mitigated during GNSS processing, by using a software capable of dealing with the atmospheric differences at distinct altitudes or by post-processing the data through low-pass filters.

Gaps in the network cover of the slopes were identified on the left bank, probably being located on the shadow of the SAR signal, leading to the absence of PSs. The used SAR images were acquired from a descending pass of the satellite; thus, slopes facing northwest and with large inclinations were likely to be affected by shadows. This might be a recurrent problem to the application of the method to reservoir banks. Adding GNSS stations or artificial reflectors would not solve the problem, as the steep slopes might reduce the amount of visible GNSS satellites to insufficient numbers and SAR artificial reflectors obviously would not be able to

receive the signal at a shadow area. A possible solution might be the usage of SAR images from distinct acquisition geometries, even from a different sensor, as long as the analysed slope was not in the shadow area of the new geometry. The projection of LOS displacements into slope direction would allow the direct comparison of data achieved through different datasets, increasing the spatial resolution of the measurements.

The presence of vegetation on the slopes might have avoided PS detection on the slopes, which could be minimised by the usage of SAR images acquired in L-band, as in Chapter 3.

A PS gap also occurred on the dam crest. The lacunae might be due to the fact that the segment of the crest without PSs was almost parallel to the projection of LOS into the horizontal plane, which may have led to a small reflection of the SAR signal back to the sensor; thus, not originating PSs. This hypothesis was reinforced by the low reflectivity of that area of the dam in the reflectivity map (Figure 96).

Figure 96 – Reflectivity map of the dam from the descending pass acquisition geometry; red circumference highlights the zone in the dam crest with gaps in PS acquisition and low reflectivity.

4.5.5. The proposed strategy enabled the displacement analysis at several points on the dam crest. Seasonal behaviour compatible to the response of concrete arch dams to thermal expansion in the radial direction was detected, as well as a delay in that response, compatible with thermal inertia. A decrease in displacement magnitude was found from the dam centre towards the banks, which also met the structure expected behaviour. The displacement time series were noisy, which hindered the detection of possible small magnitude anomalies. Linear trends or ageing effects were not detected; however, the time interval considered in the study was too short for an effective trend evaluation. The displacement time series should be updated

in order to analyse a longer interval with more recent observations. Displacements were computed along LOS with *a posteriori* standard deviations between 1.6 mm and 2.5 mm. These standard deviations were lower than those achieved through GNSS (5.5 mm along LOS). Therefore, the proposed method enabled displacement measurement with lower uncertainty (for this case study), at a larger number of points and with lower cost than using additional GNSS equipment. Therefore, despite being unable to determine three-dimensional displacements, the proposed method may be useful to complement the data from other techniques.

Regarding the slope stability, the method followed to project the LOS displacements into slope direction (Schlögel *et al.*, 2015) provided acceptable results for the points at the left bank, due to the relative geometry between LOS and slope configuration. However, many points at the right bank were located on slopes whose configuration was approximately orthogonal with respect to LOS, which resulted into enhanced magnitude displacement values and uncertainties. The points located on slopes with these characteristics were identified and excluded from the analysis. Four distinct behaviour were identified, with two sets of points presenting movement possibly related to the decrease of the reservoir water level. Nevertheless, signs of slope instability were not detected by the end of the study time interval.

Regarding the computational performance of the proposed algorithm, the case study evaluated in this Chapter took 2.6 minutes to process in a laptop with 2.40 GHz CPU and 8 GB of RAM.

4.6 Conclusions

In conclusion, the proposed method enabled structure monitoring at both a concrete dam and at slopes around the water reservoir through combined data from InSAR and GNSS. The GNSS monitoring sub-system was expanded through PSs, resulting in a larger number of points on the dam crest and on the slopes available for analysis. The method enabled lower displacement uncertainty than the GNSS (for this particular case study and when projected to LOS). Therefore, the application of this method may be advantageous to complement existing structure monitoring systems.

The expansion of the monitoring system through this method was cost-effective, as the GNSS equipment was already installed and the added points did not require materialisation, since they naturally existed in the terrain. The used SAR images and EU-DEM were freely distributed through Copernicus program; however, the software for GNSS and PSI processing

had costs associated, as well as the electrical power and Wi-Fi connections required for the GNSS system.

The major limitations of the method were:

- The determination of displacements only along the LOS direction;
- The lack of points at some regions, such as shadow of the SAR signal, vegetation cover or low reflectivity zones;
- The noise in the displacement time series.

For future research, the inclusion of more points in the local reference frame will be an important step to improve the adjusted displacements and to achieve a more homogeneous spatial distribution of *a posteriori* variances. Additional GNSS antennas or artificial reflectors to SAR signal can be used for that purpose.

The analysis of the achieved displacements did not detect signs of behaviour anomalies neither on the dam nor on the slopes.

Chapter 5. Uncertainty assessment for InSAR displacements

This chapter proposes a new model of artificial passive reflector to the SAR signals from the sensors on board of Sentinel-1A/B, capable of providing observations for both ascending and descending geometries at the same point. The new CR is visible at SAR amplitude images from both geometries and keeps its reflective behaviour stable during the executed tests, originating PSs and enabling displacement measurements. The CR is used to perform InSAR displacement validation and uncertainty assessment through the comparison between PSI-derived displacements and measurements from reference techniques, such as geometric levelling and GNSS. Uncertainties around 2 mm are achieved for PSI-derived displacements along LOS, vertical and east – west directions.

5.1 Introduction

According to Marinkovic *et al.* (2007), it is not easy to assess the uncertainty of InSAR displacements, as the exact point in the object in which the signal is reflected is not known, there is no redundancy in the observations and phase ambiguities are not known neither.

Many studies have used artificial reflectors to evaluate the quality of InSAR displacements. These devices keep their reflective properties stable, so that they behave as PSs. Besides, their design assures that their reflective centre is known; therefore, their displacements can be measured through reference techniques, more precise than InSAR, and used to validate the InSAR displacements and to assess their uncertainty.

There are two types of artificial reflectors: passive and active. Passive artificial reflectors are metallic corners, oriented towards the sensor, which reflect the signal every time a new image

is acquired. Their reflective behaviour is affected by the accumulation of water, snow or dirt, requiring frequent maintenance. Their dimension is often seen as a limitation and they are prone to be subjected to vandalism.

Compact Active Transponders (CATs) are active artificial reflectors, i.e. they are electronic devices that receive the signal from the sensor, amplify it, and send it back. These equipment are light weighted and easy to install; however, either they have large cost associated, or less expensive versions are not able to keep their phase stable (Mahapatra, 2015), which is critical to InSAR.

Passive artificial CR have been widely used for quality control experiments of InSAR displacements. Marinkovic *et al.* (2007) performed a controlled experiment with CR to assess the precision of the measurements. They observed five reflectors for almost five years and compared their displacements with those of precise levelling. A functional model was defined considering that vertical double-differences from InSAR and levelling should be equal (the observations from both techniques were obtained within 24 hours). A stochastic model was also used, enabling the estimation of *a posteriori* precision of the InSAR vertical displacements: 2.8 mm for ERS-2 and 1.6 mm for EnviSat data.

Yu *et al.* (2013) proposed the usage of trihedral CR to increase the density of the scatterers for subsidence monitoring with TerraSAR-X images in a rural area (Figure 97). Both fixed and portable[21] CR were used, with displacement uncertainty being similar for both types of devices. The differences between InSAR and levelling displacements ranged between 5.4 mm away from the sensor and 3.6 mm towards it.

Figure 97 – CR of the model used in Yu *et al*. (2013).

[21] CR that can be uninstalled and reinstalled at other epochs.

Qin and Perissin (2015) presented the monitoring of a subsiding area in Hong Kong using four CR for TerraSAR-X data. For validation purposes, vertical displacements were imposed on three of them, while the fourth was used as reference. Levelling observations were compared to the InSAR displacements and a linear correlation was verified between the results from the two techniques ($R^2 = 0.999$). The achieved RMSE was of 0.67 mm.

Besides the quality control tests, CR can also be used to increase the scatterer density in vegetated areas. Ye *et al*. (2004) did an attempt to monitor a landslide and an unstable surface near the Three Gorges region, in China, through DInSAR, due to the concern that the rise in the water level could be the trigger for ground instability. However, they were not successful as there was not enough coherence in their area of interest. To overcome the problem, they installed a set of 10 CRs. Instead of analysing the whole low coherence area, the processing was focused only on the pixels with the CR (CRInSAR). Small anomalies were observed, which might be caused by atmospheric changes or noise, leading to the conclusion that both areas were stable. Results were validated by imposing vertical displacements to two of the devices, which were then detected by InSAR with errors of 0.1 mm and 0.4 mm.

Some authors used bidirectional CRs, which consisted on two CRs pointing to different LOS and that enabled the combination of images from ascending and descending geometries for the same object point. Ferretti, Savio, *et al.* (2007) presented an experiment for assessing the precision of vertical and horizontal (east – west direction) displacements determined from two acquisition geometries obtained at a bidirectional CR. Their CR was composed by two dihedrals, each of them pointing to different acquisition geometries (ascending and descending). A compromise in the orientation was applied to assure the CR were visible in both EnviSat and Radarsat images. Two of these devices were installed on a roof, with one of them being the reference and the second one having a mechanism to impose pre-defined displacements. Vertical displacements for the moving reflector were also observed through GPS at the beginning and end of the experiment. The standard deviation of the differences between the InSAR and the known imposed displacements was computed to assess the InSAR precision: 0.75 mm in the vertical direction and 0.58 mm in the east – west one.

Quin and Loreaux (2013) also presented a bidirectional CR system named MUSE – MUltipass Scattering Equipment, developed for TerraSAR-X images. The reflectors were formed by two triangular trihedrals oriented towards different directions. An experiment using four MUSE was deployed, with one of the devices being used as a reference and installed on the ground, while the other three were located on tables with a mechanism to move them in the vertical and east – west direction with constant velocities. This study only presented the results

obtained in one direction (LOS), not benefitting yet of the bidirectionality of the CR. An uncertainty of 0.48 mm was achieved for the displacements.

Dheenathayalan *et al.* (2017) proposed a small dimension bidirectional CR (28.2 cm x 14.5 cm) for X-band sensors (Figure 98). The backscatter of this reflector was so small that the authors recommended the installation of a set of them forming a pattern (like an arrow, for example) in order to enable their identification in the images. Signal processing techniques were applied to improve the signal quality. The standard deviation of the obtained displacements was 1.3 mm in the vertical component and 2.1 mm in the east – west one.

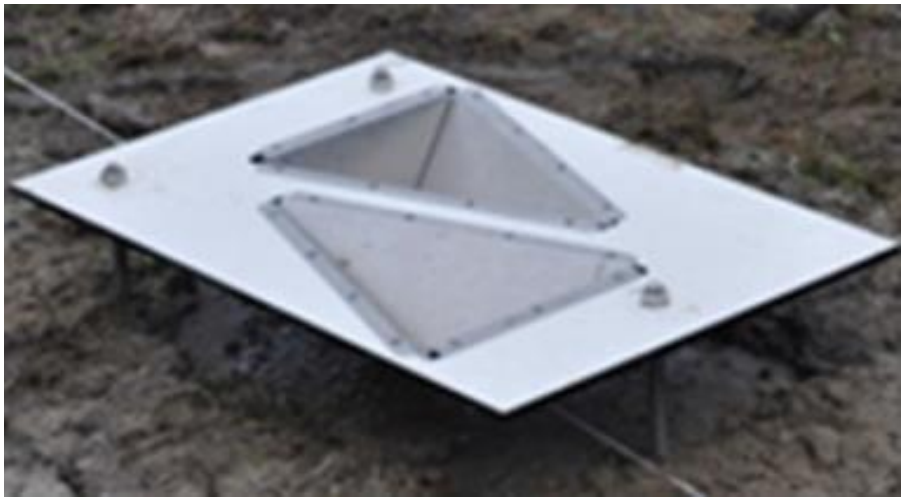

Figure 98 – Small bidirectional CR (Dheenathayalan *et al*., 2017).

Bányai *et al.* (2020) did an attempt to reduce the dimension of corner reflectors, by truncating triangular trihedrals along their axis in order to remove the part of the structure that was not involved in the SAR signal reflection. The authors deployed two truncated CRs, one for the ascending and another one for the descending geometry of Sentinel-1, on the same base and facing each other, in order to reduce the base dimension (Figure 99). The device was also prepared to have a GNSS antenna installed between the two CRs. Signal interference between the pair of reflectors did not occur and displacement error along LOS varied between 0.2 mm and 0.4 mm, determined based on signal-to-clutter (SCR) ratios at a landslide area.

Quality control tests have also been performed using low-cost CAT (Figure 100). Mahapatra *et al*. (2014) designed an experiment with CATs and CRs in a calibration field. They computed the double-differences between each pair of equipment and determined their standard deviation, which varied between 1.8 mm and 4.6 mm. The same quality control test performed with CR led to values between 1.5 mm and 2.6 mm, showing that CAT and CR displacements have similar precisions.

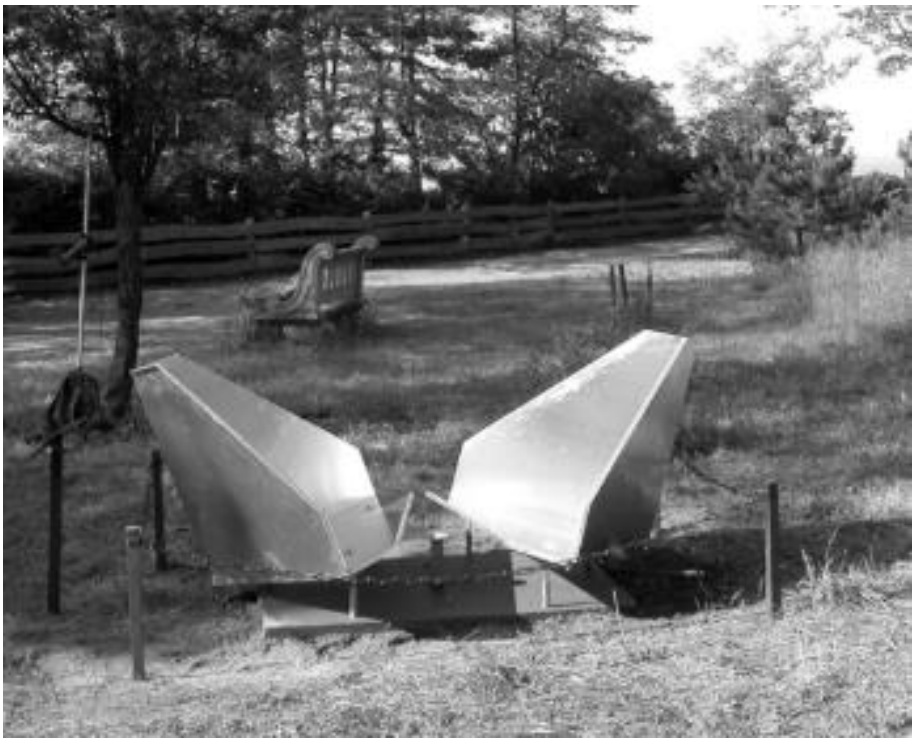

Figure 99 – Truncated twin corner reflectors (Bányai *et al.*, 2020).

Figure 100 – Example of CAT device (Mahapatra, 2015).

Park *et al.* (2014) presented a different model of CAT. It was designed to work with KOMPSAT-5 images in the X-band and requirements in the isolation between the receiving and the transmitting antennas forced it to have large dimensions (around 2 m height). However, this device had a system to introduce a delay in the signal that created a virtual CAT in a low backscatter area, enabling a larger contrast with background than in its real location. Evaluation of displacement measurement quality was not provided in the study.

Table 10 summarizes the studies presented above.

Table 10 – Comparison of studies that used artificial reflectors to assess InSAR measurements uncertainty.

Study	Type of artificial reflector	Problem	Quality control		
			Vertical	East – west	LOS
Ye *et al*. (2004)	Passive; triangular trihedral	Landslide and unstable surface near dam	0.1 – 0.4 mm *[1]		
Ferretti, Savio, *et al.* (2007)	Passive; bidirectional; dihedral	Quality control experiment	0.75 mm *[2]	0.58 mm *[2]	
Marinkovic *et al*. (2007)	Passive; unknown	Quality control experiment	1.6 – 2.8 mm *[3]		
Quin and Loreaux (2013)	Passive; bidirectional; triangular trihedral	Quality control experiment			0.48 mm *[2]
Yu *et al.* (2013)	Passive; triangular trihedral	Subsidence	–5.4 – +3.6 mm *[4]		
Mahapatra *et al.* (2014)	Active; CAT	Quality control experiment			1.8 – 4.6 mm *[2]
Qin and Perissin (2015)	Passive; rectangular trihedral	Subsidence	0.67 mm *[5]		
Dheenathayalan *et al*. (2017)	Passive; bidirectional; triangular trihedral	Quality control experiment	1.3 mm *[6]	2.1 mm *[6]	
Bányai *et al.* (2020)	Passive; bidirectional; triangular trihedral	Quality control experiment and landslide			0.2 – 0.4 mm *[7]

*[1] Absolute error
*[2] Standard deviation of errors
*[3] *A posteriori* precision
*[4] Difference range
*[5] RMSE
*[6] Displacement standard deviation
*[7] Error based on SCR

5.2 Methods

In this Chapter, a new model of bidirectional corner reflector for Sentinel-1 is proposed, whose goal is the validation of InSAR measurements and the assessment of InSAR displacement uncertainty.

The proposed CR has the capability of reflecting the SAR signal from both ascending and descending passes of the satellite, allowing the determination of vertical and horizontal (east – west) displacement components. InSAR displacements are validated through comparison to GNSS and geometric levelling data. Besides, a moving device enables the imposition of known displacements along different directions to validate displacements and to assess measurement uncertainty in distinct conditions. The performance of the proposed CR is also compared to that of traditional CRs found in the literature. The present section exposes the strategy followed to deploy and install the CR and to perform the displacement validation and uncertainty assessment.

The CR proposed in this thesis is inspired in those presented in Qin *et al.* (2013), which is an individual CR of the rectangular trihedral model. Three metallic plates, orthogonal to each other, form this type of CR. Two of the plates have rectangular shape, united by their longest edge, which is placed in the vertical direction. The third plate is a square, with the size having the same length as the shortest edges of the rectangular plates and it is united to the rectangular dihedral as a horizontal base (Figure 101).

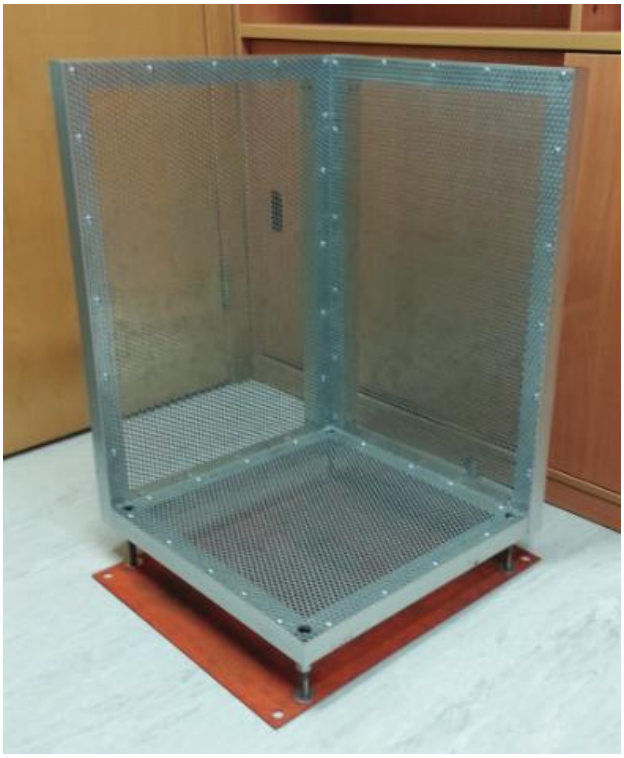

Figure 101 – Example of rectangular corner reflector, from Qin *et al.* (2013).

Unlike triangular trihedrals or square trihedrals, this model of CR is only oriented towards the LOS in azimuth, not being required to steer the structure in elevation, which reduces the chances of orientation error. According to Li *et al.* (2012), who used physical optics concepts to determine CR reflective properties as a function of its shape and orientation error, rectangular trihedrals reach larger reflective capability than triangular trihedrals. However, they are more sensitive to orientation error. Reflectivity is evaluated through the CR RADAR Cross Section (RCS), which is the strength of the signal reflected by the target in the direction of the sensor (Li *et al.*, 2012). RCS for rectangular trihedrals is determined through Equation (53), in square metres, where RCS_{RT} is the RCS of a rectangular trihedral CR, a and b are the sizes of the edges of the rectangular plates and λ is the RADAR signal wavelength, as adapted from Qin *et al.* (2013).

$$RCS_{RT} = \frac{12\pi a^2 b^2}{\lambda^2} \tag{53}$$

The dimension of an individual rectangular trihedral CR must be defined in order to assure a minimum SCR of 100 or 20 dB (Qin *et al.*, 2013; Bányai *et al.*, 2020), where SCR is defined as in Equation (54):

$$SCR = \frac{RCS_{RT}}{RCS_{bg}} \tag{54}$$

with RCS_{bg} being the RCS of the background area where the CR will be installed. The average RCS of the background, in dBm^2, is determined through Equation (55):

$$RCS_{bg} = \sigma^0 \cdot A \tag{55}$$

where σ^0 is the backscatter coefficient, or sigma nought, which measures the brightness of a distributed target and A is the area of an image pixel projected on the ground (Garthwaite, 2017). The backscatter coefficient is computed from SAR amplitude images, following a procedure that depends on the sensor (SkyWatch Space Applications Inc., 2019). The area of the image pixel projected on the ground is determined through Equation (56):

$$A = \frac{p_r \cdot p_a}{\sin\theta} \tag{56}$$

where p_r and p_a are spatial resolution in range and azimuth directions, respectively, and θ is the incidence angle (Garthwaite, 2017).

In order to decrease the resistence of the CR with respect to the wind, to avoid rainwater accumulation and to decrease the structure weight, perforated metallic plates are used to build the CR, which leads to a loss of RCS due to transmittivity through the holes. The loss of RCS is determined through Equation (58):

$$T = 20 \cdot \log\left(\frac{3 \cdot a \cdot b \cdot \lambda}{2\pi \cdot d^3 \cdot \cos\theta}\right) + \frac{32 \cdot t}{d} \tag{58}$$

where T is the RCS loss in dBm^2, a is the horizontal distance between two adjacent holes'centres, b is the vertical distance between two adjacent holes'centres, d is the hole diameter, λ is the wavelength, θ is the incidence angle and t is the plate thickness (Qin *et al.*, 2013). The final SCR (SCR_{final}) of each CR is assessed through Equation (59):

$$SCR_{final} = \frac{RCS_{RT} - T}{RCS_{bg}} \tag{59}$$

SCR influences the dispersion of the LOS displacements achieved at the CR, following Equation (60):

$$\sigma_{d^{LOS}} = \frac{\lambda}{4\pi} \cdot \sqrt{\frac{1}{2 \cdot SCR_{final}}} \tag{60}$$

where $\sigma_{d^{LOS}}$ is the standard deviation of LOS displacements (Qin *et al.*, 2013). Equation (60) is used to verify if the SCR is large enough to assure sub-millimetre displacement dispersion at the CR.

In the scope of the present research, two rectangular trihedrals of the same dimension were built using perforated metallic plates, whose dimensions enabled sub-millimetric LOS displacement dispersion at the location selected for installation (this will be explained in detail in section 5.3). The two CRs were welded by their vertical edges to a common vertical metallic rod, assuring the reflective centre from both individual structures was the same. However, instead of joining the two CRs in a way that all the vertical plates would form 90º angles, they were oriented in order to assure that each individual reflector was aligned towards one pass of the satellite (Figure 102). The simpler orthogonal configuration would lead to orientation errors, which are critical to rectangular trihedral CRs (Li *et al.*, 2012). As the projection of LOS onto the horizontal plane has, approximately, the direction west-northwest – east-southeast for the descending pass and the direction east-northeast – west-southwest for the ascending one, the individual CRs were oriented in a way that the angle separating them facing south was smaller than the angle facing north. Let us consider the angle between the projection of the LOS onto the horizontal plane and the east – west direction, β, as defined in Equation (14) in Chapter 3. The angle between the closest horizontal edges from both individual reflectors facing south, ε_{south}, is given by Equation (61):

$$\varepsilon_{south} = \frac{\pi}{2} + 2 \cdot \beta \tag{61}$$

while the angle between the closest horizontal edges from both individual reflectors facing north, ε_{north}, is given by Equation (62).

$$\varepsilon_{north} = \frac{\pi}{2} - 2 \cdot \beta \tag{62}$$

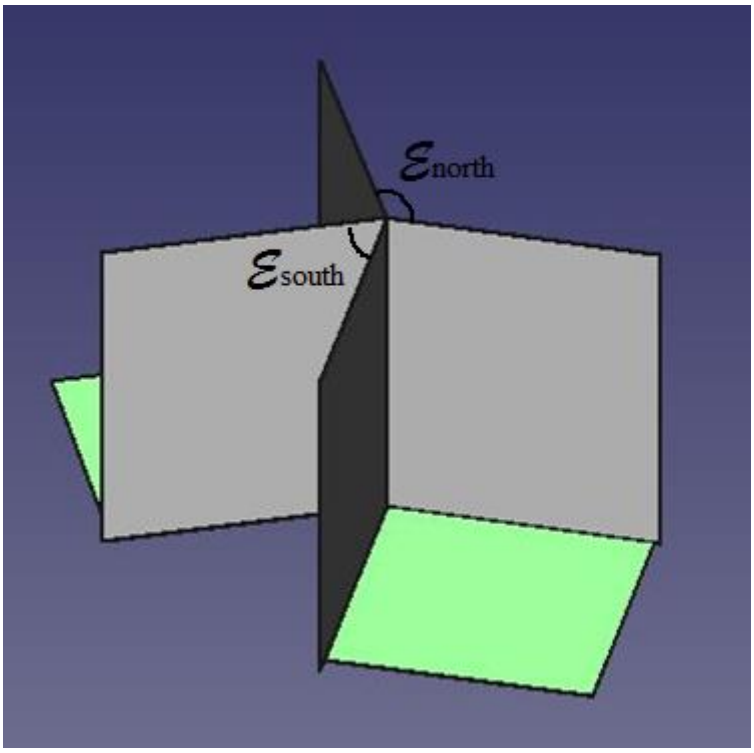

Figure 102 – Proposed model for the bidirectional CR: green faces are the horizontal square bases and grey faces are the vertical rectangular plates.

The bidirectional CR presented some features to allow displacement measurement through techniques other than InSAR. The vertical rod, where the individual CRs were welded, contained a screw thread at its top to allow the installation of a GNSS antenna. Besides, the bidirectional CR was installed on a metallic base, which contained a stair-like structure, authored by a team of LNEC's Scientific Instrumentation Centre, which enabled the bidirectional reflector to be moved along pre-defined directions by steps of fixed length. These features will be further explained in section 5.3.

The performed tests were complemented by the usage of two CRs of the triangular trihedral model, built in aluminium, which belong to the Faculty of Sciences of the University of Lisbon. The main idea was to compare the performance of the new proposed model with that of the CRs frequently found in the literature. As will be further discussed in section 5.3, one of these CRs was fixed, i.e., it was not equipped with the stair-like structure, while the other one was equipped with it and was subjected to the same tests as the bidirectional CR.

The InSAR displacements at the CRs were validated through comparison to other displacement measurement techniques: geometric levelling and continuous GNSS. Levelling was used for vertical displacement measurements at all CRs with respect to benchmarks considered fixed and located in the CRs' neighbourhood. GNSS was used only for the bidirectional CR to determine 3D displacements with respect to a reference GNSS antenna

installed nearby. For the comparison among distinct geodetic techniques, InSAR measurements from ascending and descending passes at the bidirectional CR were combined into vertical and horizontal displacements in the east – west direction, according to Equations (18) and (19) from Chapter 3. InSAR-derived vertical displacements were compared to the levelling and to the vertical GNSS measurements, while the east – west ones were compared to the GNSS east – west data. For individual CRs, both triangular and rectangular, the InSAR measurements were compared to the step lengths of the stair-like structure determined in laboratory.

5.3 Application to case study

5.3.1 Bidirectional corner reflector

The bidirectional corner reflector was installed at LNEC *campus*, in Lisbon, Portugal, in October 2017. The deployment of this CR comprehended two steps:

i. The selection of the installation place;
ii. The design of the CR in order to assure sub-millimeteric displacement dispersion at the selected location.

The location of the CR installation needed to have good visibility for both ascending and descending passes of the satellite, without any barriers, e.g., buildings or tall trees, which might block the signal between the CR and the sensor. A ground field with an area of, approximately, 200 m^2 and covered with grass was selected for the installation. The area was bordered at the north by a three storey building, there were two tall trees at opposite ends of the area and a small one, which did not block satellite visibility (Figure 103).

A concrete block with a base area of 1.30 m x 1.30 m and 0.60 m high was used for the CR installation. It was placed at the centre of the grass area, around 20 m away from the building, in order to avoid interference on the CR reflected signal caused by reflections on the building. The concrete block was installed in June 2016, several months before the CR, to allow it to settle due to its own weight before the beginning of the tests.

Two Sentinel-1A images from IW acquisition mode and level-1 Ground Range Detected (GRD) type were used to determine the average backscatter coefficient at the location for CR installation, for both the ascending and descending passes. The images' digital numbers were converted to backscatter coefficient values at Sentinel-1 toolbox, in SNAP software, freely provided by ESA. The conversion was based on a Look-Up-Table (LUT) provided with the

image metadata. Range-Doppler Terrain Correction was used to orthorectify the image[22], with 3" Shuttle RADAR Topography Mission (SRTM) DEM, from which resulted a spatial resolution of 7.9 m x 9.9 m projected on the ground for both ascending and descending passes. The average backscatter coefficient for the selected location was 0.2, in both passes, which led to a RCS_{bg} of, approximately, 16 dBm^2.

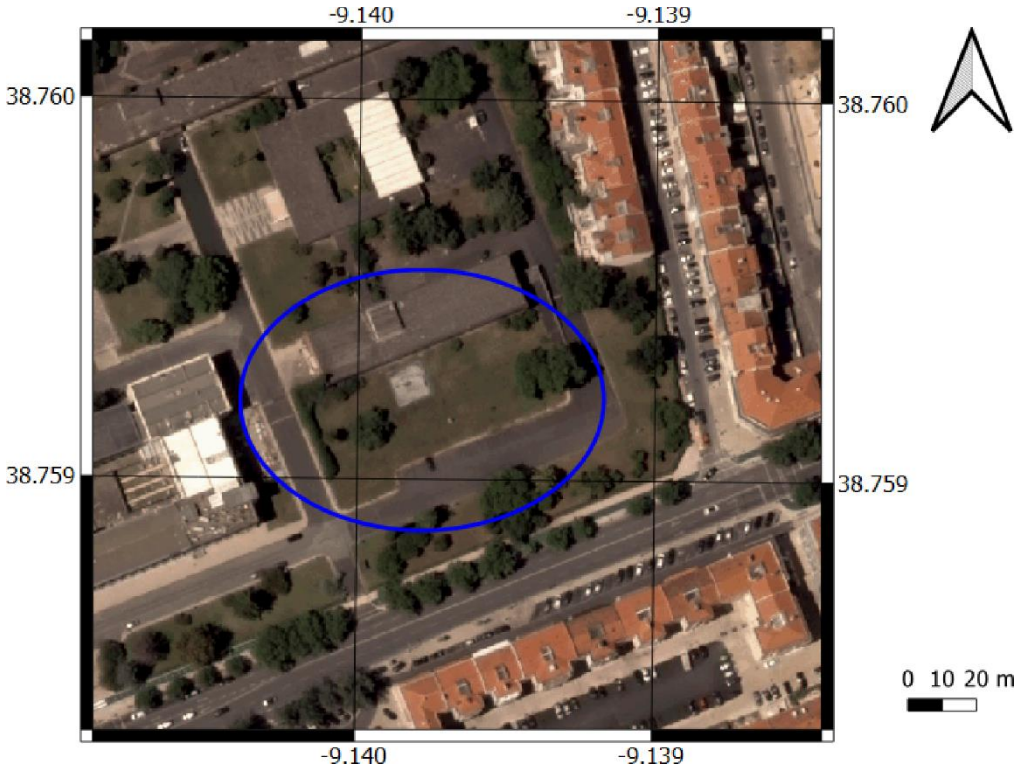

Figure 103 – Grass field and building (blue ellipse) where the experiment with the bidirectional CR was performed. Coordinate grid in WGS84.

The CR was constructed in aluminium, using perforated sheets. The used plates had a thickness of 1.5 mm, with holes having a diameter of 5 mm and organized in a staggered format forming angles of 60º. The horizontal distance between holes was 8 mm and the vertical distance was 7 mm. These plate properties led to a transmittivity of 33.4 dBm^2 for the ascending pass and of 32.8 dBm^2 for the descending one. The size of the vertical edge of the CR was fixed in 1 m and the size of the horizontal edge was determined in order to assure an SCR greater than 100, given the RCS_{bg} and the transmittivity T. The minimum size for the horizontal edge to allow the fulfilment of the mentioned requirements was 0.55 m, for both passes. In order to compensate eventual additional losses, e.g., due to plate undulation or non-orthogonality of the plates in each individual CR, the horizontal edge was set to a length of 0.60 m, which led to an

[22] Image distortions were corrected based on a DEM to approximate the image to the terrain geometry (ESA, 2020).

SCR of 147 for the ascending pass and of 164 for the descending one. The achieved SCRs led to a displacement dispersion $\sigma_{d^{LOS}}$ of 0.3 mm for the ascending pass and of 0.2 mm for the descending one. The cause for the distinct values was the difference of almost 5º in the incidence angle between the two passes, which induced a larger loss of signal for the ascending geometry. Both reflectors fulfiled the requirement of enabling sub-millimetre precision measurements.

The angles between the horizontal edges of the individual CRs were determined. The angle between the projection of the LOS onto the horizontal plane and the east – west direction, β, for the CR latitude and Sentinel-1A orbit was found to be -10.5º, which resulted in a ε_{south} of 69º and a ε_{north} of 111º. The orientation of the bidirectional reflector was aided by a magnetic compass, with the individual CR for the descending pass being aligned with its respective LOS. The CR construction requirements assured the correct orientation of the individual CR of the ascending pass towards its LOS, after the orientation of the descending one. The descending pass individual CR was oriented with respect to the geographic north. In order to allow the correct orientation of the CR using the magnetic compass, the difference between the geographic and the magnetic norths was considered. A topographic map at the scale 1:25000 from 2009 by the Centre of Geospatial Information of the Army was used to determine the angle between magnetic and geographic norths, which in 2017 when the CR was installed, was of 2º. Therefore, the individual CR for the descending pass was aligned with the direction forming an angle of 102.5º with respect to the magnetic north. The error comitted in the orientation with the magnetic compass was 2º, which corresponded to the smallest division in the measuring scale. Figure 104 shows the proposed bidirectional CR after installation.

The base of the CR contained three stair-like structures, which supported the CR and along which it was displaced. Ascending and descending pass images at the ROI were acquired with a difference of six days. The bidirectional CR was left at the same step of the stair-like structure until one image from each geometry was acquired. After that, the CR was moved into the following step. In this particular application, the CR was moved during the time interval between the acquisition of the descending pass at 6:43 am and the acquisition of the ascending pass at 6:35 pm six days later. Thus, for each CR position on the stair, there was an image with ascending geometry and another from the descending one. The stair-like structure had an inclination that assured the CR was displaced along a direction that formed an angle to the vertical equal to the incidence angle of the LOS of the descending pass. The stair-like structure could be rotated around the vertical axis in order to allow the displacement of the CR to occur in other directions.

Figure 104 – Bidirectional corner reflector proposed in this study.

Three displacement tests were designed: one set of displacements along the descending pass LOS, another set along the east – west direction and a final set along east-northeast, such that the angle between this direction and east – west was the same angle between LOS and east – west. The idea behind the rotations was to verify and quantify the eventual loss of measurement precision when the movement occurred along different directions. Although the stair-like structure was rotated, the CR design assured each individual CR kept oriented towards the respective LOS. The stair was composed of 14 steps, of 12 mm each (Figure 105).

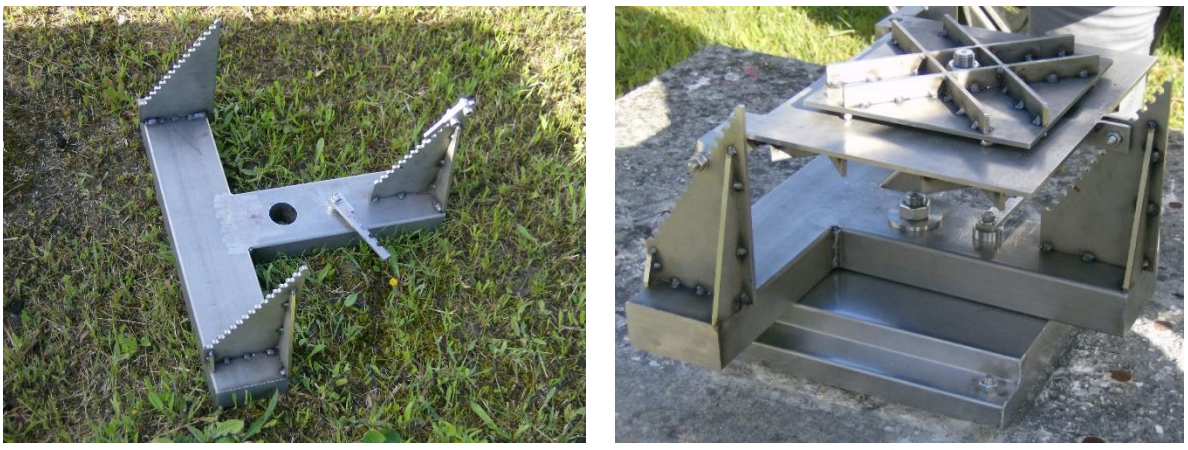

(a) (b)

Figure 105 – Stair-like structure to move the bidirectional CR with the handle at the central part of the structure allowing the rotation of the stairs around the vertical axis (a) and installation of the stair-like structure on the concrete block (b).

5.3.2 Triangular trihedral corner reflectors

The installation of the triangular trihedral CRs followed the opposite logic of that of the bidirectional one. As the CRs were already built, it was necessary to select a location at LNEC *campus* where CRs with their characteristics would enable displacement determination with sub-millimetric precision. The CRs are formed by three isosceles triangles, with the edge that contains the CR vertex having a length of 1 m. RCS of triangular trihedral CR is determined from Equation (63) instead of Equation (53):

$$\mathrm{RCS_{TT}} = \frac{4\pi a^4}{3\lambda^2} \tag{63}$$

where $\mathrm{RCS_{TT}}$ is the RCS for a triangular trihedral CR, a is the edge length and λ is the wavelength (Qin *et al.*, 2013). This resulted in a RCS of 31 $\mathrm{dBm^2}$. In order to achieve an SCR above 100, $\mathrm{RCS_{bg}}$ had to be lower than 11 $\mathrm{dBm^2}$, which corresponded to a backscatter coefficient of 0.15. The final SCR was of 106. Sentinel-1A images from IW acquisition mode and level-1 GRD type, used at section 5.3.1 for the bidirectional CR, were used to identify the locations where the backscatter coefficient criterion was met. Besides the backscatter coefficient, other information was considered in the selection, such as a grass background, unobstructed view to the satellite and the feasibility of transporting and installing the concrete blocks used as bases. The two CRs were installed around 80 m apart from each other and 400 m away from the bidirectional CR (Figure 106).

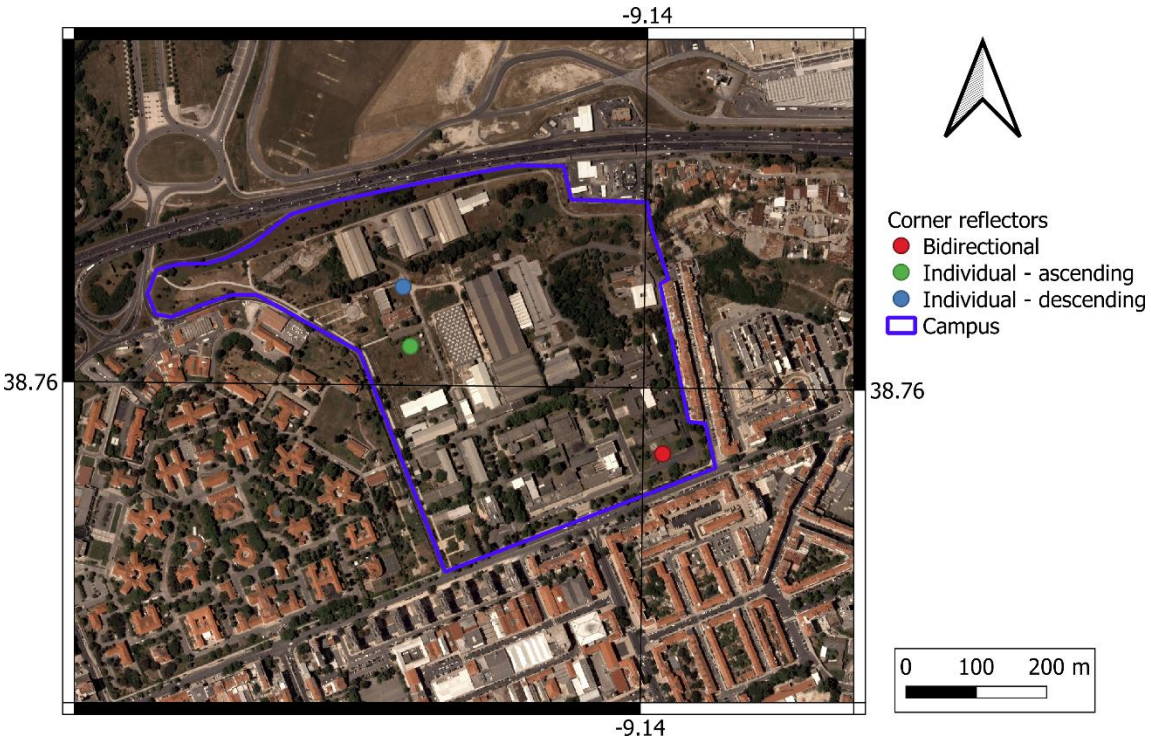

Figure 106 – Location of the three CRs at LNEC *campus*. Coordinate grid in WGS84.

One of the triangular trihedrals was oriented towards the ascending pass and the other to the descending. The CR for the ascending pass was installed in December 2016. It was fixed during the whole testing time, as it was not equipped with the movable device. The CR was oriented using the magnetic compass, towards the ascending geometry LOS. The angle between the LOS projection onto the horizontal plane and the magnetic north was 261.7º. The magnetic declination used to correct the difference between the geographic and magnetic norths was refered to the year 2016, as this CR was installed earlier than the bidirectional one. This CR also had to be oriented at the vertical plane, being aligned to the ascending pass LOS.

The CR oriented towards the descending pass was installed in March 2017. It was equipped with a moving device equal to that of the bidirectional CR, which enabled its movement along 14 steps of 12 mm each. The shape of the stair-like structure and the rotation mechanism were equal to those of the bidirectional CR, in order to compare the performance of each model under the same conditions. The horizontal orientation was executed in the same way of the previous CRs, aligning the device with the same azimuthal direction of the bidirectional CR. This triangular trihedral device was tilted around a horizontal axis, similar to the one oriented towards the ascending pass, until it became aligned with the descending pass LOS (Figure 107).

Figure 107 – Individual CR of the triangular trihedral model oriented towards the LOS of the descending pass.

5.3.3 Validation and uncertainty assessment tests

The CRs were prepared to be subjected to four validation and uncertainty assessment tests: one static and three sequences of imposed displacements. However, due to a failure in one of the CRs that reduced the time available for the tests, only the static and two of the sequences of imposed displacement were executed. The installation of the CR infrastructure was completed in October 2017 and InSAR, levelling and GNSS data started to be collected.

5.3.3.1. The first performed test was the static one. The three CRs were left static during the whole test, levelling was performed every two weeks and GNSS data was continuously acquired. Sentinel-1A/B images were used, with a new image acquisition every six days.

On March 2018, strong wind damaged the base of the bidirectional CR, causing vibrations in the structure. The device had to be uninstalled, repaired and reinstalled. Although there were not gaps in the image acquisition and the design of the CR assured the recuperation of the original orientation, the GNSS data revealed the failure occurred a few days before its detection and images had been acquired with the damaged CR. Therefore, the previous measurements were discarded and March 2018 became the reference epoch for the analysis. The test was executed between March and December 2018.

During the tests, it was verified the concrete block of the bidirectional CR was tilting towards west. The concrete block was installed at a small slope facing south (to assure enough distance with respect to the nearby building) and it was levelled placing stone blocks under it. The burial of some of the blocks due to the concrete block weight might have caused the tilting. In order not to change the CR orientation during the tests, the concrete block was levelled, in September 2019, between the first and the second sequences of imposed displacements, by placing additional stone blocks. Besides the mentioned tilting of the concrete block for the bidirectional CR, all concrete blocks settled during the first months after installation and after that they presented seasonal displacements, with an amplitude of, approximately, 2 mm, showing uplift in winter and settlement in summer, compatible to displacements caused by seasonal variations of moisture on the ground. After the damage in March 2018, the bidirectional CR did not show signs of ageing until the end of the tests. On the other hand, the individual triangular trihedral CRs displayed signs of progressive degradation throughout the tests, such as increasing vibration or screw loss.

5.3.3.2. The second test was the first sequence of imposed displacements, in which the bidirectional CR and the individual triangular trihedral CR oriented towards the descending pass were moved along the LOS direction of the descending pass. This test was executed

between January and June 2019. The CRs were moved between the acquisition times of a descending and the following ascending images. Only Sentinel-1A images were utilized, with a new image every 12 days, to enable the conciliation of this work with the other tasks of the levelling team. GNSS data was acquired continuously. The levelling operation was performed at the days the CRs were lifted. The levelling of the centre of the individual triangular trihedral oriented towards the descending pass was interrupted on the 8th position of the stair-like structure, as due to the terrain configuration, CR inclination and direction of movement, the levelling rod was obstructed by the CR wall. As the vertical distance between the steps in the stair-like structure was known with a precision of one tenth of millimetre (measured at laboratory) and vertical displacements of the corners of the concrete block were known from levelling, the vertical displacement of the CR centre was estimated by adding the concrete block and the step vertical displacements, assuming the remaining metallic structure did not contribute to the vertical displacements.

5.3.3.3. The third test was the second sequence of imposed displacements, with the bidirectional CR and the individual triangular trihedral CR oriented towards the descending pass being moved along the east – west direction. The test was executed between September 2019 and February 2020. Only Sentinel-1A images were used, with a new acquisition every 12 days. Levelling kept being performed on the days the CRs were lifted. Due to team unavailability, it was not possible to execute one of the moving operations. On the following lifting of the CRs, the devices were moved two steps instead of one to compensate the missing observation and to keep the simulation of linear displacement. Besides, the double step enabled the evaluation of the capability of InSAR to deal with displacement steps of larger magnitude than those being tested in this experiment. Due to the difference in the CR displacement direction with respect to the previous test, it was possible to level the centre of the individual triangular trihedral CR oriented towards the descending pass for all epochs. However, one of the corners of its concrete block was excluded from the levelling operation, as it was obstructed by the moving device. The ascending and descending images corresponding to the missing step were not included in the InSAR processing. In December 2019, one of the levelling benchmarks was vandalised and a new point was materialised. This rematerialisation was not a problem, as the levelling line included a second benchmark. Therefore, for this test, only the second benchmark was used. GNSS was continuously acquired and processed into daily solutions.

5.3.3.4. InSAR displacement validation was performed through comparison of double-differences from InSAR and from one of the *in situ* techniques, where displacements between two epochs (differencing in time) for both techniques were referred to the displacements of the

benchmarks of those techniques (differencing in space), on the assumption that there were no relative displacements between the two benchmarks. In some cases, the length of the stair-like structure steps, measured in laboratory, was also used for validation.

This evaluation was executed through a hypothesis test. Let us assume the double-differences achieved through InSAR or one of the validation *in situ* geodetic techniques were samples from a random variable with normal distribution. The test evaluated if the average values of the populations of double-differences from each pair of techniques could be considered equivalent for a certain level of significance. As each technique had distinct precision levels associated, it was considered that the sample variances were different; therefore, the Welch t test for unequal variances was executed (Welch, 1938; Hayes and Li, 2007). The test statistic, v, was as in Equation (64):

$$v = \frac{\overline{d_{InSAR}} - \overline{d_{reference}}}{\sqrt{\frac{S_{InSAR}{}^2}{n_{InSAR}} + \frac{S_{reference}{}^2}{n_{reference}}}} \tag{64}$$

where $\overline{d_{InSAR}}$ was the average double-difference achieved through InSAR for a certain CR for all observation epochs, $\overline{d_{reference}}$ was the average double-difference achieved through one of the reference techniques for the same CR for all observation epochs, $S_{InSAR}{}^2$ was the sample variance of the InSAR double-differences, $S_{reference}{}^2$ was the sample variance of the reference double-differences, n_{InSAR} was the sample size of InSAR double-differences and $n_{reference}$ was the sample size of reference technique double-differences. Test statistic v could be approximated by a t distribution with degrees of freedom f as in Equation (65), rounded to the closest integer, adapted from Welch (1938):

$$f = \frac{\left(\frac{S_{InSAR}{}^2}{n_{InSAR}} + \frac{S_{reference}{}^2}{n_{reference}}\right)^2}{\frac{S_{InSAR}{}^4}{n_{InSAR}{}^2 \cdot (n_{InSAR} - 1)} + \frac{S_{reference}{}^4}{n_{reference}{}^2 \cdot (n_{reference} - 1)}} \tag{65}$$

with the same variable meanings as in Equation (64).

The null hypothesis for the test H_0 was the average double-differences from both techniques were equal, against the alternative hypothesis H_A – the average double-differences from both techniques were different. The test statistic v was compared to a t distribution with f degrees of freedom, t_f, for a level of significance of 0.05. A two-tail test was performed using Excel t-Test: Two-Sample Assuming Unequal Variances algorithm. The acceptance region for H_0 was the interval between $-t_f$ and $+t_f$; therefore, if the test statistic was inside the acceptance region, H_0 was accepted, meaning both techniques measured the same average double-differences. If the

test statistic was outside the acceptance region, H_0 was rejected and the average double-differences from both techniques were considered to be different from each other.

The method used for uncertainty evaluation was that proposed in Ferretti, Savio, *et al.* (2007), which determined the measurements' precision based on the standard deviation of the differences between the two techniques. The method was identified on Table 10 with the symbol $*^2$.

5.3.4 PSI processing

The InSAR technique whose uncertainty was evaluated in this thesis was the PSI method implemented in SARPROZ© software (Perissin *et al.*, 2011). The PSI method used for this evaluation was not the one used in the previous Chapters, though. As only a small neighbourhood of each CR was analysed, APS estimation was not required, because, due to the proximity between the PS on the CR and the reference PS, both points were subjected to the same atmospheric conditions and when the double-differences were computed, the atmospheric component was cancelled. Therefore, the *small areas* module implemented in the software was used instead of the main PSI algorithm. This module is appropriate to perform local analyses, e.g., for individual structures, instead of the analysis at regional scale common in PSI.

For each executed test, a distinct dataset of SAR images was used and the several datasets were processed independently of each other. The pre-processing steps for the usual PSI method and the one applied in this Chapter were the same. For each dataset, an area of 16 km x 16 km was selected for the pre-processing steps of the analysis. A master image was selected in order to minimise the temporal and normal baselines and the remaining images were coregistred with respect to its geometry. A GCP was manually selected to align the SAR data with the EU-DEM, which was used together with the orbits to remove flat terrain and topographic components of phase. Instead of progressing to APS estimation after this step, the analysis was continued in the *small areas* module, where an area corresponding to LNEC *campus* was selected on the reflectivity map. A selection of points to analyse was performed, based on their reflectivity values, for which residual height and average velocity were estimated. Unlike the research in previous Chapters, a linear displacement model was used for all tests, as that was the type of movement imposed on the CRs. Only the PSs on the CRs and the benchmark PSs were considered for analysis.

The images used in this research were from Sentinel-1A/B satellites, from IW imaging mode, TOPSAR acquisition mode and provided in SLC format, similar to the Sentinel-1 data

used in previous Chapters. The orbits also presented an accuracy of 2 cm to 3 cm at radial and cross-track directions, respectively, and of 5 cm at along-track direction (Sandwell *et al.*, 2016). Spatial resolution was of 20 m in azimuth and 5 m in slant range. The wavelength of the signal emitted by the SAR-C sensor on Sentinel-1A was 55 mm.

The first test (the static test) used Sentinel-1A/B images acquired between March and December 2018, every six days. The images from the ascending pass were from relative orbit 45 and subswath 2. Forty-eight images were available from both satellites. Scenes from Sentinel-1A were from March 21, 2018 to December 22, 2018 and those from Sentinel-1B were from March 27, 2018 to December 28, 2018. The image from July 31, 2018 was automatically selected as master, originating maximum temporal baselines of five months and normal baselines lower than 110 m (Figure 108).

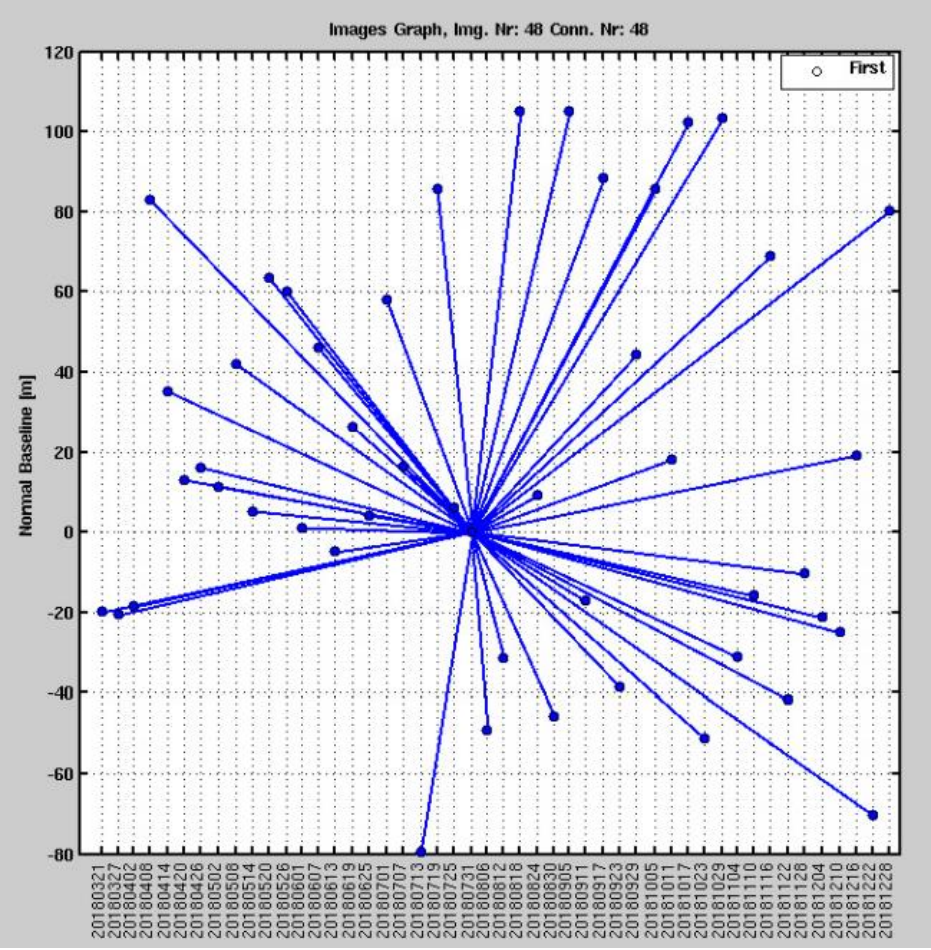

Figure 108 – Distribution of normal and temporal baselines for the ascending pass at the first test.

The images from the descending pass were from relative orbit 125 and subswath 1. This dataset was also composed by 48 images from the sensors on both satellites, with scenes from Sentinel-1A acquired between March 27, 2018 to December 28, 2018 and those from Sentinel-

1B between March 21, 2018 to December 22, 2018. The master image was from August 12, 2018. Temporal baselines reached five months and normal baselines were also lower than 110 m (Figure 109).

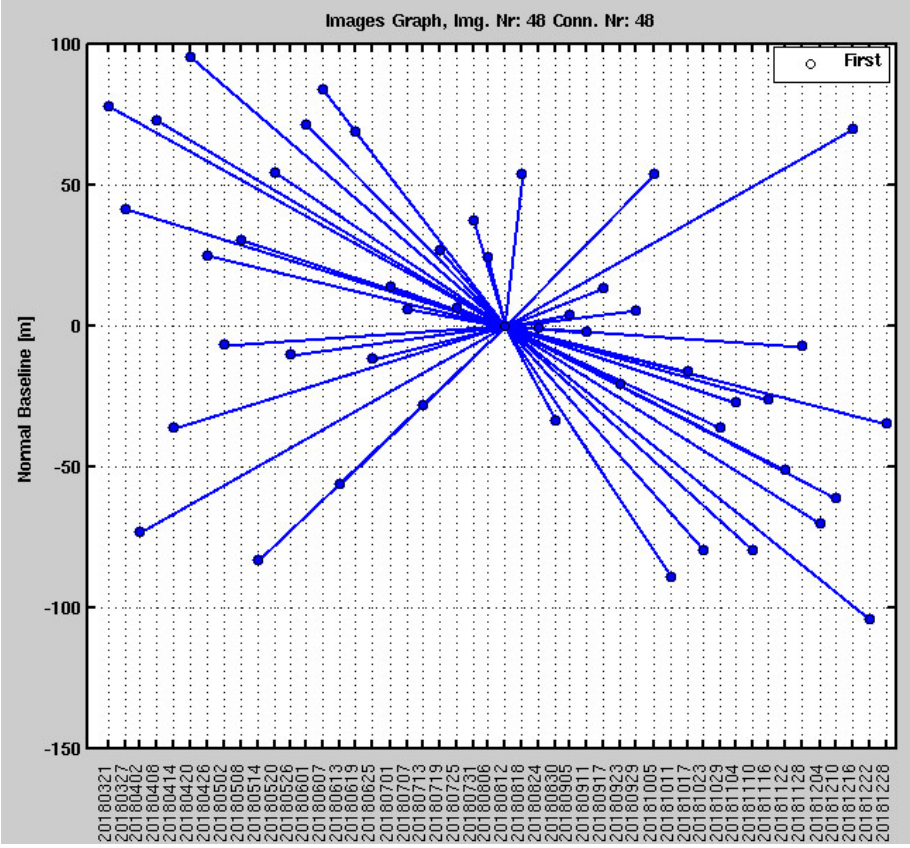

Figure 109 – Distribution of normal and temporal baselines for the descending pass for the first test.

The second test (first sequence of imposed displacements) was performed with Sentinel-1A images, acquired every 12 days. The same relative orbits of the static test were used (orbit 45 for ascending pass and 125 for the descending). The test was performed between January and June 2019 and 14 images of each geometry were considered: one for each step of the stair-like structure. Ascending images were from January 3, 2019 to June 8, 2019, with master in April 9, 2014.Descending images were from January 9 to June 14, 2019 and the master was from March 22, 2019. Temporal baselines reached three months in maximum at both geometries. However, descending pass presented larger normal baselines: while for the ascending pass the baselines were lower than 100 m, for the descending one they reached 180 m (Figure 110).

The third test (second sequence of imposed displacements) also used images only from Sentinel-1A images, with a revisit period of 12 days. The same relative orbits and subswaths from the previous tests were used and the analysis was executed between September 2019 and February 2020. The ascending pass included only 12 images instead of the planned 14: one was

purposefully removed due to the missing lift of the reflector (section 5.3.3) and the other was an acquisition gap from the sensor. The images were acquired between September 24, 2019 and February 15, 2020, with master image from November 23, 2019. For the descending pass, there was only one gap in the image time series, which corresponded to the excluded image. Thus, 13 scenes were used. The data were acquired between September 18, 2019 and February 21, 2020, with master image from November 29, 2019. Both datasets presented maximum temporal baselines of three months. Normal baselines were lower than 150 m for the ascending pass and lower than 180 m for the descending one.

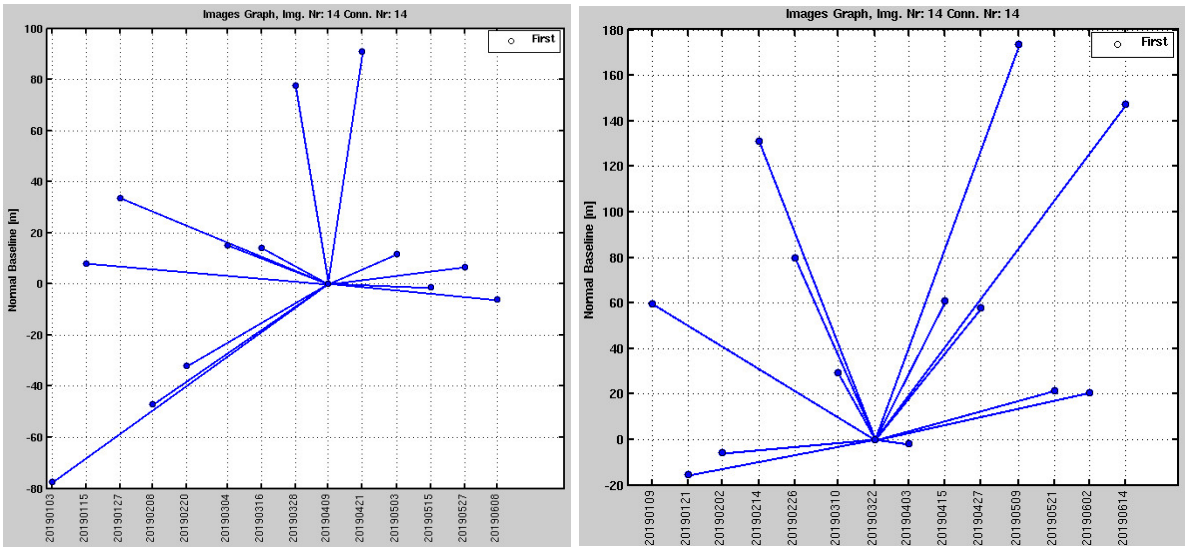

(a) (b)

Figure 110 – Distribution of normal and temporal baselines for the ascending pass (a) and for the descending pass (b) for the second test.

5.3.5 *In situ* measurements

Two *in situ* geodetic techniques were used to validate the PSI measurements at the CRs: geometric levelling and GNSS (Figure 111). Geometric levelling allowed the measurement of vertical displacements with a precision of one tenth of the millimetre. It was executed using an optical precision level Wild NA2 with an optical micrometre GPM3 and a levelling rod with an invar scale. The level was installed at the middle of the two object points whose height difference was intended to be determined. The levelling rod was placed on each object point and the height difference between them corresponded to the difference between the readings at the levelling rod. The surveys were performed by the topographic team of LNEC's AGU. For each CR, vertically stable points in the neighbourhood were identified and selected as benchmarks for the operation. These points were located on small walls and were materialised

through nails in order to not damage the wall and to not attract attention, trying to prevent vandalism. Two levelling lines were built at LNEC. The line for the bidirectional reflector was formed by eight points: two benchmarks and six object points. One of the benchmarks was located on a wall east of the CR, while the other one was located on the floor, next to a traffic signal, west of the CR. This last benchmark was included because it was verified on PSI processing that there was a PS at that location, which was needed to perform the validation. The object points were the four corners of the concrete block used as base, which were observed to evaluate the stability of the block where the CR was deployed, and two nails at the CR, one in each individual reflector. The selected nails were the closest to the CR reflective centre.

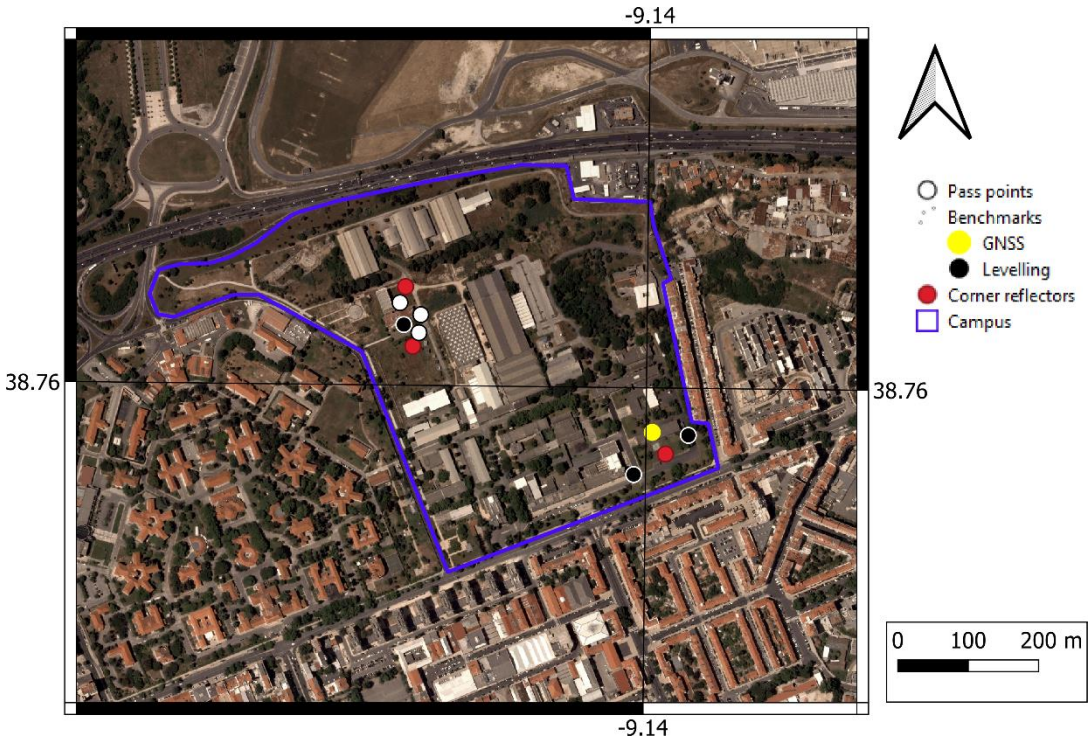

Figure 111 – Location of CRs, pass points (except concrete block corners) and benchmarks for levelling and GNSS. Coordinate grid in WGS84.

The second levelling line included the two individual triangular trihedral CRs. There were 14 points at the line: one benchmark, three passing points and 10 object points. The benchmark was located on a small wall and it was materialised by a nail. The passing points were used to transport the height values from one CR to the other and were located at the base of a lamp post and on sidewalks. The object points were the four corners of each concrete block and the centres of the CRs. It was not possible to assure multitemporal measurements exactly at the same point at the triangular trihedrals' corners, due to the difficulty in placing the levelling rod univocally at all epochs. Therefore, a metallic piece was placed at the CR corner in order to allow the placing of the levelling rod without being obstructed by the CR walls (Figure 112). As the base

of the levelling rod was flat, this strategy assured the highest point in the metallic piece was the observed point at all epochs.

Figure 112 – Levelling rod at the centre of triangular trihedral with the aid of a metallic piece.

The levelling operation was composed by two parts: levelling and counter-levelling. During the levelling, all points were observed following a certain order. The points were then observed in reverse order (counter-levelling) and the height differences between the same points from levelling and counter-levelling were compared. Whenever the difference between the observations was larger than the tolerance 0.35 mm, the measurements were repeated. The average value of the height differences of both observations was considered to transport the height information for all the points in the levelling line. Levelling operation was executed on the days the CRs were moved along the stair-like structure. Thus, for each step of the stair, there was always a levelling measurement and a PSI observation at ascending and descending passes.

The other technique used for validation was GNSS. Two sets of equipment were used for displacement measurement. The receivers were Topcon GB-1000, which enabled a precision measurement for horizontal displacement of 3 mm + 0.5 ppm of the baseline length and 5 mm + 0.5 ppm of the baseline length for vertical displacement in static mode (UNAVCO, 2020b). Choke ring antennas were used combined with those receivers to reduce multipath effects. The two sets of equipment were deployed to enable the observation in relative mode. One of the antennas was installed at the screw thread at the top of the vertical rod of the bidirectional CR. The antenna was connected to the receiver through a 30 m long cable, as the receiver was installed at the basement of the nearby building to enable its connection to electrical power. The second antenna was installed at

the roof of the building and it was connected to the receiver installed inside the building. This was the reference antenna and the displacements of the antenna on the CR were determined with respect to this one. Data from both GPS and GLONASS (GLObal NAvigation Satellite System, a Russian system) were used in the calculations, which were performed through Topcon Pinnacle® commercial software. Thanks to the small distance between the two antennas (around 38 m), only L1 observations were used and a mask for rejecting satellites observed at less than 10º above the horizon was applied. The Goad-Goodman model was used to model atmospheric effects, which considered the atmosphere divided into two parts (Goad and Goodman, 1974 as cited in Şanlioğlu and Zeybek, 2012). Both antennas were installed permanently and were continuously registering data. Whenever precise orbital data were not available, they were downloaded from NASA[23]. Daily solutions were computed for all days since the beginning of the experiment and noise reduction techniques such as low pass filters were not applied.

5.4 Results

5.4.1 Amplitude analysis

This section presents the results achieved for the tests performed at the CR infrastructure.

The first quality verification of the CRs' deployment was their representation on the SAR amplitude images. Figure 113 presents a backscatter coefficient image acquired after the CRs installation from an ascending geometry. Both bidirectional and individual triangular trihedral CRs were represented by a bright pixel in the image, meaning their reflectivity was high. The backscatter coefficient of the bidirectional CR (1.7) was larger than that of the individual triangular trihedral (1.2). The CRs' reflectivities also influenced neighbour pixels of those corresponding to the CRs, maybe due to signal saturation. The backscatter coefficients of the bidirectional and of the individual triangular trihedral corner reflector oriented towards the descending pass were also high in the corresponding image (Figure 114). The difference between CR reflectivities was even more evident in this case, with the bidirectional CR presenting a value of 2.6 and the individual trihedral of 0.8. Thus, for both geometries, the bidirectional CR proposed in this thesis achieved a larger reflectivity than those from the traditional model.

[23] ftp://cddis.nasa.gov/gnss/products/

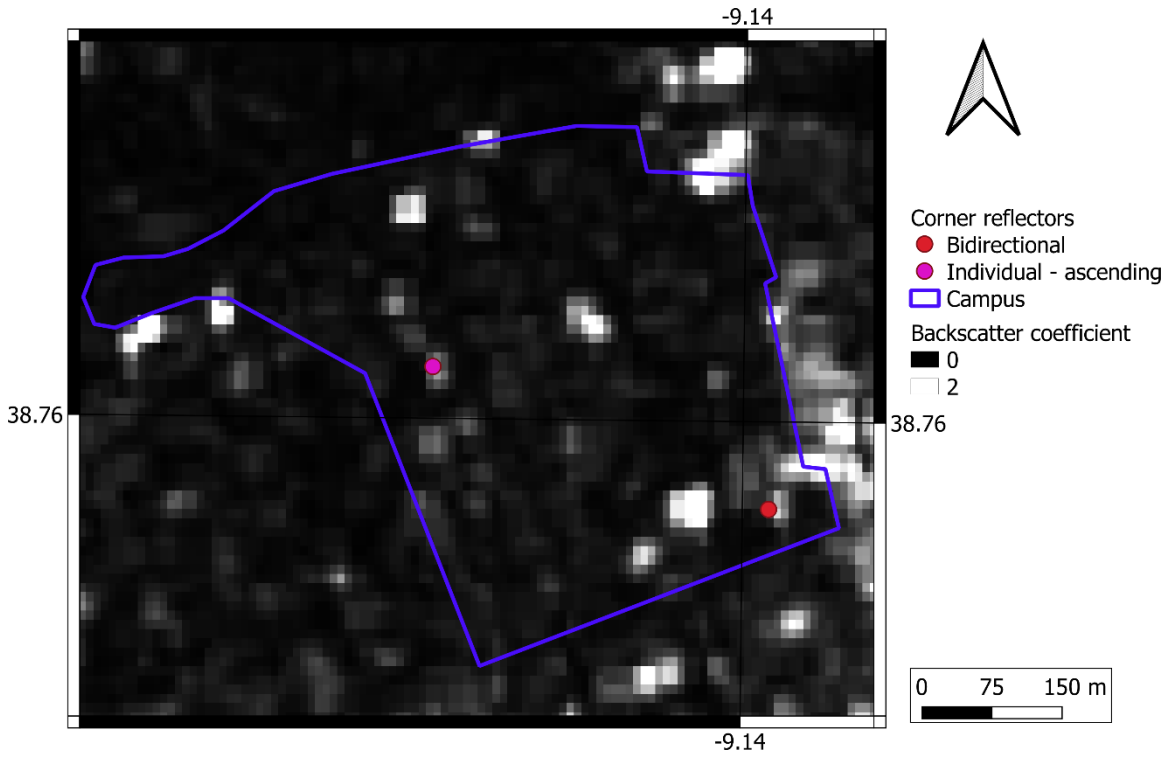

Figure 113 – CRs oriented towards the ascending pass represented on a backscatter coefficient image from October 30, 2019. Coordinate grid in WGS84.

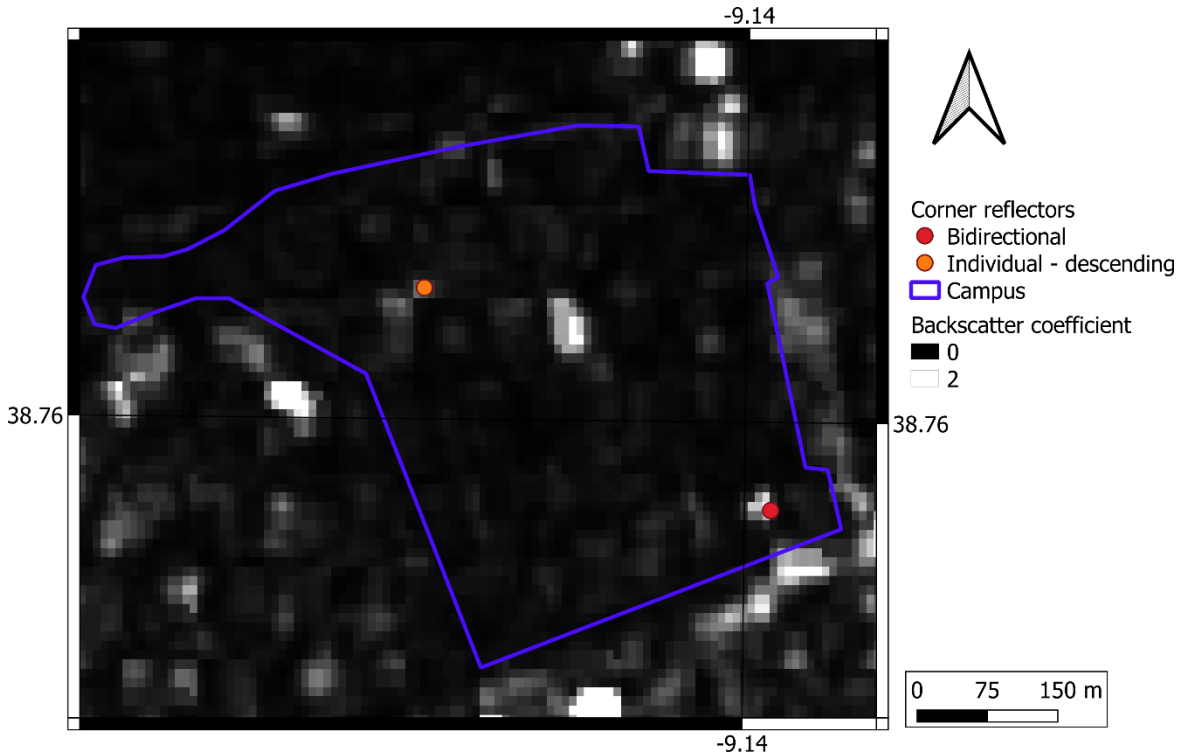

Figure 114 – CRs oriented towards the descending pass represented on a backscatter coefficient image from November 5, 2019. Coordinate grid in WGS84.

The larger reflectivity of the bidirectional CR with respect to those of the traditional model might be due to the better reflective performance of rectangular trihedrals with respect to

triangular ones. Table 11 presents the RCS for each CR tested in this research, following Equations (53) and (63). Each rectangular trihedral from the bidirectional CR was considered as an individual CR. Both rectangular CRs presented larger RCS than the triangular ones. Besides, the larger backscatter coefficient of the rectangular trihedral for the descending pass with respect to the ascending one might also be explained by the differences in RCS, as the rectangular CR for the descending pass had a larger RCS due to the smaller transmittivity, when compared to that of the ascending pass.

Table 11 – RCS of rectangular and triangular trihedrals with the properties tested in this experiment.

Corner reflector		RCS (m^2)
Rectangular	Ascending	2297
	Descending	2572
Triangular	Ascending	1385
	Descending	1385

The CRs' amplitudes were evaluated during the static test. All models presented relatively stable amplitude during the nine months of the evaluation (Figure 115). The rectangular trihedrals had larger amplitude than the triangular ones from the corresponding geometries. Instabilities in the amplitude time series, more evident at the triangular trihedral CRs, might be due to the presence of water or dirt during image acquisitions. For comparison purposes, the amplitude time series of a natural PS is presented in Annex A.3 Figure 160, where the larger variability along the time series and the lower amplitude values of the PS with respect to the CRs are visible.

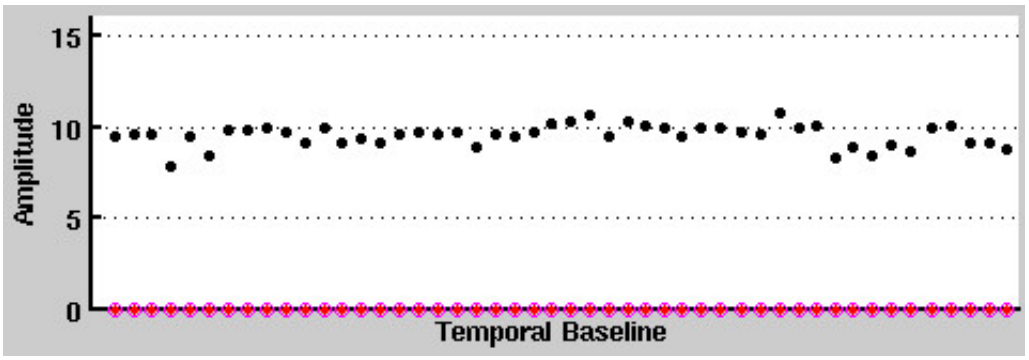

(a)

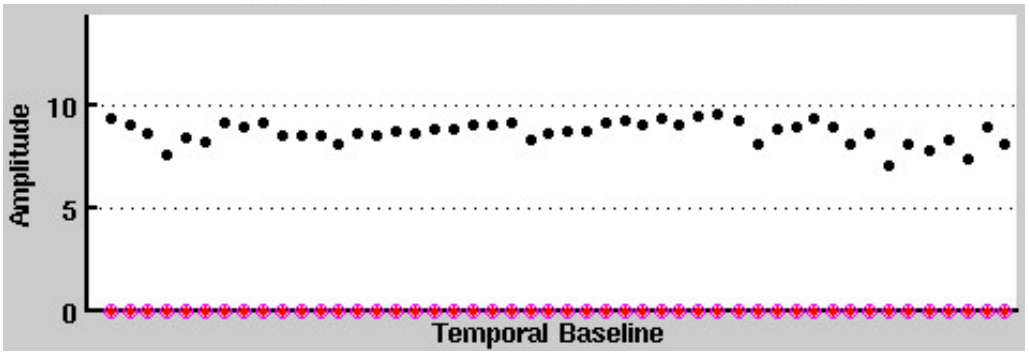

(b)

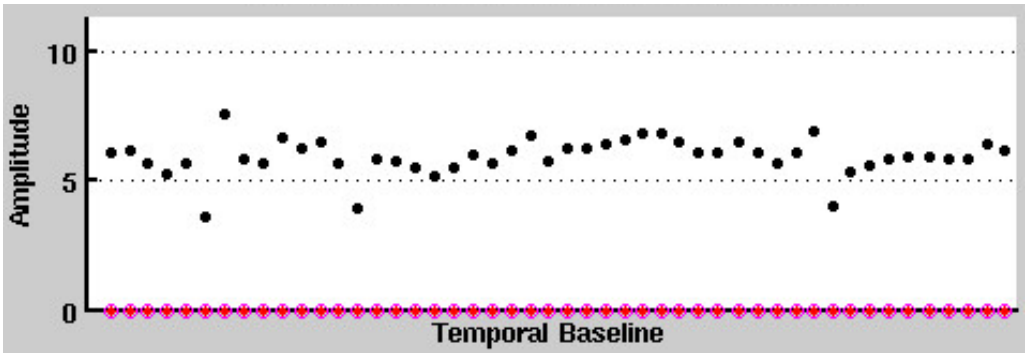

(c)

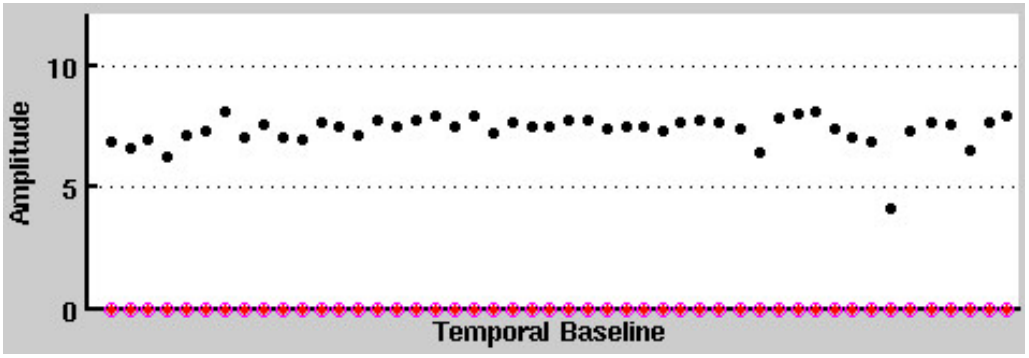

(d)

Figure 115 – Amplitude (equalised and non-calibrated values) time series achieved for the CRs during the static test: (a) rectangular trihedral for ascending pass, (b) rectangular trihedral for descending pass, (c) triangular trihedral for ascending pass and (d) triangular trihedral for descending pass.

5.4.2 Displacement analysis – static test

The second quality assessment of the CRs performance was the displacement validation and uncertainty determination. The first proposed test was the static one, in which all CRs were fixed during the whole experiment. The execution of the static test was hindered by a meteorologic event. In October 2018, Lisbon was hit by hurricane Leslie, which was characterised by strong winds and caused some damage at LNEC *campus*, namely the fall of tree branches. At that time, displacement anomalies were found in some of the analysed data that suggested the elements behaving as PSs that were being used as benchmarks for PSI had been displaced during the hurricane (Annex A.3 Figure 161). Therefore, the conditions assumed for the tests execution were not met and those tests were excluded from the analysis.

Performance evaluation was executed for individual rectangular and triangular trihedrals through comparison of PSI, GNSS and levelling double-differences along LOS, which corresponded to the CR displacements with respect to a benchmark. In the following text, the words double-difference and displacement are used with the same meaning.

The used measurements have associated uncertainties. In the case of PSI double-differences, they resulted from the propagation of the displacement dispersions of the PS in the CR and of the PS used as reference to the double-difference between the two PSs, following Equation (28) in Chapter 4. In this case, point p in Equation (28) was the PS on the CR and point q was the reference PS. The displacement dispersion of each PS depended on the point temporal coherence and it was computable from Equation (20) in section 3.4.1. The uncertainty of the levelling measurements was considered to be of 0.3 mm, corresponding to the tolerance value to the difference between levelling and counter-levelling observations projected to LOS. The uncertainty of the GNSS measurements was assessed during the data processing. The standard deviation of the three dimensional double-differences reached a maximum of 0.4 mm for both horizontal components and a maximum of 1.0 mm for the vertical one[24], which resulted in a standard deviation of 0.8 mm for double-differences along LOS.

The performance of the individual rectangular and triangular CRs oriented towards the ascending pass was evaluated by comparison of PSI to levelling. For the rectangular trihedral, only the benchmark to the west of the CR was considered (Figure 116). From May 2 to May 14, 2018, there was a discontinuity at PSI double-differences time series, with the CR seeming to have moved 6 mm away from the sensor. As the levelling showed the CR did not present

[24] The baseline had a length of 38 m, the baseline component in north – south direction was 32 m, in the east – west direction was 18 m and in the vertical direction was 11 m.

that behaviour, it was likely that the observed anomaly occurred at the reference PS, which might be a traffic sign on the sidewalk.

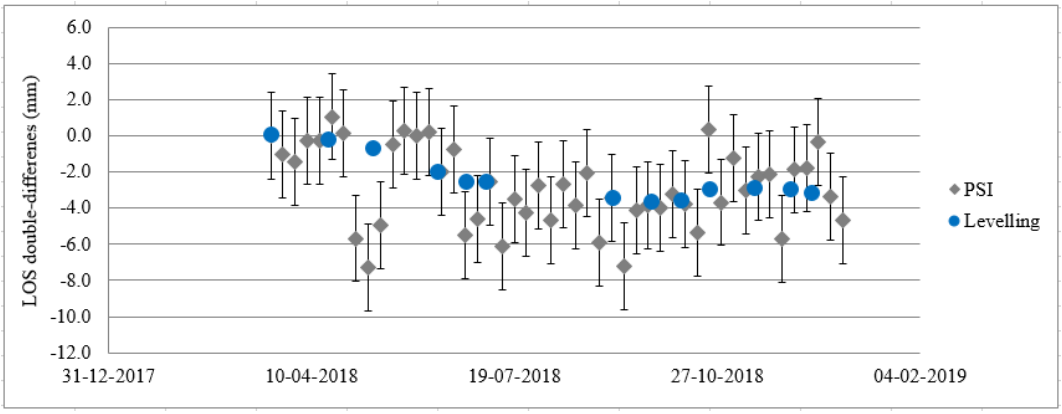

Figure 116 – LOS displacement from PSI and levelling for the rectangular trihedral CR for the ascending pass in the static test, for the reference PS to the west of the CR; error bars are the uncertainty of double-differences.

For the triangular trihedral CR (Figure 117), PSI reference was considered to be the closest PS to the levelling benchmark and the double-differences from both techniques were similar.

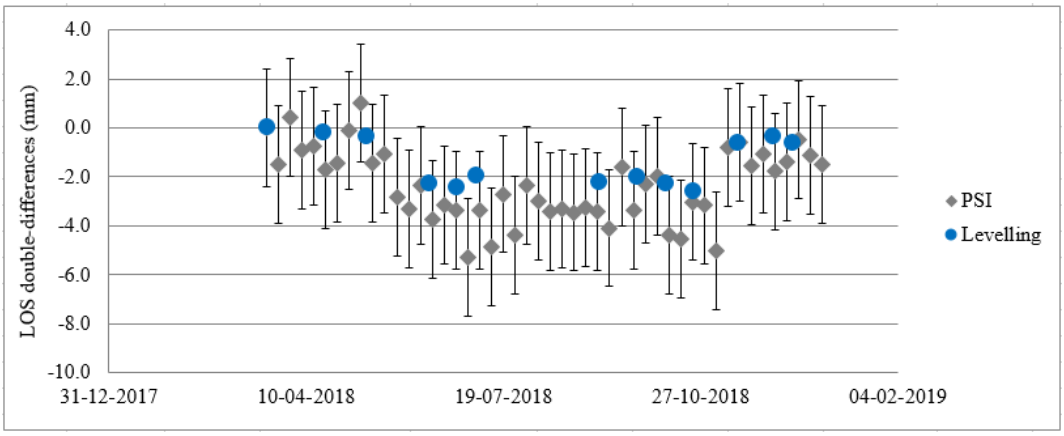

Figure 117 – LOS displacement from PSI and levelling for the triangular trihedral CR for the ascending pass in the static test; error bars are the uncertainty of double-differences.

Table 12 presents the coherence of PSs on the CRs oriented towards the ascending pass and of the respective PSs used as references, for the tested CR models. All PSs on the CRs presented temporal coherences greater or equal to 0.90. In this test, the rectangular trihedral led to a temporal coherence greater than that of the triangular model. The dispersion of double-differences from both CRs was equal, which meant the quality of PSI measurements was equal for both CRs. However, a smaller uncertainty was achieved for the triangular trihedral than for the rectangular one. The standard deviation of differences between the double-differences from

both techniques was at the millimetre level at the rectangular trihedral, while it was sub-millimetric for the triangular one.

Table 12 – Temporal coherence for the PSs used at each validation, double-difference dispersion, standard deviation of differences for each validation, f – degrees of freedom for Welch t test, v – test statistic for Welch t test and t_f – critical value (for a level of significance of 0.05) at individual CRs oriented towards the ascending pass, for different CR models for the static test.

Type of CR	*In situ* technique	Coherence PS on CR	Coherence reference PS	Double-difference dispersion (mm)	Standard deviation of differences (mm)	f	v	t_f
Rectangular	Levelling	0.97	0.89	2.4	2.1	33	-0.87	2.03
Triangular	Levelling	0.90	0.96	2.4	0.7	28	-2.69	2.03

The Welch t test of equal averages with differing variances showed that the null hypothesis could only be accepted for the results achieved at the rectangular trihedral, for a level of significance of 0.05. As for the triangular trihedral, the PSI double-differences could not be considered equivalent to the levelling ones, to a level of significance of 0.05. Figure 117 shows PSI measurements overestimated the levelling data (PSI presented larger displacement away from the sensor), which might be due to relative displacement between the benchmarks from the two techniques. The results of the Welch t test for the ascending oriented CRs are presented in Annex A.3 Table 24 and 25.

The same analysis was performed for the individual CRs oriented towards the descending pass. For the rectangular trihedral, the benchmark to the west of the bidirectional CR was used as reference and the double-differences from PSI and levelling presented similar behaviour, with movement away from the sensor that became stable after some months. (Figure 118).

The test at the triangular trihedral also showed similarities between PSI and levelling double-differences. The CR presented an oscillatory behaviour similar in PSI and levelling data, despite the amplitude of those displacements being larger for PSI than for the *in situ* technique. A few discontinuities at isolated epochs were present at the PSI time series, more likely to correspond to changes at the reference PS than at the CR (Figure 119).

Large temporal coherences were achieved for both CRs, but the smaller temporal coherence of the reference PS of the triangular trihedral led to a larger double-difference dispersion for that CR. Nevertheless, the standard deviation of dfferences between techniques was similar for both models, being at the millimetre level (Table 13). The measurements at both CR models led to the acceptance of the null hypothesis of the Welch t test; thus, the average LOS

displacements from PSI and levelling could be considered equal at both CRs, for a level of significance of 0.05. Details from the Welch t test are presented in Annex A.3 Table 26 and 27.

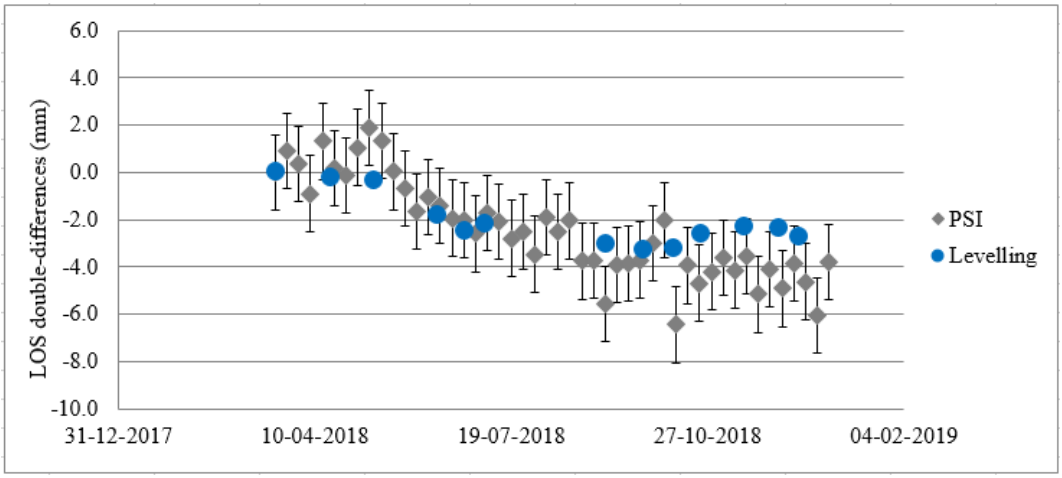

Figure 118 – LOS displacement from PSI and levelling for the rectangular trihedral CR for the descending pass in the static test, for the reference PS to the west of the CR; error bars are the uncertainty of double-differences.

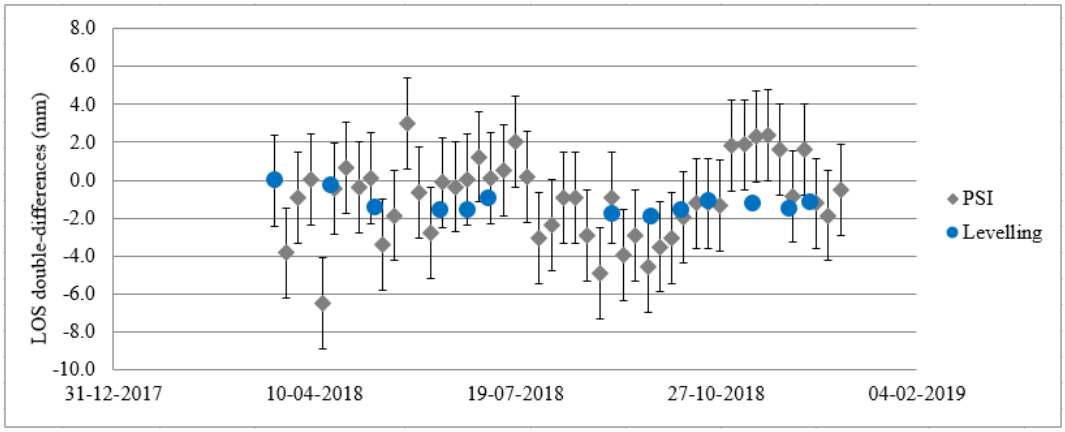

Figure 119 – LOS displacement from PSI and levelling for the triangular trihedral CR for the descending pass in the static test; error bars are the uncertainty of double-differences.

Table 13 – Temporal coherence for the PSs used at each validation, double-difference dispersion, standard deviation of differences for each validation, f – degrees of freedom for Welch t test, v – test statistic for Welch t test and t_f – critical value (for a level of significance of 0.05) at individual CRs oriented towards the descending pass, for different CR models for the static test.

Type of CR	In situ technique	Coherence PS on CR	Coherence reference PS	Double-difference dispersion (mm)	Standard deviation of differences (mm)	f	v	t_f
Rectangular	Levelling	0.97	0.96	1.6	1.4	36	-0.85	2.03
Triangular	Levelling	0.98	0.88	2.4	1.5	59	0.90	2.00

From Table 12 and 14, it seemed to exist a relationship between the temporal coherence of the reference PSs and the standard deviation of differences between PSI and levelling, with lower coherence values corresponding to larger uncertainties. The relationship was explored in Figure 120, which shows both variables were linearly correlated, with a coefficient of determination of 0.94. This analysis considered the whole set of executed tests, including those excluded from the previous evaluations, in order to utilise a larger range of coherence values.

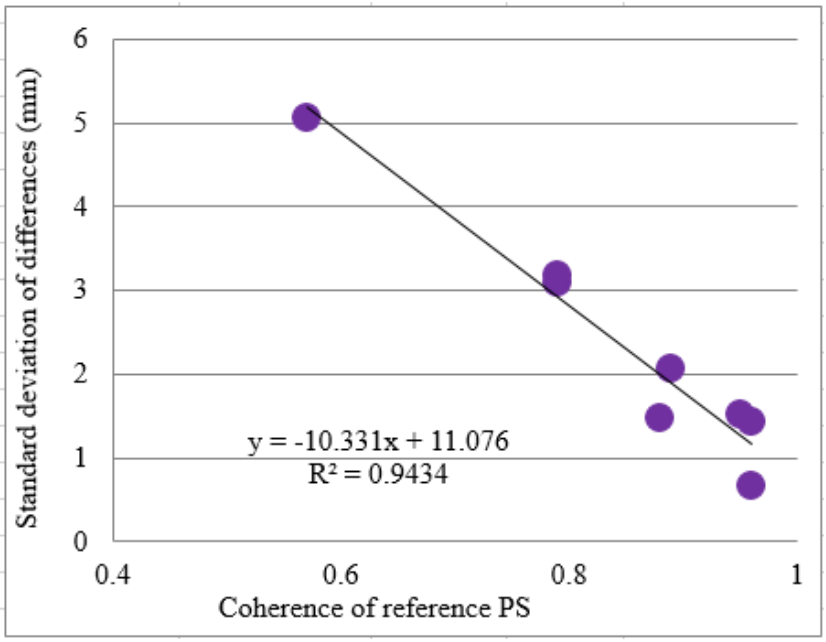

Figure 120 – Relationship between temporal coherence of reference PSs and the standard deviation of diferences from PSI and levelling.

5.4.2 Displacement analysis – first sequence of imposed displacements

The second displacement analysis test was the first sequence of imposed displacements, in which the bidirectional CR and the triangular trihedral oriented towards the descending pass were moved along the descending pass LOS direction by steps of 12 mm. It must be noted that the PSs achieved in this test were not the same as in the previous one, as a new set of SAR images led to a new set of stable reflective targets (PSs). As the triangular trihedral oriented towards the ascending pass remained fixed, it was not analysed in this section.

The rectangular trihedral oriented towards the ascending pass was subjected to the imposed displacements along the descending pass LOS and the double-differences were determined with respect to the reference PS to the west of the bidirectional CR. The imposed displacements had both vertical and horizontal components; therefore, ascending LOS measurements and levelling

data projected to LOS, which considered only vertical displacements, were not directly comparable. In order to assess the quality measurement at this geometry, the theoretically expected displacement to be detected by the ascending pass was determined by projecting the descending LOS displacement to the ascending LOS direction. The descending LOS displacements were determined at laboratory through the measurement of the length of the steps at the stair-like structure and have an error of a few tens of millimetre. Figure 121 shows both datasets presented similar values until the seventh step. From March 2019 on, PSI underestimated the expected displacements.

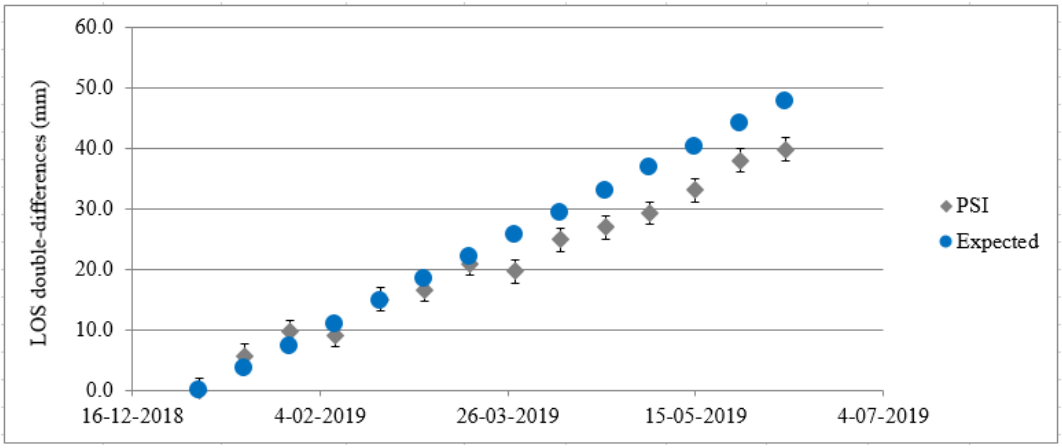

Figure 121 – LOS displacement from PSI and laboratory measurements for the rectangular trihedral CR for the ascending pass in the first sequence of imposed displacements test; error bars are the uncertainty of double-differences.

The vertical displacements of the corners of the concrete block used as base for the bidirectional CR determined by levelling showed the tilting of the concrete block accelerated in March 2019 (Figure 122), with the northwest and the southwest corners settling at a larger rate than the northeast and southeast ones. This suggested the tilting of the concrete block base might be the cause for the discrepancy between the observed and the expected double-differences.

The rectangular and triangular trihedrals oriented towards the descending pass were also moved along vertical and horizontal directions. As levelling only measures vertical displacement and GNSS was not available for the triangular trihedral CR, the results evaluation was performed again through comparison to the step lengths determined at the laboratory.

Similar behaviour was detected from the two techniques at the rectangular trihedral (Figure 123), with PSI slightly underestimating the expected values at the last four epochs. The smaller influence of the concrete block tilting on the double-differences observed in this geometry suggested the rotation axis of the concrete block might be closer to the reflective centre of the

CR for the descending pass than to that of the ascending one. This occurred as the two reflective centres were separated by a few centimetres due to the diameter of the vertical rod that held the GNSS antenna.

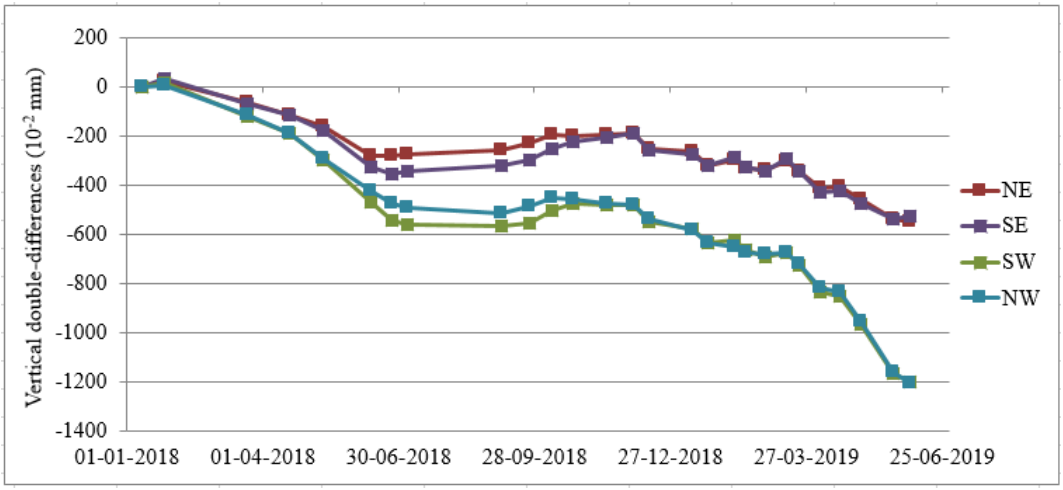

Figure 122 – Levelling vertical double-differences for the corners of the concrete block used as base for the bidirectional CR, with respect to the benchmark to the east of the CR. NE was the northeast corner, SE was the southeast corner, SW was the southwest corner and NW was the northwest corner.

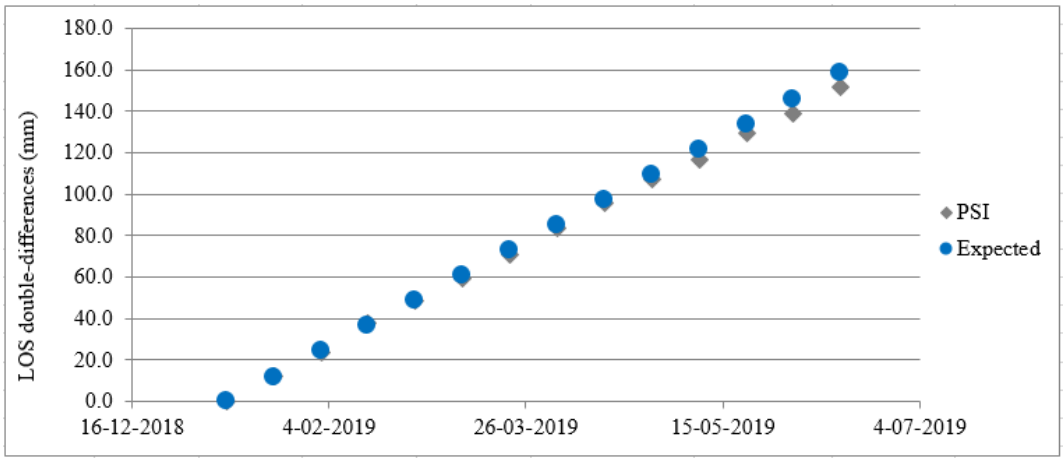

Figure 123 – LOS displacement from PSI and laboratory measurements for the rectangular trihedral CR for the descending pass in the first sequence of imposed displacements test. Error bars are not visible at this scale.

Similar observations between the two datasets were achieved also for the triangular trihedral CR (Figure 124). Discrepancies of a few millimetres (around 6 mm) were observed at some epochs; however, the levelling at the concrete block corners showed that there was only a small magnitude tilting towards north (0.5 mm), unable to cause the differences. Perhaps these might be due to the seasonal behaviour of the concrete block (of larger magnitude than the tilting), which also affected the CR displacements, but not the laboratory measurements.

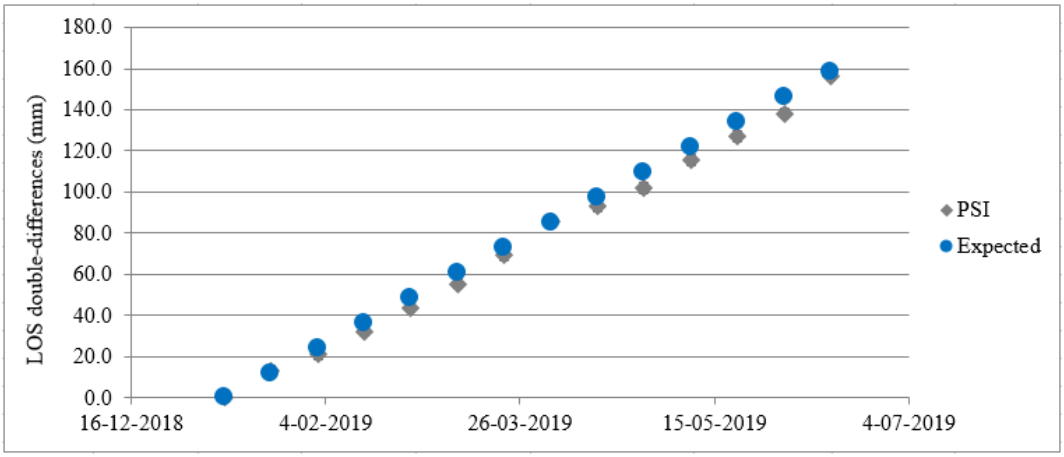

Figure 124 – LOS displacement from PSI and laboratory measurements for the triangular trihedral CR for the descending pass in the first sequence of imposed displacements test. Error bars are not visible at this scale.

All CRs provided PSs with large temporal coherence. The rectangular trihedral CRs showed smaller double-difference dispersion than the triangular trihedral one, due to the larger coherence of reference PSs used for the first CRs. Nevertheless, the larger observation precision at the rectangular CRs did not correspond to a smaller standard deviation of differences between techniques, as the rectangular trihedral oriented towards the ascending pass presented the largest value of this variable. This might be due to the discrepancy between the two datasets after the seventh step of the imposed displacements. Despite the observed differences between PSI and the reference technique, all the tests led to the acceptance of the null hypothesis of the Welch t test, for a level of significance of 0.05. Therefore, the average of PSI double-differences could be considered equal to the average of the reference data for the three tests (Table 14 and Annex A.3 Table 28 to 30).

The bidirectional CR performance was also evaluated regarding the measurement of vertical and east – west double-differences. Figure 125 shows the vertical double-differences determined from PSI and from levelling for the bidirectional CR. PSI vertical double-differences were achieved through Equation (18) from Chapter 3, considering the double-differences of the PSs identified on both ascending and descending parts of the CR with respect to the corresponding reference PSs located to the west of the device. The vertical double-differences from levelling were determined from the average of the readings at the ascending- and descending-oriented parts of the CR with respect to the levelling benchmark located to its west. Data from both techniques were similar until March 2019, when PSI started to underestimate the levelling measurements.

Table 14 – Temporal coherence for the PSs used at each validation, double-difference dispersion, standard deviation of differences for each validation, f – degrees of freedom for Welch t test, v – test statistic for Welch t test and t_f – critical value (for a level of significance of 0.05) at individual CRs, for different CR models, for the first sequence of imposed displacements test.

Type of CR	*In situ* technique	Coherence PS on CR	Coherence reference PS	Double-difference dispersion (mm)	Standard deviation of differences (mm)	f	v	t_f
Rectangular[25]	Levelling	0.98	0.93	1.9	3.6	25	-0.61	2.06
Rectangular[26]	Levelling	0.96	0.99	1.4	2.7	26	0.12	2.06
Triangular	Levelling	0.99	0.86	2.5	2.9	26	0.20	2.06

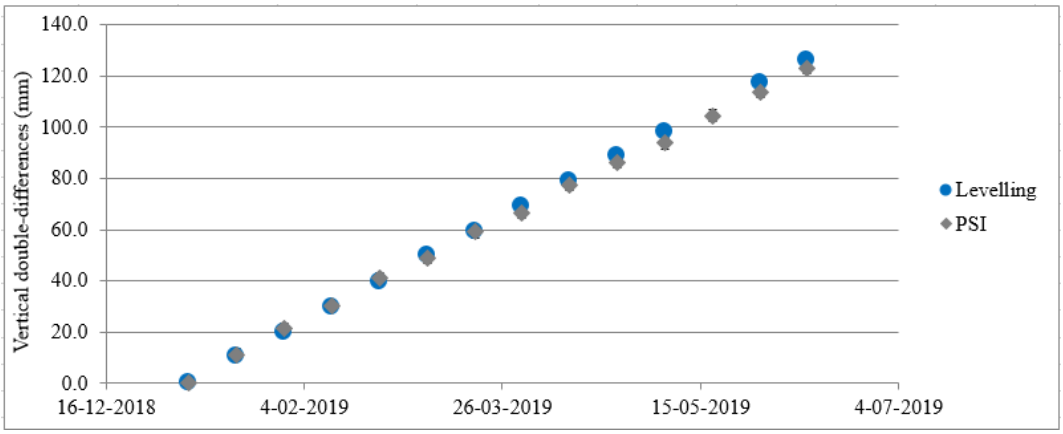

Figure 125 – Vertical double-differences from PSI and levelling for the bidirectional CR in the first sequence of imposed displacements test.

The same evaluation was performed with GNSS. In this case, the reference PS was located at the roof of the building where the reference GNSS antenna was installed and it likely was originated by the reflection of the SAR signal on the fragile tiles that cover the roof. Similar to the previous results, similar displacements were observed until March 2019, when the double-differences from both techniques started diverging (Figure 126).

East – west displacements were computed from ascending and descending geometries' data, using Equation (19) in Chapter 3. Discrepancies between the double-differences of the two techniques were found for a few epochs, almost all at the same time of the concrete block tilting acceleration (Figure 127). The tilting of the concrete block influenced the measurements performed along the ascending geometry, which were reflected on both vertical and east – west double-differences.

[25] Ascending pass.
[26] Descending pass.

The three-dimensional GNSS double-differences were projected to the descending pass LOS and used for validation / uncertainty assessment of the PSI data along this direction. The data from both sources were similar to each other for almost all epochs, with the largest difference being observed at the ninth step (Figure 128).

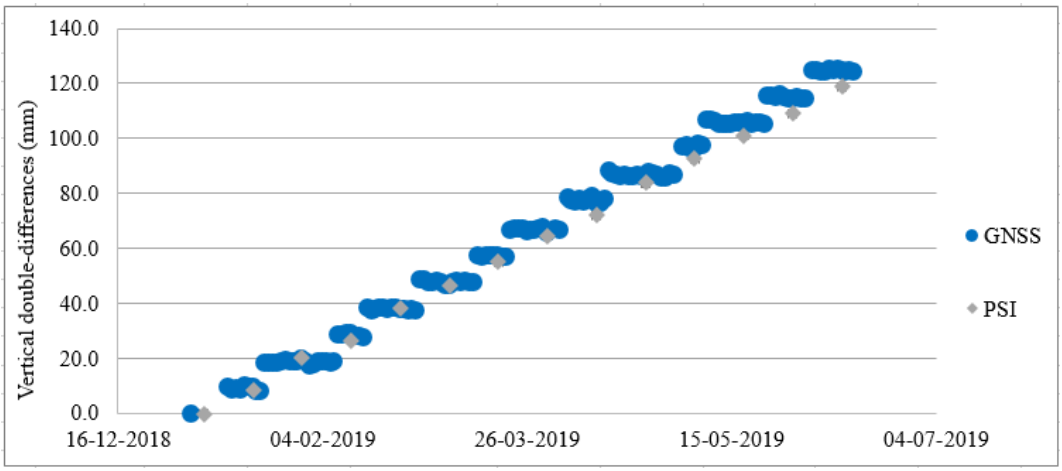

Figure 126 – Vertical double-differences from GNSS and PSI for the bidirectional CR in the first sequence of imposed displacements test.

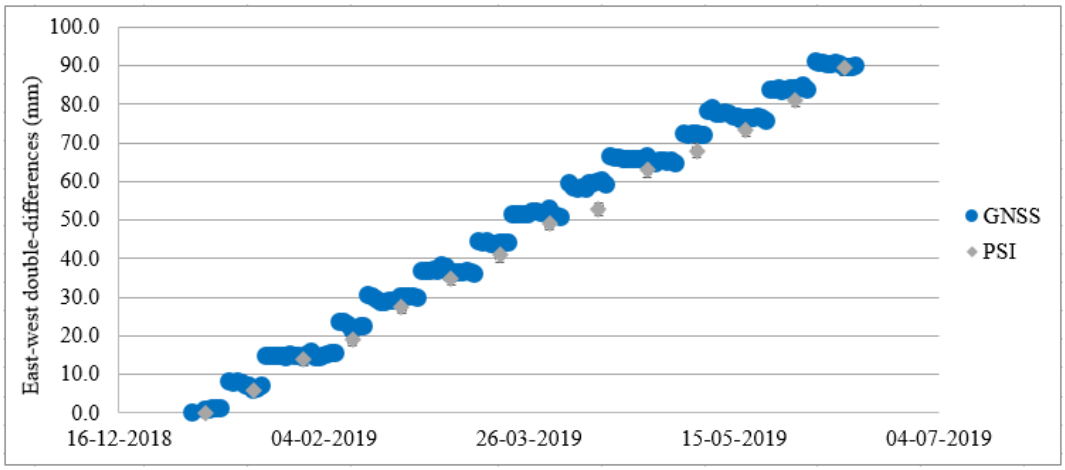

Figure 127 – East – west double-differences from GNSS and PSI for the bidirectional CR in the first sequence of imposed displacements test.

The dispersion of double-differences along the vertical, east – west and LOS directions were similar. That similarity was also found for the standard deviations of the differences between PSI and the reference *in situ* techniques, where values close to 2.0 mm were achieved for all directions. The Welch t test indicated the average PSI measurements could be considered equal to the average double-differences achieved from the reference geodetic methods for all tested situations (Table 15 and Annex A.3 Table 31 to 34).

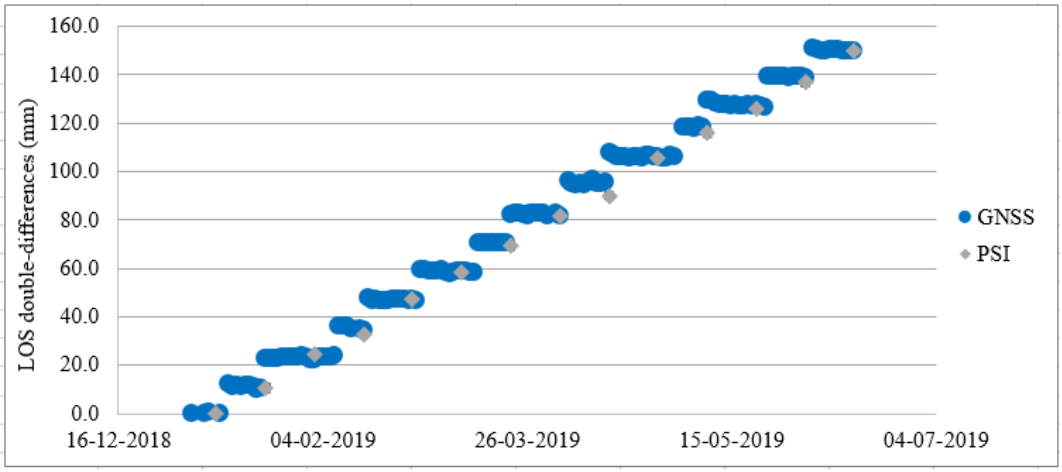

Figure 128 – LOS double-differences from GNSS and PSI for the bidirectional CR in the first sequence of imposed displacements test.

Table 15 – Double-difference dispersion for vertical, east – west and LOS double-differences, standard deviation of differences, f – degrees of freedom for Welch t test, v – test statistic for Welch t test and t_f – critical value (for a level of significance of 0.05) at the bidirectional CR, for the first sequence of imposed displacements test.

Type of CR	*In situ* technique	Dispersion of double-difference along direction of interest (mm)	Standard deviation of differences (mm)	f	v	t_f
Bidirectional	Levelling	1.5	1.9	25	0.14	2.06
Bidirectional	GNSS[27]	1.4	2.1	15	-0.32	2.13
Bidirectional	GNSS[28]	1.8	1.9	15	-0.41	2.13
Bidirectional	GNSS[29]	1.9	1.8	15	-0.18	2.13

5.4.3 Displacement analysis – second sequence of imposed displacements

At the second sequence of imposed displacements, the bidirectional CR and the triangular trihedral oriented towards the descending pass were moved along a sequence of pre-defined displacements at the vertical plane containing the east – west direction and along a direction whose angle with the vertical was equal to the incidence angle of the descending pass. Only the results achieved for vertical and east – west double-differences at the bidirectional CR were evaluated.

[27] Vertical double-differences.
[28] East – west double-differences.
[29] LOS double-differences.

The vertical displacements measured through PSI and levelling at the bidirectional CR during the second sequence of imposed displacements were almost coincident for all epochs (Figure 129), with the difference between the two techniques being of 0.0 mm for the first eight epochs and of 0.1 mm for the last four. This resulted in a standard deviation of differences of 0.0 mm. On the other hand, the same vertical PSI double-differences presented some differences with respect to the GNSS data (Figure 130). A possible cause for these discrepancies might be the differences in their observation times. While PSI measurements corresponded to an observation of short duration, GNSS double-differences were achieved from observation sessions with the duration of 24 hours. The same effect might be the cause for the observed discrepancies at the east – west double-differences (Figure 131).

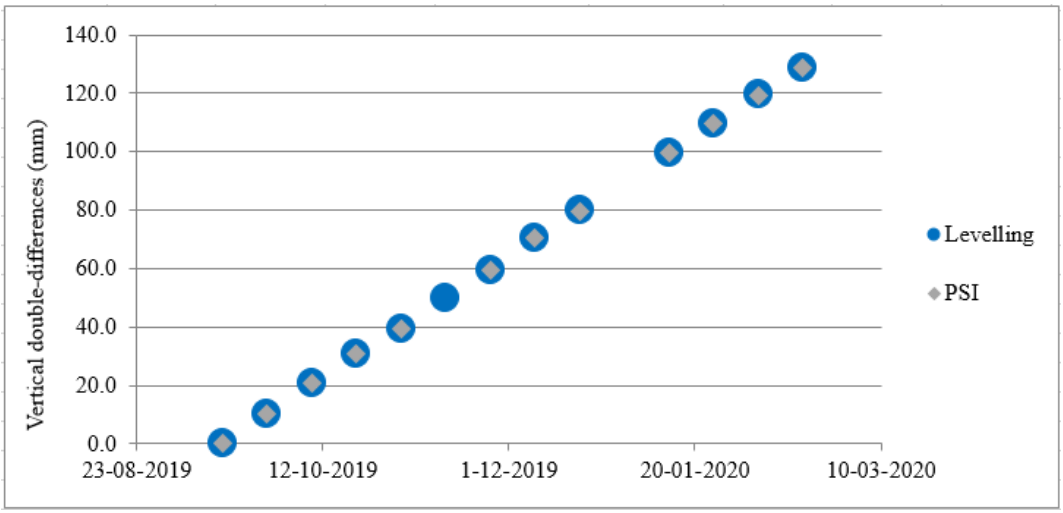

Figure 129 – Vertical double-differences from PSI and levelling for the bidirectional CR in the second sequence of imposed displacements test.

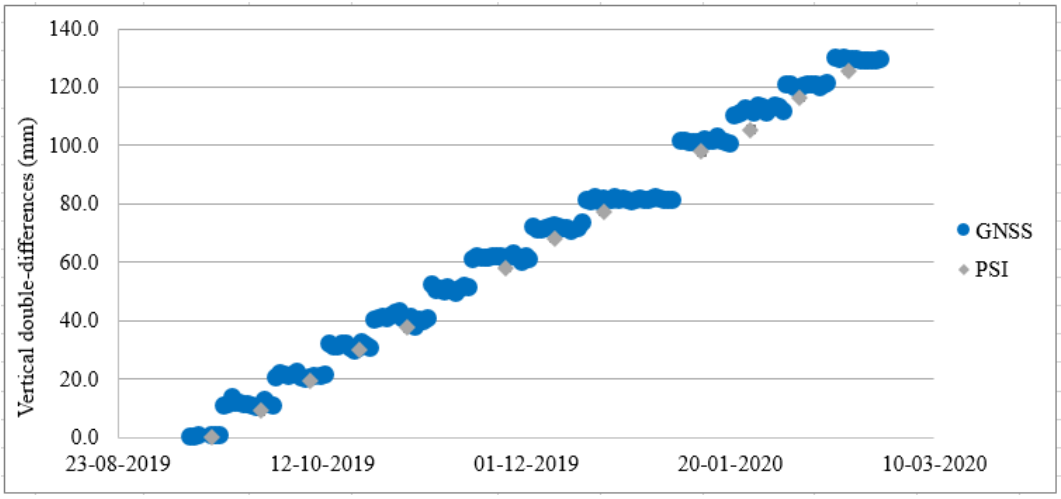

Figure 130 – Vertical double-differences from GNSS and PSI for the bidirectional CR in the second sequence of imposed displacements test.

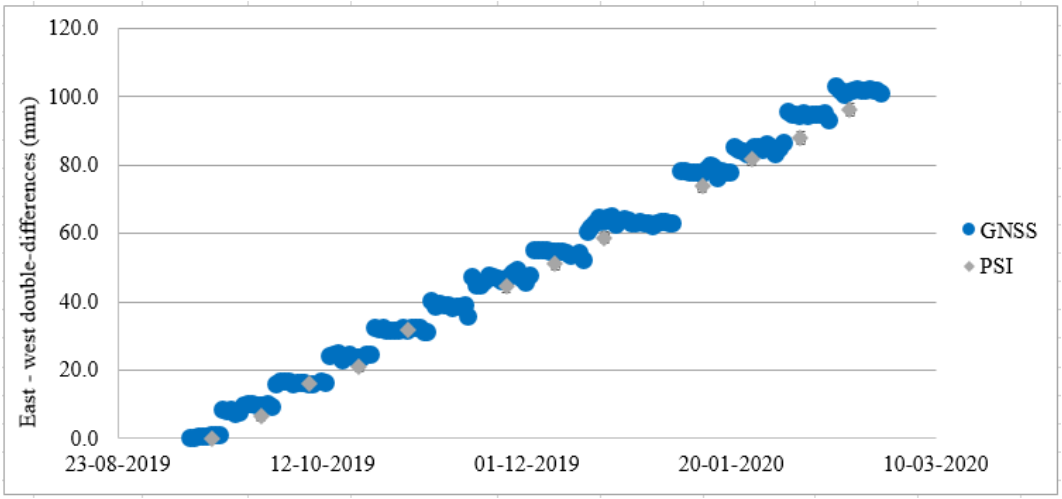

Figure 131 – East-west double-difference from GNSS and PSI for the bidirectional CR in the second sequence of imposed displacements test.

Similar dispersion of double-differences were achieved for the three tests. The standard deviation of differences led to distinct results according to the reference *in situ* techniques. A value of 0.0 mm was achieved for levelling, while values close to 2.0 mm were achieved again at the comparison to GNSS (Table 16). The Welch t test confirmed the three PSI average double-differences could be considered equal to those from the reference techniques, for a level of significance of 0.05 (Annex A.3 Table 35 to 37).

Table 16 – Double-difference dispersion for vertical and east – west displacements, standard deviation of differences, f – degrees of freedom for Welch t test, v – test statistic for Welch t test and t_f – critical value (for a level of significance of 0.05) at the bidirectional CR, for the second sequence of imposed displacements test.

Type of CR	In situ technique	Dispersion of double-differences along direction of interest (mm)	Standard deviation of differences (mm)	f	v	t_f
Bidirectional	Levelling	1.7	0.0	23	0.06	2.07
Bidirectional	GNSS[30]	1.3	1.7	12	1.98	2.18
Bidirectional	GNSS[31]	1.8	2.1	12	1.99	2.18

[30] Vertical displacements.
[31] East-west displacements.

5.5 Discussion

In this Chapter, a new model of artificial passive reflector to SAR signal was proposed (the bidirectional CR) and its performance was evaluated and compared to that of a model frequently found in the literature (triangular trihedral).

5.5.1. Both CR models were visible as bright pixels at Sentinel-1 amplitude images, for ascending and descending passes, which indicated both types of structures had potential to behave as PSs. CRs of the rectangular trihedral model led to larger amplitude values and to more stable amplitude time series. Their amplitude stability might have been influenced by the usage of perforated aluminium, which avoided water accumulation during precipitation events. The triangular trihedrals were found to be obstructed by water a few times, which might correspond to the discontinuities observed at the amplitude time series.

The CRs' potential to behave as PSs was confirmed, as all the tested devices kept their reflective behaviour stable during the three executed tests, generating PSs. All CR models led to PSs with temporal coherence above 0.90. Except for the triangular trihedral oriented towards the ascending pass during the static test, which presented a temporal coherence of 0.90, temporal coherences greater or equal to 0.96 were achieved at all other experiments.

5.5.2. Regarding displacement validation, all CR models allowed PSI measurements whose averages could be considered equal to those from the reference *in situ* techniques, to a level of significance of 0.05; except for the triangular trihedral CR oriented towards the ascending pass during the static test. In that case, the PSI double-differences overestimated the reference data, perhaps due to relative displacements between the benchmarks of PSI and levelling.

The absence of relative displacement between benchmarks could be guaranteed by using a CR as a common benchmark for all techniques. Nevertheless, the usage of natural PSs as benchmarks in this experiment led to the conclusion that the PS temporal coherence is a critical factor for the PSI displacement uncertainty, which must be considered at monitoring tasks performed using natural PSs, such as those presented in Chapters 3 and 4.

5.5.3. PSI measurement uncertainty was evaluated through the standard deviation of differences between PSI and *in situ* techniques.

The comparison between the performance of triangular and rectangular individual CRs was assessed at the static and at the first sequence of imposed displacements tests. The evaluation of the CRs oriented towards the descending pass showed similar uncertainties for both CR models, with the rectangular CR presenting slightly smaller values. Nevertheless, for the ascending geometry, the triangular CR led to a smaller uncertainty than the rectangular one

during the static test, being the only experiment where sub-millimetric accuracy was achieved. This CR was the only one without the stair-like structure, which suggested this equipment might have caused some instability at the remaining CRs.

In these experiments, an uncertainty of 1.8 mm was obtained for double-differences along the LOS direction, which was comparable to Quin and Loreaux (2013)'s 0.48 mm and to the range 1.8 mm – 4.6 mm achieved by Mahapatra *et al.* (2014) using CATs. For vertical displacements, values ranging from 0.0 mm to 1.9 mm were achieved against 0.75 mm by Ferretti, Savio, *et al.* (2007). For east – west displacements, the values in these experiments varied from 1.9 mm to 2.1 mm, while Ferretti, Savio, *et al.* (2007) achieved 0.58 mm. The larger uncertainties at some of the presented tests might be due to the usage of natural PSs as benchmarks and to the duration of the GNSS sessions. In this research, daily GNSS observations were considered instead of hourly ones, due to the higher precision level of daily data. In future research, the usage of hourly GNSS observations post-processed with low pass filters might be considered. The larger temporal resolution of this solution would enable displacement measurements at epochs similar to those of the SAR image acquisitions, decreasing the differences of the environmental conditions between the two acquisitions. Post-processing of the data should be applied in order to achieve precisions similar to those of the daily observations (LNEC, 2018).

For vertical double-differences, lower uncertainty was achieved at the second sequence of imposed displacements, while for horizontal double-differences lower uncertainty was obtained at the first sequence. In order to interpret these results, the theoretical standard deviations expected for vertical and east – west displacement components for two hypothetical PSs were determined. Those PSs were originated from SAR images with the properties of those used in this study, both with temporal coherence 0.90 (corresponding to a LOS displacement standard deviation of 2.0 mm), at the location of the bidirectional CR and varying the horizontal displacement direction of 360º (Figure 132).

The displayed standard deviation resulted from the propagation of the LOS displacements' standard deviations (determined through temporal coherence) from each of those hypothetical PSs to vertical and east – west displacement components. The direction displayed at x-axis in the figure is the direction perpendicular to the direction of movement; therefore, displacement towards north corresponds to an azimuth of 270º in the chart, displacement towards east corresponds to an azimuth of 0º, displacement towards south corresponds to an azimuth of 90º and displacement towards west corresponds to an azimuth of 180º. It was assumed horizontal displacement occurred only along the considered direction.

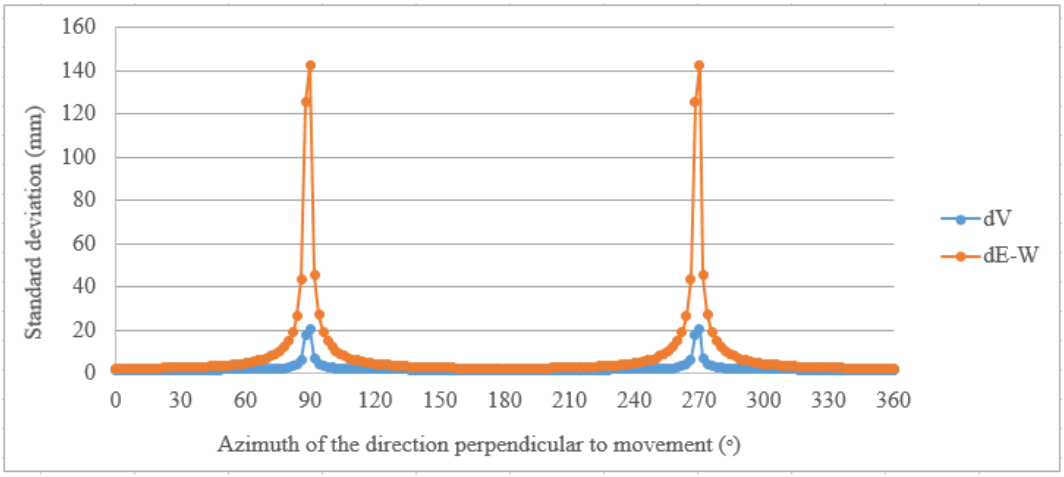

Figure 132 – Standard deviations for vertical (dV) and east – west (dE-W) displacements for different movement directions.

The standard deviation of vertical displacement was lower than that of the east – west component, for any displacement direction. It was verified that standard deviations of both vertical and east – west displacements depended on the direction along which the displacement horizontal component occurred. Both displacement components presented the largest uncertainties when displacement was along the north – south direction and the lowest when it was along east – west. For vertical displacements, it was only possible to achieve uncertainties below 2.0 mm when displacement direction was more than 20º away from the north – south direction. The maximum standard deviation for east – west displacement occurred when displacement horizontal component was along the north – south direction and the minimum was verified when it was along the east – west direction, similar to vertical displacements. Displacement direction outside the buffer of 20º around the north – south direction enabled east – west displacement uncertainty lower than 7.1 mm.

In the presented experiments, the azimuth difference between the two tested directions was of 12.6º. The expected differences between standard deviations when displacements occur along east – west and along a direction 12.6º away from it are of 0.1 mm in east – west displacement component and 0.0 mm in the vertical component. This might be the reason for the small differences achieved at the experiments for the standard deviation of differences for both displacement components when horizontal displacement occurred along the two directions.

5.5.4. At the experiment of the second sequence of imposed displacements, there was a jump over one of the positions on the stair-like structure, which led to a displacement of 24 mm, instead of 12 mm, between two SAR images. Nevertheless, the PSI technique was successful at measuring that larger displacement value, as the displacement rate was kept.

5.6 Conclusions

In this Chapter, a method for PSI displacement validation and uncertainty assessment was designed, which consisted on the execution of a series of comparisons between double-differences from PSI and from *in situ* techniques (levelling, GNSS and laboratory measurements) at an infrastructure of artificial passive corner reflectors to the signal from Sentinel-1A/B SAR-C sensor. Besides traditional CR models shaped as triangular trihedrals, a new model of CR, composed by the union of two rectangular trihedrals with a common vertical axis, was proposed and its performance was compared to those of the traditional models. Three types of tests were performed: static CRs and two sequences of imposed displacements along pre-defined directions.

The experiments performed enabled PSI displacement validation and its uncertainty assessment for distinct situations. For all but one of the tests, average PSI double-differences were considered equal to those of the *in situ* techniques, for a level of significance of 0.05. The experiment in which equality was not achieved was suspected to be affected by relative motion between the benchmarks of the compared techniques. The obtained uncertainties, quantified by the standard deviation of differences between techniques, were similar to those found in the literature. Standard deviation of differences of 1.8 mm was achieved for LOS displacements, 0.0 mm – 2.1 mm for vertical and 1.9 mm – 2.1 mm for east – west displacement components.

The new CR model proposed in this research showed larger reflectivity capability than the traditional CRs and a similar measurement uncertainty level.

The experiments showed PS temporal coherence is of the utmost importance on the measurement uncertainty, which is especially relevant for monitoring activities using natural PSs.

The main limitations identified for this type of experiments were the exposure to meteorological events that may cause damage to the CRs and affect the measurement quality, ground instability at the device installation site and relative motion between benchmarks for different geodetic techniques.

For future research, there are still some uncertainty assessment experiments that can be performed using the CR infrastructure. Both bidirectional CR and the triangular trihedral oriented towards the descending pass are prepared to perform a third sequence of imposed displacements, rotating the stair-like structure around the vertical axis counterclockwise of 12.6º from the east – west direction. The uncertainty associated to other PSI algorithms could be evaluated as well. PSI using non-linear displacement model (as used in Chapters 3 and 4) could be analysed by simulating oscillations at the CRs' displacements by moving the

equipment forward and backward along the stair-like structure. Techniques using partially coherent targets, such as Quasi-permanent scatterers (Perissin and Wang, 2012), could be studied by covering the CR during the acquisition of some of the images.

Chapter 6. Discussion

In this Chapter, a discussion on the contributions of the methods developed in the previous Chapters to promote the usage of InSAR data for SHM is presented. This research addressed some of the issues reported in the literature that limit the application of InSAR for displacement measurement to be used for SHM.

6.1. The microwave band used for the SAR image acquisition had an important role in the field of SHM. In the present research, C- and L-band data were both used for displacement measurement at vegetated slopes: L-band at Odelouca, in Chapter 3, and C-band at Baixo Sabor, in Chapter 4. A density of 346 PSs/km^2 was achieved with L-band, while, through C-band, the obtained density was 125 PSs/km^2. This result led to the conclusion that L-band allowed the identification of a larger number of object points than C-band, confirming reports found in the literature, e.g. in Shi *et al*. (2019). The larger point density was achieved with L-band, despite the lower quality of the SAR image dataset, which was composed of a small number of images and presented many gaps in the acquisition time series. That lack of quality in the dataset might be the reason for the unwrapping errors identified during the analysis with the tool for inspection of InSAR displacement time series. This result showed the importance of having a regular acquisition frequency of SAR images. Although ESA assumed the compromise of keeping a regular frequency acquisition for Sentinel-1 data at global level, other space agencies only provide regular data for some regions.

X-band data was not used in this research, but according to the literature (Roque *et al.*, 2016; Giardina *et al.*, 2019), it would be interesting to use high resolution image to analyse Lisbon Downtown in an attempt to achieve more than one PS per building. This would enable the analysis of differential displacements at building-level instead of building-block level, which

would be much more informative. Besides the large costs associated to that type of images, they are available only for a limited number of large cities.

Although C-band images are not optimal neither for urban nor for vegetated areas' applications when compared to X- or L-bands, respectively, they provide a compromise solution, allowing the monitoring of both types of regions of interest.

6.2. Shadow, foreshortening and layover effects resulted from the side-looking geometry of LOS and caused gaps of PSs in the monitored areas. Although layover can be overcome through techniques such as TomoSAR, it is not possible to obtain measurements at shadow areas. The usage of data acquired in distinct geometries, either an ascending or descending pass, or even a parallel orbit with a distinct incidence angle, may help to fill the observation gaps, allowing PS detection at the areas not illuminated by the first SAR geometry. The method proposed for slope monitoring in Chapter 4 considered the displacements projected into the slope direction. Such strategy would enable the simultaneous analysis of results from different acquisition geometries (even from different sensors), resulting in an increased number of PSs.

6.3. In this research, reference points to PSI technique far from the structures being monitored were selected, in order to minimise eventual movement of the benchmark caused by the influence of the structure (e.g., the influence on the slopes of the weight of the water reservoir for dam monitoring). Strategies to minimise or even to remove the reference point behaviour reflected on the displacements of the other points were applied, by averaging the displacement time series of points considered stable (Chapter 3) or by using double-difference observations (Chapter 4).

An alternative strategy to overcome the problem of reference point movement would be to use a CR, following the model proposed in Chapter 5, as a reference point. The CR would behave as a PS for acquisition geometries from ascending and descending passes that would be identified at PSI processing. The GNSS observations would enable the determination of the CR movement with respect to a national geodetic reference frame and that movement could then be removed from all PSs being analysed. This strategy would enable the determination of displacements at tens of thousands of points with respect to the national geodetic reference frame with a revisit period of a few days.

6.4. A national network of bidirectional CRs following the model proposed in this study could be an interesting geodetic infrastructure, as it would allow available reference points with known displacements for PSI processing at any area in the country. The network would also be valuable in case of interest to build an InSAR-based deformation map at national scale, as many countries are pursuing (Ferretti *et al.*, 2015; Novellino *et al.*, 2017). In case of spatial proximity,

those CRs could be integrated in the local reference frames of PS / GNSS networks like those proposed for structure monitoring in Chapter 4.

The latitude range in Portugal mainland might require the readjustment of some of the design parameters of the CR, namely the angles between the individual rectangular trihedral CRs oriented towards south and north, ε_{south} and ε_{north}, respectively, as in Equations (61) and (62). The differences in latitude would originate a difference of 0.9º between the angles β (Equation 14 in section 3.2) for a location at the north and another at the south of the country. This would result in a difference of 1.6º for both ε_{south} and ε_{north} for points at the country's extreme locations. For a bidirectional CR at the north of the country, ε_{south} would be 1.6º smaller than for a bidirectional CR at the south (Figure 133). Consequently, ε_{north} would be 1.6º larger. The magnitude of this correction would be lower than the orientation error commited with the magnetic compass (2º in Chapter 5). Therefore, the values proposed in this study for ε_{south} and ε_{north} could be used in the whole country. Another advantage of the CR model presented in this thesis would be that it would not need to be steered in the vertical direction, being independent of the incidence angle. In conclusion, the bidirectional CR proposed in Chapter 5 could be installed at any location of Portugal mainland without major changes in its design. Eventual adjustments in its size might be required depending on the reflectivity to SAR signal of the installation area.

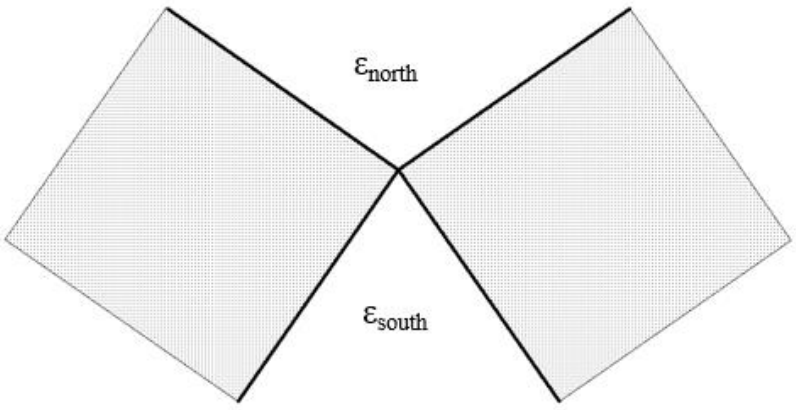

Figure 133 – Identification of ε_{south} and ε_{north} at a sketch of the bidirectional CR base.

6.5. The three topics developed in this research can be interconnected in order to form a structure monitoring protocol, applicable to any type of structure. The first step is to select the SAR images to use, given the characteristics of the structure to monitor (e.g., the type of structure, orientation, expected displacement rate), the time interval of interest and the available budget.

In case back-analysis is not required, the deployment of CRs following the model of those proposed in Chapter 5 can be considered for locations of interest. After selecting the places for installation, the dimensions and geometric configuration must be determined for each CR, being recommended that perforated aluminium is used to build it.Their installation must be carefully executed, ensuring the place stability and correct orientation.

The PSs / GNSS antennas on the CRs can integrate the local reference frame of the structure monitoring system (which may already have some points or not). PSI processing must be performed using the selected SAR dataset, in order to achieve PSs on the structure being monitored, which can then form a network together with the points of the local reference frame. The network analysis proposed in Chapter 4 can be applied to determine adjusted LOS displacements and *a posteriori* variances for the achieved PSs.

The RADAR interpretation method proposed in Chapter 3 can then be used to explore space-time structure behaviour patterns through the analysis of the adjusted displacement time series, providing the experts on structural behaviour with displacements at a large number of points, observation frequency of a cycle every few days and millimetric uncertainty. The proposed strategy may be useful to the early detection of behaviour anomalies and to aid the planning of other monitoring activities through more precise techniques.

Chapter 7. Conclusions

This chapter presents the main conclusions resulting from the research presented in the previous chapters and indicates suggestions for future work.

7.1 Main conclusions

The main objective of this thesis was to evaluate the potential and limitations of InSAR displacements to be used for SHM and to develop strategies to overcome some of the identified difficulties. Three research fields were identified in this study that needed improvement in order to promote the operationalisation of the usage of InSAR data for SHM.

Regarding the first research field, a RADAR interpretation method to deal with the big data problem of extracting information from a large number of InSAR displacement time series was developed. The method is applicable to any type of structure and does not require prior information, as it only relies on the displacement time series. A computer tool was developed that can aid civil engineers to detect space-time patterns in the InSAR data, to identify eventual structural behaviour anomalies and to plan *in situ* monitoring activities.

To fulfil the second research field, InSAR and GNSS data were combined in order to extend an existing GNSS monitoring sub-system to the structure and its surroundings, increasing the number of object points. For the particular case of the presented case study, lower uncertainties were achieved for displacements resulting from the techniques' combination than from the GNSS alone. A computer tool was also developed to apply the proposed method to any case study.

Considering the third research field, an infrastructure of artificial passive CRs to the SAR signal from Sentinel-1 was designed, implemented and operated at LNEC *campus*. A new model of CR was proposed and tested against a model frequently found in the literature. The

new model of CR presented larger reflective capability and similar displacement uncertainty when compared to the traditional model. InSAR average displacements were verified to be equal to those from more precise *in situ* techniques, except at one situation, in which relative motion between benchmarks is suspected. Displacement uncertainty was evaluated for LOS, vertical and east – west displacement components when the CRs were static and when displacement occurred along two distinct directions. Millimetre-level uncertainty was achieved for all situations, except for two cases, in which sub-millimetre was obtained.

Satellite-based InSAR enables displacement measurement at a large number of points, spread throughout a wide area, with a revisit period of a few days and millimetric uncertainty. This information is relevant for SHM problems, as it allows behaviour analysis at the structure and its surroundings, which are not monitored as often as the structure itself. The research in this thesis showed that InSAR may have other roles to aid SHM, namely in the planning of *in situ* monitoring systems. InSAR displacements are referred to a reference point selected among the most stable points in the monitored area, which is often located far from the area of influence of the structure; thus, providing confidence on the point stability. This was observed at Chapters 3 and 4 for the case studies of Odelouca and Baixo Sabor slopes, respectively, where the reference points were a few kilometres away from the water reservoirs. An InSAR displacement analysis may inform geodetic, geotechnical and structural experts on the stability of the structure surroundings, aiding to identify optimal locations for benchmarks to *in situ* monitoring systems. Therefore, InSAR may contribute to improve the *in situ* measurements.

It was verified that InSAR is able to detect structural responses to many loads applied on the structures. Odelouca and Baixo Sabor slopes were found to settle or to move downhill, possibly due to the influence on the slopes of changes in the reservoirs' water levels. Baixo Sabor concrete dam showed seasonal behaviour compatible to thermal expansion and thermal inertia. Buildings at Lisbon Downtown revealed tilting, perhaps due to ground instability, and thermal expansion. However, not all loads can be detected by the technique. It is the case of tidal loading, known to affect the Downtwon area, whose effect on the buildings was not identified. This is a consequence of the periodicity of the SAR image acquisition, unable to detect structural responses with diurnal and semidiurnal periods. The technique performs well both on civil and geotechnical structures.

The technique is also able to detect differential displacements on a structure or set of structures, as performed for Lisbon Downtown. Differential displacements may correspond to structural damages and structural experts may use their identification as warnings. This data provide information on the possible damage location, extension and its evolution in time, which

is useful information for SHM and may aid the planning of other monitoring activities, such as visual inspections.

The experimental part of this thesis (Chapter 5) revealed that InSAR displacement uncertainty is related to two factors: temporal coherence and displacement direction. Given the availability of worldwide SAR datasets, acquired at a regular frequency and with good orbital parameters, such as those freely provided by Copernicus programme, large temporal coherence may be achievable from good quality SAR datasets for most type of structures. The main limitation in this topic may be to achieve PSs on the locations of interest; however, it was verified that artificial corner reflectors like those used in this research generate PSs with temporal coherence above 0.90, which is enough to provide displacement measurements with millimetric uncertainty. If some specific conditions are fulfilled, namely the reference PS is close enough to the PSs on the structure to mitigate orbital inaccuracies and atmospheric effects and the PSs have good reflective properties, sub-millimetric uncertainty might be achieved.

The performed experiments enabled the analysis of the influence of displacement direction when data from different geometries are combined or projected in order to achieve displacements along a direction of interest. Whenever displacement direction is approximately orthogonal to LOS direction, the computed displacements have high uncertainties associated. It is well-known it occurs when displacements are approximately along the north – south direction. However, that is not the only displacement geometry along which high uncertainties are achieved. It can also be observed for situations where the horizontal component of displacement is parallel to LOS, like in the right bank of Baixo Sabor reservoir in Chapter 4. Some regions at the surface of the right bank were almost orthogonal to the descending pass LOS used for monitoring. This problem was not verified at the left bank, as the west-facing slope led to displacements along directions approximately parallel to LOS. As performed on this thesis, a threshold on the values of the inner product between the LOS and the slope unit vectors can assist the identification of the points with enough quality for the slope (or other structure) monitoring.

InSAR, through the application of PSI technique to Sentinel-1 images, provided displacements with uncertainties around 2 mm for LOS, vertical and east – west displacement components. This value is larger than the uncertainties achieved through some *in situ* techniques, which measure displacements at the sub-millimetre level (e.g. geometric levelling). However, there are also other displacement measurement techniques, commonly used for SHM, such as triangulations or traverses, with uncertainties similar to those from InSAR. Therefore,

InSAR is an interesting option to complement existing structure monitoring systems, by adding new object points and providing an observation period of a few days.

In conclusion, InSAR is an applied geodetic technique with potential to inform structure monitoring systems. Although it is not as precise as some of the *in situ* techniques used to acquire data for SHM, its cost-effective capability to increase the number of object points and to be operated remotely make InSAR an interesting option to complement existing structure monitoring systems or to create new ones at cases where the implementation of the traditional systems is not viable.

The objectives proposed in the beginning of this research were fulfilled.

7.2 Future research

The research presented in this thesis can be further developed in order to contribute to the increasing usability of InSAR data in SHM.

In the field of slope monitoring, the combination of InSAR displacements from different geometries, either ascending and descending passes or different sensors, should be explored, in an attempt to increase the number of object points on the slopes and to fill the PS cover gaps obtained from a single geometry. The conversion of LOS displacements from distinct geometries to slope direction would enable the simultaneous application of the proposed RADAR interpretation method and the analysis of all the data from different sources. The identification of the PSs' physical nature should be researched in order to improve the data interpretation, as PSs often correspond to elements that do not reflect the slope behaviour, such as lamp posts or fences. Water level and rainfall data should be considered to aid in the displacement interpretation as well.

Concrete dam monitoring could also benefit from the integration of displacements from different geometries. Besides filling eventual PS gaps on the structure, in the case of common targets for distinct geometries, displacement combination would allow the determination of displacement components along two directions of interest. For example, at Baixo Sabor, vertical and radial displacements could be separated. The improvement of the extended GNSS / InSAR sub-monitoring system would also be beneficial for the analysis, namely regarding noise mitigation and a more homogeneous spatial distribution of *a posteriori* variances. Besides the noise originally present in the InSAR displacements, the integration of GNSS data into the network analysis added even more noise. Therefore, the level of noise in the GNSS data should be reduced, either by applying low-pass filters or by reprocessing the data in order to mitigate

the atmospheric differences that contribute to the noise level. An improved spatial distribution of *a posteriori* variances could be achieved by adding points into the local reference frame. Those additional points may be GNSS antennas, if available, or more economic solutions as artificial reflectors. The resulting adjusted displacements can be compared to structural behaviour models in order to assess whether the structure fulfils safety requirements. An important improvement would be the adaptation of this method in order to retrieve three-dimensional displacements instead of LOS alone.

Regarding urban areas monitoring, the developed RADAR interpretation method should be subjected to some improvements, namely the partition of the displacement time series into smaller segments, in order to increase the sensitivity of the algorithm to detect early behaviour changes. In the particular case of Lisbon Downtown, it would be interesting to perform *in situ* monitoring activities at the building-blocks presenting differential displacements, in an attempt to detect possible damages. Another interesting analysis would be to remove the PSs in the clusters with centimetre-level displacements from the dataset and to execute the clustering operation to the remaining points, in order to identify new structural behaviour patterns of smaller magnitude and to cross those results to known settlements, such as those monitored by LNEC's AGU at Praça do Comércio.

Concerning the experimental part of the study, the bidirectional CR may be used for InSAR displacement uncertainty assessment at other situations, e.g. when displacements occur along other directions, for different displacement models (non-linear displacements) or other InSAR techniques besides PSI. The CR installed at LNEC *campus* may be used as a reference point with displacements known with respect to the national geodetic reference frame for any PSI processings at the city of Lisbon, for both ascending and descending passes of Sentinel-1. Furthermore, it could also be included in an eventual future CR network at national scale.

References

Aalst, M. K. Van (2006) 'The impacts of climate change on the risk of natural disasters', *Disasters*, 30(1), pp. 5–18. doi: 10.1111/j.1467-9523.2006.00303.x.

Abanda, A., Mori, U. and Lozano, J. A. (2019) 'A review on distance based time series classification', *Data Mining and Knowledge Discovery*, 33(2), pp. 378–412. doi: 10.1007/s10618-018-0596-4.

Aghabozorgi, S., Shirkhorshidi, A. S. and Wah, T. Y. (2015) 'Time-series clustering - A decade review', *Information Systems*, 53, pp. 16–38. doi: 10.1016/j.is.2015.04.007.

Águas do Algarve (2020) *Barragem de Odelouca*. Available at: https://www.aguasdoalgarve.pt/content/barragem-de-odelouca-0 (Accessed: 30 July 2020).

Alamdari, M. M., Ge, L., Kildashti, K., Zhou, Y., Harvey, B. and Du, Z. (2019) 'Non-contact structural health monitoring of a cable-stayed bridge: case study', *Structure and Infrastructure Engineering*, 15(8), pp. 1119–1136. doi: 10.1080/15732479.2019.1609529.

Amelung, F., Galloway, D. L., Bell, J. W., Zebker, H. A. and Laczniak, R. J. (1999) 'Sensing the ups and downs of Las Vegas: InSAR reveals structural control of land subsidence and aquifer-system deformation', *Geology*, 27(6), pp. 483–486. doi: 10.1130/0091-7613(1999)027.

Anantrasirichai, N., Biggs, J., Albino, F., Hill, P. and Bull, D. (2018) 'Application of machine learning to classification of volcanic deformation in routinely generated InSAR data', *Journal of Geophysical Research: Solid Earth*, 123(8), pp. 6592–6606. doi: 10.1029/2018JB015911.

Antunes, C. (2007) *Previsão de Marés dos Portos Principais de Portugal*. Available at: http://webpages.fc.ul.pt/~cmantunes/hidrografia/hidro_mares.html (Accessed: 30 July 2020).

Azevedo, A. (2010) *Sistema integrado de modelação para apoio à prevenção e mitigação de acidentes de hidrocarbonetos em estuários e orla costeira*. PhD thesis. Universidade de Lisboa.

Bakon, M., Oliveira, I., Perissin, D., Sousa, J. J. and Papco, J. (2017) 'A data mining approach for multivariate outlier detection in postprocessing of multitemporal InSAR results', *IEEE Journal of Selected Topics in Applied Earth Observations and Remote Sensing*, 10(6), pp. 2791–2798. doi: 10.1109/JSTARS.2017.2686646.

Bamler, R. and Hartl, P. (1998) 'Synthetic aperture radar interferometry', *Inverse Problems*, 14 (4), pp. R1–R54. doi: 10.1088/0266-5611/14/4/001.

Bányai, L., Nagy, L., Hooper, A., Bozsó, I., Szucs, E. and Wesztergom, V. (2020) 'Investigation of integrated twin corner reflectors designed for 3-D InSAR applications', *IEEE Geoscience and Remote Sensing Letters*, 17(6), pp. 1013–1016. doi: 10.1109/LGRS.2019.2939675.

Bartier, P. M. and Keller, C. P. (1996) 'Multivariate interpolation to incorporate thematic surface data using Inverse Distance Weighting (IDW)', *Computers & Geosciences*, 22(7), pp. 795–799. doi: 10.1016/0098-3004(96)00021-0

Bateson, L., Novali, F. and Cooksley, G. (2010) 'Terrafirma User Guide', *ESA GMES Project Publication*, p. 49. doi: 10.13140/RG.2.2.16889.88161.

Benoit, A., Pinel-Puysségur, B., Jolivet, R. and Lasserre, C. (2020) 'CorPhU: an algorithm based on phase closure for the correction of unwrapping errors in SAR interferometry', *Geophysical Journal International*, 221(3), pp. 1959–1970. doi: 10.1093/gji/ggaa120.

Berardino, P., Fornaro, G., Lanari, R. and Sansosti, E. (2002) 'A new algorithm for surface deformation monitoring based on small baseline differential SAR interferograms', *IEEE Transactions on Geoscience and Remote Sensing*, 40(11), pp. 2375–2383. doi: 10.1109/TGRS.2002.803792.

Bergroth, L., Hakonen, H. and Raita, T. (2000) 'A survey of longest common subsequence algorithms', in *Seventh International Symposium on String Processing and Information Retrieval. SPIRE 2000*. Curuna, Spain, 27-29 September: IEEE, pp. 39–48. doi: 10.1109/spire.2000.878178.

Berndt, D. and Clifford, J. (1994) 'Using dynamic time warping to find patterns in time series', in *Workshop on Knowledge Discovery in Databases*. Seattle, Washington, July, pp. 359-370.

Berti, M., Corsini, A., Franceschini, S. and Iannacone, J. P. (2013) 'Automated classification of Persistent Scatterers Interferometry time series', *Natural Hazards and Earth System Sciences*, 13(8), pp. 1945–1958. doi: 10.5194/nhess-13-1945-2013.

Bonì, R., Pilla, G. and Meisina, C. (2016) 'Methodology for detection and interpretation of ground motion areas with the A-DInSAR time series analysis', *Remote Sensing*, 8(8), p. 686. doi: 10.3390/rs8080686.

Brownjohn, J. (2007) 'Structural health monitoring of civil infrastructure', *Philosophical Transactions A: Mathematical, Physical and Engineering Sciences*, 365(1851), pp. 589–622. doi: 10.1098/rsta.2006.1925.

Bru, G., Fernández-Merodo, J. A., García-Davalillo, J. C., Herrera, G. and Fernández, J. (2018) 'Site scale modeling of slow-moving landslides, a 3d viscoplastic finite element modeling approach', *Landslides*, 15(2), pp. 257–272. doi: 10.1007/s10346-017-0867-y.

Van Camp, M. and Vauterin, P. (2005) 'Tsoft: Graphical and interactive software for the analysis of time series and Earth tides', *Computers and Geosciences*, 31(5), pp. 631–640. doi: 10.1016/j.cageo.2004.11.015.

Carlà, T., Intrieri, E., Raspini, F., Bardi, F., Farina, P., Ferretti, A., Colombo, D., Novali, F. and Casagli, N. (2019) 'Perspectives on the prediction of catastrophic slope failures from satellite InSAR',

Scientific Reports, 9(1), p. 14137. doi: 10.1038/s41598-019-50792-y.

Carlà, T., Tofani, V., Lombardi, L., Raspini, F., Bianchini, S., Bertolo, D., Thuegaz, P. and Casagli, N. (2019) 'Combination of GNSS, satellite InSAR, and remote sensing monitoring to improve the understanding of a large landslide in high alpine environment', *Geomorphology*, 335, pp. 62-75. doi: 10.1016/j.geomorph.2019.03.014.

Casaca, J., Braz, N. and Conde, V. (2015) 'Combined adjustment of angle and distance measurements in a dam monitoring network', *Survey Review*, 47(342), pp. 181–184. doi: 10.1179/1752270614Y.0000000106.

Casaca, J., Henriques, M. J., Coelho, J. and Candeias, H. (2009) 'O papel do quadro de referência na monitorização de deslocamentos: Um caso de estudo', in *2º Encontro Nacional de Geodesia Aplicada*. Lisbon, October 12-13.

Casaca, J., Henriques, M. J. and Mateus, P. (2009) 'O ajustamento de grandezas heterogéneas pelo método das components de variância', in *2º Encontro Nacional de Geodesia Aplicada*. Lisboa, October 12-13.

Catalão, J., Nico, G., Hanssen, R. and Catita, C. (2011) 'Merging GPS and atmospherically corrected InSAR data to map 3-D terrain displacement velocity', *IEEE Transactions on Geoscience and Remote Sensing*, 49(6), pp. 2354–2360. doi: 10.1109/TGRS.2010.2091963.

Catalão, J., Nico, G., Lollino, P., Conde, V., Lorusso, G. and Silva, C. (2016) 'Integration of InSAR analysis and numerical modeling for the assessment of ground subsidence in the city of Lisbon, Portugal', *IEEE Journal of Selected Topics in Applied Earth Observations and Remote Sensing*, 9(4), pp. 1663–1673. doi: 10.1109/JSTARS.2015.2428615.

Cerchiello, V., Tessari, G., Velterop, E., Riccardi, P., Defilippi, M. and Pasquali, P. (2017) 'Building damage risk by modeling interferometric time series', *IEEE Geoscience and Remote Sensing Letters*, 14(4), pp. 509–513. doi: 10.1109/LGRS.2017.2651938.

Chang, L. and Hanssen, R. (2016) 'A probabilistic approach for InSAR time-series postprocessing', *IEEE Transactions on Geoscience and Remote Sensing*, 54(1), pp. 421–430. doi: 10.1109/TGRS.2015.2459037.

Chang, P. C., Flatau, A. and Liu, S. C. (2003) 'Review paper: Health monitoring of civil infrastructure', *Structural Health Monitoring*, 2(3), pp. 257–267. doi: 10.1177/1475921703036169.

Chen, Q., Liu, G., Ding, X., Hu, J. C., Yuan, L., Zhong, P. and Omura, M. (2010) 'Tight integration of GPS observations and persistent scatterer InSAR for detecting vertical ground motion in Hong Kong', *International Journal of Applied Earth Observation and Geoinformation*, 12(6), pp. 477–486. doi: 10.1016/j.jag.2010.05.002.

Ciampalini, A., Bardi, F., Bianchini, S., Frodella, W., del Ventisette, C., Moretti, S. and Casagli, N. (2014) 'Analysis of building deformation in landslide area using multisensor PSInSAR™ technique', *International Journal of Applied Earth Observation and Geoinformation*, 33(1), pp. 166–180. doi: 10.1016/j.jag.2014.05.011.

Ciampalini, A., Raspini, F., Lagomarsino, D., Catani, F. and Casagli, N. (2016) 'Landslide susceptibility map refinement using PSInSAR data', *Remote Sensing of Environment*, 184, pp. 302–315. doi: 10.1016/j.rse.2016.07.018.

Cigna, F., Tapete, D. and Casagli, N. (2012) 'Semi-automated extraction of Deviation Indexes (DI) from satellite Persistent Scatterers time series: tests on sedimentary volcanism and tectonically-induced motions', *Nonlinear Processes in Geophysics*, 19(6), pp. 643–655. doi: 10.5194/npg-19-643-2012.

Cigna, F., Del Ventisette, C., Liguori, V. and Casagli, N. (2011) 'Advanced radar-interpretation of InSAR time series for mapping and characterization of geological processes', *Natural Hazards and Earth System Science*, 11(3), pp. 865–881. doi: 10.5194/nhess-11-865-2011.

Cleveland, R. B., Cleveland, W. S., McRae, J. E. and Terpenning, I. (1990) 'STL: A seasonal-trend decomposition procedure based on Loess', *Journal of Official Statistics*, 6(1), pp. 3–73.

Cloude, S. R. (2011) 'POLInSAR : From SIR-C to TanDEM-X', in *IEEE Geoscience and Remote Sensing Symposium*. Vancouver, Canada, July 24 - 29: IEEE, pp. 2570–2573. doi: 10.1109/igarss.2011.6049766.

Cohen, J. (1960) 'A coefficient of agreement for nominal scales', *Educational and Psychological Measurement*, 20(1), pp. 37–46. doi: 10.1177/001316446002000104.

Colesanti, C., Ferretti, A., Novali, F., Prati, C. and Rocca, F. (2003) 'SAR monitoring of progressive and seasonal ground deformation using the permanent scatterers technique', *IEEE Transactions on Geoscience and Remote Sensing*, 41(7), pp. 1685–1701. doi: 10.1109/TGRS.2003.813278.

Confuorto, P. (2016) *From site-scale to large areas monitoring of ground deformation phenomena by integration of different DInSAR techniques in Crotone Province (Southern Italy)*. PhD thesis. Università degli Studi di Napoli "Federico II".

Copernicus Programme (2020) *EU-DEM v1.1*. Available at: https://land.copernicus.eu/imagery-in-situ/eu-dem/eu-dem-v1.1?tab=metadata (Accessed: 9 March 2020).

Corporation, M. and Weston, S. (2018) *doParallel: Foreach Parallel Adaptor for the 'parallel' Package. R package version 1.0.14*. Available at: https://cran.r-project.org/package=doParallel (Accessed: 30 July 2020).

Corr, D. G., Cloude, S. R., Ferro-Famil, L., Hoekman, D. H., Partington, K., Pottier, E. and Rodrigues, A. (2003) 'A review of the applications of SAR polarimetry and polarimetric interferometry - An

ESA funded study', in *POLinSAR: Applications of SAR Polarimetry and Polarimetric Interferometry*. Frascati, January 14-16: European Space Agency, ESA Special Publication, pp. 1–9.

Costantini, M. (1998) 'A novel phase unwrapping method based on network programming', *IEEE Transactions on Geoscience and Remote Sensing*, 36(3), pp. 813–821. doi: 10.1109/36.673674.

Costantini, M., Falco, S., Malvarosa, F. and Minati, F. (2008) 'A new method for identification and analysis of Persistent Scatterers in series of SAR images', in *IEEE International Geoscience and Remote Sensing Symposium*. Boston, United States of America, July 6-11, pp. 449–452. doi: 978-1-4244-2808-3/08.

Costantini, M., Zhu, M., Huang, S., Bai, S., Cui, J., Minati, F., Vecchioli, F., Jin, D. and Hu, Q. (2018) 'Automatic detection of building and infrastructure instabilities by spatial and temporal analysis of InSAR measurements', in *International Geoscience and Remote Sensing Symposium*. Valencia, Spain, July 22-27: IEEE, pp. 2224–2227. doi: 10.1109/IGARSS.2018.8518270.

Czikhardt, R., Papco, J., Bakon, M., Liscak, P., Ondrejka, P. and Zlocha, M. (2017) 'Ground stability monitoring of undermined and landslide prone areas by means of Sentinel-1 multi-temporal InSAR, case study from Slovakia', *Geosciences (Switzerland)*, 7(3), pp. 1–17. doi: 10.3390/geosciences7030087.

Dentz, F., van Halderen, L., Boudewijn, P., Esfahany, S. S., Slobbe, C. and Wortel, T. (2006) *'POSEIDON' On the potential of satellite radar interferometry for monitoring dikes of the Netherlands - A technical feasibility study*. Report, Delft University of Technology.

Devanthéry, N., Crosetto, M., Monserrat, O., Cuevas-González, M. and Crippa, B. (2014) 'An approach to persistent scatterer interferometry', *Remote Sensing*, 6(7), pp. 6662–6679. doi: 10.3390/rs6076662.

Dheenathayalan, P., Caro Cuenca, M., Hoogeboom, P. and Hanssen, R. F. (2017) 'Small reflectors for ground motion monitoring with InSAR', *IEEE Transactions on Geoscience and Remote Sensing*, 55(12), pp. 6703–6712. doi: 10.1109/TGRS.2017.2731424.

Ding, H., Trajcevski, G., Scheuermann, P., Wang, X. and Keogh, E. (2008) 'Querying and mining of time series data: Experimental comparison of representations and distance measures', *Very Large Data Bases Endowment*, 1(2), pp. 1542–1552. doi: 10.14778/1454159.1454226.

Dubois, C., Thiele, A. and Hinz, S. (2013) 'Pixel-based approach for building heights determination by SAR radargrammetry', *ISPRS Annals of the Photogrammetry, Remote Sensing and Spatial Information Sciences*, II(3/W3), pp. 19–24. doi: 10.5194/isprsannals-II-3-W3-19-2013.

ElKobtan, H., Salem, M., Attia, K., Ahmed, S. and Abou El-Magd, I. (2016) 'Sedimentological study of Lake Nasser; Egypt, using integrated improved techniques of core sampling, X-ray diffraction

and GIS platform', *Cogent Geoscience*, 2(1), pp. 1–20. doi: 10.1080/23312041.2016.1168069.

Emadali, L., Motagh, M. and Haghighi, M. H. (2017) 'Characterizing post-construction settlement of the Masjed-Soleyman embankment dam, Southwest Iran, using TerraSAR-X SpotLight radar imagery', *Engineering Structures*, 143, pp. 261–273. doi: 10.1016/j.engstruct.2017.04.009.

ESA (2020) *Satellite Missions Database*. Available at: https://directory.eoportal.org/web/eoportal/satellite-missions (Accessed: 30 July 2020).

Esling, P. and Agon, C. (2012) 'Time-series data mining', *ACM Computing Surveys*, 45(1), pp. 1-34. doi: 10.1145/2379776.2379788.

Farolfi, G., Bianchini, S. and Casagli, N. (2019) 'Integration of GNSS and satellite InSAR data: Derivation of fine-scale vertical surface motion maps of Po Plain, Northern Apennines, and Southern Alps, Italy', *IEEE Transactions on Geoscience and Remote Sensing*, 57(1), pp. 319–328. doi: 10.1109/TGRS.2018.2854371.

Farolfi, G., Piombino, A. and Catani, F. (2019) 'Fusion of GNSS and satellite radar interferometry: Determination of 3D fine-scale map of present-day surface displacements in Italy as expressions of geodynamic processes', *Remote Sensing*, 11(4), p. 394. doi: 10.3390/rs11040394.

Farr, T. G. and Kobrick, M. (2000) 'Shuttle radar topography mission produces a wealth of data', *Eos*, 81(48), pp. 583–585. doi: 10.1029/EO081i048p00583.

Farrar, C. R. and Worden, K. (2010) 'An introduction to structural health monitoring', in *New trends in vibration based structural health monitoring*, pp. 1–17. Springer, Vienna. doi: 10.1007/978-3-7091-0399-9_1.

Fernandes, P., Jorge, R. C. G. S., Rodrigues, B., Pereira, Z. and Oliveira, J. T. (2012) 'Caracterização geoquímica da Formação da Brejeira (Grupo do Flysch do Baixo Alentejo): Resultados preliminares', in *X Congresso de Geoquímica dos Países de Língua Portuguesa XVI Semana de Geoquímica*. Cape Verde, pp. 293–299.

Ferretti, A., Colombo, D., Fumagalli, A., Novali, F. and Rucci, A. (2015) 'InSAR data for monitoring land subsidence: Time to think big', *Proceedings of the International Association of Hydrological Sciences*, 372, pp. 331–334. doi: 10.5194/piahs-372-331-2015.

Ferretti, A., Fumagalli, A., Novali, F., Prati, C., Rocca, F. and Rucci, A. (2011) 'A new algorithm for processing interferometric data-stacks: SqueeSAR', *IEEE Transactions on Geoscience and Remote Sensing*, 49(9), pp. 3460–3470. doi: 10.1109/TGRS.2011.2124465.

Ferretti, A., Prati, C. and Rocca, F. (2000) 'Nonlinear subsidence rate estimation using permanent scatterers in differential SAR interferometry', *IEEE Transactions on Geoscience and Remote Sensing*, 38(5), pp. 2202–2212. doi: 10.1109/36.868878.

Ferretti, A., Prati, C. and Rocca, F. (2001) 'Permanent scatterers in SAR interferometry', *IEEE Transactions on Geoscience and Remote Sensing*, 39(1), pp. 8–20. doi: 10.1109/36.898661.

Ferretti, A., Savio, G., Barzaghi, R., Borghi, A., Musazzi, S., Novali, F., Prati, C. and Rocca, F. (2007) 'Submillimeter accuracy of InSAR time series: Experimental validation', *IEEE Transactions on Geoscience and Remote Sensing*, 45(5), pp. 1142–1153. doi: 10.1109/TGRS.2007.894440.

Ferretti, A., Monti-Guarnieri, A., Prati, C., Rocca, F. and Massonnet, D. (2007) *InSAR Principles: Guidelines for SAR Interferometry Processing and Interpretation*. ESA Public. Edited by Fletcher, K.. Noordwijk, The Netherlands. doi: 10.1073/pnas.81.17.5399.

Fornaro, G. and Serafino, F. (2006) 'Imaging of single and double scatterers in Urban areas via SAR tomography', *IEEE Transactions on Geoscience and Remote Sensing*, 44(12), pp. 3497–3505. doi: 10.1109/TGRS.2006.881748.

Fu, T. C. (2011) 'A review on time series data mining', *Engineering Applications of Artificial Intelligence*, 24(1), pp. 164–181. doi: 10.1016/j.engappai.2010.09.007.

Fuhrmann, T. and Garthwaite, M. C. (2019) 'Resolving three-dimensional surface motion with InSAR: Constraints from multi-geometry data fusion', *Remote Sensing*, 11(3), p. 241. doi: 10.3390/rs11030241.

Fujita, H. (1977) 'Influence of water level fluctuations in a reservoir on slope stability', *Bulletin of the International Association of Engineering Geology-Bulletin de l'Association Internationale de Géologie de l'Ingénieur*, 16(1), pp. 170–173. doi: 10.1007/bf02591474.

Garthwaite, M. C. (2017) 'On the design of radar corner reflectors for deformation monitoring in multi-frequency InSAR', *Remote Sensing*, 9(7), p. 648. doi: 10.3390/rs9070648.

Giardina, G., Milillo, P., DeJong, M. J., Perissin, D. and Milillo, G. (2019) 'Evaluation of InSAR monitoring data for post-tunnelling settlement damage assessment', *Structural Control and Health Monitoring*, 26(2), p. e2285. doi: 10.1002/stc.2285.

Goad, C. C. and Goodman, L. (1974) 'A modified Hopfield tropospheric refraction correction model', in *Fall Annual Meeting American Geophysical Union*. San Francisco, California, December 12-17.

Gold, O. and Sharir, M. (2018) 'Dynamic time warping and geometric edit distance: Breaking the quadratic barrier', *ACM Transactions on Algorithms*, 14(4), pp. 1-14. doi: 10.1145/3230734.

Goldstein, R. M., Zebker, H. A. and Werner, C. L. (1988) 'Satellite radar interferometry: Two-dimensional phase unwrapping', *Radio Science*, 23(4), pp. 713–720. doi: 10.1029/RS023i004p00713.

Grupo Cimpor (2020) *Aproveitamento Hidroelétrico do Baixo Sabor*. Available at:

http://www.cimpor.com/artigo.aspx?lang=pt&id_object=1247&name=Aproveitamento-Hidroeletrico-do-Baixo-Sabor (Accessed: 26 March 2020).

Gudmundsson, S., Gudmundsson, M. T., Björnsson, H., Sigmundsson, F., Rott, H. and Carstensen, J. M. (2002) 'Three-dimensional glacier surface motion maps at the Gjálp eruption site, Iceland, inferred from combining InSAR and other ice-displacement data', *Annals of Glaciology*, 34(1), pp. 315–322. doi: 10.3189/172756402781817833.

Guglielmino, F., Nunnari, G., Puglisi, G. and Spata, A. (2011) 'Simultaneous and integrated strain tensor estimation from geodetic and satellite deformation measurements to obtain three-dimensional displacement maps', *IEEE Transactions on Geoscience and Remote Sensing*, 49(6), pp. 1815–1826. doi: 10.1109/TGRS.2010.2103078.

Hair, J. F., Black, W. C., Babin, B. J. and Anderson, R. E. (2009) *Multivariate Data Analysis*. 7th edn. Upper Saddle River: Prentice Hall.

Hayes, A. F. and Li, C. (2007) 'Further evaluating the conditional decision rule for comparing two independent means', *British Journal of Mathematical and Statistical Psychology*, 60(2), pp. 217–244. doi: 10.1348/000711005X62576.

Heleno, S. I. N., Oliveira, L. G. S., Henriques, M. J., Falcão, A. P., Lima, J. N. P., Cooksley, G., Ferretti, A., Fonseca, A. M., Lobo-Ferreira, J. P. and Fonseca, J. F. B. D. (2011) 'Persistent Scatterers Interferometry detects and measures ground subsidence in Lisbon', *Remote Sensing of Environment*, 115(8), pp. 2152–2167. doi: 10.1016/j.rse.2011.04.021.

Hensley, S., Wheeler, K., Sadowy, G., Jones, C., Shaffer, S., Zebker, H., Miller, T., Heavey, B., Chuang, E., Chao, R., Vines, K., Nishimoto, K., Prater, J., Carrico, B., Chamberlain, N., Shimada, J., Simard, M., Chapman, B., Muellerschoen, R., Le, C., Michel, T., Hamilton, G., Robison, D., Neumann, G., Meyer, R., Smith, P., Granger, J., Rosen, P., Flower, D. and Smiths, R. (2008) 'The UAVSAR instrument: Description and first results', in *2008 IEEE Radar Conference*. Rome, Italy, May 26-30, pp. 0–5. doi: 10.1109/RADAR.2008.4720722.

Hong, C. Y., Zhang, Y. F., Zhang, M. X., Leung, L. M. G. and Liu, L. Q. (2016) 'Application of FBG sensors for geotechnical health monitoring, a review of sensor design, implementation methods and packaging techniques', *Sensors and Actuators, A: Physical*, 244, pp. 184–197. doi: 10.1016/j.sna.2016.04.033.

Hooper, A. J. (2008) 'A multi-temporal InSAR method incorporating both persistent scatterer and small baseline approaches', *Geophysical Research Letters*, 35(16), pp. 1–5. doi: 10.1029/2008GL034654.

Hooper, A. and Zebker, H. A. (2007) 'Phase unwrapping in three dimensions with application to InSAR time series', *Journal of the Optical Society of America A*, 24(9), p. 2737. doi:

10.1364/josaa.24.002737.

Hooper, A., Zebker, H., Segall, P. and Kampes, B. (2004) 'A new method for measuring deformation on volcanoes and other natural terrains using InSAR persistent scatterers', *Geophysical Research Letters*, 31(23), p. L23611. doi: 10.1029/2004GL021737.

Hu, J., Ding, X. L., Li, Z. W., Zhang, L., Zhu, J. J., Sun, Q. and Gao, G. J. (2016) 'Vertical and horizontal displacements of Los Angeles from InSAR and GPS time series analysis: Resolving tectonic and anthropogenic motions', *Journal of Geodynamics*, 99, pp. 27–38. doi: 10.1016/j.jog.2016.05.003.

Hu, J., Li, Z. W., Ding, X. L., Zhu, J. J., Zhang, L. and Sun, Q. (2014) 'Resolving three-dimensional surface displacements from InSAR measurements: A review', *Earth-Science Reviews*, 133, pp. 1–17. doi: 10.1016/j.earscirev.2014.02.005.

Hui, L. (2015) 'Yangtze riverbank slope stability by water level change in the Three Gorges reservoir', *Electronic Journal of Geotechnical Engineering*, 20, pp. 1847–1856.

ICEYE (2020) *ICEYE*. Available at: https://www.iceye.com/ (Accessed: 30 July 2020).

Infante, D., Di Martire, D., Calcaterra, D., Miele, P., Scotto di Santolo, A. and Ramondini, M. (2019) 'Integrated procedure for monitoring and assessment of linear infrastructures safety (I-Pro MONALISA) affected by slope instability', *Applied Sciences*, 9(24), p. 5535. doi: 10.3390/app9245535.

JAXA, J. A. E. A. (2008) *ALOS Data Users Handbook, Earth Observation Research and Application Center Japan Aerospace Exploration Agency*. Available at: http://www.eorc.jaxa.jp/ALOS/en/doc/fdata/ALOS_HB_RevC_EN.pdf (Accessed: 30 July 2020).

Kalpakis, K., Gada, D. and Puttagunta, V. (2001) 'Distance measures for effective clustering of ARIMA time-series', in *2001 IEEE International Conference on Data Mining*. San Jose, United States of America, 29 November-2 December: IEEE Computer Society, pp. 273–280. doi: 10.1109/icdm.2001.989529.

Kampes, B. M. (2005) *Displacement parameter estimation using permanent scatterer interferometry*. PhD thesis. Technische Universiteit Delft.

Kasischke, E. S., Bourgeau-Chavez, L. L., French, N. H., Harrell, P. and Christensen, N. L. (1992) 'Initial observations on using SAR to monitor wildfire scars in boreal forests', *International Journal of Remote Sensing*, 13(18), pp. 3495–3501. doi: 10.1080/01431169208904137.

Keogh, E., Chakrabarti, K., Pazzani, M. and Mehrotra, S. (2001) 'Dimensionality reduction and similarity search in large time series databases', *Knowledge and Information Systems*, 3(3), pp. 263–286. doi: 10.1007/pl00011669.

van de Kerkhof, B., Pankratius, V., Chang, L., van Swol, R. and Hanssen, R. F. (2020) 'Individual

scatterer model learning for satellite interferometry', *IEEE Transactions on Geoscience and Remote Sensing*, 58(2), pp. 1273–1280. doi: 10.1109/TGRS.2019.2945370.

Ketelaar, V. B. H. (2008) *Monitoring surface deformation induced by hydrocarbon production using satellite radar interferometry*. PhD thesis. Technische Universiteit Delft.

Kim, S., Torbol, M. and Chou, P. H. (2013) 'Remote structural health monitoring systems for next generation SCADA', *Smart Structures and Systems*, 11(5), pp. 511–531. doi: 10.12989/sss.2013.11.5.511.

Komac, M., Holley, R., Mahapatra, P., van der Marel, H. and Bavec, M. (2015) 'Coupling of GPS/GNSS and radar interferometric data for a 3D surface displacement monitoring of landslides', *Landslides*, 12(2), pp. 241–257. doi: 10.1007/s10346-014-0482-0.

Lanari, R., Berardino, P., Bonano, M., Casu, F., Manconi, A., Manunta, M., Manzo, M., Pepe, A., Pepe, S., Sansosti, E., Solaro, G., Tizzani, P. and Zeni, G. (2010) 'Surface displacements associated with the L'Aquila 2009 Mw 6.3 earthquake (central Italy): New evidence from SBAS-DInSAR time series analysis', *Geophysical Research Letters*, 37(20), p. L20309. doi: 10.1029/2010GL044780.

Lanari, R., Lundgren, P., Manzo, M. and Casu, F. (2004) 'Satellite radar interferometry time series analysis of surface deformation for Los Angeles, California', *Geophysical Research Letters*, 31(23), pp. 1–5. doi: 10.1029/2004GL021294.

Lazecky, M., Hlavacova, I., Bakon, M., Sousa, J. J., Perissin, D. and Patricio, G. (2017) 'Bridge displacements monitoring using space-borne X-band SAR interferometry', *IEEE Journal of Selected Topics in Applied Earth Observations and Remote Sensing*, 10(1), pp. 205–210. doi: 10.1109/JSTARS.2016.2587778.

Lazecky, M., Perissin, D., Bakon, M., De Sousa, J. M., Hlavacova, I. and Real, N. (2015) 'Potential of satellite InSAR techniques for monitoring of bridge deformations', in *2015 Joint Urban Remote Sensing Event*. Lausanne, Switzerland, March 30 - April 1, pp. 4–7. doi: 10.1109/JURSE.2015.7120506.

Leick, A. (2004) *GPS Satellite Surveying*. 3rd edn. New Jersey: John Wiley & Sons, Inc.

van Leijen, F., Samiei-Esfahany, S., van derMarel, H. and Hanssen, R. (2017) 'A standardized approach for the integration of geodetic data for deformation analysis', in *IEEE International Geoscience and Remote Sensing Symposium*. Fort Worth, United States of America, July 23-28, pp. 957–960. doi: 10.1109/igarss.2017.8127112.

Li, C., Yin, J., Zhao, J., Zhang, G. and Shan, X. (2012) 'The selection of artificial corner reflectors based on RCS analysis', *Acta Geophysica*, 60(1), pp. 43–58. doi: 10.2478/s11600-011-0060-y.

Lima, J. N. (2015a) 'A utilização de filtros digitais em séries temporais GNSS', in *VIII CNCG*

Conferência Nacional de Cartografia e Geodesia. Amadora, Portugal, October 29-30, pp. 1–8.

Lima, J. N. (2015b) 'Monitorização de deslocamentos em barragens de aterro com o GNSS', in *VIII CNCG Conferência Nacional de Cartografia e Geodesia*. Amadora, Portugal, October 29-30, pp. 1–8.

Lima, J. N., Conde, V. and Candeias, H. (2015) 'Quality assessment of GNSS with short-length session in the displacement measurement of a large embankment dam', in *Second International Dam World Conference*. Lisbon, Portugal, pp. 1–10.

Lima, J. N. P. (2009) 'O efeito da carga oceânica nas séries temporais GNSS', in *2º Encontro Nacional de Geodesia Aplicada*. Lisbon, Portugal, October 12 - 13, pp. 1–6.

LNEC (1989) *Critérios e métodos de observação de barragens de betão*. Laboratório Nacional de Engenharia Civil, Memory No. 740.

LNEC (2001) *O Método da Variação de Coordenadas na Observação Geodésica de Barragens*. Laboratório Nacional de Engenharia Civil, Report, Series ICT, ITB 21 – DBB/NGA.

LNEC (2013) *A Resolução de Problemas Mal Colocados na Observação Geodésica de Barragens*. Laboratório Nacional de Engenharia Civil, Report, Series ICT, INCB 20 – DBB/NGA.

LNEC (2016) *Barragem do Baixo Sabor: Resultados da observação geodésica efetuada em abril de 2016*. Laboratório Nacional de Engenharia Civil, Technical Report No. 62/2016 – DBB/NGA.

LNEC (2017a) *Ala Ocidental da Praça do Comércio: Resultados do nivelamento geométrico efetuado em setembro de 2017*. Laboratório Nacional de Engenharia Civil, Technical Report No. 132/2017 – DBB/NGA.

LNEC (2017b) *Barragem do Baixo Sabor: Resultados Preliminares da Monitorização de Deslocamentos com o GNSS*. Laboratório Nacional de Engenharia Civil, Report No. 92/2017 – DBB/NGA.

LNEC (2018) *Barragem do Baixo Sabor: Resultados da medição de deslocamentos com o GNSS entre maio de 2016 e dezembro de 2017*. Laboratório Nacional de Engenharia Civil, Report No. 222/2018 – DBB/NGA.

LNEC (2020) *Estudo sobre a fissuração em revestimentos de paredes no edifício Ivens Arte*. Laboratório Nacional de Engenharia Civil. Report No. 162/2020 – DED/NRI.

Lombardini, F. (2005) 'Differential tomography: A new framework for SAR interferometry', *IEEE Transactions on Geoscience and Remote Sensing*, 43(1), pp. 37–44. doi: 10.1109/TGRS.2004.838371.

Lynch, J. P. and Loh, K. J. (2006) 'A summary review of wireless sensors and sensor networks for structural health monitoring', *The Shock and Vibration Digest*, 38(2), pp. 91–128. doi:

10.1177/0583102406061499.

Mahapatra, P., der Marel, H. van, van Leijen, F., Samiei-Esfahany, S., Klees, R. and Hanssen, R. (2018) 'InSAR datum connection using GNSS-augmented radar transponders', *Journal of Geodesy*, 92(1), pp. 21–32. doi: 10.1007/s00190-017-1041-y.

Mahapatra, P. S. (2015) *Geodetic Network Design for InSAR. Application to ground deformation monitoring*. PhD thesis. Technische Universiteit Delft. doi: 10.1109/TGRS.2014.2381598.

Mahapatra, P. S., Samiei-Esfahany, S., Van Der Marel, H. and Hanssen, R. F. (2014) 'On the use of transponders as coherent radar targets for SAR interferometry', *IEEE Transactions on Geoscience and Remote Sensing*, 52(3), pp. 1869–1878. doi: 10.1109/TGRS.2013.2255881.

Majumder, M., Gangopadhyay, T. K., Chakraborty, A. K., Dasgupta, K. and Bhattacharya, D. K. (2008) 'Fibre Bragg gratings in structural health monitoring-Present status and applications', *Sensors and Actuators, A: Physical*, 147(1), pp. 150–164. doi: 10.1016/j.sna.2008.04.008.

Marendić, A., Paar, R., Grgac, I. and Damjanović, D. (2016) 'Monitoring of oscillations and frequency analysis of the railway bridge "Sava" using robotic total station', in *Proceedings of 3rd Joint International Symposium on Deformation Monitoring*. Vienna, Austria, March 30 - April 1, pp. 1–8.

Marinkovic, P., Ketelaar, G., van Leijen, F. and Hanssen, R. (2007) 'InSAR quality control: Analysis of five years of corner reflector time series', in *FRINGE 2007 Workshop (ESA-SP 649) Vol. 26*. Frascati, Italy, November 26-30, pp. 1-8.

Di Martire, D., Iglesias, R., Monells, D., Centolanza, G., Sica, S., Ramondini, M., Pagano, L., Mallorquí, J. J. and Calcaterra, D. (2014) 'Comparison between Differential SAR interferometry and ground measurements data in the displacement monitoring of the earth-dam of Conza della Campania (Italy)', *Remote Sensing of Environment*, 148, pp. 58–69. doi: 10.1016/j.rse.2014.03.014.

Massonnet, D. and Feigl, K. L. (1998) 'Radar interferometry and its application to changes in the Earth's surface', *Reviews of Geophysics*, 36(4), pp. 441–500. doi: 8755-1209/98/97 RG-03139.

Mateus, P., Catalão, J. and Nico, G. (2017) 'Sentinel-1 interferometric SAR mapping of precipitable water vapor over a country-spanning area', *IEEE Transactions on Geoscience and Remote Sensing*, 55(5), pp. 2993–2999. doi: 10.1109/TGRS.2017.2658342.

Menges, C. H., Bartolo, R. E., Bell, D. and Hill, G. J. E. (2004) 'The effect of savanna fires on SAR backscatter in northern Australia', *International Journal of Remote Sensing*, 25(22), pp. 4857–4871. doi: 10.1080/01431160410001712945.

Meteored (2020) *Histórico do tempo para Lisboa*. Available at: https://www.tempo.pt/lisboa-sactual.htm (Accessed: 30 July 2020).

Metropolitano de Lisboa E.P.E (2018) *Um pouco de história*. Available at: https://www.metrolisboa.pt/institucional/conhecer/historia-do-metro/ (Accessed: 30 July 2020).

Milillo, P., Bürgmann, R., Lundgren, P., Salzer, J., Perissin, D., Fielding, E., Biondi, F. and Milillo, G. (2016) 'Space geodetic monitoring of engineered structures: The ongoing destabilization of the Mosul dam, Iraq', *Scientific Reports*, 6(1), 37408, p. 1-7. doi: 10.1038/srep37408.

Milillo, P., Giardina, G., DeJong, M., Perissin, D. and Milillo, G. (2018) 'Multi-temporal InSAR structural damage assessment: The London crossrail case study', *Remote Sensing*, 10(2), p. 287. doi: 10.3390/rs10020287.

Milillo, P., Giardina, G., Perissin, D., Milillo, G., Coletta, A. and Terranova, C. (2019) 'Pre-collapse space geodetic observations of critical infrastructure: The Morandi Bridge, Genoa, Italy', *Remote Sensing*, 11(12), p. 1403. doi: 10.3390/rs11121403.

Milillo, P., Perissin, D., Salzer, J. T., Lundgren, P., Lacava, G., Milillo, G. and Serio, C. (2016) 'Monitoring dam structural health from space: Insights from novel InSAR techniques and multi-parametric modeling applied to the Pertusillo dam Basilicata, Italy', *International Journal of Applied Earth Observation and Geoinformation*, 52, pp. 221–229. doi: 10.1016/J.JAG.2016.06.013.

Milone, G. and Scepi, G. (2011) 'A clustering approach for studying ground deformation trends in Campania Region through PS-InSAR™ time series analysis', *Journal of Applied Sciences*, 11(4), pp. 610–620. doi: 10.3923/jas.2011.610.620.

Mittermayer, E. (1972) 'A generalisation of the least - squares method for the adjustment of free networks', *Bulletin Géodésique (1946 - 1975)*, 104(1), pp. 139–157. doi: 10.1007/bf02530298.

Monserrat, O., Crosetto, M. and Luzi, G. (2014) 'A review of ground-based SAR interferometry for deformation measurement', *ISPRS Journal of Photogrammetry and Remote Sensing*, 93, pp. 40–48. doi: 10.1016/j.isprsjprs.2014.04.001.

Moreira, A., Prats-Iraola, P., Younis, M., Krieger, G., Hajnsek, I. and Papathanassiou, K. P. (2013) 'A tutorial on synthetic aperture radar', *IEEE Geoscience and Remote Sensing Magazine*, 1(1), pp. 6–43. doi: 10.1109/MGRS.2013.2248301.

Muller, C., Del Potro, R., Biggs, J., Gottsmann, J., Ebmeier, S. K., Guillaume, S., Cattin, P.-H. and Van Der Laat, R. (2015) 'Integrated velocity field from ground and satellite geodetic techniques: application to Arenal volcano', *Geophysical Journal International*, 200(2), pp. 861–877. doi: 10.1093/gji/ggu444.

Nakamura, R., Nakamura, S. and Kudo, N. (2007) 'Precise orbit determination for ALOS and the accuracy verification by SLR', *The Journal of Space Technology and Science*, 23(1), pp. 1_14-1_19. doi: 10.11230/jsts.23.1_14.

Nemus - Gestão e Requalificação Ambiental, Lda. (2007) *Plano de Ordenamento da Albufeira de Odelouca Relatório Volume 2*. Report, Nemus - Gestão e Requalificação Ambiental, Lda.

Nöther, N., Wosniok, A., Krebber, K. and Thiele, E. (2009) 'A distributed fiber-optic sensing system for monitoring of large geotechnical structures', in *4th International Conference on Structural Health Monitoring of Intelligent Infrastructure (SHMII-4) 2009*. Zurich, Switzerland, pp. 1–9.

Notti, D., Calò, F., Cigna, F., Manunta, M., Herrera, G., Berti, M., Meisina, C., Tapete, D. and Zucca, F. (2015) 'A user-oriented methodology for DInSAR time series analysis and interpretation: Landslides and subsidence case studies', *Pure and Applied Geophysics*, 172(11), pp. 3081–3105. doi: 10.1007/s00024-015-1071-4.

Novellino, A., Cigna, F., Brahmi, M., Sowter, A., Bateson, L. and Marsh, S. (2017) 'Assessing the feasibility of a national InSAR ground deformation map of great britain with Sentinel-1', *Geosciences (Switzerland)*, 7(2), pp. 1–14. doi: 10.3390/geosciences7020019.

Osmanoğlu, B., Dixon, T. H., Wdowinski, S., Cabral-Cano, E. and Jiang, Y. (2011) 'Mexico City subsidence observed with persistent scatterer InSAR', *International Journal of Applied Earth Observation and Geoinformation*, 13(1), pp. 1–12. doi: 10.1016/J.JAG.2010.05.009.

Panuccio, A., Bicego, M. and Murino, V. (2002) 'A hidden Markov model-based approach to sequential data clustering', *Structural, Syntactic, and Statistical Pattern Recognition*. Edited by Caelli, T., Amin, A., Duin, R. P. W., Kamel, M. and de Ridder, D. *Lecture Notes in Computer Science*, 2396. Springer-Verlag Berlin Heidelberg. doi: 10.1007/3-540-70659-3_77.

Park, D. J., Yeom, K. W., Ahn, S. Il and Lim, H. S. (2014) 'Validation of an active transponder for KOMPSAT-5 SAR image calibration', *Advances in Space Research*, 54(8), pp. 1552–1562. doi: 10.1016/j.asr.2014.06.016.

Paronuzzi, P., Rigo, E. and Bolla, A. (2013) 'Influence of filling-drawdown cycles of the Vajont reservoir on Mt. Toc slope stability', *Geomorphology*, 191, pp. 75–93. doi: 10.1016/j.geomorph.2013.03.004.

Paziewski, J., Sieradzki, R. and Baryla, R. (2018) 'Multi-GNSS high-rate RTK, PPP and novel direct phase observation processing method: Application to precise dynamic displacement detection', *Measurement Science and Technology*, 29(3), p. 035002. doi: 10.1088/1361-6501/aa9ec2.

Paziewski, J., Sieradzki, R. and Baryla, R. (2019) 'Detection of structural vibration with high-rate precise point positioning: Case study results based on 100 Hz multi-GNSS observables shake-table simulation', *Sensors (Switzerland)*, 19(22), p. 4832. doi: 10.3390/s19224832.

Pei, H. F., Teng, J., Yin, J. H. and Chen, R. (2014) 'A review of previous studies on the applications of optical fiber sensors in geotechnical health monitoring', *Measurement: Journal of the International Measurement Confederation*, 58, pp. 207–214. doi:

10.1016/j.measurement.2014.08.013.

Pereira, Z., Matos, J., Fernandes, P. and Oliveira, J. T. (2008) *Palynostratigraphy and systematic palynology of the Devonian and Carboniferous sucessions of the South Portuguese Zone, Portugal*. Memory, Instituto Nacional de Engenharia, Tecnologia e Inovação.

Perissin, D. and Wang, T. (2012) 'Repeat-pass SAR interferometry with partially coherent targets', *IEEE Transactions on Geoscience and Remote Sensing*, 50(1), pp. 271–280. doi: 10.1109/TGRS.2011.2160644.

Perissin, D., Wang, Z. and Wang, T. (2011) 'The SARPROZ InSAR tool for urban subsidence / manmade structure stability monitoring in China', in *34th International Symposium for Remote Sensing of the Environment*. Sydney, Australia, April 10-15, p. 4.

Piyush, A. and Zebker, H. (2010) 'Edgelist phase unwrapping algorithm for time series InSAR analysis', in *Fringe 2009 Workshop*. Frascati, Italy, 30 November – 4 December 2009: ESA SP-677, March 2010, pp. 1-6.

Polcari, M., Fernández, J., Albano, M., Bignami, C., Palano, M. and Stramondo, S. (2017) 'An improved data integration algorithm to constrain the 3D displacement field induced by fast deformation phenomena tested on the Napa Valley earthquake', *Computers and Geosciences*, 109, pp. 206–215. doi: 10.1016/j.cageo.2017.09.002.

Polcari, M., Palano, M., Fernández, J., Samsonov, S. V., Stramondo, S. and Zerbini, S. (2016) '3D displacement field retrieved by integrating Sentinel-1 InSAR and GPS data: The 2014 south Napa earthquake', *European Journal of Remote Sensing*, 49(1), pp. 1–13. doi: 10.5721/EuJRS20164901.

Poreh, D., Iodice, A., Riccio, D. and Ruello, G. (2016) 'Railways' stability observed in Campania (Italy) by InSAR data', *European Journal of Remote Sensing*, 49(1), pp. 417–431. doi: 10.5721/EuJRS20164923.

Pratesi, F., Tapete, D., Terenzi, G., Del Ventisette, C. and Moretti, S. (2015) 'Rating health and stability of engineering structures via classification indexes of InSAR Persistent Scatterers', *International Journal of Applied Earth Observation and Geoinformation*, 40, pp. 81–90. doi: 10.1016/j.jag.2015.04.012.

ProjectJupyter (2020) *Jupyter*. Available at: https://jupyter.org/ (Accessed: 30 July 2020).

Psimoulis, P., Pytharouli, S., Karambalis, D. and Stiros, S. (2008) 'Potential of Global Positioning System (GPS) to measure frequencies of oscillations of engineering structures', *Journal of Sound and Vibration*, 318(3), pp. 606–623. doi: 10.1016/j.jsv.2008.04.036.

Pulvirenti, L., Pierdicca, N., Chini, M. and Guerriero, L. (2011) 'An algorithm for operational flood mapping from Synthetic Aperture Radar (SAR) data using fuzzy logic', *Natural Hazards and*

Earth System Science, 11(2), pp. 529–540. doi: 10.5194/nhess-11-529-2011.

Qin, X., Liao, M., Zhang, L. and Yang, M. (2017) 'Structural health and stability assessment of high-speed railways via thermal dilation mapping with time-series InSAR analysis', *IEEE Journal of Selected Topics in Applied Earth Observations and Remote Sensing*, 10(6), pp. 2999–3010. doi: 10.1109/JSTARS.2017.2719025.

Qin, Y. and Perissin, D. (2015) 'Monitoring ground subsidence in Hong Kong via spaceborne radar: Experiments and validation', *Remote Sensing*, 7(8), pp. 10715–10736. doi: 10.3390/rs70810715.

Qin, Y., Perissin, D. and Lei, L. (2013) 'The design and experiments on corner reflectors for urban ground deformation monitoring in Hong Kong', *International Journal of Antennas and Propagation*, 2013, pp. 1-8. doi: 10.1155/2013/191685.

Quin, G. and Loreaux, P. (2013) 'Submillimeter accuracy of multipass corner reflector monitoring by PS technique', *IEEE Transactions on Geoscience and Remote Sensing*, 51(3), pp. 1775–1783. doi: 10.1109/TGRS.2012.2206600.

R Core Team (2018) 'R: A language and environment for statistical computing.' Vienna, Austria: R Foundation for Statistical Computing. Available at: http://www.r-project.org/ (Accessed: 29 August 2019).

Raspini, F., Bianchini, S., Ciampalini, A., Del Soldato, M., Solari, L., Novali, F., Del Conte, S., Rucci, A., Ferretti, A. and Casagli, N. (2018) 'Continuous, semi-automatic monitoring of ground deformation using Sentinel-1 satellites', *Scientific Reports*, 8(1), p. 7253. doi: 10.1038/s41598-018-25369-w.

Reale, D., Fornaro, G. and Pauciullo, A. (2013) 'Extension of 4-D SAR imaging to the monitoring of thermally dilating scatterers', *IEEE Transactions on Geoscience and Remote Sensing*, 51(12), pp. 5296–5306. doi: 10.1109/TGRS.2012.2233205.

Ribeiro, F. (2000) *Metro aplica paliativos após acidente*. Available at: https://www.publico.pt/2000/06/11/jornal/metro-aplica-paliativos-apos-acidente-145105 (Accessed: 30 July 2020).

Rodrigues, E. (2013) *Barragem de Odelouca abre portas a visitas do público no sábado*. Available at: https://www.sulinformacao.pt/2013/07/barragem-de-odelouca-abre-portas-ao-publico-no-sabado/ (Accessed: 30 July 2020).

Romano, E. and Scepi, G. (2006) 'Integrating time alignment and self-organizing maps for classifying curves', in *Electronic Proceedings of Knowledge Extraction and Modeling*. Anacapri, Italy, September 4-6, pp. 1–5.

Roque, D., Afonso, N., Fonseca, A. M. and Heleno, S. (2014) 'OBIA flood delimitation assisted by

threshold determination with principal component analysis', *Photogrammetric Engineering and Remote Sensing*, 80(6), pp. 551–557. doi: 10.14358/PERS.80.6.551-557.

Roque, D., Fonseca, A. M., Afonso, N., Henriques, M. J. and Muralha, J. (2015) 'Visual inspection aided by digital photography: application to the slopes of Foz Tua dam', in *Second International Dam World Conference*. Lisbon, Portugal, April 21 – 24, pp. 1-8.

Roque, D., Henriques, M. J., Perissin, D., Falcão, A. P. and Fonseca, A. M. (2016) 'Combined InSAR and geodetic measurements for displacement analysis at the metallic roof of MEO Arena building, Portugal', *Procedia Computer Science*, 100, pp. 1115–1120. doi: 10.1016/j.procs.2016.09.260.

Roque, D., Perissin, D., Falcão, A. P., Amado, C., Lemos, J. V. and Fonseca, A. M. (2018) 'Analysis of InSAR displacements for the slopes around Odelouca reservoir', in *Procedia Computer Science*, 138, pp. 338–345. doi: 10.1016/j.procs.2018.10.048.

Rosen, P. A., Hensley, S., Wheeler, K., Sadowy, G., Miller, T., Shaffer, S., Muellerschoen, R., Jones, C., Zebker, H. and Madsen, S. (2006) 'Uavsar: A new NASA airborne SAR system for science and technology research', in *IEEE National Radar Conference*. Verona, United States of America, April 24-27, pp. 22–29. doi: 10.1109/RADAR.2006.1631770.

Rosi, A., Tofani, V., Tanteri, L., Tacconi Stefanelli, C., Agostini, A., Catani, F. and Casagli, N. (2018) 'The new landslide inventory of Tuscany (Italy) updated with PS-InSAR: geomorphological features and landslide distribution', *Landslides*, 15(1), pp. 5–19. doi: 10.1007/s10346-017-0861-4.

Sakoe, H. and Chiba, S. (1978) 'Dynamic programming algorithm optimization for spoken word recognition', *IEEE Transactions on Acoustics, Speech, and Signal Processing*, ASSP-26(1), pp. 43–49. doi: 10.1016/b978-0-08-051584-7.50016-4.

Saleh, M., Masson, F., Mohamed, A. M. S., Boy, J. P., Abou-Aly, N. and Rayan, A. (2018) 'Recent ground deformation around lake Nasser using GPS and InSAR, Aswan, Egypt', *Tectonophysics*, 744, pp. 310–321. doi: 10.1016/j.tecto.2018.07.005.

Sandwell, D., Mellors, R., Tong, X., Xu, X., Wei, M. and Wessel, P. (2016) *GMTSAR : An InSAR Processing System Based on Generic Mapping Tools*. Scripps Institution of Oceanography, Technical Report.

Şanlioğlu, I. and Zeybek, M. (2012) 'Investigation on GPS heighting accuracy with use of tropospheric models in commercial GPS softwares for different heights', in *FIG Working Week 2012*. Rome, Italy, May 6 - 10, pp. 1–15.

Schlögel, R., Doubre, C., Malet, J. P. and Masson, F. (2015) 'Landslide deformation monitoring with ALOS/PALSAR imagery: A D-InSAR geomorphological interpretation method', *Geomorphology*, 231, pp. 314–330. doi: 10.1016/j.geomorph.2014.11.031.

Seemkooei, A. A. (2001) ‘Strategy for designing geodetic network with high reliability and geometrical strength’, *Journal of Surveying Engineering*, 127(3), pp. 104–117.

Shi, X., Yang, C., Zhang, Lu, Jiang, H., Liao, M., Zhang, Li and Liu, X. (2019) ‘Mapping and characterizing displacements of active loess slopes along the upstream Yellow River with multi-temporal InSAR datasets’, *Science of the Total Environment*, 674, pp. 200–210. doi: 10.1016/j.scitotenv.2019.04.140.

Shi, X., Zhang, L., Tang, M., Li, M. and Liao, M. (2017) ‘Investigating a reservoir bank slope displacement history with multi-frequency satellite SAR data’, *Landslides*, 14(6), pp. 1961–1973. doi: 10.1007/s10346-017-0846-3.

Shirzaei, M., Bürgmann, R., Foster, J., Walter, T. R. and Brooks, B. A. (2013) ‘Aseismic deformation across the Hilina fault system, Hawaii, revealed by wavelet analysis of InSAR and GPS time series’, *Earth and Planetary Science Letters*, 376, pp. 12–19. doi: 10.1016/j.epsl.2013.06.011.

Silva, D. F., de Souza, V. M. A. and Batista, G. E. A. P. A. (2013) ‘Time series classification using compression distance of recurrence plots’, in *IEEE International Conference on Data Mining*. Dallas, United States of America, December 7-10, pp. 687–696. doi: 10.1109/ICDM.2013.128.

SkyWatch Space Applications Inc. (2019) ‘Calibration Operator’. Manual of Sentinel-1 Toolbox, SkyWatch Space Applications Inc.

Solari, L., Soldato, M. Del, Raspini, F. and Barra, A. (2020) ‘Review of satellite interferometry for landslide detection in Italy’, *Remote Sensing*, 12(1351), p. 29. doi: 10.3390/rs12081351.

Del Soldato, M., Tomás, R., Castillo, J. P., Herrera García, G., Lopez-Davalillos, G., Carlos, J. and Mora, O. (2016) ‘A multi-sensor approach for monitoring a road bridge in the Valencia harbor (SE Spain) by SAR Interferometry (InSAR)’, *Rend. Online Soc. Geol. It.*, 41, pp. 235–238. doi: 10.3301/ROL.2016.137.

Sousa, J. J. and Bastos, L. (2013) ‘Multi-temporal SAR interferometry reveals acceleration of bridge sinking before collapse’, *Natural Hazards and Earth System Science*, 13(3), pp. 659–667. doi: 10.5194/nhess-13-659-2013.

Sousa, J. J., Hooper, A. J., Hanssen, R. F., Bastos, L. C. and Ruiz, A. M. (2011) ‘Persistent Scatterer InSAR: A comparison of methodologies based on a model of temporal deformation vs. spatial correlation selection criteria’, *Remote Sensing of Environment*, 115(10), pp. 2652–2663. doi: 10.1016/j.rse.2011.05.021.

Sousa, J. J., Magalhães, L. G., Ruiz, A. M., Sousa, A. M. R. and Cardoso, G. (2013) ‘The viStaMPS tool for visualization and manipulation of time series interferometric results’, *Computers and Geosciences*, 52, pp. 409–421. doi: 10.1016/j.cageo.2012.11.012.

Sousa, R. (2011) *Controlo de Qualidade na Execução de Fundações numa Barragem – Aproveitamento Hidroelétrico do Baixo Sabor – Estudo de Caso*. Master thesis. Universidade do Porto.

Stiros, S. C. and Psimoulis, P. A. (2012) 'Response of a historical short-span railway bridge to passing trains: 3-D deflections and dominant frequencies derived from Robotic Total Station (RTS) measurements', *Engineering Structures*, 45, pp. 362–371. doi: 10.1016/j.engstruct.2012.06.029.

Sun, H. (1997) 'A two-dimensional analytical solution of groundwater response to tidal loading in an estuary', *Water Resources Research*, 33(6), pp. 1429–1435. doi: 10.1029/97wr00482.

Tapete, D., Morelli, S., Fanti, R. and Casagli, N. (2015) 'Localising deformation along the elevation of linear structures: An experiment with space-borne InSAR and RTK GPS on the Roman Aqueducts in Rome, Italy', *Applied Geography*, 58, pp. 65–83. doi: 10.1016/j.apgeog.2015.01.009.

Tomás, R., Pagán, J. I., Navarro, J. A., Cano, M., Pastor, J.L., Riquelme, A., Cuevas-González, M., Crosetto, M., Barra, A., Monserrat, O., Lopez-Sanchez, J. M., Ramón, A., Ivorra, S., Del Soldato, M., Solari, L., Bianchini, S., Raspini, F., Novali, F., Ferretti, A., Costantini, M., Trillo, F., Herrera, G., Casagli, N. (2019) 'Semi-automatic identification and pre-screening of geological–geotechnical deformational processes using persistent scatterer interferometry datasets', *Remote Sensing*, 11(14), p. 1675. doi: 10.3390/rs11141675

Di Traglia, F., Nolesini, T., Ciampalini, A., Solari, L., Frodella, W., Bellotti, F., Fumagalli, A., De Rosa, G. and Casagli, N. (2018) 'Tracking morphological changes and slope instability using spaceborne and ground-based SAR data', *Geomorphology*, 300, pp. 95-112. doi: 10.1016/j.geomorph.2017.10.023.

UNAVCO (2020a) *Synthetic Aperture Radar (SAR) Satellites*. Available at: https://www.unavco.org/instrumentation/geophysical/imaging/sar-satellites/sar-satellites.html (Accessed: 30 July 2020).

UNAVCO (2020b) *Topcon GB-1000 - Product Brochure and Specifications*. Available at: https://kb.unavco.org/kb/article/topcon-gb-1000-product-brochure-and-specifications-23.html (Accessed: 30 July 2020).

Walkinshaw, J. L. and Santi, P. M. (1996) 'Chapter 21: Shales and other degradable materials', in *Landslides: Investigation and mitigation*, TRB Special Report 247, pp. 555–576. Edited by Turner, A. K., Schuster, R. L.. Transportation Research Board, National Research Council: Washington, DC.

Wang, T., Perissin, D., Rocca, F. and Liao, M. S. (2011) 'Three Gorges Dam stability monitoring with time-series InSAR image analysis', *Science China Earth Sciences*, 54(5), pp. 720–732. doi: 10.1007/s11430-010-4101-1.

Wegmüller, U., Werner, C., Wiesmann, A. and Strozzi, T. (2003) 'Radargrammetry and space

triangulation for DEM generation and image ortho-rectification', in *International Geoscience and Remote Sensing Symposium*. Toulouse, France, July 21-25, pp. 179–181. doi: 10.1109/igarss.2003.1293716.

Welch, B. L. (1938) 'The significance of the difference between two means when the population variances are unequal', *Biometrika*, 29(3/4), pp. 350–362. doi: 10.2307/2332010.

Werner, C., Wegmüller, U., Strozzi, T. and Wiesmann, A. (2003) 'Interferometric point target analysis for deformation mapping', in *International Geoscience and Remote Sensing Symposium*. Toulouse, France, July 21-25, pp. 4362–4364. doi: 10.1109/igarss.2003.1295516.

Xiong, Y. and Yeung, D.-Y. (2004) 'Time series clustering with ARMA mixtures', *Pattern Recognition*, 37(8), pp. 1675–1689. doi: 10.1016/j.patcog.2003.12.018.

Ye, X., Kaufmann, H. and Guo, X. F. (2004) 'Landslide monitoring in the Three Gorges area using D-InSAR and corner reflectors', *Photogrammetric Engineering & Remote Sensing*, 70(10), pp. 1167–1172. doi: 10.14358/pers.70.10.1167.

Ye, X. W., Su, Y. H. and Han, J. P. (2014) 'Structural health monitoring of civil infrastructure using optical fiber sensing technology: A comprehensive review', *Scientific World Journal*, 2014, pp. 1-11. doi: 10.1155/2014/652329.

Yigit, C. O. and Gurlek, E. (2017) 'Experimental testing of high-rate GNSS precise point positioning (PPP) method for detecting dynamic vertical displacement response of engineering structures', *Geomatics, Natural Hazards and Risk*, 8(2), pp. 893–904. doi: 10.1080/19475705.2017.1284160.

Yu, B., Liu, G., Li, Z., Zhang, R., Jia, H., Wang, X. and Cai, G. (2013) 'Subsidence detection by TerraSAR-X interferometry on a network of natural persistent scatterers and artificial corner reflectors', *Computers and Geosciences*, 58, pp. 126–136. doi: 10.1016/j.cageo.2013.04.020.

Zanotta, D., Ferreira, M. and Zortea, M. (2019) 'Processamento de imagens de satélite'. Available at: https://books.google.com/books?hl=pt-PT&lr=&id=l6SWDwAAQBAJ&oi=fnd&pg=PT5&dq=Zanotta,+Ferreira+and+Zortea,+2019&ots=YuR5Q6kda3&sig=TbDYlNBJuWdYy-aL_Jrg0WHQN8A (Accessed: 31 July 2020).

Zhao, J., Wu, J., Ding, X. and Wang, M. (2017) 'Elevation extraction and deformation monitoring by multitemporal InSAR of Lupu Bridge in Shanghai', *Remote Sensing*, 9(9), p. 897. doi: 10.3390/rs9090897.

Zhu, M., Wan, X., Fei, B., Qiao, Z., Ge, C., Minati, F., Vecchioli, F., Li, J. and Costantini, M. (2018) 'Detection of building and infrastructure instabilities by automatic spatiotemporal analysis of satellite SAR interferometry measurements', *Remote Sensing*, 10(11), p. 1816. doi: 10.3390/rs10111816.

Zhu, W., Zhang, Q., Ding, X., Zhao, C., Yang, C., Qu, F. and Qu, W. (2014) 'Landslide monitoring by combining of CR-InSAR and GPS techniques', *Advances in Space Research*, 53(3), pp. 430–439. doi: 10.1016/j.asr.2013.12.003.

Zouhal, L. M. and Denoeux, T. (1998) 'An evidence-theoretic k-NN rule with parameter optimization', *IEEE Transactions on Systems, Man and Cybernetics Part C: Applications and Reviews*, 28(2), pp. 263–271. doi: 10.1109/5326.669565.

Annexes

Annex A.1 – RADAR interpretation

This Annex contains figures and tables that complement the research in Chapter 3.

Table 17 – Parameters for cluster analysis for Odelouca case study; the symbol "/" separates the options selected at different tests.

Parametre	Value
Number of clusters	Automatic / 7
Coordinates of rectangular ROI (WGS84)	
Lower latitude	37.2586
Higher latitude	37.3685
Lower longitude	-8.4988
Higher longitude	-8.3455
Coherence threshold	0.9
Number of images	20
EPSG[32] code of additional raster	3763
Year of the beginning of time series	2006
Sample number of first image in the beginning year	8
Year of the ending of time series	2011
Sample number of last image in the ending year	3
Cluster method	Ward / Complete / Single
Additional data in raster format	Slope, Curvature

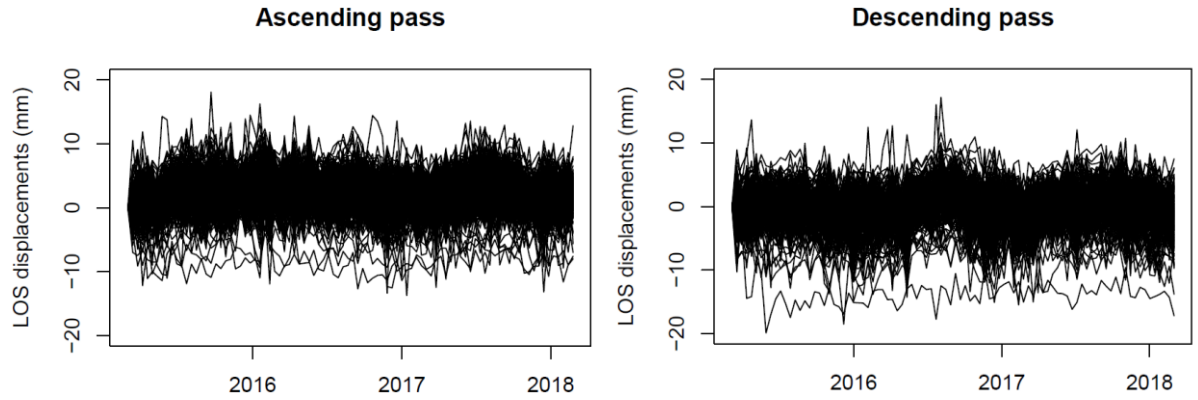

(a) (b)

Figure 134 – LOS displacement time series for all PSs considered stable for (a) the ascending pass and (b) the descending one, at Lisbon Downtown.

[32] EPSG: European Petroleum Survey Group, who publishes a database of coordinate systems represented by codes.

Table 18 – Parameters for cluster analysis for Lisbon Downtown case study; the symbol "/" separates the options selected at different tests.

Parametre	Value
Number of clusters	Automatic / 10
Coordinates of rectangular ROI (WGS84)	
Lower latitude	38.7032
Higher latitude	38.7166
Lower longitude	-9.1440
Higher longitude	-9.1292
Coherence threshold	0.9
Number of images ascending pass	89
Number of images descending pass	86
Incidence angle ascending pass	40.6º
Incidence angle descending pass	35.7º
Satellite orbit inclination ascending pass	98.18º
Satellite orbit inclination descending pass	98.18º
Azimuth of direction perpendicular to displacement	0º
EPSG code of additional raster	3763
Year of the beginning of time series	2015
Sample number of first image in the beginning year	6
Year of the ending of time series	2018
Sample number of last image in the ending year	5
Cluster method	Complete
Time series to cluster	2D
Additional data in raster format	Slope, Curvature, Distance to faults, Distance to subway, Distance to river

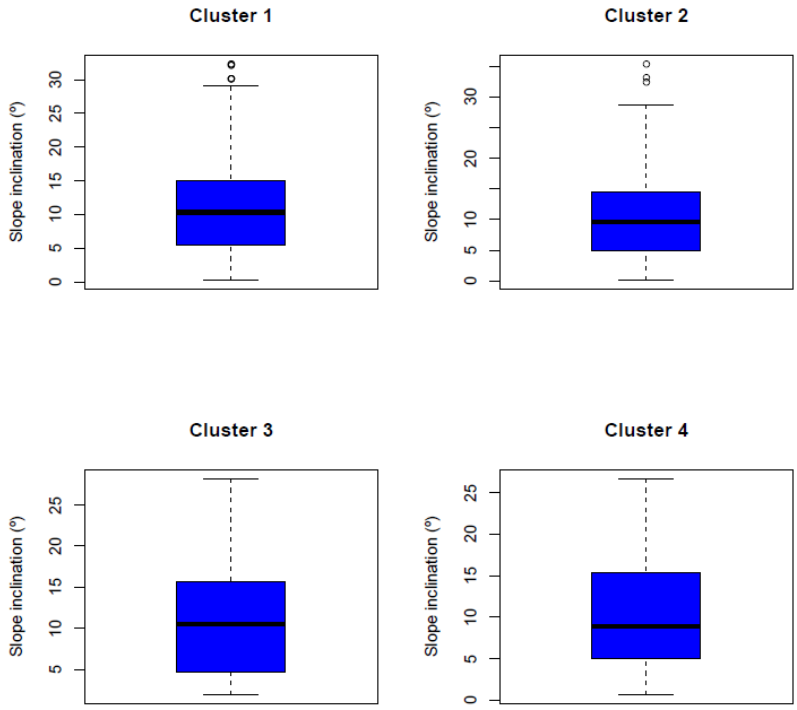

Figure 135 – Boxplots of slope inclination for the clustering solution using Ward method at Odelouca.

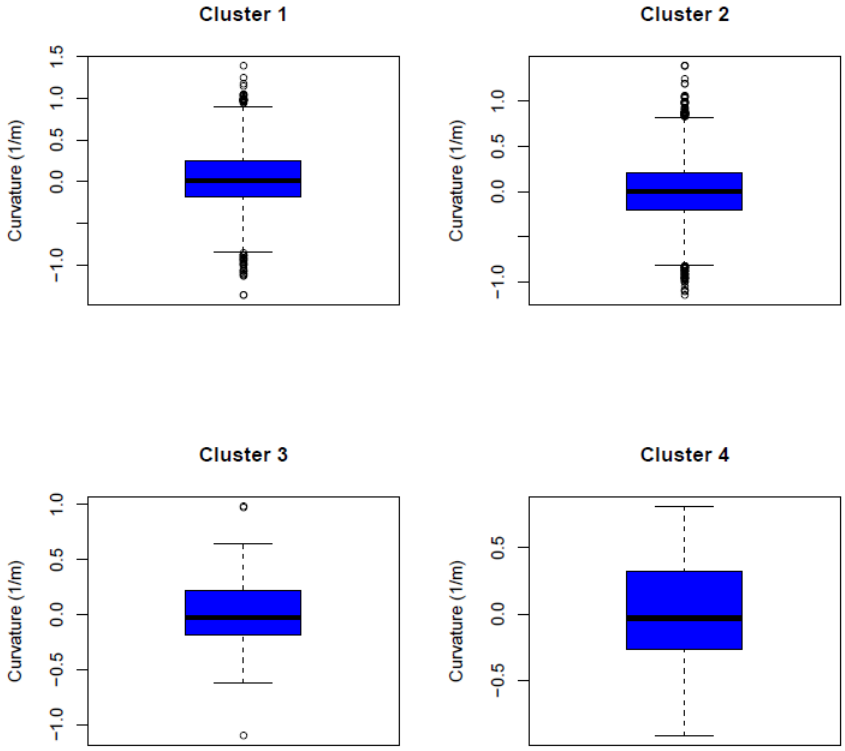

Figure 136 – Boxplots of slope curvature for the clustering solution using Ward method at Odelouca.

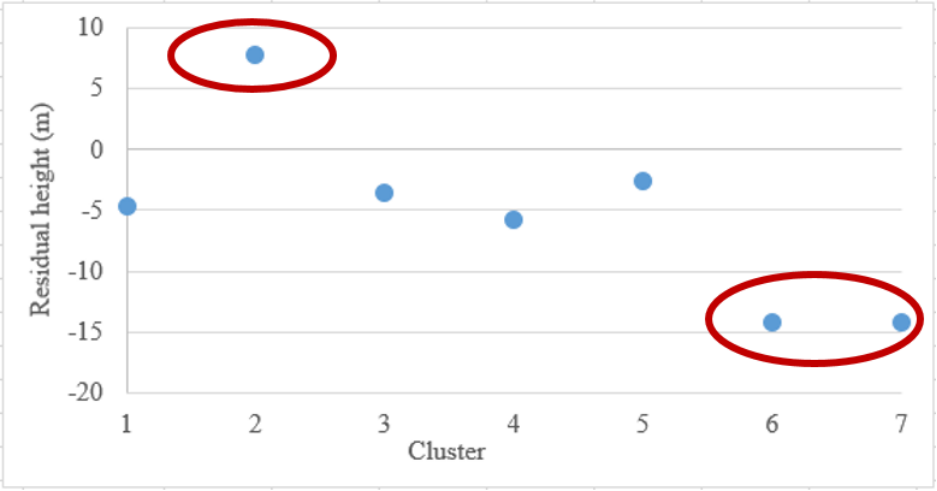

Figure 137 – Residual height centroids for the manual seven-cluster solution with complete linkage at Odelouca slopes; red ovals identify the clusters with outlier residual height centroids, which may correspond to unwrapping errors.

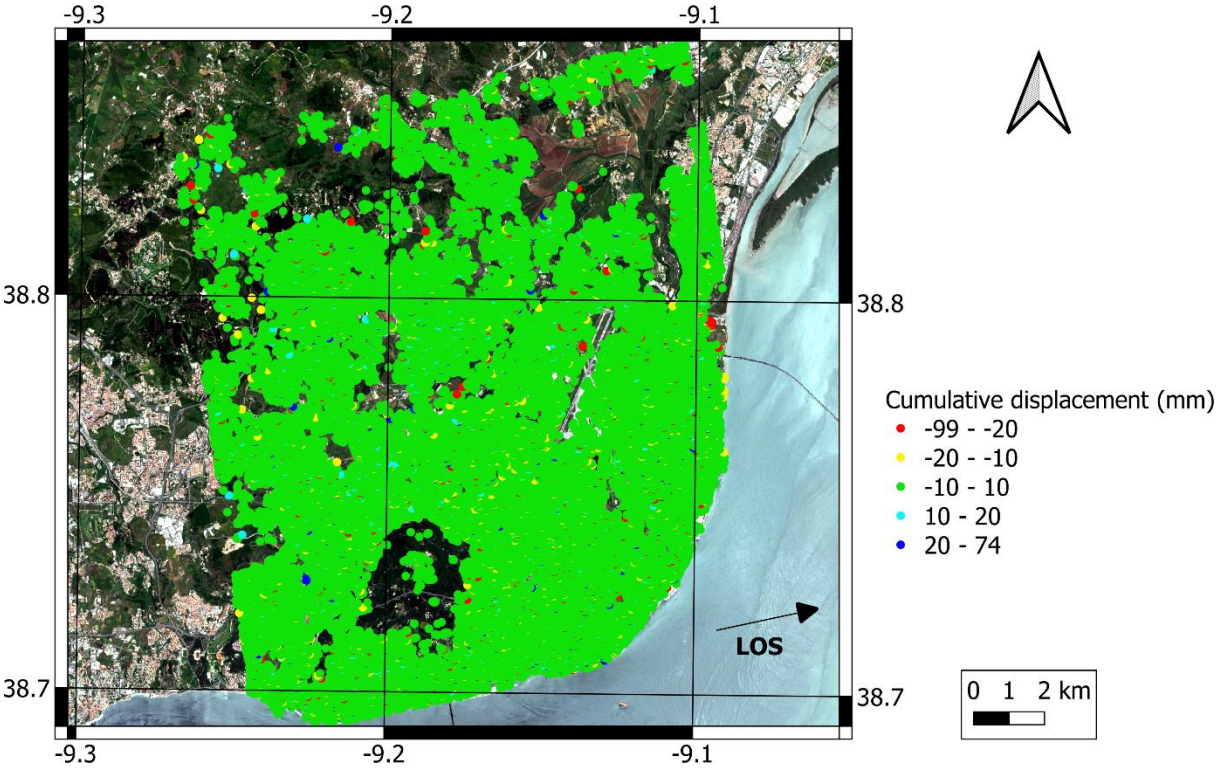

Figure 138 – Cumulative displacement map for Lisbon city (ascending pass); background image from Sentinel-2 acquired in May 2020. Coordinate grid in WGS84.

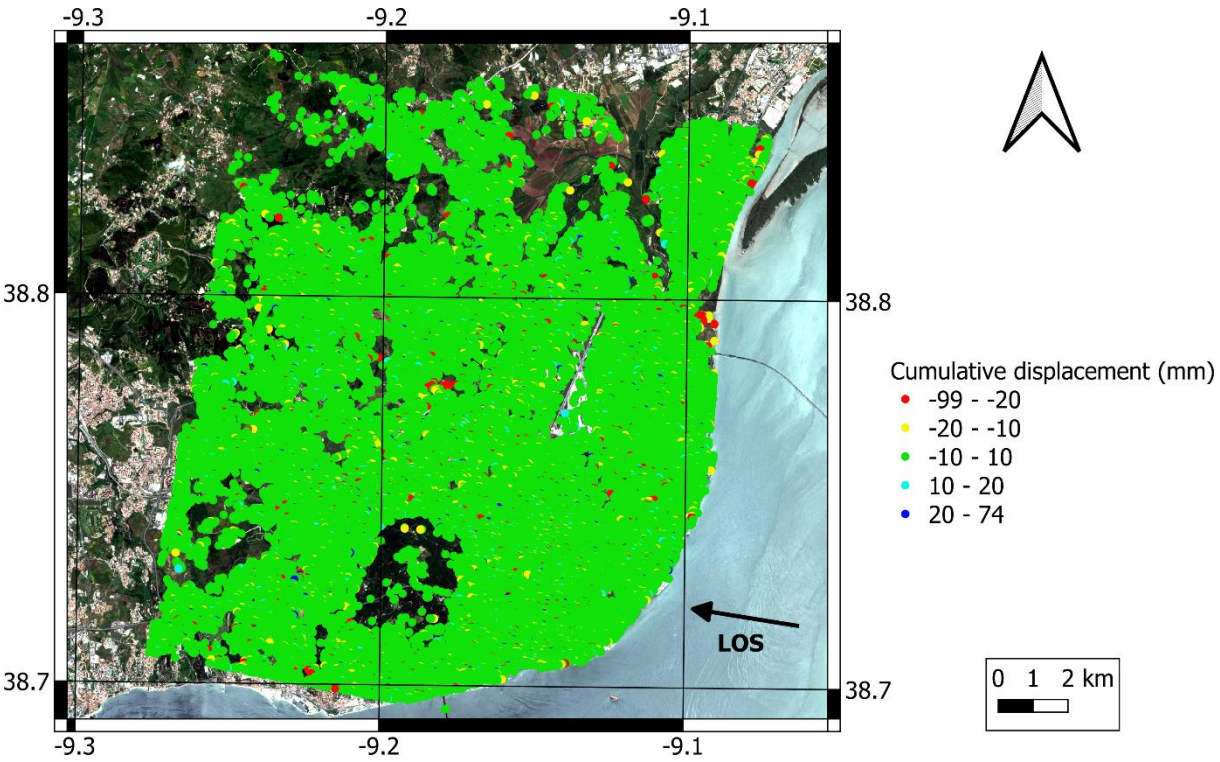

Figure 139 – Cumulative displacement map for Lisbon city (descending pass); background image from Sentinel-2 acquired in May 2020. Coordinate grid in WGS84.

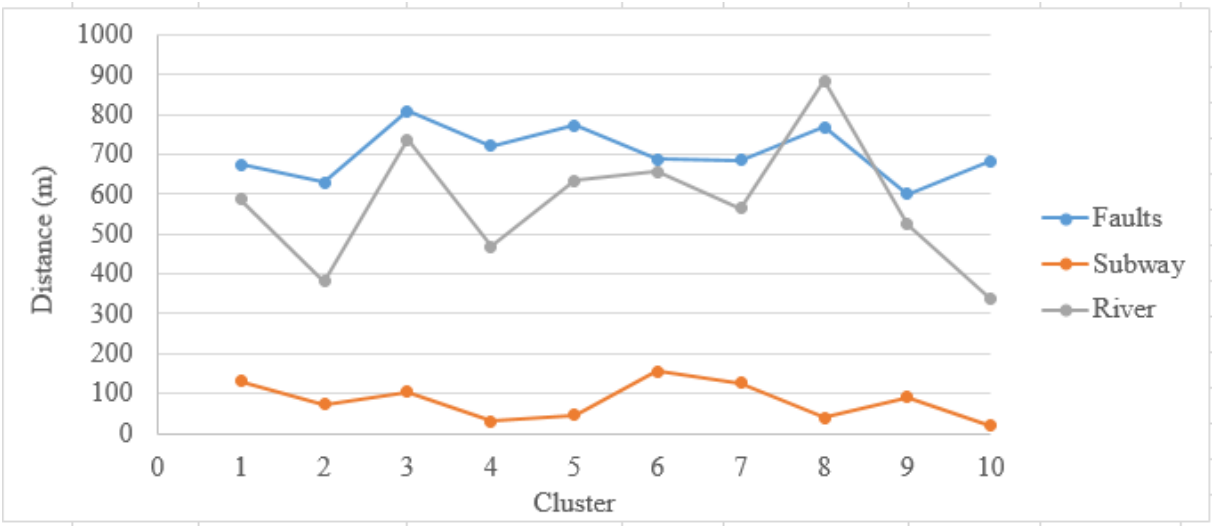

Figure 140 – Centroids for distance variables at Lisbon Downtown.

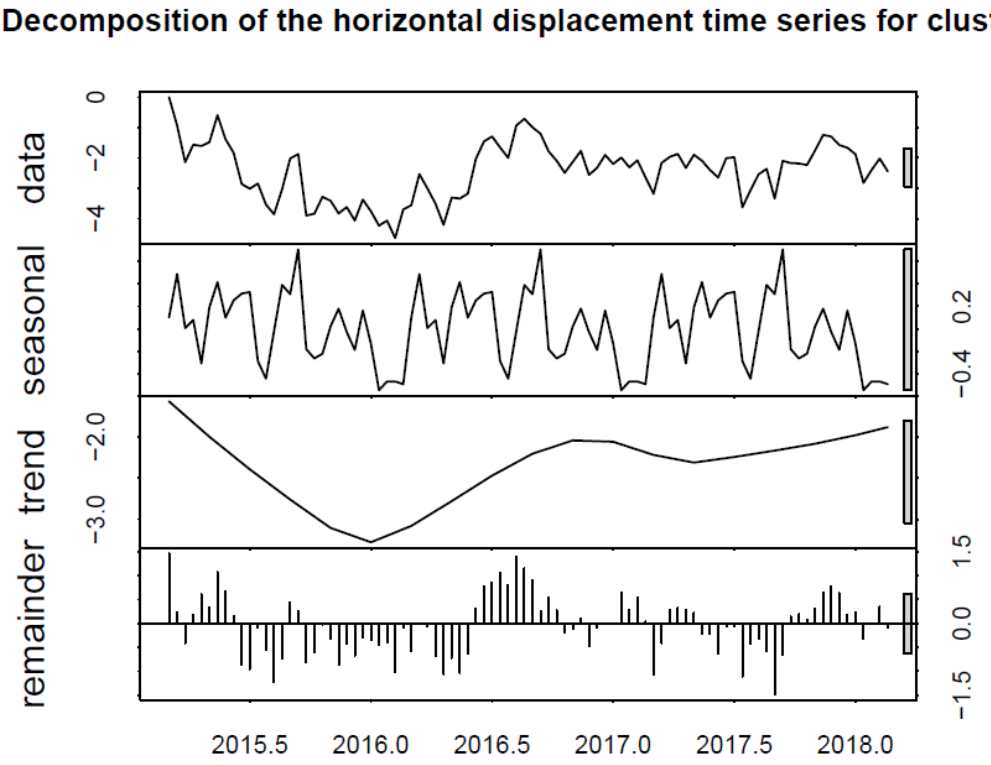

Figure 141 – Decomposition of representative horizontal displacement time series for cluster 1 from 10 cluster solution at Lisbon Downtown.

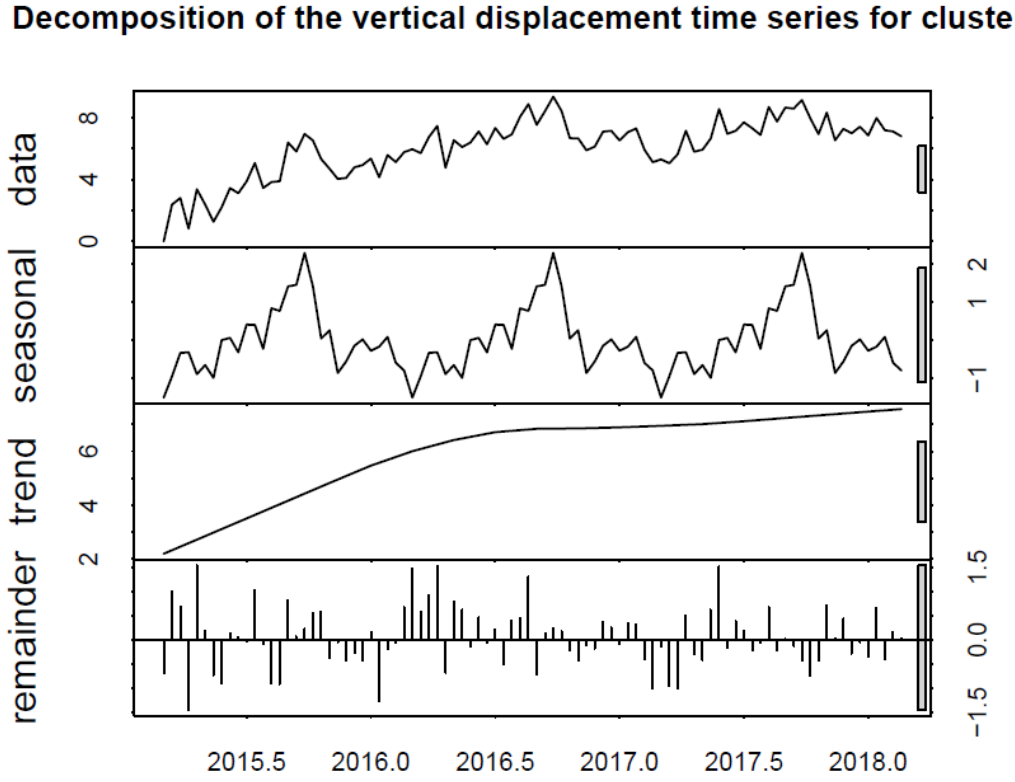

Figure 142 – Decomposition of representative vertical displacement time series for cluster 2 from 10 cluster solution at Lisbon Downtown.

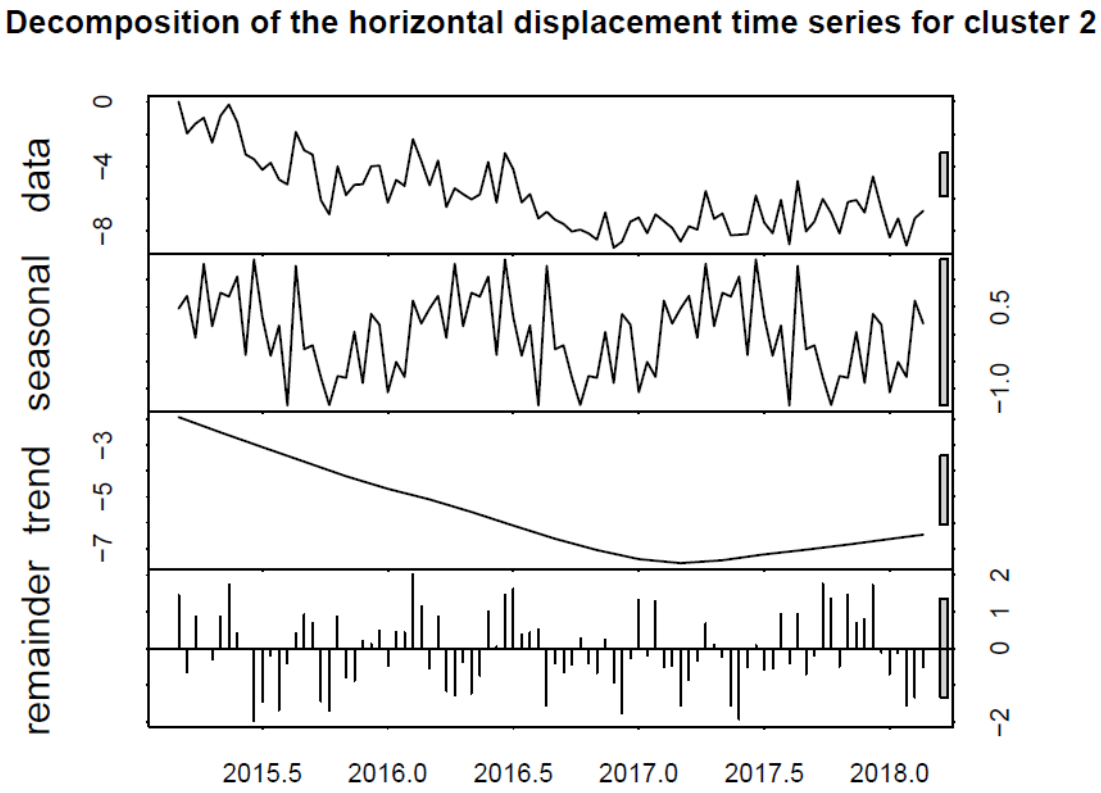

Figure 143 – Decomposition of representative horizontal displacement time series for cluster 2 from 10 cluster solution at Lisbon Downtown.

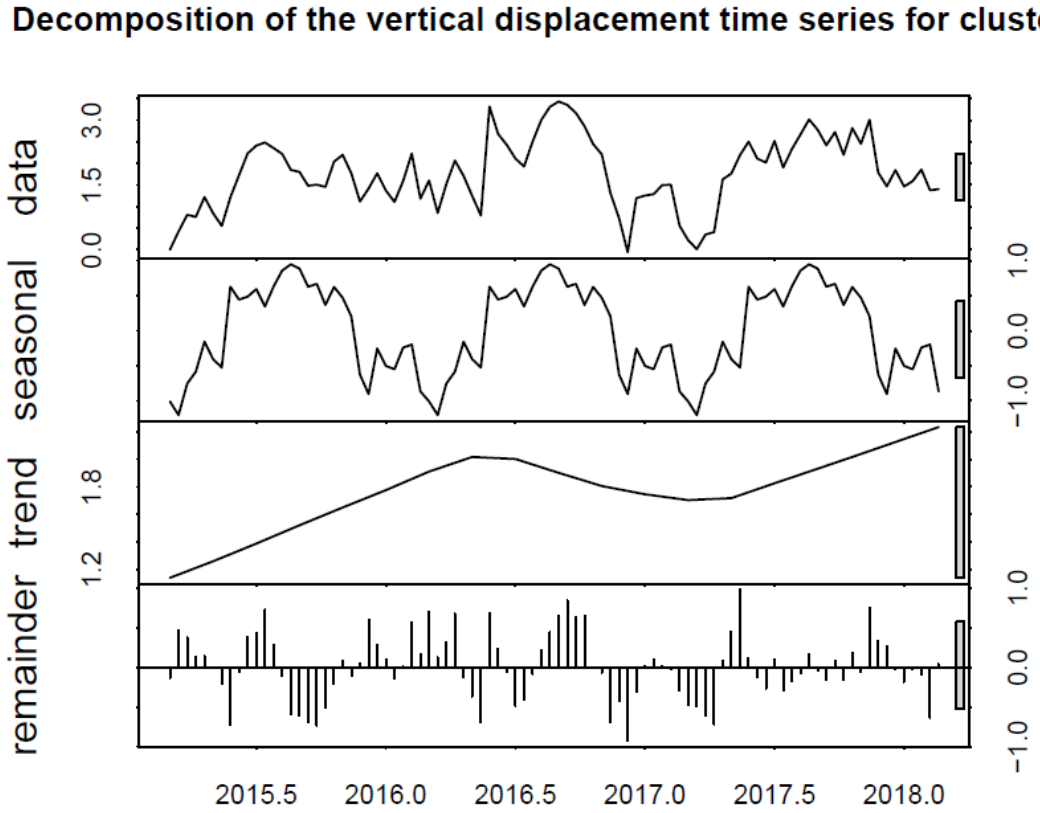

Figure 144 – Decomposition of representative vertical displacement time series for cluster 3 from 10 cluster solution at Lisbon Downtown.

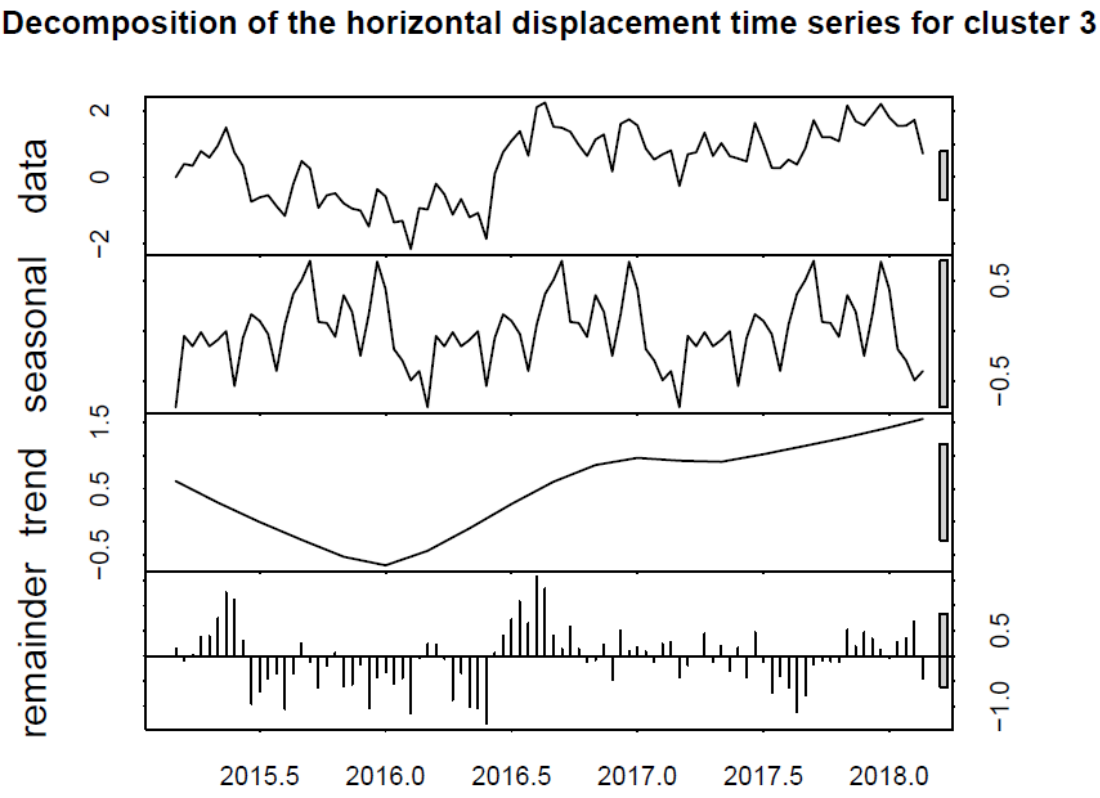

Figure 145 – Decomposition of representative horizontal displacement time series for cluster 3 from 10 cluster solution at Lisbon Downtown.

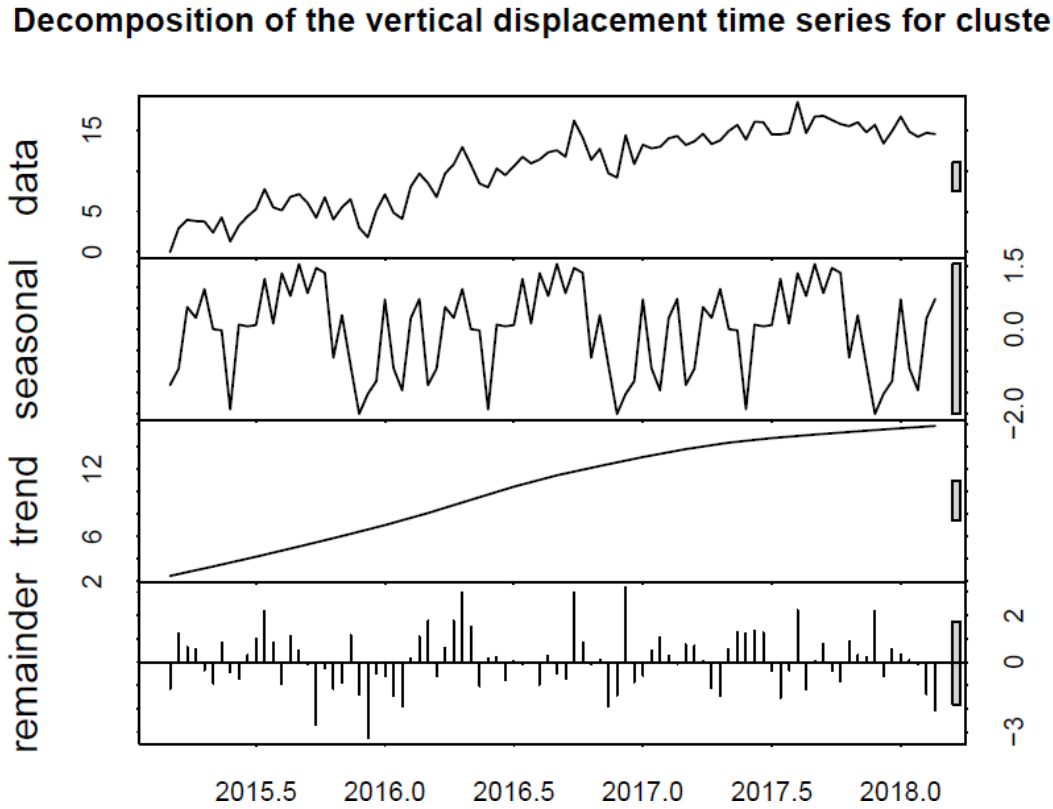

Figure 146 – Decomposition of representative vertical displacement time series for cluster 5 from 10 cluster solution at Lisbon Downtown.

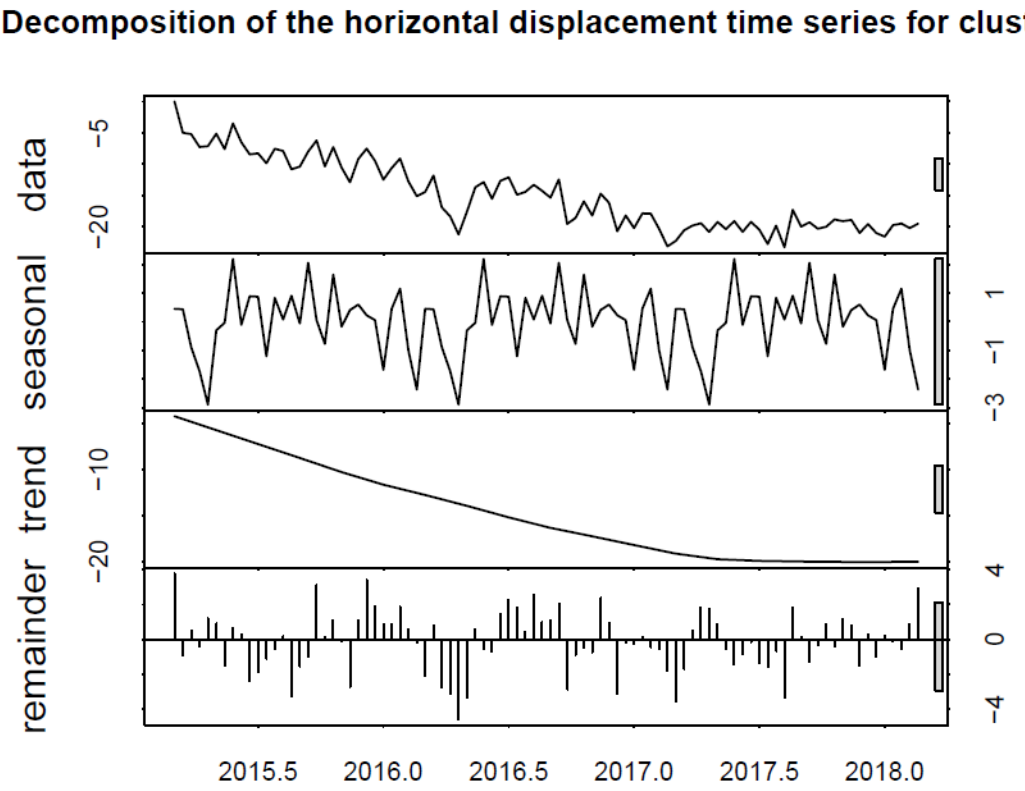

Figure 147 – Decomposition of representative horizontal displacement time series for cluster 5 from 10 cluster solution at Lisbon Downtown.

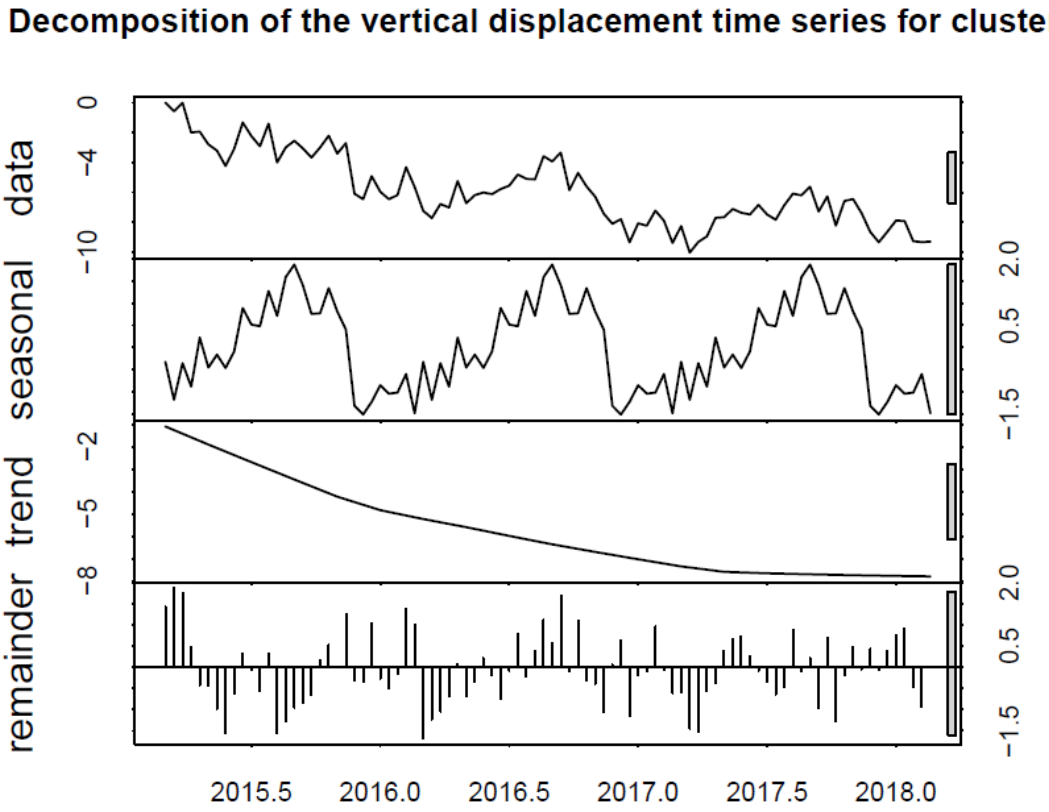

Figure 148 – Decomposition of representative vertical displacement time series for cluster 6 from 10 cluster solution at Lisbon Downtown.

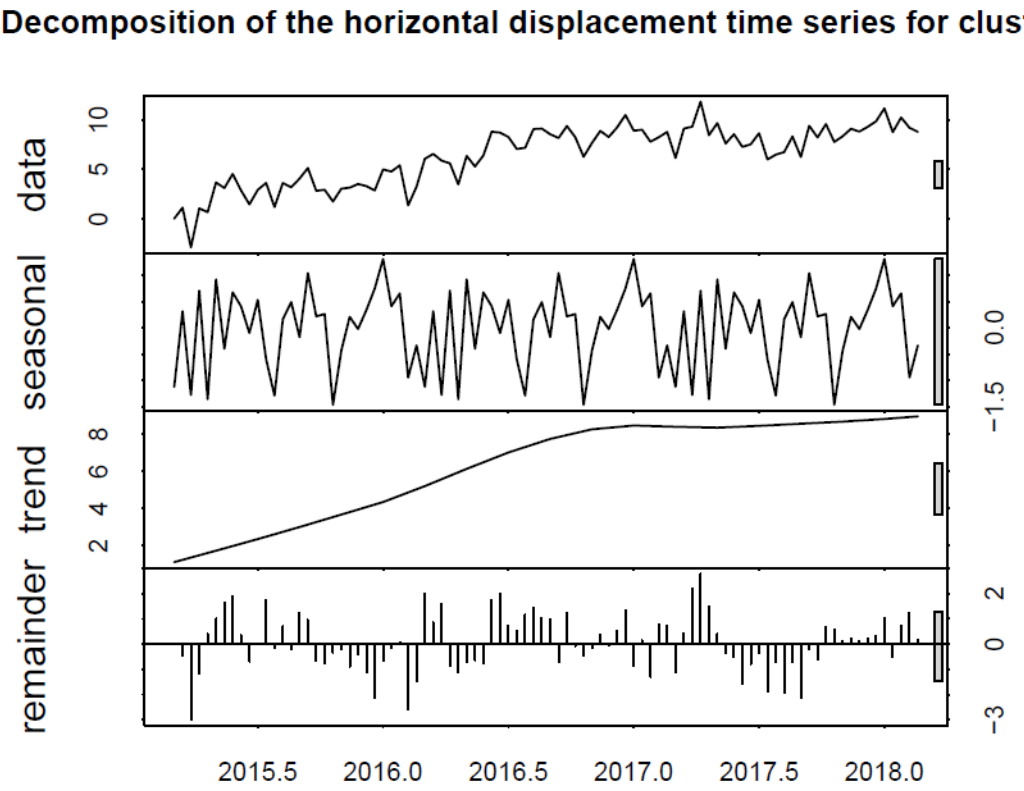

Figure 149 – Decomposition of representative horizontal displacement time series for cluster 6 from 10 cluster solution at Lisbon Downtown.

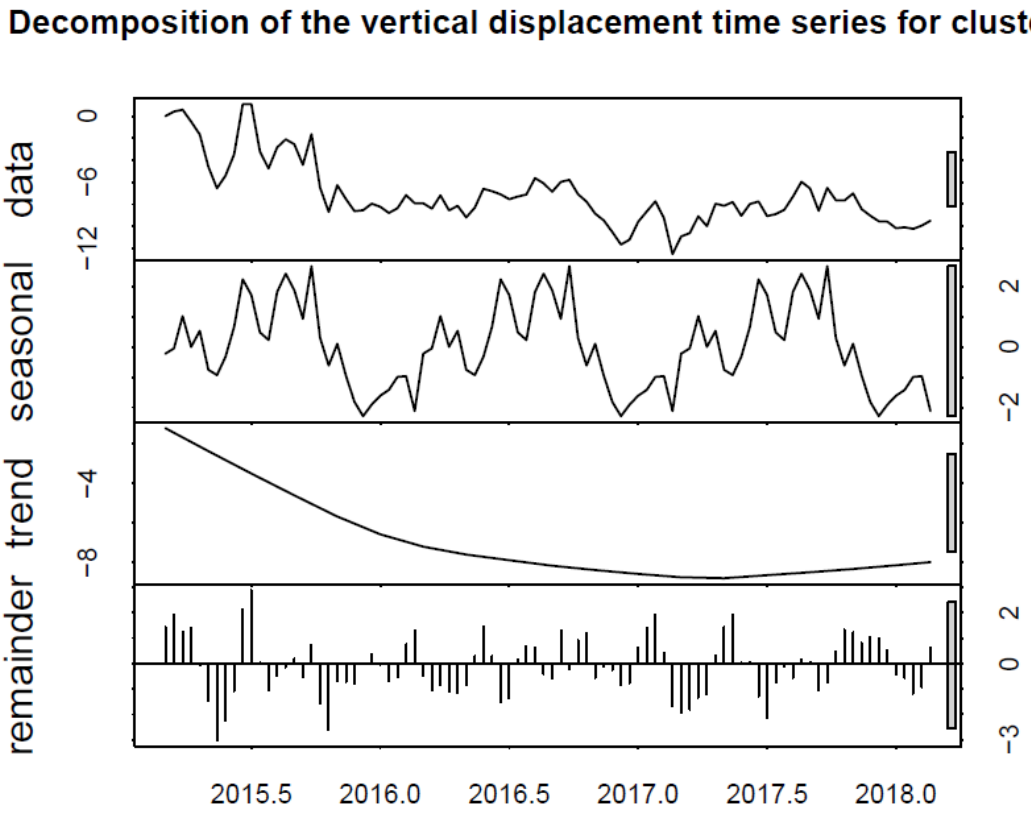

Figure 150 – Decomposition of representative vertical displacement time series for cluster 7 from 10 cluster solution at Lisbon Downtown.

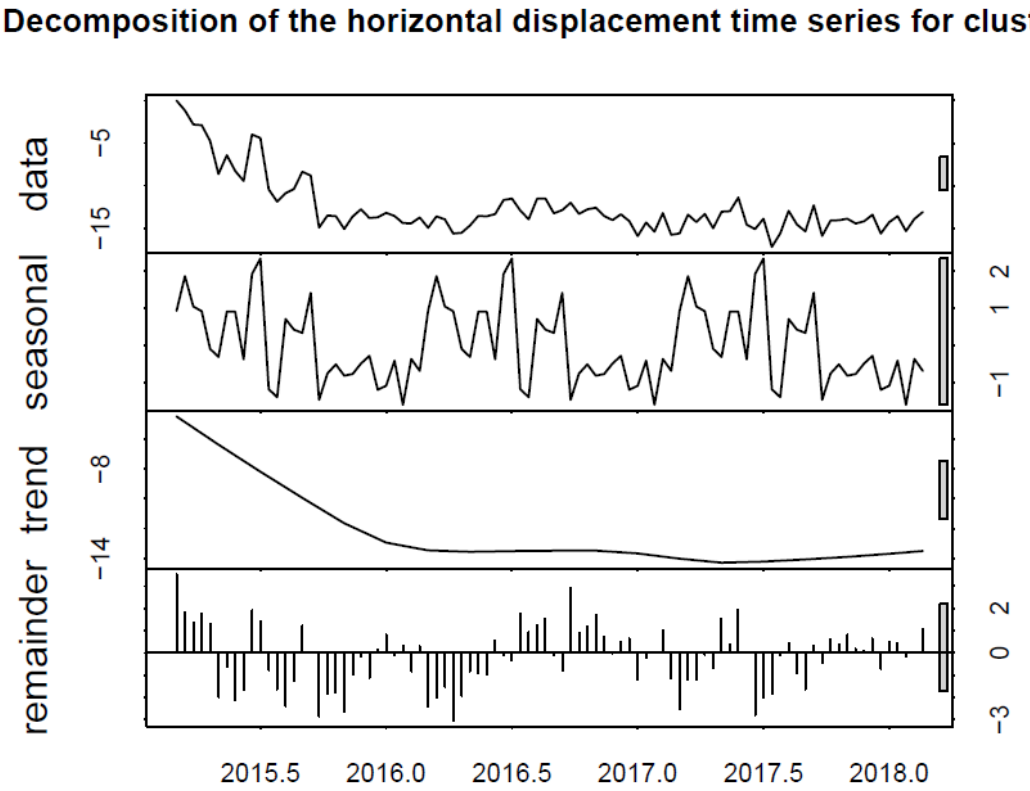

Figure 151 – Decomposition of representative horizontal displacement time series for cluster 7 from 10 cluster solution at Lisbon Downtown.

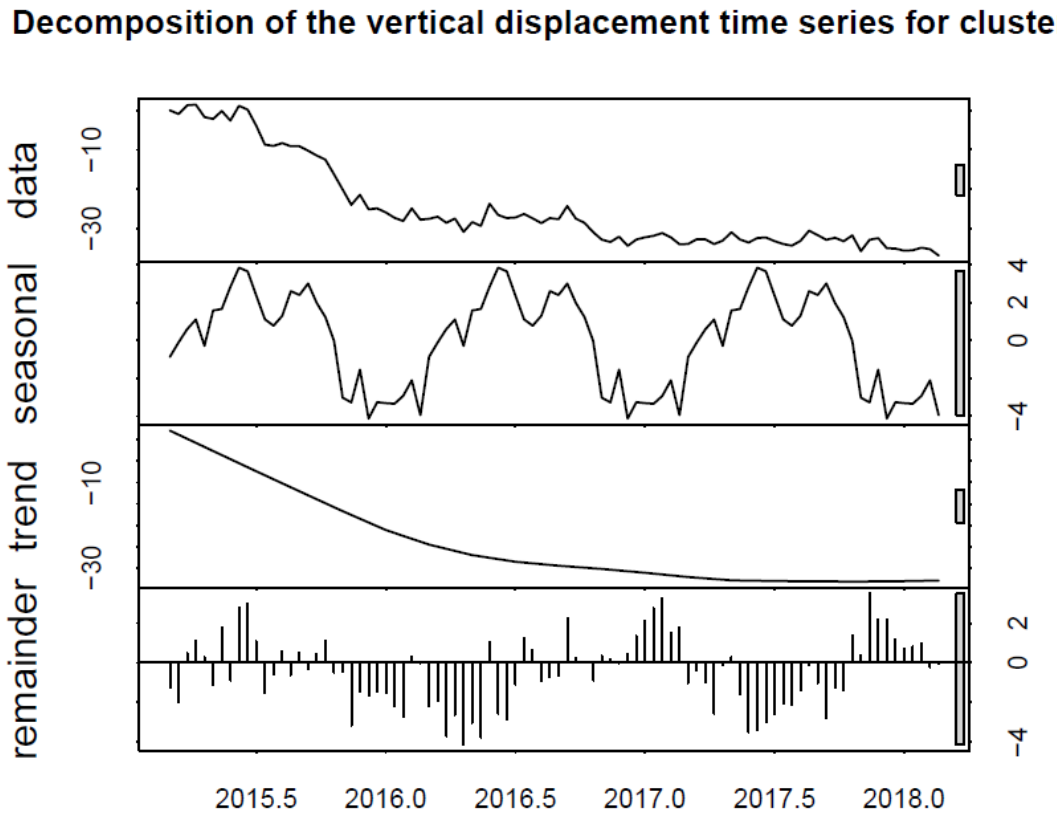

Figure 152 – Decomposition of representative vertical displacement time series for cluster 8 from 10 cluster solution at Lisbon Downtown.

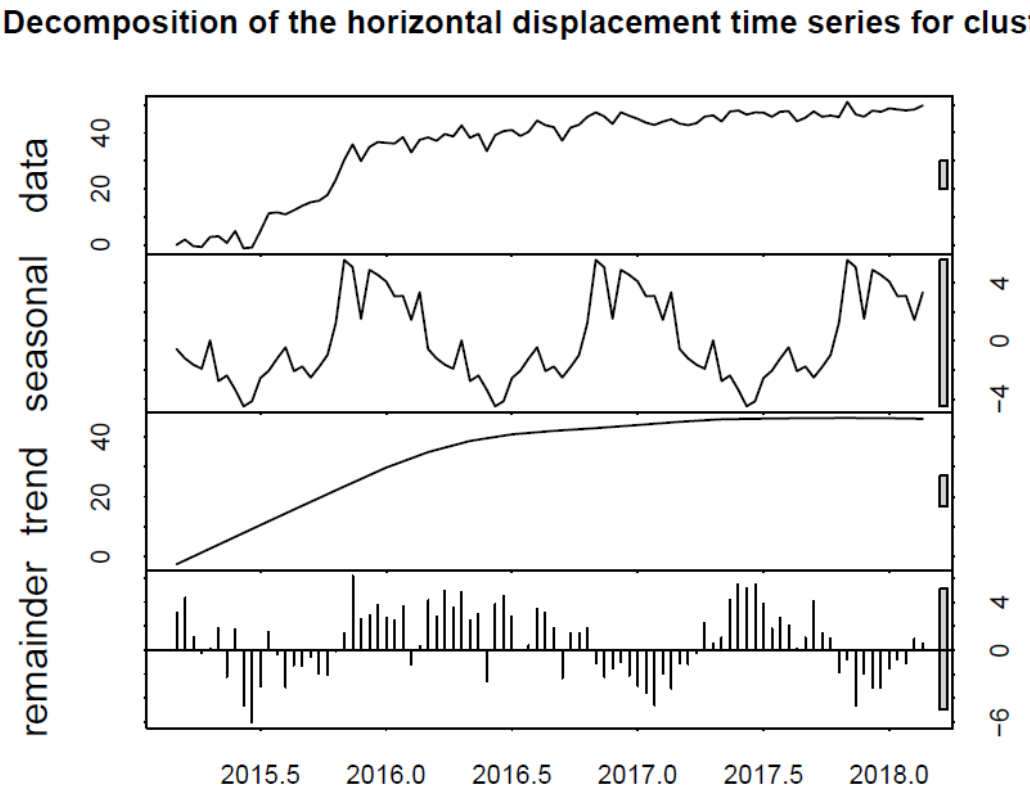

Figure 153 – Decomposition of representative horizontal displacement time series for cluster 8 from 10 cluster solution at Lisbon Downtown.

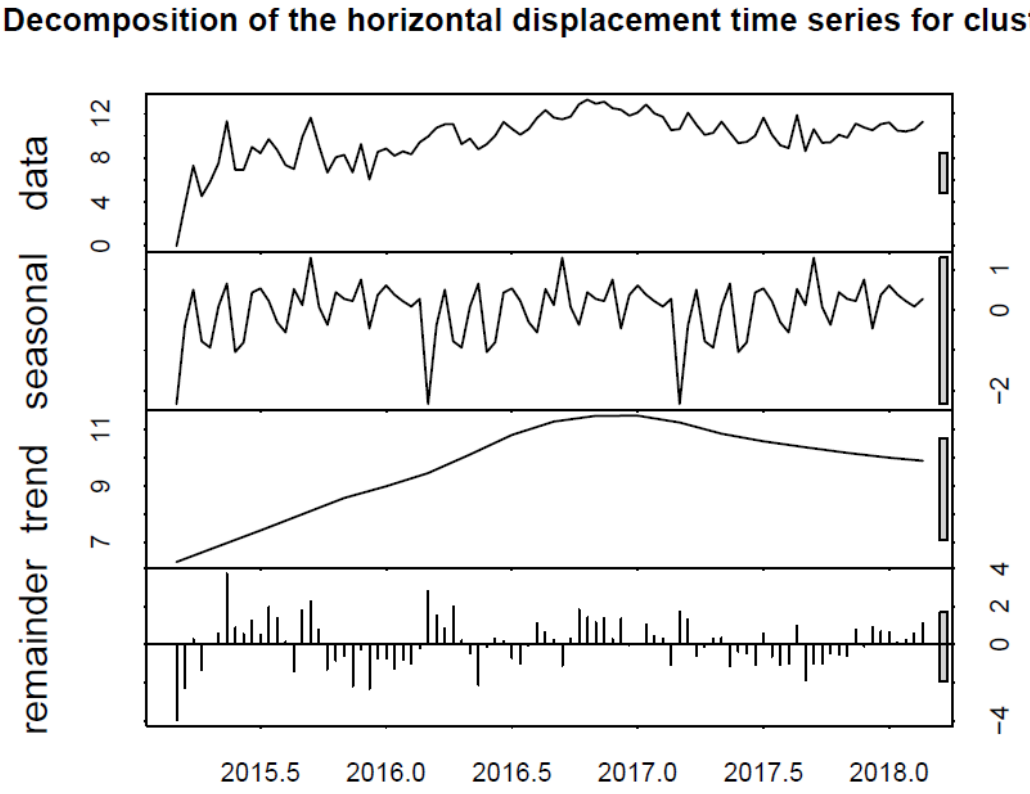

Figure 154 – Decomposition of representative horizontal displacement time series for cluster 9 from 10 cluster solution at Lisbon Downtown.

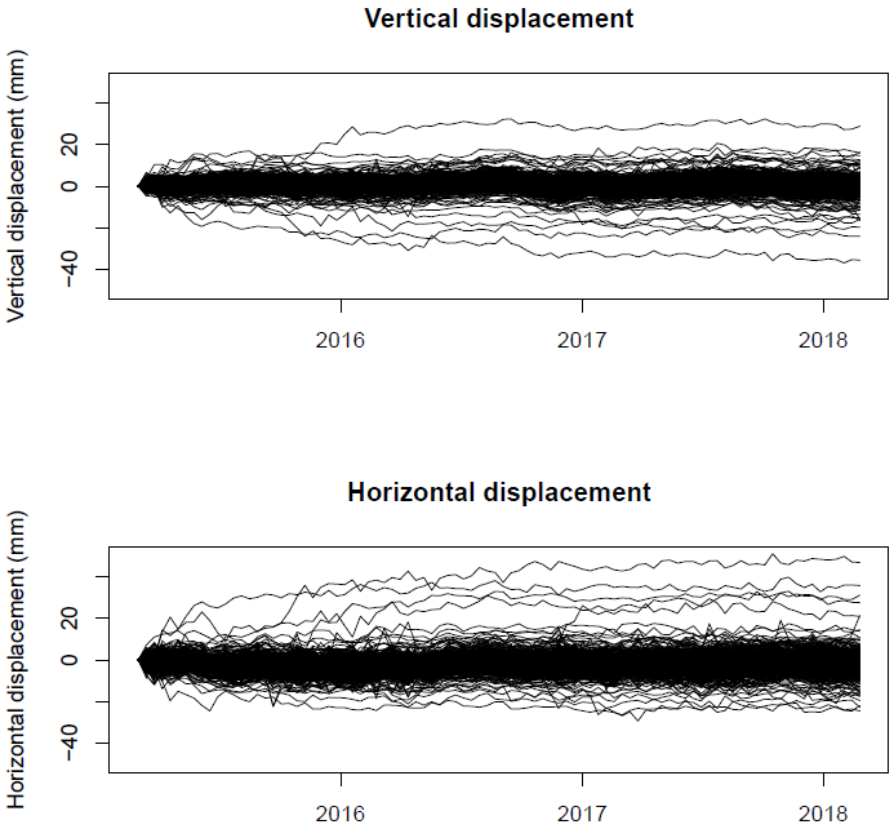

Figure 155 – Vertical (top) and horizontal (bottom) displacement time series for all PSs at Lisbon Downtown.

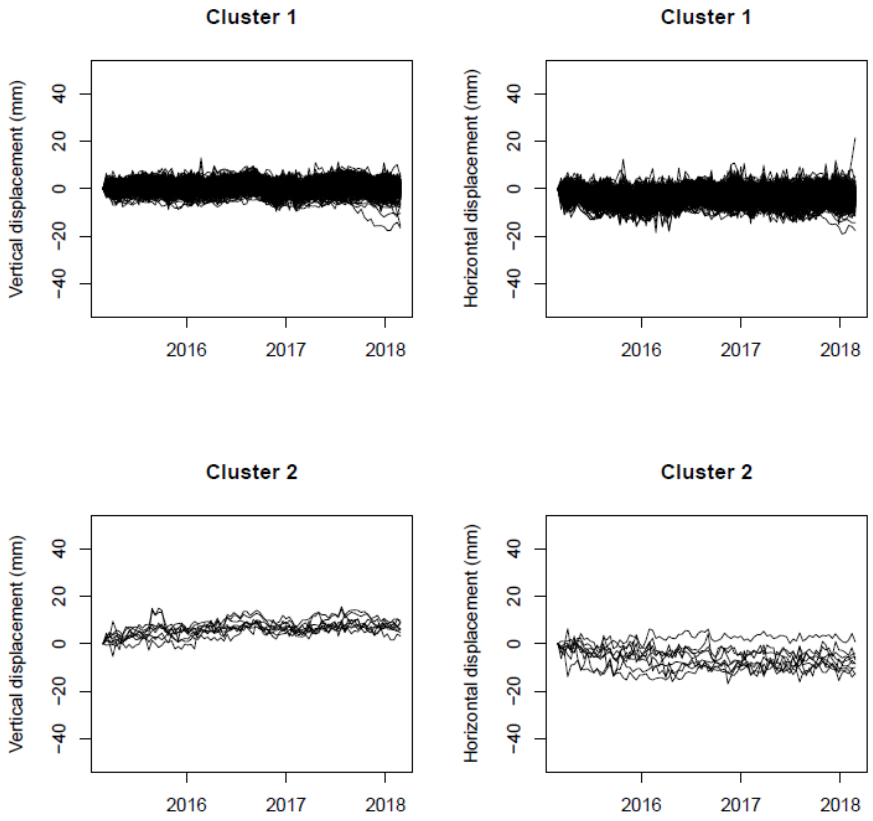

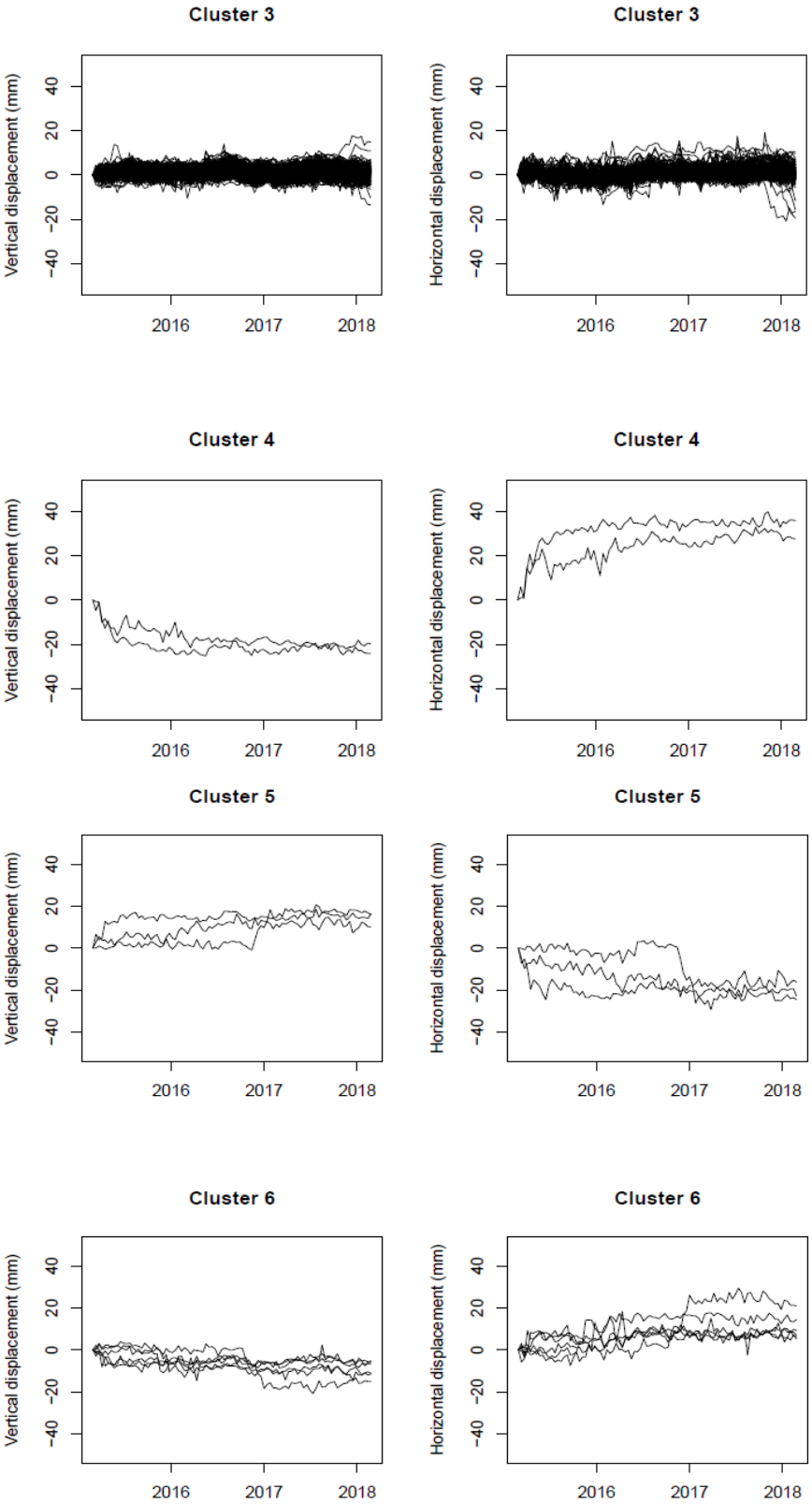
Cluster 3
Vertical displacement (mm)
Horizontal displacement (mm)
Cluster 4
Cluster 5
Cluster 6
−40
−20
0
20
40
2016
2017
2018

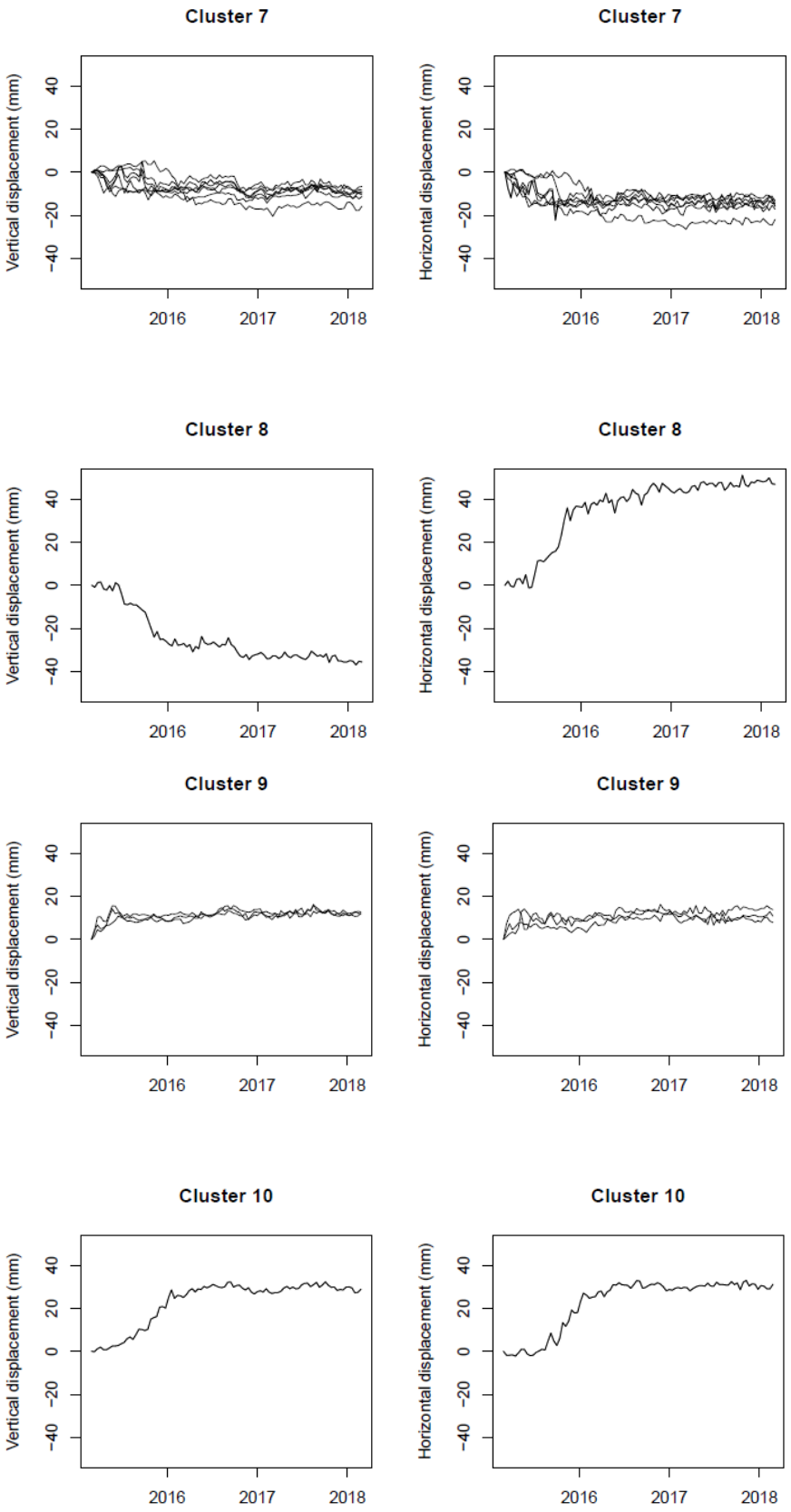

Figure 156 – Vertical (left) and horizontal (right) displacement time series of all PSs in each cluster, at Lisbon Downtown.

Annex A.2 – Integration on structure monitoring systems

This Annex contains figures and tables that complement the research in Chapter 4.

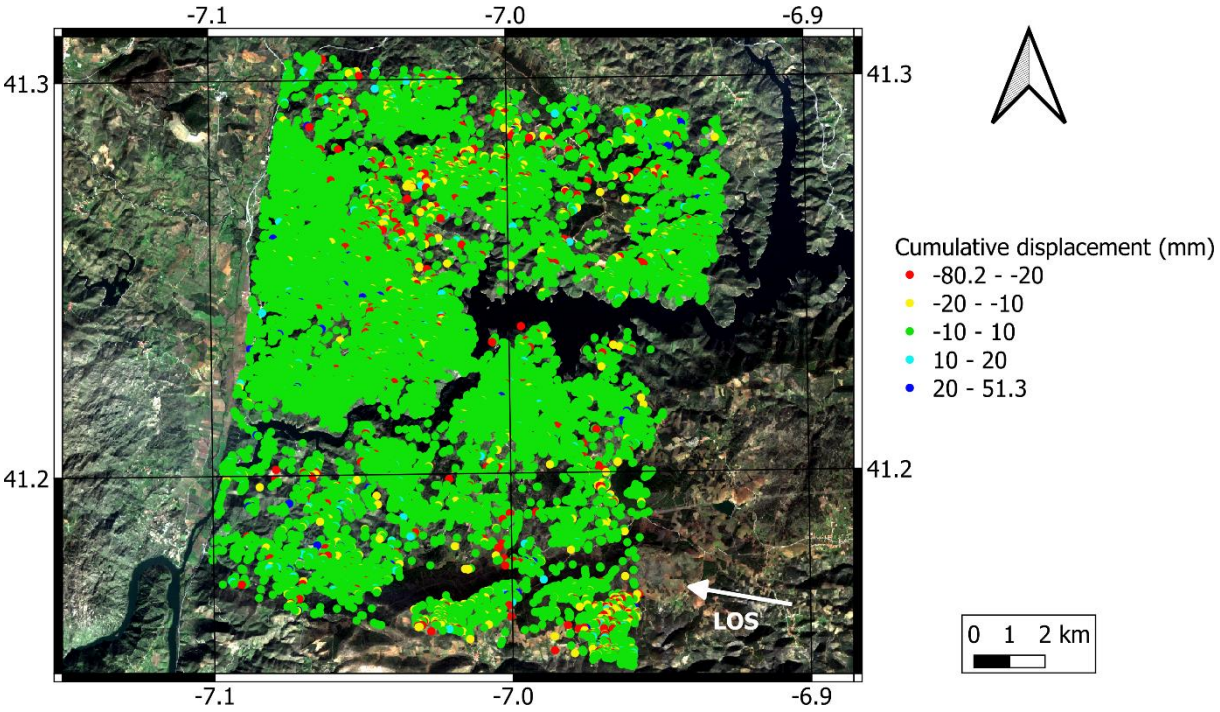

Figure 157 – LOS cumulative displacement map around Baixo Sabor dam. Background image is Sentinel-2 from February 2019. Coordinate grid in WGS84.

Table 19 – Amplitude of error interval for the precision analysis, at each vertex in the network.

Vertex ID	Error interval (mm)
1	2.6
2	3.2
3	2.6
4	3.3
5	2.9
6	3.2
7	2.5
8	2.7
9	2.3
10	3.0
11	2.7
12	2.7
13	2.9
14	2.7
15	1.9
16	2.7
17	2.3
18	3.0
19	3.3

Vertex ID	Error interval (mm)
20	2.9
21	2.5
22	2.7
23	2.7
24	3.2
25	3.3
26	2.9
27	2.6
28	3.2
29	2.6
30	3.0
31	3.3
32	2.3
33	2.6
34	2.5
35	3.2
36	2.1
37	2.9
38	3.3
39	2.7
40	2.3
41	2.5
42	2.3
43	2.3
44	2.6
45	2.9
46	2.9
47	2.1
48	3.0
49	2.6
50	3.2
51	2.3
52	2.9
53	3.3
54	2.6
55	2.9
56	2.5
57	3.3
58	2.5
59	2.7
60	3.0
61	2.7
62	3.3
63	3.0
64	2.6

Vertex ID	Error interval (mm)
65	2.6
66	3.0
67	2.9
68	2.9
69	3.3
70	3.2
71	2.6
72	3.3
73	3.3
74	2.7
75	2.6
76	2.7
77	3.2
78	2.5
79	3.0
80	3.0
81	2.5
82	2.6
83	3.3
84	3.3
85	2.7
86	3.3
87	3.0
88	2.5
89	3.3
90	3.3
91	3.0
92	3.0
93	3.2
94	3.2
95	3.0
96	2.6
97	3.3
98	3.3
99	2.6
100	3.2
101	2.6
102	3.3
103	3.0
104	3.2
105	2.9
106	2.9
107	2.6
108	3.3
109	2.3

Vertex ID	Error interval (mm)
110	3.3
111	3.2
112	3.3
113	3.3
114	2.7
115	2.3
116	3.0
117	2.7
118	2.7
119	2.7
120	3.2
121	2.5
122	2.9
123	2.6
124	2.3
125	2.9
126	3.2
127	2.9
128	2.5
129	3.2
130	2.3
131	2.6
132	3.2
133	2.5
134	3.3
135	3.0
136	2.9
137	2.5
138	3.3
139	3.3
140	2.5
141	3.0
142	3.2
143	3.2
144	3.0
145	3.0
146	2.5
147	2.7
148	2.6
149	2.1
150	3.0
151	2.6
152	2.7
153	2.7
154	2.1

Vertex ID	Error interval (mm)
155	2.9
156	3.0
157	2.7
158	2.6
159	3.2
160	2.7
161	2.9
162	2.3
163	2.1
164	2.5
165	2.9
166	3.3
167	2.5
168	2.7
169	2.6
170	3.3
171	2.9
172	2.7
173	2.6
174	0.1

Table 20 – Quadratic form of the residuals for the observations quality control, for each observation epoch.

Date	Quadratic form
June 12, 2016	0.000
July 6, 2016	0.061
July 18, 2016	2.598
July 30, 2016	2.215
August 11, 2016	6.466
August 23, 2016	2.344
September 4, 2016	1.834
September 16, 2016	0.691
September 28, 2016	0.009
October 10, 2016	0.020
October 22, 2016	0.221
November 3, 2016	0.180
November 15, 2016	1.457
November 27, 2016	3.960
December 9, 2016	0.241
December 21, 2016	0.007
January 2, 2017	0.712
January 14, 2017	0.794
January 26, 2017	1.568

Date	Quadratic form
February 7, 2017	2.042
February 19, 2017	2.202
March 3, 2017	0.016
March 15, 2017	2.032
March 27, 2017	1.055
April 8, 2017	2.110
April 20, 2017	7.826
May 2, 2017	0.462
May 14, 2017	0.218
May 26, 2017	2.807
June 7, 2017	6.584
June 19, 2017	2.302
July 1, 2017	0.010
July 13, 2017	0.016
July 25, 2017	6.257
August 6, 2017	2.301
August 18, 2017	0.515
August 30, 2017	6.936
September 11, 2017	1.210
September 23, 2017	0.566
October 5, 2017	0.695
October 17, 2017	1.695
October 29, 2017	0.349
November 10, 2017	0.134
November 22, 2017	4.626
December 4, 2017	2.391
December 16, 2017	1.309
December 28, 2017	0.075
January 9, 2018	0.518
January 21, 2018	2.226
February 2, 2018	8.205
February 14, 2018	5.815
February 26, 2018	6.323
March 10, 2018	8.738
March 22, 2018	3.318
April 3, 2018	0.985
April 15, 2018	0.006
April 27, 2018	11.761
May 9, 2018	0.075
May 21, 2018	0.887

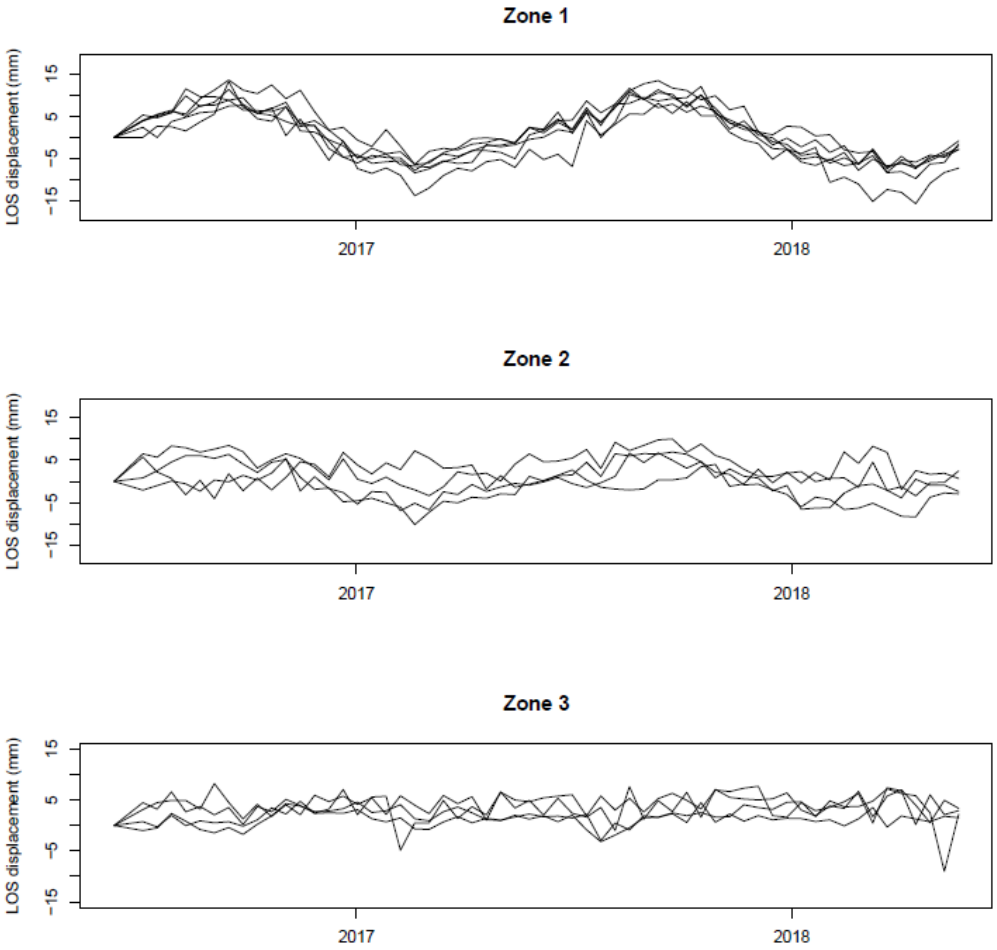

Figure 158 – Original LOS displacement time series for the vertices on each zone.

Table 21 – *A priori* and *a posteriori* standard deviations for LOS displacements at vertices on the dam.

	Standard deviation	
Vertex ID	*a priori*	*a posteriori*
1	2.0	2.0
2	1.9	1.8
3	2.3	2.2
4	2.0	2.1
5	2.1	2.3
6	1.7	2.0
7	1.5	2.0
8	1.8	2.1
9	2.1	1.9
10	2.4	1.9
11	1.8	2.1
12	2.0	2.0
13	1.9	1.8
14	2.4	2.5
15	2.1	1.6
16	2.0	1.9
17	1.9	2.0

Table 22 – *A priori* and *a posteriori* standard deviations for LOS displacements at vertices on the slopes.

	Standard deviation	
Vertex ID	*a priori*	*a posteriori*
1	1.9	2.0
2	2.3	1.6
3	1.9	2.0
4	2.4	2.1
5	2.1	2.3
6	2.3	2.2
7	1.8	2.1
8	2.0	2.2
9	1.7	2.3
10	2.2	2.0
11	2.0	2.0
12	2.0	2.0
13	2.1	2.2
14	2.0	2.2
15	1.4	2.4
16	2.0	2.1
17	1.7	2.1
18	2.2	1.9
19	2.4	2.2

	Standard deviation	
Vertex ID	*a priori*	*a posteriori*
20	2.1	2.4
21	1.8	2.1
22	2.0	2.6
23	2.0	2.5
24	2.3	2.6
25	2.4	2.4
26	2.1	2.2
27	1.9	2.2
28	2.3	2.2
29	1.9	2.0
30	2.2	2.4
31	2.4	2.2
32	1.7	2.1
33	1.9	2.1
34	1.8	2.2
35	2.3	2.2
36	1.5	2.3
37	2.1	2.2
38	2.4	2.0
39	2.0	2.2
40	1.7	2.1
41	1.8	2.4
42	1.7	2.1
43	1.7	2.1
44	1.9	2.2
45	2.1	2.1
46	2.1	1.9
47	1.5	2.0
48	2.2	2.0
49	1.9	2.1
50	2.3	2.2
51	1.7	2.1
52	2.1	1.9
53	2.4	1.9
54	1.9	2.0
55	2.1	2.1
56	1.8	1.6
57	2.4	2.3
58	1.8	1.7
59	2.0	1.3
60	2.2	2.3
61	2.0	1.9
62	2.4	2.5
63	2.2	1.9

	Standard deviation	
Vertex ID	*a priori*	*a posteriori*
64	1.9	1.9
65	1.9	1.9
66	2.2	2.2
67	2.1	2.0
68	2.1	1.6
69	2.4	2.2
70	2.3	1.7
71	1.9	2.3
72	2.4	1.9
73	2.4	2.3
74	2.0	2.2
75	1.9	1.7
76	2.0	2.3
77	2.3	1.5
78	1.8	2.4
79	2.2	2.0
80	2.2	2.5
81	1.8	1.9
82	1.9	1.2
83	2.4	2.5
84	2.4	1.7
85	2.0	1.8
86	2.4	1.6
87	2.2	1.5
88	1.8	1.3
89	2.4	1.5
90	2.4	2.5
91	2.2	2.3
92	2.2	1.9
93	2.3	2.3
94	2.3	1.4
95	2.2	2.8
96	1.9	2.2
97	2.4	1.6
98	2.4	2.7
99	1.9	2.2
100	2.3	2.3
101	1.9	1.8
102	2.4	1.8
103	2.2	2.6
104	2.3	2.4
105	2.1	2.6
106	2.1	2.3
107	1.9	2.6

	Standard deviation	
Vertex ID	*a priori*	*a posteriori*
108	2.4	2.1
109	1.7	1.7
110	2.4	2.5
111	2.3	2.5
112	2.4	2.5
113	2.4	2.4
114	2.0	2.2
115	1.7	1.9
116	2.2	2.0
117	2.0	1.5
118	2.0	2.3
119	2.0	2.4
120	2.3	2.5
121	1.8	2.5
122	2.1	2.4
123	1.9	2.2
124	1.7	2.4
125	2.1	2.2
126	2.3	2.2
127	2.1	2.3
128	1.8	2.2
129	2.3	1.8
130	1.7	2.3
131	1.9	2.4
132	2.3	2.5
133	1.8	2.2
134	2.4	2.4
135	2.2	2.3
136	2.1	2.4
137	1.8	2.4
138	2.4	2.5
139	2.4	2.4
140	1.8	2.4
141	2.2	2.4
142	2.3	2.7
143	2.3	2.0
144	2.2	2.4
145	2.2	2.5
146	1.8	2.5
147	2.0	2.3
148	1.9	2.3
149	1.5	2.5
150	2.2	2.3
151	1.9	2.2

	Standard deviation	
Vertex ID	*a priori*	*a posteriori*
152	2.0	2.5
153	2.0	2.4
154	1.5	2.2
155	2.1	2.6
156	2.2	2.1
157	2.0	2.0

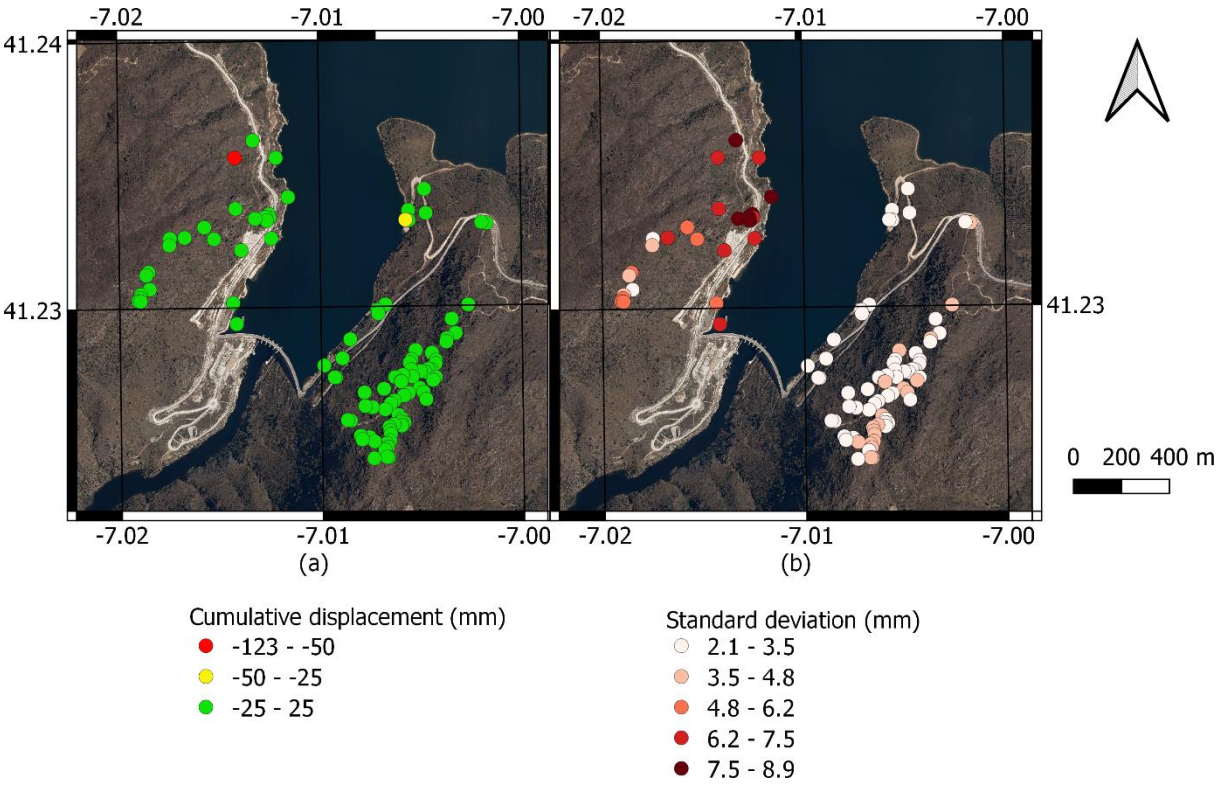

Figure 159 – Cumulative displacement along the slope direction (a) and standard deviation of displacement along the slope direction (b) for the vertices selected for slope monitoring. Coordinate grid in WGS84.

Table 23 – Parameters for cluster analysis at Baixo Sabor slopes; the symbol "/" separates the options selected at different tests.

Parametre	Value
Number of clusters	Automatic / 4
Coordinates of rectangular ROI (WGS84)	
Lower latitude	41.2194
Higher latitude	41.2452
Lower longitude	-7.0265
Higher longitude	-7.0049
Coherence threshold	0.9
Number of images	59
EPSG code of additional raster	3763
Year of the beginning of time series	2016
Sample number of first image in the beginning year	13
Year of the ending of time series	2018
Sample number of last image in the ending year	13
Cluster method	Complete
Additional data in raster format	Distance to river, slope, aspect

Annex A.3 – Uncertainty assessment

This Annex contains figures and tables that complement the research in Chapter 5.

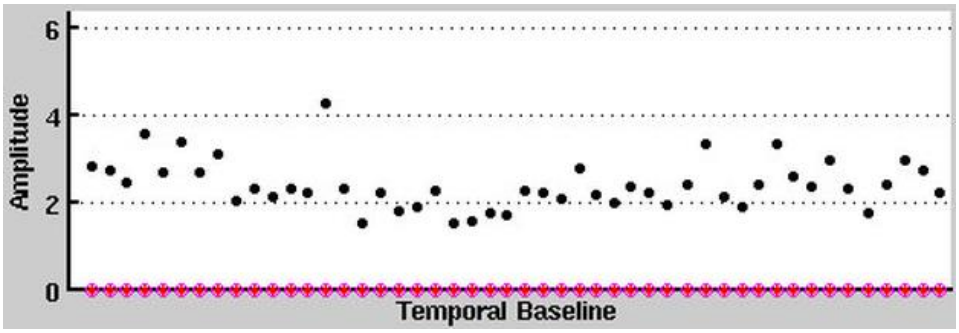

Figure 160 – Amplitude time series for a natural PS.

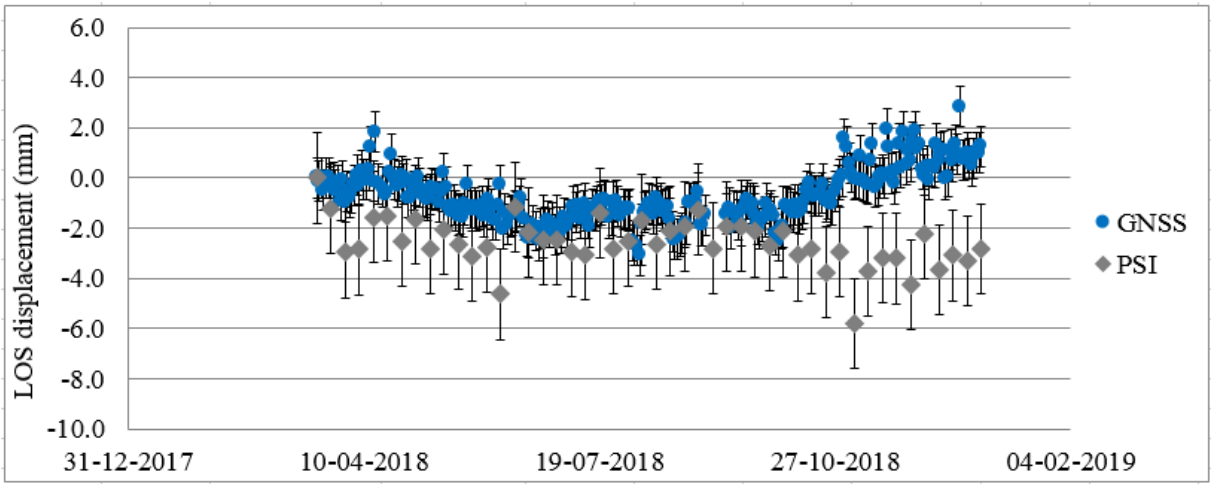

Figure 161 – LOS displacement from PSI and GNSS for the rectangular trihedral CR for the ascending pass in the static test; error bars are the uncertainty of double-differences.

Table 24 – Welch t test for PSI and levelling double-differences at rectangular trihedral CR oriented towards the ascending pass using the reference PS to the west of the CR, for the static test.

t-Test: Two-Sample Assuming Unequal Variances

	Variable 1	*Variable 2*
Mean	-2.8327083	-2.4194472
Variance	4.753318	1.6256869
Observations	48	13
Hypothesized Mean Difference	0	
df	33	
t Stat	-0.873017	
P(T<=t) one-tail	0.1944812	
t Critical one-tail	1.6923603	
P(T<=t) two-tail	0.3889623	
t Critical two-tail	2.0345153	

Table 25 – Welch t test for PSI and levelling double-differences at triangular trihedral CR oriented towards the ascending pass, for the static test.

t-Test: Two-Sample Assuming Unequal Variances

	Variable 1	*Variable 2*
Mean	-2.3508333	-1.3988114
Variance	2.2639865	1.0129692
Observations	48	13
Hypothesized Mean Difference	0	
df	28	
t Stat	-2.6917872	
P(T<=t) one-tail	0.0059286	
t Critical one-tail	1.7011309	
P(T<=t) two-tail	0.0118573	
t Critical two-tail	2.0484071	

Table 26 – Welch t test for PSI and levelling double-differences at rectangular trihedral CR oriented towards the descending pass using the reference PS to the west of the CR, for the static test.

t-Test: Two-Sample Assuming Unequal Variances

	Variable 1	*Variable 2*
Mean	-2.44	-2.0692513
Variance	4.3266085	1.3009927
Observations	48	13
Hypothesized Mean Difference	0	
df	36	
t Stat	-0.8500772	
P(T<=t) one-tail	0.2004503	
t Critical one-tail	1.6882977	
P(T<=t) two-tail	0.4009006	
t Critical two-tail	2.028094	

Table 27 – Welch t test for PSI and levelling double-differences at triangular trihedral CR oriented towards the descending pass, for the static test.

t-Test: Two-Sample Assuming Unequal Variances

	Variable 1	*Variable 2*
Mean	-0.96	-1.2680997
Variance	4.3903915	0.3174856
Observations	48	13
Hypothesized Mean Difference	0	
df	59	
t Stat	0.905047	
P(T<=t) one-tail	0.1845608	
t Critical one-tail	1.671093	
P(T<=t) two-tail	0.3691215	
t Critical two-tail	2.0009954	

Table 28 – Welch t test for PSI and theoretically expected double-differences at rectangular trihedral CR oriented towards the ascending pass, for the first sequence of imposed displacements test.

t-Test: Two-Sample Assuming Unequal Variances

	Variable 1	*Variable 2*
Mean	20.61428571	23.801676
Variance	146.7228571	235.67191
Observations	14	14
Hypothesized Mean Difference	0	
df	25	
t Stat	-0.60987846	
P(T<=t) one-tail	0.273723125	
t Critical one-tail	1.708140761	
P(T<=t) two-tail	0.54744625	
t Critical two-tail	2.059538553	

Table 29 – Welch t test for PSI and laboratory measured displacement double-differences at rectangular trihedral CR oriented towards the descending pass, for the first sequence of imposed displacements test.

t-Test: Two-Sample Assuming Unequal Variances

	Variable 1	*Variable 2*
Mean	79.02656567	76.80714286
Variance	2597.998842	2357.957637
Observations	14	14
Hypothesized Mean Difference	0	
df	26	
t Stat	0.11796151	
P(T<=t) one-tail	0.453502377	
t Critical one-tail	1.70561792	
P(T<=t) two-tail	0.907004755	
t Critical two-tail	2.055529439	

Table 30 – Welch t test for PSI and laboratory measured displacement double-differences at triangular trihedral CR oriented towards the descending pass, for the first sequence of imposed displacements test.

t-Test: Two-Sample Assuming Unequal Variances

	Variable 1	*Variable 2*
Mean	79.02656567	75.23571429
Variance	2597.998842	2442.727088
Observations	14	14
Hypothesized Mean Difference	0	
df	26	
t Stat	0.199781024	
P(T<=t) one-tail	0.421603081	
t Critical one-tail	1.70561792	
P(T<=t) two-tail	0.843206162	
t Critical two-tail	2.055529439	

Table 31 – Welch t test for PSI and levelling vertical double-differences at bidirectional CR, for the first sequence of imposed displacements test.

t-Test: Two-Sample Assuming Unequal Variances

	Variable 1	*Variable 2*
Mean	62.6737187	60.52308
Variance	1520.88877	1619.609
Observations	14	13
Hypothesized Mean Difference	0	
df	25	
t Stat	0.14082668	
P(T<=t) one-tail	0.44456772	
t Critical one-tail	1.70814076	
P(T<=t) two-tail	0.88913545	
t Critical two-tail	2.05953855	

Table 32 – Welch t test for PSI and GNSS vertical double-differences at bidirectional CR, for the first sequence of imposed displacements test.

t-Test: Two-Sample Assuming Unequal Variances

	Variable 1	*Variable 2*
Mean	59.884408	63.298726
Variance	1459.7863	1454.4469
Observations	14	157
Hypothesized Mean Difference	0	
df	15	
t Stat	-0.3204352	
P(T<=t) one-tail	0.3765295	
t Critical one-tail	1.7530504	
P(T<=t) two-tail	0.753059	
t Critical two-tail	2.1314495	

Table 33 – Welch t test for PSI and GNSS east – west double-differences at bidirectional CR, for the first sequence of imposed displacements test.

t-Test: Two-Sample Assuming Unequal Variances

	Variable 1	*Variable 2*
Mean	44.22254	47.508917
Variance	819.37427	757.81518
Observations	14	157
Hypothesized Mean Difference	0	
df	15	
t Stat	-0.4128875	
P(T<=t) one-tail	0.3427652	
t Critical one-tail	1.7530504	
P(T<=t) two-tail	0.6855305	
t Critical two-tail	2.1314495	

Table 34 – Welch t test for PSI and GNSS LOS double-differences at bidirectional CR, for the first sequence of imposed displacements test.

t-Test: Two-Sample Assuming Unequal Variances

	Variable 1	*Variable 2*
Mean	74.957143	77.385973
Variance	2310.058	2116.5888
Observations	14	157
Hypothesized Mean Difference	0	
df	15	
t Stat	-0.1818007	
P(T<=t) one-tail	0.4290866	
t Critical one-tail	1.7530504	
P(T<=t) two-tail	0.8581731	
t Critical two-tail	2.1314495	

Table 35 – Welch t test for PSI and levelling vertical double-differences at bidirectional CR, for the second sequence of imposed displacements test.

t-Test: Two-Sample Assuming Unequal Variances

	Variable 1	*Variable 2*
Mean	63.9708	62.93077
Variance	1955.68	1809.601
Observations	12	13
Hypothesized Mean Difference	0	
df	23	
t Stat	0.05983	
P(T<=t) one-tail	0.476404	
t Critical one-tail	1.713872	
P(T<=t) two-tail	0.952808	
t Critical two-tail	2.068658	

Table 36 – Welch t test for PSI and GNSS vertical double-differences at bidirectional CR, for the second sequence of imposed displacements test.

t-Test: Two-Sample Assuming Unequal Variances

	Variable 1	*Variable 2*
Mean	62.16382	36.974468
Variance	1868.0814	500.67827
Observations	12	94
Hypothesized Mean Difference	0	
df	12	
t Stat	1.9852001	
P(T<=t) one-tail	0.0352296	
t Critical one-tail	1.7822876	
P(T<=t) two-tail	0.0704592	
t Critical two-tail	2.1788128	

Table 37 – Welch t test for PSI and GNSS east – west double-differences at bidirectional CR, for the second sequence of imposed displacements test.

t-Test: Two-Sample Assuming Unequal Variances

	Variable 1	*Variable 2*
Mean	47.496925	28.332979
Variance	1078.636	284.90912
Observations	12	94
Hypothesized Mean Difference	0	
df	12	
t Stat	1.988093	
P(T<=t) one-tail	0.0350516	
t Critical one-tail	1.7822876	
P(T<=t) two-tail	0.0701031	
t Critical two-tail	2.1788128	